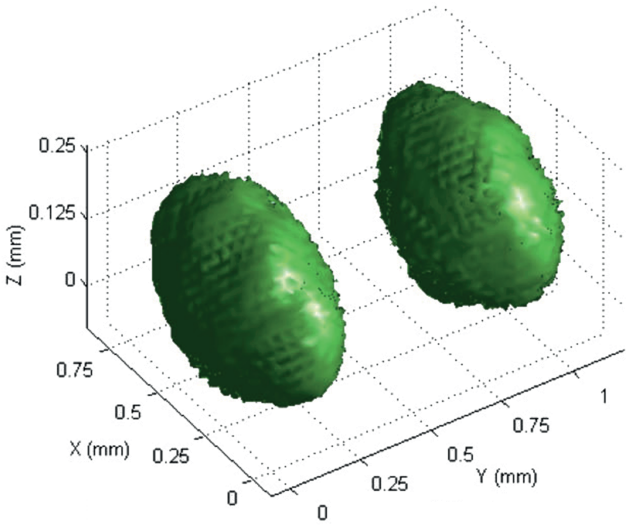


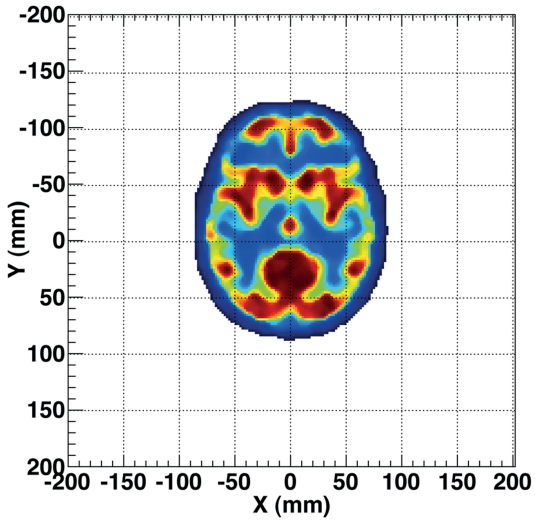


Paulo Jorge Magalhães Martins

# IMAGING TECHNIQUES IN RPC-PET

Tese de Doutoramento em Física, Especialidade de Física Experimental, orientada pelos Professores Doutores Paulo Alexandre Vieira Crespo e Rui Ferreira Marques e apresentada ao Departamento de Física da Faculdade de Ciências e Tecnologia da Universidade de Coimbra.

Julho 2014

· U C ·

Universidade de Coimbra


# Imaging Techniques in RPC-PET

Paulo Jorge Magalhães Martins

Department of Physics

University of Coimbra

A thesis submitted for the degree of
*PhilosophiæDoctor (PhD)*

July 2014

# Resumo

A tomografia por emissão de positrões baseada em detectores do tipo câmaras de placas resistivas (RPC-PET) foi proposta para aplicação em ensaios com pequenos animais e na prática clínica. Neste trabalho, apresentamos primeiramente resultados experimentais obtidos a partir de um protótipo RPC-PET de alta aceitação para pequenos animais.

Foram obtidas imagens de fontes do radioisótopo $^{22}$Na, uma quase pontual e outra planar. Usámos dois módulos de detectores RPC com uma área activa de $6.4 \times 6.4\,\mathrm{cm}^2$ e uma espessura de 5 mm, constituída por 6 vidros empilhados e 5 espaços gasosos definidos entre eles. Os dados adquiridos incluíram linhas de coincidência (LORs) inclinadas até um ângulo de $58\,^\circ$, tornando essencial a medida precisa da profundidade de interacção. A identificação dos espaços gasosos onde ocorreram as avalanches permitiu demonstrar a ausência de erro de paralaxe nas medidas realizadas com o RPC-PET para pequenos animais. A partir da reconstrução dos dados processados com o algoritmo *maximum likelihood expectation-maximization* (MLEM), obtivemos uma resolução espacial com largura a meia altura (FWHM) de 0.4 mm, excelente e estável. Em paralelo, continuámos a estudar as potencialidades de um protótipo RPC-PET de corpo inteiro e cama única, orientado para pessoas. Já foi anteriormente demonstrado por simulação que um *scanner* RPC-PET com 2.4 m de campo de visão axial (AFOV) é viável e permitirá o aumento de sensibilidade de pelo menos uma ordem de grandeza em relação aos *scanners* PET com cristais. Duas outras virtudes do RPC-PET são a sua capacidade de medição do tempo de voo (TOF) dos fotões e a elevada resolução espacial ao nível do detector.

Na segunda parte deste trabalho apresentamos um algoritmo de reconstrução, totalmente tridimensional, capaz de processar LORs muito inclinadas em sistemas com um AFOV longo, como é o caso do RPC-PET. Este algoritmo acrescenta um kernel ao algoritmo MLEM, baseado na informação de TOF. Com uma resolução temporal de 300 ps FWHM, já experimentalmente comprovada, é possível rejeitar 63% dos eventos dispersados no corpo humano. Exibimos imagens reconstruídas obtidas a partir de simulações do fantoma antropomórfico, NCAT, com lesões oncológicas situadas em diferentes locais do corpo humano. A comparação entre imagens conseguidas com resoluções temporais de 300 ps e 600 ps FWHM, permite observar uma detectabilidade acrescida associada à melhor resolução de TOF. Por último, são estudados os tempos de convergência da reconstrução. Um método inovador e alternativo, que consiste na divisão dos dados do corpo humano em nove regiões e na reconstrução independente desses dados com recurso a unidades de processamento gráfico (GPUs), permite uma reconstrução seis vezes mais rápida do que a reconstrução de corpo inteiro também com o auxílio de GPUs. A partir de dados de $1.6 \times 10^{10}$ aniquilações ocorridas durante uma aquisição de 7 minutos e para uma actividade injectada de 2 mCi, um *scanner* RPC-PET com uma resolução temporal de 300 ps FWHM permitirá obter uma imagem reconstruída apenas 4 minutos após o fim da aquisição. Podemos assim concluir que o RPC-PET está bem colocado para competir no mercado dos *scanners* PET comerciais.

# Abstract

Positron emission tomography based on resistive plate chambers (RPC-PET) has been proposed for both preclinical and clinical applications. We firstly present imaging results of needle-like and planar $^{22}$Na sources obtained with a prototype of a high-acceptance small-animal RPC-PET.

The two detector modules utilized in this experiment had an effective front face of $6.4 \times 6.4\,\mathrm{cm}^2$ and consisted of 5 gas gaps and 6 glass electrodes with a total thickness of 5 mm. The data included lines of response (LORs) inclined up to 58 °, and the depth of interaction (DOI) was accurately measured, demonstrating the parallax-free property inherent to RPC-PET. The maximum likelihood expectation-maximization (MLEM) reconstruction of the acquired data yielded an excellent and stable resolution of 0.4 mm full width at half maximum (FWHM). Concurrently, we pursued studies of a suggested whole-body single-bed RPC-PET. It has been shown by simulation that RPC-PET with an axial field-of-view (AFOV) of 2.4 m is feasible and yields an absolute sensitivity at least one order of magnitude superior to that of typical crystal-based PET scanners. In addition, RPC-PET offers an important time-of-flight (TOF) advantage and provides a potentially very-high spatial resolution at the detector level.

In the second part of this work, a fully three-dimensional reconstruction algorithm capable of processing the very inclined LORs from large AFOV systems such as RPC-PET is demonstrated. It relies on the application of a TOF-based-kernel into the MLEM algorithm. With the 300 ps FWHM time resolution, already experimentally demonstrated, a rejection of 63% of the body-scattered events is obtained. We present reconstructed results from

blind simulations corresponding to the anthropomorphic phantom, NCAT, with oncological lesions introduced into different locations within the human body. A comparison between 300 and 600 ps FWHM TOF reconstructed images is performed, with an increasing detectability being observed for a better TOF resolution. We finally compare issues related to image convergence speed. An alternative new approach, which consists in dividing the full-body data into nine different image regions that are reconstructed independently with graphical processing unit (GPU) assistance, provides a six times faster reconstruction compared with a GPU-based whole-body reconstruction. For a 300 ps FWHM RPC-PET scanner, this allows reaching a reconstructed image, that results from $1.6 \times 10^{10}$ annihilations within 7 minutes and upon injection of 2 mCi, just 4 minutes after the end of data acquisition. We conclude that RPC-PET is well oriented to compete with other commercial PET scanners in the global market.

To Inês

# Acknowledgements

I would first like to thank my supervisors for their constant support and guidance along this research project:

Professor Paulo Crespo, my advisor in the implementation of a reconstruction routine tailored to the potentialities of a single-bed whole-body RPC-PET. He came up with the strategies to address this challenge and taught me the scientific rigour. I thank him the long working hours to achieve the results presented in this thesis. His motivation, availability and friendship will hold forever.

Professor Rui Marques, who gave me precious advices during the period of this thesis. I thank him the encouragement since I first started working at LIP. The pleasure I have in working with radiation detectors has been always shared with him. I also thank the deep revision of my work at different stages of my research path. His motivation, availability and friendship will hold forever.

I would also like to thank the leader of the RPC-PET group for his hard work and guidance along these years:

Professor Paulo Fonte, my advisor in the determination of the spatial resolution of a small-animal RPC-PET prototype. As he once said: "We make a good team". He worked and guided me close-by for the development of the experimental setup and for the creation of the software tools that permitted to achieve the experimental results presented in this thesis. His motivation, availability and friendship will hold forever.

My acknowledgements to everyone else who contributed significantly to this work:

Dr. Alberto Blanco, Prof. Paulo Gordo, Prof. Fátima Ferreira Marques, Prof. Francisco Alves, Dra. Joana Ferreira, and Prof. Clara Magalhães, for their work and support in the construction of the needle-like source.

Luís Lopes, for teaching me how to construct RPC detectors and for his efforts on bringing out the ideal resistive ink. Nuno Carolino, for all his work with the RPC-PET electronics. Américo Pereira and Luís Lopes, who taught me how to learn from experience and how to solve the problems by myself.

Américo Pereira, Luís Lopes, Rui Alves, Joaquim Oliveira, Carlos Silva, Nuno Dias, and Orlando Cunha, for your dedication to your work. I really admire the efforts you put in everything you do. I also thank you the environment and the good mood that turn the working days easier.

Elisabete Neves, Teresa Dias, and Ricardo Caeiro, for having provided along these years an excellent administrative support, always with great kindness.

Dr. Miguel Oliveira, Prof. Helmut Wolters, Gonçalo Borges, João Martins, and João Silva, for their support to the computational work of this thesis, part of which has been performed in the HPC Milipeia center and in the Grid computing cluster.

Dr. Paul Segars, from Johns Hopkins University, for providing the software-based anthropomorphic phantom.

Dr. Alberto Blanco, Prof. Nuno Chichorro, Prof. Miguel Couceiro, as members of the RPC-PET group, I thank the numerous fruitful scientific discussions. I also thank Dr. Alberto Blanco for all the support given in the laboratory.

HADES DAQ group, for supplying the acquisition system that permitted to acquire the events of the small-animal RPC-PET prototype.

My colleagues, Sharif Ghithan and Luís Pereira, for all interesting discussions and companionship. Sharif is one of the most kind persons I ever met and it has been a pleasure to share the same office with him. I also thank Luís Pereira, for providing the Monte Carlo simulation code, which was adapted to simulate the events of the small-animal RPC-PET. Thank you Luís for the good mood that you bring to the office.

Hugo Simões, for reviewing the benefits of a true whole-body PET, thus emphasizing the virtues of an RPC-PET with axial field-of-view of 2.4 m. This review helped to complement this work.

I thank Laboratório de Instrumentação e Física Experimental de Partículas for providing me with all the institutional support needed for my work.

I also acknowledge the support given by the Fundação para a Ciência e a Tecnologia, through the grant SFRH/BD/45040/2008.

I owe a debt of gratitude to my mentors in earlier stages of my learning process, *Professora* Armanda, Prof. Helena Santos, and Prof. Etelvina Rita, who kept me on track for studying physics.

A special acknowledgement to my mentor, Professor José Raposo, a person that I extremely admire, and a great teacher that helped me enormously to get engaged with mathematics.

To my friends, Rui, Andreia, Andrêa, Zé, Idália, Luís, Miguel, Joana, Daniela, Marta, Manu, Philipp, and Michael, thank you for walking with me on this journey.

To Francisco, thank you very much for everything you have done for me.

To my family, all my gratitude for what they have given to me. Pai, Mãe, vocês são os meu pilares. Devo-vos tudo o que sou. Meu irmão, grande companheiro desta vida e meu mestre, foste sempre o exemplo que eu procurei seguir, até chegar aqui. À minha avó Filomena, obrigado pela tua sapiência, é tão bom conversar contigo. À Clara, agradeço-te teres-me sempre incentivado para a ciência. À Inês da Saragoça, à Bela e à Dete, obrigado por me terem ajudado a crescer entre vocês. À Lena e ao Félix por me trazerem

alegria numa praia sonolenta. À Joana Patrício, obrigado pelos teus conselhos sempre certeiros e pela profunda amizade. Ao Zé Carlos e à Augusta, obrigado por saberem tomar conta de nós. Ao b., que sem saber, foi uma grande companhia nas noitadas de trabalho.

Inês, se fores feliz, eu serei feliz.

# Contents

# List of Figures

## LIST OF FIGURES

# List of Tables

# List of Abbreviations

| | |
|---|---|
| **$^{18}$F-FDG** | 18-Fluorodeoxyglucose |
| **3D** | Three Dimensional |
| **ACS** | Absolute Central Point Source Sensitivity |
| **ADC** | Analog to Digital Converter |
| **ADMM** | Alternate Direction of Minimization Method |
| **AFOV** | Axial Field-of-View |
| **ART** | Algebraic Reconstruction Techniques |
| **AW** | Attenuation Weighting |
| **$BaF_2$** | Barium Fluoride |
| **BMI** | Body Mass Index |
| **CAD** | Computer-Aided Design |
| **CFOV** | Central Field-of-View |
| **CHUC** | Centro Hospitalar e Universitário de Coimbra |
| **CMRG** | Cerebral Metabolic Rate of Glucose |
| **CPU** | Central Processing Unit |
| **CRC** | Contrast Recovery Coefficient |
| **CsF** | Caesium Fluoride |
| **CT** | Computed Tomography |
| **CTS** | Central Trigger System |
| **CUDA** | Compute Unified Device Architecture |
| **CZT** | Cadmium Zinc Telluride |
| **DAQ** | Data Acquisition |
| **DEW** | Dual Energy Window |
| **DNL** | Differential Non-Linearity |
| **DOI** | Depth of Interaction |
| **DSP** | Digital Signal Processing |
| **ED** | End-Diastolic |
| **EF** | Ejection Fraction |
| **EM** | Expectation-Maximization |
| **ES** | End-Systolic |
| **ETW** | Estimation of Trues Method |
| **FBP** | Filtered Backprojection |
| **FEE** | Front-End Electronics |
| **FFT** | Fast Fourier Transform |
| **FORE** | Fourier Rebinning |
| **FOV** | Field-of-View |
| **FPGA** | Field Programmable Gate Array |
| **FSI** | Fine Structure Imaging |
| **GATE** | GEANT4 Application for Tomographic Emission |
| **GBe** | Gigabit Ethernet Standard |
| **GE** | General Electric |
| **GPU** | Graphical Processing Unit |
| **GRID** | Grid Computing Cluster |
| **GSO** | Gadolinium Oxyorthosilicate |
| **HADES** | High Acceptance Di-Electron Spectrometer |
| **HLD** | HADES List-Mode Data |
| **HPTDC** | High Precision Time to Digital Converter |
| **HV** | High Voltage |
| **ICNAS** | Instituto de Ciências Nucleares Aplicadas à Saúde |

**ISTA** Iterative Shrinkage/Thresholding Algorithm

**IT.** Iteration

**JFET** Junction Gate Field-Effect Transistors

**LNA** Low Noise Amplifier

**LOR** Line of Response

**LS** Line Source

**LSB** Least Significant Bit

**LSO** Lutetium Oxyorthosilicate

**LUT** Look-up-Table

**LuYAP** Lutetium-Yttrium Aluminum Perovskite

**LVDS** Low Voltage Differential Signaling

**LYSO** LutetiumYttrium Oxyorthosilicate

**MAP** Maximum a Posteriori Maximum Likelihood

**MC** Monte Carlo

**MCA** Multi-Channel Analyser

**MIF** Misidentified Fraction

**MIP** Minimum Ionizing Particle

**ML** Maximum Likelihood

**MLEM** Maximum Likelihood Expectation-Maximization

**MMIC** Monolithic Microwave Integrated Circuit

**MRI** Magnetic Resonance Imaging

**MSPS** Mega-Samples Per Second

**MTW** Multiple Time Window

**MWPC** Multiwire Proportional Chamber

**NaCl** Sodium Chloride

**NCAT** NURBS-Based Cardiac-Torso

**NEC** Noise Equivalent Count

**NECR** Noise Equivalent Count Rate

**NEMA** National Electrical Manufacturers Association

**NES** Noise Equivalent Sensitivity

**NSCLC** Non-Small-Cell Lung Carcinoma

**OI** Optical Imaging

**OSEM** Ordered Subset Expectation-Maximization

**PC** Principal Component

**PCA** Principal Component Analysis

**PCB** Printed Circuit Board

**PECL** Positive Emitter-Coupled Logic

**PET** Positron Emission Tomography

**PMT** Photomultiplier

**PRD** Positron Range Distribution

**PSAPD** Position Sensitive Avalanche Photodiodes

**PSF** Point Spread Function

**PVC** Polyvinyl Chloride

**QGS** Quantitative Gated SPECT

**R** Random

**RAMLA** Row-Action Maximum Likelihood

**RBI-EMML** Re-Scaled Block-Iterative Expectation-Maximization

**RF** Radio Frequency

**RMSE** Root Mean Squared Error

**ROI** Region of Interest

**RPC** Resistive Plate Chamber

**RT** Radiotherapy

**S** Scatter

**SAI-UTSW** Small Animal Imager - University of Texas Southwestern Medical Center

**SBDIS** Stanford Breast Dedicated Imaging System

**SF** Scatter Fraction

**SiPM** Silicon Photomultiplier

**SNR** Signal-to-Noise Ratio

**SPECT** Single Photon Emission Computed Tomography

**SRF** Scatter Rejection Fraction

**SSH** Secure Shell

**SSQ** Sum-of-Squares

**SSRB** Single-Slice Rebinning

**SSS** Single Scatter Simulation

**T** True

**TDC** Time to Digital Converter

**TEW** Triple Energy Window

**TFO** Trapezoidal Filter Output

**TOF** Time-of-Flight

**TRB** HADES TDC Read-out Board

**tRPC** Timing Resistive Plate Chamber

**TTL** Transistor-Transistor Logic

**TV** Total Variation

**VOI** Volume of Interest

**WB** Whole-Body

# 1

# Introduction

## 1.1 Overview

Positron emission tomography (PET) has been dominated by scintillation crystals since its creation in the mid-1970s. In the same decade, the first gamma ray detecting system based on gaseous detectors for applications in nuclear medice has been proposed [1]. The problem for the application of multi-wire proportional chambers (MWPCs) in PET was their low efficiency in conjunction with difficulties in matching the performance of scintillation detectors in terms of counting-rate, timing resolution or energy resolution [2].

In 2000, Fonte *et al.* developed timing RPCs (tRPCs) [3], opening perspectives of affordable and reliable high-granularity large-area TOF detectors, with an efficiency and a time resolution comparable to existing, at the time, scintillator-based TOF technology, but with significantly, up to an order of magnitude, lower price per channel. In 2003, Blanco *et al.* addressed the feasibility of PET based on RPCs (RPC-PET) [4]. The extremely good time and position resolutions of RPCs were, at the time, already very promising.

Later, the time resolution of the tRPCs intended for a TOF-PET system was measured [5], demonstrating a very competitive TOF resolution of 300 ps full width at half maximum (FWHM), for photon-photon coincidence. The image spatial resolution has also been measured by means of a first small animal RPC-PET prototype, demonstrating sub-millimeter resolutions of 0.51 mm FWHM using filtered backprojection (FBP) and 0.31 mm FWHM after reconstruction by a maximum likelihood

expectation-maximization (MLEM) type algorithm [6].

Concerning sensitivity, simulations of an optimized complete small-animal RPC-PET system suggest values of up to 2.1% at the center of the field-of-view (CFOV) [6]. Monte Carlo (MC) simulations aiming at full-body human PET systems with an axial field-of-view (AFOV) in the order of 200 cm indicate that the sensitivity of such systems may exceed the present crystal-based PET technology by a factor up to 20 [7]. This result is dominated by the solid angle, and it grows strongly with the AFOV and with the axial acceptance angle [8]. This sensitivity enhanced value was obtained with the NEMA NU-2 1994 protocol which, however, does not correlate directly with lesion detectability. For that reason, we assessed the planar (slice) sensitivity with a NEMA NU2-2001 line-source phantom, which is better correlated to lesion detectability [9]. For 1.5 m scans (head to mid-legs), the planar sensitivity of RPC-PET is expected to outperform 16-cm (22-cm) AFOV scanners by a factor 9.2 (5.3) without considering the TOF benefit. An additional sensitivity gain, by a factor 4 to 5 in respect to non-TOF scanners, is expected when the 300 ps FWHM TOF resolution of RPC-PET is taken into account.

The simulations also suggest that scatter fraction is almost independent from the geometry of the scanner [8]. Object scatter in an anthropomorphic phantom seems to be similar for RPC-PET and modern, scintillator-based scanners [9]. In this work, we will show that RPC-PET benefits further if its TOF information is utilized to exclude scatter events occurring outside the anthropomorphic phantom.

System count rate performance simulations for the small-animal RPC-PET indicate a peak noise equivalent count rate (NECR) up to 320 kcps for a total activity of 88 MBq in the phantom [6]. The peak NECR of the whole-body single-bed RPC-PET, following the NEMA NU-2 2001 protocol, is expected to be of 167 kcps at 7.6 kBq/cm$^3$ ($\tau_{ps} = 3$ $\mu$s). For a 1 $\mu$s dead time in the position signals ($\tau_{ps}$), no peak NECR was found, the NECR being 349 kcps at 7.6 kBq/cm$^3$ [10].

The main contributions of our group to the development of RPC-PET technology here summarized have been fully reviewed by Crespo *et al.* [11].

Spatial resolution is a major feature of small-animal PET. The limit, so far, remains within the 0.8 mm FWHM (e.g. [12, 13, 14, 15, 16]). Moreover, commercial preclinical PET systems do not yet go beyond what is necessary to accurately study the functioning of the small structures of small-animal organs, like the ones of mice brain. A different

well-established concept is explored and developed here in order to provide PET images with very high resolution at lower cost. We believe that RPC-PET is well positioned to compete in the short term with existing scanners in the global market.

Present reconstruction algorithms are not prepared to handle lines of response (LORs) within a large AFOV of 2.4 m. Therefore, a different reconstruction algorithm must be implemented in order to deal with whole-body single-bed RPC-PET needs. This algorithm should be tailored to the TOF capabilities of RPC-PET and capable of integrating the attenuation correction calculated from computed tomography (CT) data. Due to the high sensitivity of such large AFOV systems, a much lower dose has to be injected into the patient, and the acquisition time will be shortened. To test the performance and assess image quality, we simulate one popular anthropomorphic phantom used in medical imaging research, the NURBS-based cardiac-torso (NCAT) phantom. By inserting simulated lesions in the phantom, we can perform a lesion detectability study and evaluate the advantages of a 300 ps FWHM TOF resolution. Finally, the fact that reconstruction speed is a major issue, pushed us towards delivering reconstructed images in the shortest time possible. The reconstruction algorithm developed within this thesis is proven to meet such needs.

## 1.2 Objectives

The objectives pursued with the present work are the determination of the image spatial resolution of a small-animal RPC-PET prototype and the development of a reconstruction routine tailored to the capabilities of human whole-body single-bed RPC-PET. The motivations for this work emanate from the increasing potential of PET technology in the assessment of novel drug therapies (small-animal RPC-PET) and detection of smaller lesions in the largest number of patients possible for diagnosing oncological disease in the shortest scan time possible (human RPC-PET).

Since it is possible today to mimic a plethora of human diseases in small animals, as well as to study their underlying physiological mechanisms, preclinical imaging devices are experiencing an exponential growth in research facilities around the world. Spatial resolution and sensitivity are two essential features in small-animal PET that distinguish a current scanner from an outstanding one. We will focus on the former of those features, keeping in mind, e.g., the efforts of neuroscientists to differentiate the small

structures of mice brain. By reaching our sub-millimeter target, we believe that we are prepared to rise to the challenge of penetrating in the preclinical imaging market.

The proposed fully-3D reconstruction algorithm must be capable of processing the very inclined lines of response from large axial field-of-view systems, such as RPC-PET. We will present a direct-TOF implementation of the MLEM and ordered subsets expectation-maximization (OSEM) algorithms allowing for all events acquired with RPC-PET being directly processed without rebinning, and directly inserted inside the object image by means of a TOF kernel. Such kernel avoids slow voxel-wise image navigation, and permits handling list-mode data. Time consumption in both data acquisition and image reconstruction is a major concern in the clinical field. Pedroso de Lima considers that the main goals of the functional studies with radioisotopes are the detection and quantification of the radioactive tracers in the human body as a function of time. He thus looks at time as the most important and characteristic variable in nuclear medicine [17]. Therefore, this work tries to emphasize the time needs, together with lesion detectability capabilities of an RPC-PET system. We believe that the reduction of the time required to obtain a PET image combined to an increasing detectability are of fundamental importance given the challenges of providing a fast and accurate diagnostic imaging.

In the first part of this thesis, we present the steps taken from detector construction towards system spatial resolution determination. In the second part, we develop the whole-body reconstruction routine by means of simulated data and present several reconstructed images. The following objectives for this work were defined:

**Aim 1: To produce 40 RPC detector modules, 10 for each of the 4 heads of the scanner.** These modules complete the small-animal RPC-PET scanner. Each detector consists of six stacked glass electrodes defining five 0.35 mm gas gaps.

**Aim2: To assemble an experimental setup with two modules parallel to each other, separated by 4 cm, and image a source placed between them.** The setup assemblage also includes handling with dedicated front-end electronics for charge signal amplification and time signal read-out. A step motor is used to move the source in the vertical direction by remote control. A data acquisition (DAQ) system provided by the HADES group [18] permits to collect the charge signal in 192 ADC channels. Several hardware measurements to ensure proper operation of the RPC detectors and the overall system are performed.

**Aim3: To outline a processing chain capable of providing the charge and time signal information for coincidence events.** The time consumed in this step should be minimized. Therefore, faster codes to decode and digitally process the data must be conceived. Most random events are removed at this stage, the remaining being eliminated afterwards by software cuts on the time spectra. For this study of small-animal RPC-PET, no scatter or attenuation correction are involved.

**Aim4: To develop an event analysis capable of identifying the gap where the avalanche developed and its fine positioning in the detector.** We make use of clustering and multivariate statistical techniques ("$k$-means" algorithm and principal component analysis (PCA), respectively) to measure the depth of interaction. Following the approach of other authors [19, 20, 21], the fine positioning method determines the position distribution of the triggered events in the detector.

**Aim5: To develop a reconstruction routine tailored to the needs of the small-animal RPC-PET scanner and determine its image spatial resolution.** Although reconstruction time is not as critical as in human RPC-PET, the reconstructed images should be obtained in reasonable short time. We simulate two phantoms and recreate the experiment in order to validate the reconstruction. The data obtained from the imaging of two sources are reconstructed and the point spread function profiles determined, allowing to extract the image spatial resolution.

**Aim6: To develop a reconstruction routine tailored to the needs of the human RPC-PET scanner.** The anthropomorphic phantom NCAT (adapted to Geant4) is used to validate the reconstruction routine. We have used a voxelized version of the NCAT phantom to simulate the whole-body activity distribution and the attenuated photon emission from the human body. We simulate $1.6 \times 10^{10}$ annihilations corresponding to an injected activity of just 2 mCi for an acquisition time of 440 s. Six lesions with 10 mm diameter are simulated in the anthropomorphic phantom with a lesion to background activity ratio of 10:1. A method to reject the scattered events based on its TOF information is investigated. Then, a proper attenuation correction based on the NCAT attenuation phantom is performed. A study on the TOF kernel filling determines the number of samples inside the Gaussian kernel of 300 ps FWHM. The list-mode data is reconstructed with MLEM and OSEM, including a TOF probability density function. To accelerate the convergence speed of the algorithm, a

multi-threaded GPU-based parallelization of the reconstruction code is proposed. Additionally, a TOF-assisted data division method is suggested with the data being divided into nine different body regions. This permits to reconstruct the data from those regions independently and in a much faster way. Several reconstructed images of the whole-body NCAT phantom are shown and the contrast recovery coefficients of the six lesions are calculated.

## 1.3 Outline

This thesis, *Imaging Techniques in RPC-PET*, lies within the project of construction of a prototype for small-animal and for a human RPC-PET. It is divided in two parts: (i) small-animal RPC-PET imaging (experimental results); (ii) human RPC-PET imaging (simulation results).

Chapter 2 was designed to be the framework for the imaging techniques presented in the following chapters. This chapter begins by reviewing the physical principles inherent to the interactions of photons with matter. Then, it presents the concepts underlying PET technology and subsequently integrates those concepts with the results achieved in our RPC-PET group. Sections 2.3 and 2.4 describe the state of the art of RPCs applied to PET [11]. A summarized description of state of the art small-animal PET scanners, and a brief review on the image reconstruction methods are addressed in sections 2.5 and 2.6, respectively.

The aim of chapters 3 and 4 is to determinate the image spatial resolution of a small-animal RPC-PET prototype. Chapter 3 describes the experimental setup and reports the hardware utilized to measure the charge and time signals induced by the avalanches developed in the RPC detectors. A detailed description of the different stages of detector construction and of the structure of a $^{22}$Na needle-like source are presented. A brief summary of the attributes of the DAQ system and its adaptation to the RPC-PET needs is explored and some hardware measurements are made in order to verify the proper operation of the detectors and the front-end electronics (FEE). Chapter 3 concludes by presenting the estimated relative activity of the sources utilized in this work. Chapter 4 complements the previous chapter with software tools to decode, process, analyse and reconstruct the data obtained from the imaging of three radioactive sources: disk, needle-like and planar. The raw data provided by the DAQ system is

decoded and digitally processed in the shortest time possible. Software analysis tools were developed to identify the fine positioning of the photon hits in the detectors and the gap where the avalanche developed. By acquiring accurate information on the 3 coordinates $(X, Y, Z)$ of the hits, we reconstruct the image with a custom-made MLEM-based algorithm. Then, we assess the spatial resolution of the system by taking profiles along the $Y$ coordinate and through the maximum intensity voxel of the reconstructed images. By placing two detector at a distance of 45 cm from each other, we attempt to measure the contribution of the non-collinearity effect to the spatial resolution. The content of chapters 3 and 4 gave rise to a paper "Towards Very High Resolution RPC-PET for Small Animals" by P. Martins *et al.*, that is currently under consideration for publication in Journal of Instrumentation [22]. This work was also presented, in the form of posters, to the 2012 IEEE Nuclear Science Symposium and Medical Imaging Conference (NSS/MIC), to the 2013 IEEE NSS/MIC and partially published in the respective conference proceedings [23, 24].

Chapter 5 presents the results of a reconstruction routine tailored to the potentialities of a whole-body single-bed human RPC-PET. In order to cope with data from the whole AFOV and incorporate the TOF information in a reconstruction algorithm, we choose an iterative algorithm capable of processing that data in list mode format: the TOF-weighted MLEM and the TOF-weighted OSEM. An attenuation correction based on the NCAT attenuation phantom is coupled to the reconstruction. To study this phantom, $1.6 \times 10^{10}$ annihilations are simulated in Geant4, corresponding to an injected dose of 2 mCi for an acquisition time of 440 s. An alternative cylindrical phantom corresponding to a patient with a large body mass index is also simulated. Both simulations assume $^{18}$F-FDG as the decaying solution and the list-mode outputs are constructed for an RPC- PET system with 120 gaps and, based on previously published simulation studies [9], and a singles detection efficiency to 511 keV perpendicular gamma rays of 19.4%. Datasets of lesions are inserted by simulation in the anthropomorphic phantom in order to study the lesion detectability performance of the reconstruction. A method of scatter rejection based on TOF information is presented, which combined to the lower efficiency of an RPC-PET detector with 121 plates to scattered events, permits to reject a high fraction of such events. A study of the number of samples inside the TOF kernel is performed in order to trade-off the image improvement stabilization and the reconstruction time. Taking into account the time

needs of such reconstruction, a TOF-assisted method for the division of the data into nine different body regions is proposed. Such method together with the performance capabilities of GPUs permits to deliver reconstructed images in a remarkably short time. A comparison between images obtained with a 300 ps FWHM TOF resolution (provided by RPC-PET) and a 600 ps FWHM TOF resolution (given by state of the art PET scanners) is presented. We put a focus on the most critical lesions, i.e., axillary and inguinal lesions and show axial slices containing those lesions. The contrast recovery coefficient (CRC) values are calculated for all lesions as a means of assessing image quality and lesion detectability. The material in this chapter is based on a paper, "A Direct Time-of-Flight Reconstruction for Whole-Body Single-Bed RPC-PET" by P. Martins *et al.*, that is currently under consideration for publication [25]. This work was also presented, in the form of posters, to the 2011 IEEE NSS/MIC, to the 2012 IEEE NSS/MIC and partially published in the respective conference proceedings [26, 27].

The conclusions from this thesis, together with future work suggestions, are presented in chapter 6.

Several appendices complementing this work were left out from the main body of the thesis for ease of reading. In order to support sections 2.4, 2.5 and 2.6 of the framework chapter, we explore, respectively in appendices A, B and C, the advantages of a true whole-body PET, the applications in small-animal PET and the current trends in image reconstruction. A summarized theoretical framework of the statistical techniques utilized in chapter 4 for gap identification and fine positioning is presented in appendices D and E.

# 2

# Framework

This chapter, divided into seven different sections, provides an overview on the topics discussed in the following chapters. The contents of the sections seek to follow the structure of the thesis. The physical principles of the interactions of photons with matter are briefly addressed in section 2.1, thus providing a guidance for the understanding of positron emission tomography (PET) concept, which is fully exposed in section 2.2, where an extensive presentation of the concepts underlying PET technology is carried out. Data correction performed in chapter 5 is also discussed in this section. Section 2.3 summarizes the main properties of resistive plate chambers (RPCs) and the contribution of our group towards the development of RPC-PET. The principal advantages provided by a true whole-body imaging scanner covering the whole human length such as RPC-PET are introduced in section 2.4. The benefits in terms of diagnostic accuracy are also addressed to justify the investment in such technology. Section 2.5 proceeds with the review of the features of the small-animal PET systems and their main applications. These devices are expanding briskly all over the world, so a special attention is given to the developments in this segment. Section 2.6 concludes with an overview over the reconstruction algorithms, with special focus on the iterative methods to be adopted in chapter 5.

## 2.1 Interaction of photons with matter

Medical imaging is originally focused on the visualization of the anatomical structures or physiological functions of the human body. To understand the image formation process, the underlying physical principles must be previously addressed. Sources of radiation are often used in medical imaging to provide images of the internal anatomy or physiology of a patient. The emitted radiation travels through the patient and interacts with radiation detectors to provide the information necessary to form the images of the patient [28]. The radiation transfers energy to the surrounding material when it interacts with matter. Ionization or excitation of the atoms usually happens through the path of the radiation in the absorbing material, being more probable with a larger mass of the emitted particle. High-energy photons, being massless, are highly penetrating. Depending on their energy, four major types of interactions may take place: Rayleigh or coherent ($rayl$) scattering, photoelectric effect ($\tau$), Compton ($\sigma$) scattering, and pair production ($\kappa$). There are other mechanisms, such as triplet production ($tripl$) and photo-nuclear reactions ($nph$), where gamma rays induce decay in the nucleus, and which require energies greater than ∼10 MeV. The only relevant physical interactions for PET are the photoelectric effect and the Compton scattering.

### 2.1.1 Coherent scattering

Coherent (Rayleigh) scattering involves the interaction of a photon with a bound electron of an atom in which the direction of the incident photon is changed with essentially no loss in energy, very little energy being transferred to the target atom. During the coherent scattering event, the electric field of the incident photon's electromagnetic wave expends energy, causing all electrons in the scattering atom to oscillate in phase. The atomic electron cloud immediately radiates this energy, emitting a photon of the same energy but in a slightly different direction. This interaction occurs mainly with very low energy x-rays, like those used in mammography (15 to 30 keV), and for events involving atoms with high atomic number. In soft tissue, coherent scattering accounts for less than 5% of x-ray interactions above 70 keV and only accounts for at most 12% of interactions at approximately 30 keV [29].

### 2.1.2 Photoelectric effect

The photoelectric effect is an interaction of photons with orbital electrons in an atom. The photon transfers its total energy to an electron, usually, a inner shell electron. The energy of the incident photon $h\nu$ overcomes the binding energy of the electron $E_B$, and the latter is ejected from the atom with a kinetic energy $E_e = h\nu - E_B$. An electron from a higher shell will then drop down to occupy the vacancy, releasing energy in the from of x-rays, or emitting a second electron (Auger electron). The total photoelectric cross section strongly depends upon atomic mass $Z$, and $h\nu$ [30]. N.C. Rasmussen has determined the empirical exponent of $Z$ which best fits a power law for the photoelectric cross-section

$$\sigma_\tau \simeq CZ^n \tag{2.1}$$

for fixed values of $h\nu$. The exponent $n$ is found to increase from about 4.0 to 4.6 as $h\nu$ increases from 0.1 MeV to 3 MeV. Davisson [31] has found the best approximate theoretical values of the photoelectric cross section to be those obtained by blending the Sauter-Stobbe values below 0.35 MeV [32, 33], the Hulme results between 0.35 MeV and 2 MeV [34], and Hall's high-energy approximation above 2 MeV [35, 36, 37].

The photoelectric effect dominates in human tissue at energies below *ca.* 100 keV. With the development of combined PET/CT, it is extremely important to understand the physics of photoelectric effect when adjusting the attenuation factors from the x-ray CT to the values appropriate for 511 keV radiation. Because of the much lower average $Z$ of glass, the Compton effect in RPC-PET is much more pronounced than in crystal-based PET scanners.

### 2.1.3 Compton scattering

Compton scatter involves the interaction of a photon with a "free" electron in which only a portion of the incident photon energy is absorbed, another photon being re-emitted with a reduced energy. The photon undergoes a change in direction and the electron is ejected from the atom. Its energy after the Compton scattering is given by

$$h\nu' = \frac{h\nu}{1 + \frac{h\nu}{m_0c^2}(1 - cos\theta)}, \tag{2.2}$$

where $m_0c^2$ is the rest-mass energy of the electron (511 keV), $h\nu$ is the energy of the incident photon and $\theta$ is the angle of the scattered photon. The angular distribution of the scattered $\gamma$-rays is predicted by the Klein-Nishina formula for the differential scattering cross section [38]:

$$\frac{d\sigma}{d\Omega} = Zr_0^2 \left(\frac{1}{1+\alpha(1-cos\theta)}\right)^2 \left(\frac{1+cos^2\theta}{2}\right) \left(1 + \frac{\alpha^2(1-cos\theta)^2}{(1+cos^2\theta)[1+\alpha(1-cos\theta)]}\right), \tag{2.3}$$

where $\alpha = h\nu/m_0c^2$ and $r_0 = \frac{1}{4\pi\epsilon_0}\frac{e^2}{m_ec^2}$ is the so-called classical electron radius [39]. The scattering probability decreases with an increasing scattering angle and reaches its minimum value for $\theta = 180°$. For low energies, i.e., for very small values of $\alpha$, equation 2.3 reduces to

$$\frac{d\sigma}{d\Omega} = \frac{r_0^2}{2}(1+cos^2\theta), \tag{2.4}$$

which is the Thomson equation [40]. For positron annihilation radiation (511 keV, $\alpha = 1$) in tissue, equation 2.3 can be reduced for first-order scattered events to give

$$\frac{d\sigma}{d\Omega} = \left(\frac{1}{2-cos\theta}\right)^2 \left(1 + \frac{(1-cos\theta)^2}{(2-cos\theta)(1+cos^2\theta)}\right). \tag{2.5}$$

Fig. 2.1 (left) is a polar plot of equation 2.3. There is a tremendous increase in the fraction of forward-scattered photon, as $\alpha$ increases. Fig. 2.1, right, plots the functions in equations 2.2 and 2.5 in the range $0 - \pi$ (rad) [41].

### 2.1.4 Pair production

When a $\gamma$-ray exceeds in energy a value corresponding to twice the electron mass ($2m_ec^2 \simeq 1.02$MeV) the process of pair ($e^+e^-$) production (also called $\gamma$-conversion) becomes energetically possible, the energy in excess of $2m_ec^2$ being shared as kinetic energy of both $e^+$ and $e^-$ [42]. The cross section for pair production is proportional to $Z^2$. At high energies it becomes independent of the energy of the photon and screening of the electric field of the nucleus by the atomic electrons has to be taken into account. Then the cross section becomes [43]

$$\sigma_{pair} \approx \frac{7}{9}\frac{A}{N_A}\frac{1}{X_0} \tag{2.6}$$

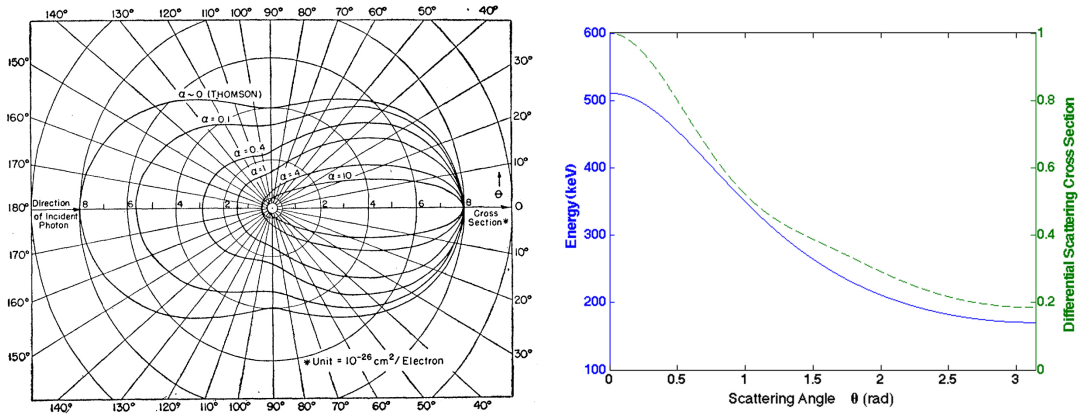


**Figure 2.1:** Compton effect. Left: Differential cross section per unit solid angle for the number of photons scattered at the angle $\theta$ [Eq. 2.3 ]. From [31]. Right: Differential scattering cross section (broken line) and energy of the emitted photon (solid line) for Compton-scattered annihilation photons.

This effect dominates at energies above 100 MeV for carbon [44]. Pair production is of no consequence in diagnostic x-ray imaging because of the high energies required for it to occur [29].

The relative importance of the three major types of $\gamma$-ray interaction (photoelectric effect ($\tau$), Compton effect ($\sigma$), pair production $\kappa$) is shown in fig. 2.2, being the shadowed region the one relevant for PET.

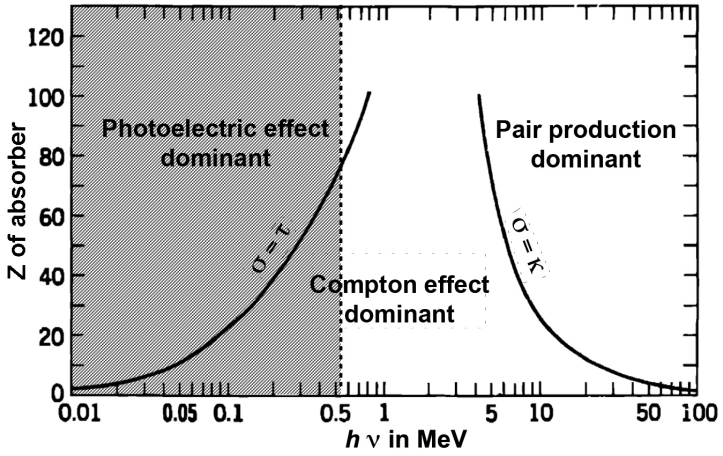


**Figure 2.2:** Relative importance of the three major types of $\gamma$-ray interaction. The lines correspond to values of $Z$ and $h\nu$ for which two effects equal probability. Adpated from [30].

### 2.1.5 Photon attenuation

The total atomic cross section is given by the sum of the cross sections for all of the individual processes [45]

$$\sigma_{tot} = \sigma_\tau + \sigma_\sigma + \sigma_{rayl} + \sigma_\kappa + \sigma_{tripl} + \sigma_{nph} \tag{2.7}$$

An example of the total cross-section as a function of photon energy for carbon is shown in fig. 2.3.

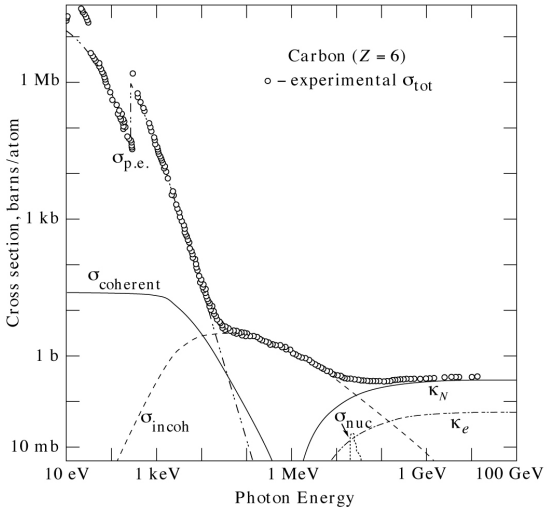


**Figure 2.3:** Contributions of (a) atomic photo-effect $\tau$, (b) coherent (Rayleigh) scattering, $\sigma_{rayl}$, (c) incoherent (Compton) scattering, $\sigma_\sigma$, (d) nuclear-field pair production, $\kappa_n$, (e) electron-field pair production, $\kappa_e$, and (f) nuclear photo-absorption, $\sigma_{nph}$, to the total measured cross section, $\sigma_{tot}$ (circles) in carbon over the photon energy range 10 eV to 100 GeV. From [46].

After presenting the major processes by which photons interact with matter, we can now examine some of the overall effects of these processes on a beam of photons as it passes through an absorber.

The probability of a photon traversing a given amount of absorber without any kind of interaction is just the product of the probabilities of survival for each particular type of interaction. Thus, a collimated $\gamma$-ray beam of initial intensity $I_0$ after traversing a thickness $x$ of absorber will have a residual intensity $I$ of unaffected primary photons equal to

$$I_x = I_0 e^{-\mu_0 x}, \tag{2.8}$$

where the quantity $\mu_0$ is the total linear attenuation coefficient. This attenuation coefficient is a measure of the number of primary photons which suffer interactions per unit path length in a medium. For example, for 100 keV photons traversing soft tissue, the linear attenuation coefficient is 0.016 $mm^{-1}$. This means that for every $10^3$ mono-energetic photons incident upon a 1 mm thickness of tissue, approximately 16 will be removed from the beam, either by absorption or scattering [29].

For any type of interaction, the mass attenuation coefficient is the linear coefficient divided by the density. The mass attenuation coefficient is related to the total cross section by

$$\mu/\rho \ (cm^2 \cdot g^{-1}) = \frac{\sigma_{tot}}{u \cdot A}, \tag{2.9}$$

where $u$ is the atomic mass unit and $A$ is the relative atomic mass of the target element [45]. These mass attenuation coefficients are really of more fundamental value than are the linear attenuation coefficients, because the former are independent of the actual density and physical state of the absorber. Fig. 5.13 shows the mass attenuation coefficients for soft tissue as function of energy.

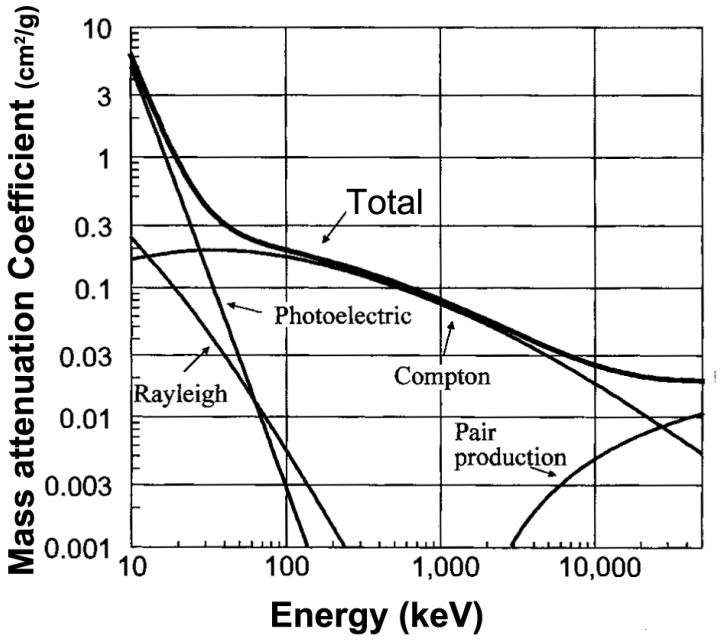


**Figure 2.4:** Graph of the photoelectric, Compton, Rayleigh, pair production, and total mass attenuation coefficients for soft tissue as a function of energy. Adapted from [29].

## 2.2 Fundamentals of positron emission tomography

Positron emission tomography (PET) is an outstanding functional imaging technique for the quantification and localization of physiological and pathophysiological activities and processes *in vivo* [47]. The basic insight for the development of PET consisted on the recognition that positron decay provides the opportunity for a coincidence detection system. This can be achieved by setting detectors that are able to capture photons, emitted in nearly 180°, originating from the annihilation process that follows the decay of a $\beta^+$ radionuclide. These detectors were originally configured on a circumferential array with an associated read-out electronics and a mathematical algorithm was conceived to reconstruct three-dimensional images of the analyzed biological probes of the living body. By labelling biochemical molecules with positron-emitting isotopes of carbon, nitrogen, oxygen, or fluorine, it was possible to image biological processes in animals and humans. These insights led Phelps to invent the first PET scanner in 1973 [48].

The medical applications are vast, ranging from the imaging of the metabolic function of the living, developing or aging brain and heart, to the changing metabolic states occurring in diseases such as Alzheimer's disease and cancer. PET provides early diagnosis and monitors the therapeutic responses in several types of cancer. PET imaging probes of neurotransmitters are employed to study the neuronal functions in neurological and psychiatric diseases, such as multi-infarct dementia, Huntington's disease, Alzheimer's disease, Parkinson's disease, depression, and adult and childhood epilepsies.

As the field of medical imaging rapidly evolves towards interdisciplinary, new techniques have emerged, combining the anatomical information provided by the computed tomography (CT) and by the magnetic resonance imaging (MRI) to the functional information provided by PET. Nowadays, PET is already a well-established world-wide medical diagnostic tool present in advanced hospitals and diagnostic centers.

### 2.2.1 Positron annihilation

The $\gamma$-rays are electromagnetic radiation emitted from the nucleus after a spontaneous nuclear decay and are typically associated to the emission of an $\alpha$ or $\beta$ particle. Moreover, they can be originated from the positron-electron annihilation process, with the

resulting annihilation radiation being produced outside of the nucleus, and often outside of the positron-emitting atom. The energy of the produced radiation is equivalent to the sum of the rest mass of the electron and positron. That energy is carried out by the two emitted photons travelling nearly at 180°. PET explores the almost perfect collinearity of the emitted photons to define the line of response (LOR) of the event that intersects two points in the detectors and crosses the point where the annihilation took place [41].

In 1895, Röntgen produced the first X-rays, and a year later Becquerel observed the spontaneous radiation emission from uranium. In 1899, Rutherford distinguished the $\alpha$-rays from $\beta$-rays, as two different particles emitted from natural radioactive decays. He would coin the term $\gamma$-ray for the most penetrating radiation, an emission from radium already discovered by Villiard in 1900. The $\beta$-decay involves the emission of an electron or a positron from the nucleus, together with another particle, firstly proposed by Pauli, in 1931, named neutrino. The general equation for positron decay from an atom is

$$ {}^{A}_{Z}X \rightarrow {}^{A}_{Z-1}Y + {}^{0}_{1}\beta^{+} + \nu^{e} + Q \ (+e^{-}), \tag{2.10} $$

where $Q$ is the energy released during the positron emission shared between the daughter nucleus, $Y$, the electron neutrino, $\nu^e$, and the positron, ${}^{0}_{1}\beta^{+}$.

According to the Fermi theory of $\beta$ decay, the shape of an allowed $\beta$-ray spectrum is given by

$$ N(\eta)d\eta = \left(\frac{64\pi^4 m_o^5 c^4 g^2}{h^7}\right)|P|^2 F(Z,\eta)\eta^2(W_o - W)^2 d\eta, \tag{2.11} $$

where $\eta$ e $W$ are respectively the momentum and the total energy (including the rest energy $m_0c^2$) and are related by $W^2 = \eta^2 + 1$. $N(\eta)d\eta$ is the probability for the emission of a $\beta$-ray whose momentum lies between $\eta$ and $\eta + d\eta$, when the nuclear disintegration energy is $W_0 = (E_{max}/m_oc^2) + 1$ and screening by atomic electrons is neglected. In a non-relativistic scenario, the Fermi function $F_N(Z,\eta) \simeq 2\pi y/(1-e^{-2\pi y})$, where $y = -Z\alpha(W/\eta)$, with $\alpha \simeq 1/137$ being the fine-structure constant and $|Z|$ the nuclear charge of the decay product. The squared modulus of the transition matrix element $|P|^2$ can be interpreted as the degree of overlap of the nucleon wave functions for the initial and final states, which is of the order of unity for allowed transitions [30].

The so-called Fermi coupling constant $g$ is related with the coupling constant of the weak interaction $g_W$ and the mass of the $W$-boson $m_W$ by the following expression

$$\frac{g}{(\hbar c)^3} = \frac{\sqrt{2} g_W^2}{8 m_W^2} = 1.16637(1) \times 10^{-5}\ GeV^{-2}. \tag{2.12}$$

Experimental tests of eq. 2.11 have been made. A nearly ideal case is $Cu^{64}$

$$\begin{array}{lll} & \beta^- \ + \ {}_{30}Zn^{64} & E_{max} = 0.57\ MeV \\ \nearrow & & \\ {}_{29}Cu^{64} & & \\ \searrow & & \\ & \beta^+ \ + \ {}_{28}Ni^{64} & E_{max} = 0.66\ MeV \end{array} \tag{2.13}$$

which emits allowed $\beta^-$ and $\beta^+$ spectra of comparable energy. In fig. 2.5, it is depicted the momentum and kinetic energy spectra of positrons emitted in the decay of $^{64}$Cu.

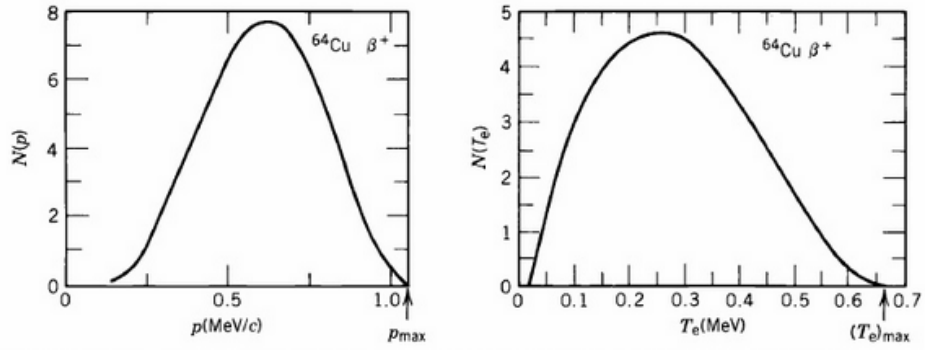


**Figure 2.5:** Momentum and kinetic energy spectra of positrons emitted in the decay of $^{64}$Cu. From [49], after [30].

Fig. 2.6 shows the calculated energy spectra for several nuclides used in PET imaging and the table 2.1 presents some of their most important features.

After being emitted from the nucleus, the positrons lose kinetic energy by interactions with the surronding matter, being the innelastic colisions with atomic electrons the dominant mechanism, thus inducing a deflection in the positron path. The positron eventually combines with an electron when both are essentially at rest and then the emisson of the $\gamma$-rays occurs. A metastable intermediate species, called positronium, may arise resulting from a bound state between the positron and an electron. It has a mean life of approximately $10^{-7}$ s and occurs with high probability in gases and metals, but represents just one-third of cases in water and human tissue.

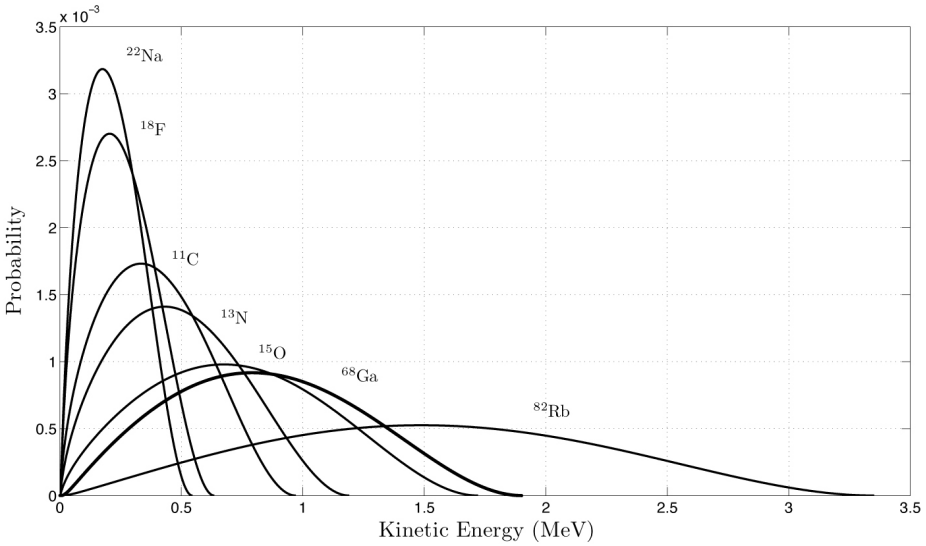


**Figure 2.6:** Calculated spectra of some positron-emitting nuclides of interest in PET. From [50].

| **Nuclide** | $T_{1/2}$ | $\mathbf{E}_{max}$ (MeV) | $\beta+$ **branching ratio** | **Use in PET** |
|---|---|---|---|---|
| $^{11}$C | 20.4 min | 0.96 | 100% | Labeling of organic molecules |
| $^{13}$N | 9.97 min | 1.2 | 100% | $^{13}NH_3$ |
| $^{15}$O | 122 s | 1.73 | 100% | $^{15}O_2$, $H_2{}^{15}O$, $C^{15}O$, $C^{15}O_2$ |
| $^{18}$F | 109.8 min | 0.63 | 97% | [$^{18}$F]-DG, $^{18}$F |
| $^{22}$Na | 2.6 y | 0.55 | 91% | Assessing system spatial resolution |
| $^{62}$Cu | 9.74 min | 2.93 | 97% | [$^{62}$Cu]-ATSM, [$^{62}$Cu]-PTSM |
| $^{64}$Cu | 12.7 h | 0.65 | 18% | [$^{64}$Cu]-DOTA-trastuzumab |
| $^{68}$Ga | 67.6 min | 1.89 | 88% | [$^{68}$Ga]-EDTA, [$^{68}$Ga]-PTSM |
| $^{76}$Br | 16.2 h | 3.98 | 54% | Imaging of Norepinephrine Transporter |
| $^{82}$Rb | 1.27 min | 3.4 | 95% | Generator-produced perfusion tracer |
| $^{86}$Y | 14.7 h | 1.4 | 33% | Quantitative imaging |
| $^{94m}$Tc | 52 min | 2.4 | 72% | $\beta^+$-emitting version of $^{99m}$Tc |
| $^{124}$I | 4.17 d | 2.13 | 22% | Iodinated molecules, quantitative imaging |

**Table 2.1:** Properties of some positron-emitting nuclides of interest in PET. From [41].

### 2.2.2 Positron range and non-collinearity

The distance travelled by the positron after emission adds some uncertainty to the localization of the decaying nucleus, which is the main goal of PET. This uncertainty is a consequence of the positron range and increases with increasing initial energy of the released positron. Due to the tortuous path of the positron in matter, it is difficult to estimate the range of the positrons based on their energy alone. Therefore, empirical measurements must be performed in order to determine the mean positron range in a specific material. For instance, the mean positron range in water varies from 0.6 mm for $^{18}$F ($E_{max}$ = 0.63 MeV) to 5.9 mm for $^{84}$Rb ($E_{max}$ = 3.4 MeV). The blurring effect on PET images ranges from a few tenths of a millimeter up to several millimeters [2]. Despite the long path length travelled by positrons, in what concerns PET imaging only the perpendicular distance from emission position to the line-of-response matters and causes mispositioning (see fig. 2.7).

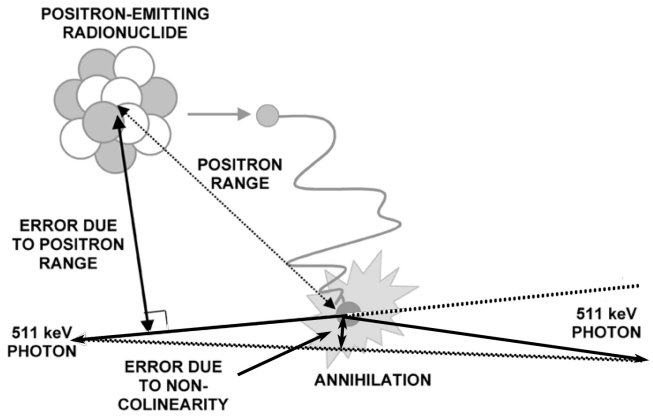


**Figure 2.7:** Illustration of the error in the determination of the location of the emitting nucleus due to positron range and photon non-collinearity. Adapted from [2].

An extensive research on the contribution of the positron range distribution (PRD) to the RPC-PET sinogram and image spatial resolution[1], as well as the calculation

[1]The acquired data may be represented in a sinogram, i.e., the angle $\phi$ versus the distance to the center of the scanner, $D$, of LORs with the same polar angle, $\theta$. The relationship between the point in the plane, $(X, Y)$, and the point in the sinogram, $(\phi, D)$ is given by: $D = Xcos\phi + Ysin\phi$. The point spread function (PSF) on the sinogram, $PSF_s$, is obtained by integrating the sinogram, $S(\phi, D)$, along the $\phi$ axis (sum of all projections). The PSF in the image, $PSF_i$, is calculated as the 1D profile across the maximum of the reconstructed image. The positron range $PSF_s$ and $PSF_i$ ($pPSF_s$ and $pPSF_i$) were calculated for each isotope by Blanco [50] and contain the contribution of positron range to both PSFs.

of the dependence of the spatial resolution on the energy of the positron emitted by seven radioisotopes, have been both carried out by Blanco [50]. Several groups have also measured [51], computed [52], or simulated [53] the distribution of the positron annihilation sites. It reveals a non-Gaussian nature, being best fitted by exponential functions.

Positron range limits the ultimate resolution attainable by PET. This constraint could be overcome by using strong magnetic fields [54, 55, 56, 57]. A magnetic field collinear with the axis of the scanner may improve the spatial resolution in the plane orthogonal to the axis. When the magnetic field strength increases up to 10 T, the system spatial resolution in directions orthogonal to the field for $^{15}$O, $^{68}$Ga and $^{82}$Rb is comparable to that of $^{18}$F without the magnetic field [57]. The positron range distribution may also in theory be deconvolved from the PET image [58, 59]. However, such approach requires high statistics, otherwise deconvolution leads to noise amplification. An alternative way is the inclusion of the positron range distribution information into iterative reconstruction algorithms.

The non-collinearity effect comes from the fact that positron and electron are not completely at rest when they annihilate. The initial energy of the positrons is irrelevant, since they lose most of that energy before they annihilate, becoming independent of the radionuclide but dependent on the temperature. Although the error introduced by non-collinearity effect is mainly dependent on the diameter of the PET scanner, it does not largely influence the spatial resolution of small-animal PET systems and for the state of the art clinical PET scanners is still far from significantly interfering with the system spatial resolution.

The small net momentum of the electron and the positron before annihilation means that the emitted annihilation photons will not be at exactly 180°, but rather with a distribution of angles around 180°. The distribution of emitted angles in water is Gaussian with a full width at half maximum (FWHM) of approximately 0.5° [58, 60]. However, PET imaging assumes that the emission is exactly back to back, leading to an error in the corresponding LOR. The angular uncertainty resulting from non-collinearity causes a Gaussian blurring whose magnitude (in mm FWHM) is given by $0.0044R$, where $R$ is the radius of the tomograph detector ring [61]. In section 4.7, we will further develop this concept and present some measurements with the small-animal RPC-PET system.

The non-collinearity contribution can also be reduced by a factor of 1.5 by cooling room temperature to -4 °C, and by a factor of 5 by cooling down to -144°C [62]. While this represents a substantial improvement, it is not a practical solution for *in vivo* studies.

### 2.2.3 Coordinate system and body planes

The dimension along the scanner axis is usually referred to as axial (see fig. 2.8). The dimensions within the plane perpendicular to the axis, the transaxial plane, are referred to as tangential if vertical, or radial if horizontal. The angle that the transaxial $(x-y)$ plane makes with the $z$-axis is referred to as the polar angle $\theta$, and the rotated $(x-y)$ plane defines an azimuthal angle $\phi$, around the object. In 2D PET, data are acquired for $\theta \approx 0°$, while in 3D PET, the polar angle can be opened up to the desired acceptance for trading-off between sensitivity gain and scatter increase.

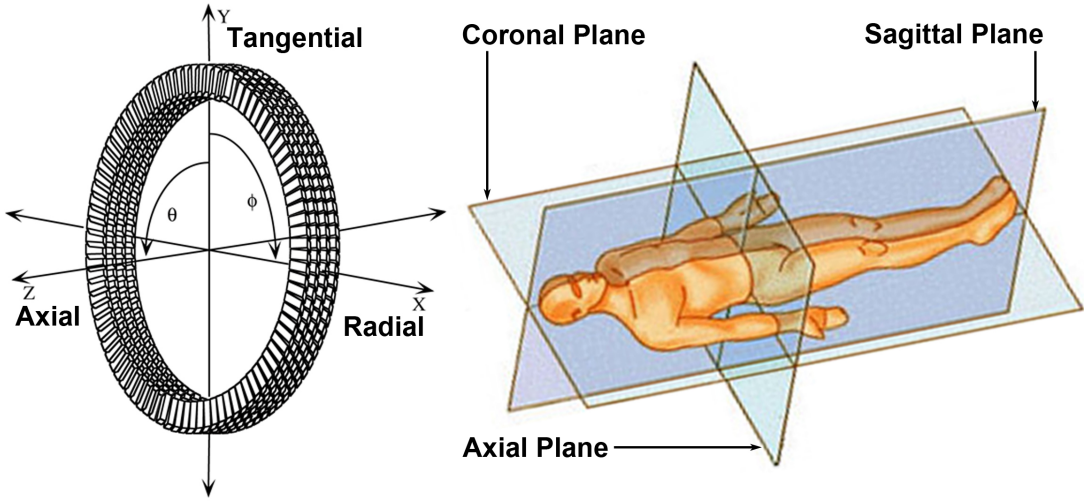


**Figure 2.8:** Coordinate system of a full-ring PET scanner (left) and planes of the body used in anatomical terminology (right). Adapted from [41] and [63].

In what respects anatomical terminology, we have the following body planes:

(i) Coronal Plane (or Frontal Plane): a vertical plane running from side to side, thus dividing the body or any of its parts into anterior and posterior;

(ii) Sagittal Plane (or Lateral Plane): a vertical plane running from front to back, thus dividing the body or any of its parts into right and left sides;

(iii) Transverse Plane (or Axial Plane): an horizontal plane, dividing the body or any of its parts into upper and lower parts.

For a better visualization of the body planes, see fig. 2.8. This terminology will be adopted in chapter 5 to show the reconstructed images of the anthropomorphic phantom. In chapter 4, the reconstructed images of the radioactive sources will have a slight alteration in the terminology employed, with the axes $X$ and $Z$ interchanged. The axial plane, at right angles to the long axis of the small-animal body, will be defined by the $Y - Z$ axes, and the sagittal plane will be defined by the $X - Y$ axes.

### 2.2.4 Type of detected events

Event detection in PET relies on electronic collimation (electronic coincidence detection). Two photons are detected by two opposite detectors, which are connected electronically, thus being capable to generate a valid event (coincidence) within a predefined electronic time window. The subsequent LOR formed between those detectors must be within a valid acceptance angle of the tomograph. This angle defines a volume where the positron annihilation may take place, and which is called the field-of-view (FOV). This is characterized by an area in the transaxial plane, transaxial FOV, and a distance along the axial axis, axial FOV (AFOV). Crystal-based PET scanners are able to measure the energy of the photons within a certain window, and the criteria for both photons being within the selected energy window must be also fulfilled to consider the event as valid.

All the events that meet the above requirements are called prompts. However, most of them are unwanted events as illustrated in fig. 2.9.

The terminology commonly used to describe the different types of events in PET is:

(i) A *single* event is a single photon counted by a detector. A PET scanner typically converts between 1% and 10% of single events into paired coincidence events[64]

(ii) A *true coincidence* is an event that emerges from a single positron-electron annihilation. The two annihilation photons both reach detectors on opposite sides of the tomograph without interacting significantly with the surrounding atoms and are recorded within the coincidence timing window;

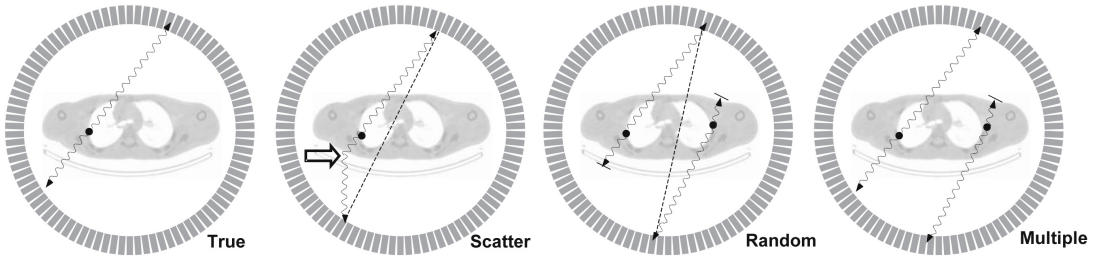


**Figure 2.9:** Illustration of the four main coincidence event types. The black dot indicates the annihilation point. From left to right: true coincidence, where both photons are detected without interaction with the object; scattered coincidence, where one or both of the photons undergo a Compton interaction (arrow); random coincidence, resulting from two annihilation positrons in which one photon from each positron annihilation is considered; multiple coincidence, arising from two positron annihilations in which three or more photons are counted. Adapted from [64].

(iii) A *random coincidence* occurs when two nuclei decay at approximately the same time. After annihilation of both positrons, four photons are emitted. Two of these photons from different annihilations are counted within the timing window and considered to correspond to the same positron, while the other two are lost. The amount of random events is a function of the activity, and their count rate between two detectors $a$ and $b$ is given by:

$$R_{ab} = 2\tau N_a N_b, \tag{2.14}$$

where $N_i$ is the single event rate counted by detector $i$, and $2\tau$ is the coincidence window width. The random event rate is approximately proportional to $N^2$. There are typically two methods for removing random events: by estimating the random event rate from measurements of the single event rates, or by employing a delayed coincidence timing window. Anyhow, both methods lead to an increase of the statistical uncertainty in true coincidence rates, so it is importante to keep the coincidence time window reasonably narrow. Further developments on the rejection of these type of events for an RPC-PET system will be addressed in section 2.4.2;

(iv) *Multiple events* happen when more than two photons are detected by distinct detectors within the same coincidence time window. Such events, whose rate depends on the detector count rate, are usually discarded;

(v) *Scattered events* arise when one or both photons from a single positron annihilation detected within the coincidence timing window have undergone a Compton interaction. Compton scattering may occur either within the imaged object or within the detector. The LOR assigned to the scattered event is uncorrelated with the position of the annihilation event. This is a common concern shared by RPC-based and crystal-based PET scanners. In chapter 5, we will develop the method of rejection of the body-scattered events by an RPC-PET system. Since Compton scattering causes a loss in the photon energy, it is important for crystal-based PET scanners to provide a good energy resolution in order to reject scattered events. Despite the absence of energy resolution in the RPC-PET system, its lower efficiency to low-energy photons (see fig. 2.36 (right)) contributes to the rejection of those unwanted events. If not corrected, the scattered events produce a low spatial frequency background that reduces contrast. This is probably the most difficult correction to perform in PET. The fraction of scattered events can range from 15% to well over 50%, depending on the size of the object, and on the geometry and energy resolution (or energy sensitivity) of the PET scanner [2].

### 2.2.5 Features of PET systems

PET systems exhibit many variations in design and different type of detectors may be employed. Despite this work focuses on the RPC detectors, the most common detectors used in PET are scintillators. The configuration of these systems varies greatly from restricted axial field of view, discrete (block-detector) systems to large, open, 3D designs. With such a range of variables, assessing performance for the purposes of comparing the capabilities of different scanners is a challenging task [64].

To objectively compare the performance of different clinical PET systems, the National Electrical Manufacturers Association (NEMA) has developed guide-lines on how certain performance parameters, such as spatial resolution and sensitivity, should be evaluated and presented [65, 66, 67, 68].

#### 2.2.5.1 Spatial resolution

Spatial resolution measures how closely two points can be resolved, i.e., the shortest distance at which two point sources are still seen as distinct [2]. It is usually character-

ized by measuring the FWHM of the profile obtained when one point source is imaged, the PSF.

In RPC-PET, the spatial resolution is mainly conditioned by the positron range and the non-collinearity effect, while in crystal-based PET scanners, other sources of error may contribute to the spatial resolution degradation.

The non-collinearity related blurring for an 80 cm diameter whole-body PET scanner with a typical acceptance angle of 45° is about 2 mm, but for a 12 cm diameter small-animal PET scanner this reduces to 0.3 mm [69, 70].

In a PET camera with 3 mm system spatial resolution, the loss of spatial resolution due to the positron range accounts for 1.3% in bone and 3.5% in soft tissue, but increases up to 22.5% in lung tissue for $^{18}$F. The corresponding figures are, respectively, 2.9%, 9.3% and 45.0% for $^{11}$C and 37.9%, 68.9% and 167% for $^{82}$Rb [70, 71].

From the hitherto mentioned blurring effects, there are other contributions to the degradation of the spatial resolution only present in crystal-based PET scanners. The width of the detector element is usually the dominating factor, because of its relation with the solid angle coverage and the initially unknown position of interaction within the crystal. Additionally, optical multiplexing possibly employed to reduce the number of electronic channels may cause imperfect decoding. Finally, the sampling error that arises from a non uniform sampling of the LORs in the scanner FOV, creates a degradation factor that has been empirically observed to multiply all the other contributions by a factor of 1.25 [72].

Although the response functions of these effects are not described by a Gaussian (notably the detector response and the positron range), it is assumed that the intrinsic reconstructed spatial resolution $G$, for a point source located at a radius $r$ from the center of a detector ring is given by

$$G = 1.25\sqrt{(d/2)^2 + s^2 + (0.0044R)^2 + b^2 + \frac{(12.5r)^2}{r^2 + R^2}} \quad (mm\ FWHM), \tag{2.15}$$

where $d$ is the crystal width, $s$ is the positron range, $b$ is the crystal decoding factor, and $R$ is the detector ring radius [61].

Moses considers that the ultimate spatial resolution just relies on the crystal width, the positron range, and the non-collinearity terms [61], the fundamental uncertainties that cannot be overcome. According to the author, considering a zero width detector, the positron range and the non-collinearity factors would combine to 0.67 mm FWHM

for preclinical PET cameras and 1.83 mm FWHM for clinical PET scanners. These would be the fundamental limits of spatial resolution, despite his assumption that practical PET cameras could nonetheless be made with resolutions of 2.36 mm FWHM and 0.84 mm FWHM for clinical and pre-clinical PET cameras, respectively [61].

After all, contrary to Moses predictions, Blanco has demonstrated a sub-millimeter spatial resolution uniform on the entire FOV of approximately 0.5 mm FWHM, experimentally measured with a point-like $^{22}$Na source for a system diameter of 60 mm [50]. In chapter 4, we will present additional results of the spatial resolution of the small-animal RPC-PET system in line with Blanco's achievements.

The spatial resolution of a human wide AFOV RPC-PET system has been studied by Couceiro [73]. Considering the photon non-collinearity effect, a detector depth of interaction resolution of 3.44 mm, and detector readout binnings of 1 and 2 mm, the spatial resolutions computed as the mean of FWHM of PSFs in three orthogonal directions ($X$, $Y$, and $Z$) were 1.47 $\pm$ 0.0 and 2.17$\pm$0.1 mm, respectively. The detailed simulations suggest that the physically limited image spatial resolution for full-body FOV RPC-PET will be less than 1 mm FWHM, including detection-process and non-collinearity errors. This study also indicates that the attainable resolution will be dominated by the accuracy of the readout system.

**Depth of interaction** The thick scintillation detectors used for PET imaging suffer from a geometric effect, which is referred to as depth of interaction (DOI), associated to the varying penetration depth of the photons in the scintillator (see fig. 2.10). Since many PET systems do not measure the DOI within the crystal, the measured position of intersection is projected to the entrance surface of the detector.

As shown in fig. 2.10, the photons impinging the ring detector at an oblique angle lead to an asymmetric blurring, occurring in the radial direction, with a progressive increase as the point source moves radially outward (*radial elongation*) [72]. For a bismuth germanate (BGO) whole-body scanner, measurements show that the spatial resolution worsens from 4.5 mm near the center of the scanner to about 8.9 mm at a radial distance of 20 cm [74].

A thin crystal with high stopping power is desirable for the reduction of parallax error in the acquired images, despite the concurrently reduction of the scanner sensitivity.

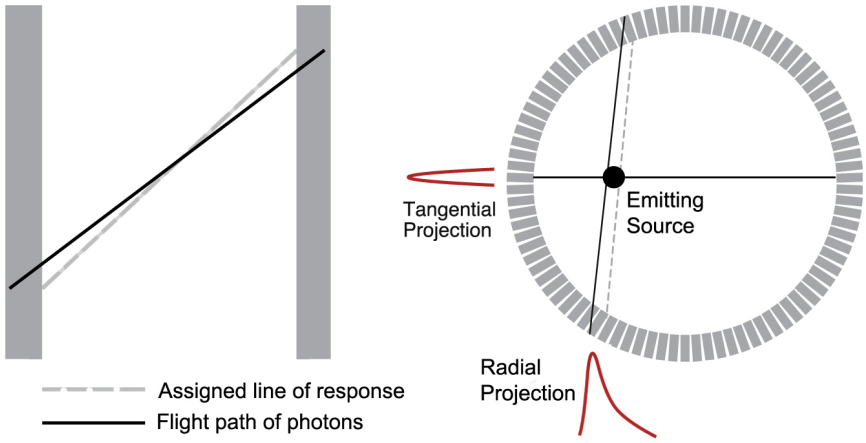


**Figure 2.10:** Schematic representation of parallax error introduced in the measured position due to the unknown depth-of-interaction of the photons within the detectors for a flat detector (left) and ring-based system (right). Gamma rays impinging normally to the detector ring (travelling horizontally in the right) interact in the crystal and independently of penetration depth, the tangential projection of source remains narrow. Those impinging at an oblique angle (travelling vertically in the figure) can even interact with different crystals, depending on penetration depth, therefore radial projection of the source becomes wide. Adapted from [41].

Research envisaging the development of PET detectors with depth-of-interaction measurement capabilities is being carried out since a long time. For instance, the *phoswich* detector [75] involves stacking thin layers of different scintillators on top of each other, instead of using a single layer of just one type. A recent experiment with a small-animal PET scanner using dual-scintillator *phoswich* detectors for DOI correction proved to reduce radial resolution loss and improve the spatial resolution in the central FOV [76]. Another technique consists of placing photo-detectors at both ends of a thick scintillator [77]. More recently, position sensitive avalanche photodiodes (PSAPDs) coupled to 294,912 $1 \times 1 \times 1$ mm$^3$ lutetiumyttrium oxyorthosilicate (LYSO) scintillation crystal elements have been used to achieve a 1 mm$^3$ resolution clinical PET system for breast cancer imaging [15, 78]. Concerning clinical TOF PET systems, a two-layer $LaBr_3$ detector has been designed, exploiting the dependence of scintillator rise time on Cerium in $LaBr_3$:Ce, while maintaining coincidence time resolution below 250 ps [79]. Nevertheless, a recent article suggests that the introduction of a given two layer DOI-correction only provides a modest improvement in image quality, when compared to the increasing TOF resolution [80].

In what concerns RPC-PET, the DOI has been accurately measured [6], rendering RPC-PET essentially parallax-free. In chapter 4, we will develop further this issue demonstrating a technique to accurately measure the DOI in the small-animal RPC-PET system.

**Voxel size** The image quality of a whole-body PET scanner can be improved significantly by reducing the transverse pixel size from 4 to 2.6 mm [80]. The pixel dimension should be of at most 0.1 × the anticipated FWHM [2]. In chapter 4, we will present reconstructed images with bin sizes of 25 $\mu$m and 50 $\mu$m in order to achieve an expected spatial resolution of 0.5 mm. As reported by Hoffman & Phelps [81], resolution improvements must be accompanied by an approximately third-power increase in sensitivity. A two fold improvement in resolution decreases the effective resolution volume in each coordinate by two and therefore a $2^3$ increase in sensitivity would be required to maintain equivalent signal-to-noise ratio per voxel. Nevertheless, image quality in PET is a strongly nonlinear function of spatial resolution [16]. According to Muehllehner [82], a 2 fold improvement of spatial resolution may compensate for a 32 fold reduction of statistics. Metzler *et al.* [83] concluded that a spatial resolution improvement by a factor 2 may compensate a 4 times worse sensitivity and produce improved image quality.

#### 2.2.5.2 Sensitivity, scatter-fraction and count-rate performance

**Sensitivity** of a PET scanner represents its ability to detect the coincident photons emitted from inside its FOV. It has traditionally been measured for comparing 2D scanners, using a line source of $^{18}$F, in a water phantom. However, with the advent of 3D scanners, and the corresponding larger influence of scatters, it became necessary to measure the absolute sensitivity that is not affected by scatter and attenuation. A method has been developed to make these absolute sensitivity measurements in PET [84], and has been adopted in the NEMA testing procedures [65]. The scanner absolute sensitivity $\eta$, and trues sensitivity $\eta_T$, are thus defined as

$$\eta = \text{events detected/events started}, \tag{2.16}$$

and

$$\eta_T = \text{true events detected/events started}, \tag{2.17}$$

The units of this measurement are cts·sec$^{-1}$MBq$^{-1}$ (counts per second and MBq).

The sensitivity is determined by two parameters of the scanner design: its geometry and the efficiency of the detectors for 511 keV photons. Since it is dominated by the solid angle and grows strongly with AFOV and with the axial acceptance angle, we estimate a sensitivity enhancement for RPC-PET by a factor up to 20 when compared with standard PET scanners (see fig. 2.11) [7].

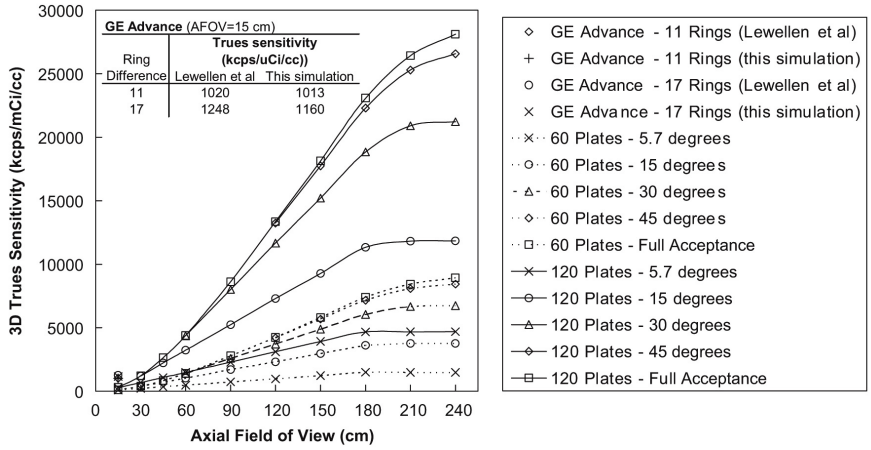


**Figure 2.11:** Absolute trues sensitivity as function of the AFOV of the RPC-PET tomograph for several values of the acceptance on the axial angle of the LORs, considering RPCs made with 60 or 120 glass plates ($\epsilon = 11.0\%$ and $\epsilon = 19.4\%$, respectively) and the gain sensitivity owed to TOF [4]. The results are compared with the ones obtained experimentally and by simulation for the GE Advance tomograph in 3D mode ($AFOV = 15$ cm). From [7].

The assessment of the practical interest of extended AFOV PET systems requires that the simulations do not only take into account the sensitivity, but also random and multiple coincidences and dead-time effects.

**Scatter fraction** Scatter fraction, $SF$, is defined as the fraction between the amount of scattered coincidences, $S$, and the total coincidences, $S + U$,

$$SF = \frac{S}{S+U} \ , \tag{2.18}$$

where $U$ is the amount of non-scattered coincidences. The random coincidences are not included in the calculation, thus assuming that they were previously corrected for [85].

The scattering may be of either, or both, of the annihilation photons, but it is predominantly scattering of one photon only. In general, scattering happens: (i) within the object containing the radionuclide; (ii) off mechanical components; (iii) within the detectors.

Scatter in 2D-PET is usually relatively small and typically less than 15% of the total events, while in 3D-PET it raises from 20% to 50%. One of the earliest demonstrations of scattered radiation in an open PET geometry was measured on the first positron tomograph PC-1 [86].

The scatter fraction depends on object size, density, acceptance angle, energy discriminator settings and radiopharmaceutical distribution.

The simulation for RPC-PET demonstrate that the scatter fraction is similar to the one obtained with crystal-based PET scanners. Additionally, it was found to be almost independent of the AFOV and LOR axial acceptance angle (see fig. 2.12) [8].

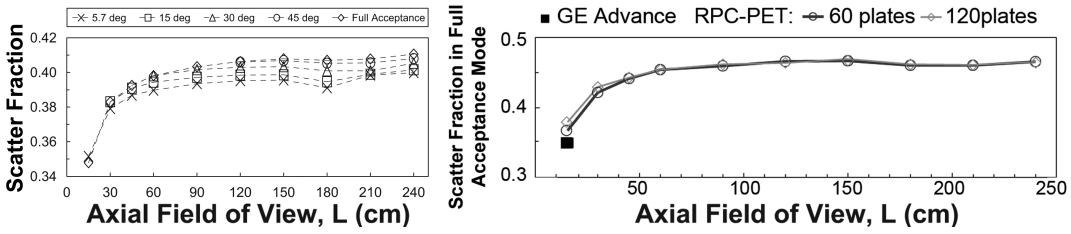


**Figure 2.12:** Scatter fraction vs. AFOV, $L$: for several values of the axial acceptance angle $\theta$, computed as the ratio of true to true+scattered LORs, for a low level discriminator of 400-650 keV and a phantom with d = 10 cm, $l = 175$ cm (left); for an RPC-PET system with 60 and 120 plates, and a GE Advance tomograph (right). Adapted from [8, 87].

**Count rate performance and NEC** Count rate performance refers to the finite time the system takes to process detected photons. After a photon is detected, a series of electronic processing steps happen, each of which requires a finite amount of time. The dead time accounts for the combination in series of these time delays. Thus, counting losses due to dead time may arise in PET systems. The purpose of defining count rate performance is motivated by the need of assessing the impact of increasing count rates on image quality. Comparison of the count rate performance of different tomographs have been difficult to achieve because of the vastly different physical components of the measured data (e.g., scatter, randoms) and the strategies

for dealing with them. The noise equivalent count (NEC) rate [88] provides a means for making meaningful inter-comparisons that incorporate these effects. NEC is the count rate which would result in the same signal-to-noise ratio for the data in the absence of scatter and random events and is defined as

$$NEC = \frac{T^2}{T + S + 2fR} \ , \tag{2.19}$$

where $T$, $S$ and $R$ are the true, scatter, and random coincidence counting rates, and $f$ is the ratio of the source diameter to the tomograph's transaxial field-of-view. The factor 2 comes from on-line randoms subtraction. The NEC provides a parameter which permits comparisons of count rate and is, therefore, an index for comparing image quality between systems.

The planar sensitivity and the NEC of a whole-body single-bed TOF-assisted human RPC-PET will be addressed in section 2.4. The relationship between NEC and AFOV for crystal-based PET scanners with reduced and extended AFOV has also been investigated [89]. The NEC also plays an important role in the determination of the optimum injected dose for 2D and 3D whole-body PET [90].

### 2.2.6 Time-of-flight

The idea of using time-of-flight information was originally proposed in the early stages of PET scanner development [91, 92, 93], and the first TOF-PET systems were developed in the 1980s [94, 95, 96, 97, 98]. These systems used caesium fluoride (CsF) and barium fluoride ($BaF_2$) scintillators and were able to deal with high-count-rate demands of research brain and heart studies with short-lives isotopes. However, they could not achieve neither the spatial resolution nor the sensitivity of conventional PET scanners with BGO scintillators. TOF-PET is particularly advantageous for whole-body imaging, since it has the potential to improve the image quality in heavy patients. The development of new scintillators that combine fast timing decay with high light output and high stopping power lead to the resurgence of TOF in PET [99, 100]. The LSO and LYSO have desirable properties for PET without TOF, so their good timing resolution should increase already good performance [101]. Additionally to the appearance of more appropriate scintillators, there have been developments in more cost-effective photomultipliers (PMTs) and on the stability of the electronics. Image reconstruction algorithms have also suffered a huge progress.

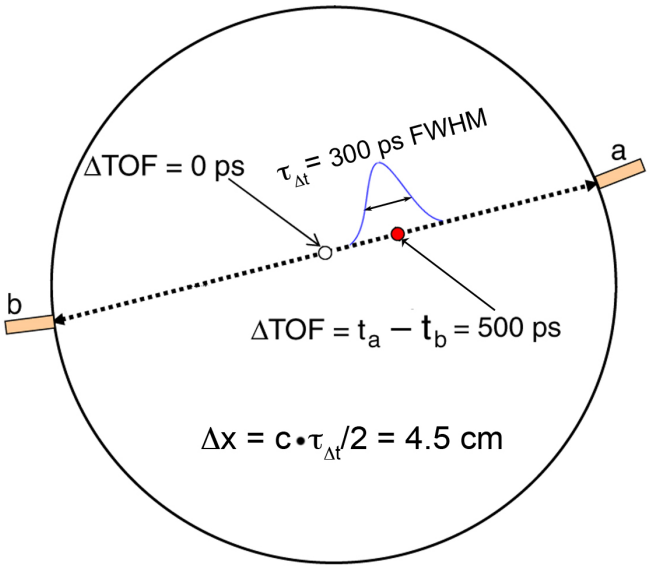


**Figure 2.13:** Principle of the time of flight technique in PET. The filled circle depicts an annihilation located 7.5 cm from the middle of the LOR between two given detectors, a and b. This corresponds to a photon path difference of 15 cm. The spatial resolution obtained with TOF-PET is half the coincidence time resolution, $\tau_{\Delta t}$, of its detectors times the speed of light. Adapted from [102].

#### 2.2.6.1 Principles of the time-of-flight technique

Good timing resolution of a PET detector, besides of reducing the number of random coincidences, can also be used to constraint the position of the annihilation point along the LOR by means of the difference in detection times of the two photons. The physics principle inherent to TOF-PET is illustrated in fig. 2.13.

Given the coincidence time resolution provided by the detectors and read-out electronics of a PET scanner, we may utilize the time difference between the detection of the annihilation photons at each detector to restrict the position of the annihilation point within the formed LOR. The distance from the center of the LOR to the annihilation point, $x$, is given by

$$x = (t_b - t_a) \cdot \frac{c}{2}, \tag{2.20}$$

where $t_b$ and $t_a$ are, respectively, the two annihilations photons arrival times at detectors $b$ and $a$, with $c$ being the speed of light [102].

The timing RPCs (tRPCs) provide a FWHM coincidence time resolution $\tau_{\Delta t} = 300$ ps, equivalent to $\sigma_t = 90$ ps, for 511 keV photon pairs [4, 5]. Thus, the uncertainty associated to the location of the annihilation point is $\Delta x_{FWHM} = 45$ mm.

The effective sensitivity gain due to TOF was estimated [103, 104] at the center of a uniform distribution to be proportional to $f = D/\Delta x$, where $D$ is the diameter of the patient. For thin (D = 20 cm), average (D = 27 cm), and heavy (D = 35 cm) patients, the calculated sensitivity gain for a uniform distribution and a time resolution of 300 ps are, respectively, 4.4, 6.0, and 7.8 [101]. Another estimate for sensitivity gain using a variance reduction argument was given by *Tomitani* as being $D/(1.6 \cdot \Delta x)$[105].

Hypothetically, with perfect TOF information, reconstruction would be unnecessary, since the position of the annihilation point could be identified on the basis of only online pair and time difference information. Nevertheless, even imperfect timing information helps to improve reconstruction, reducing convergence time propagation of noise along the LOR. The statistical noise in the analytical reconstruction process is reduced by the same factor $f$ [106]. The contribution of scattered and random photons arriving from outside the FOV is also greatly reduced, therefore enhancing the signal to noise ratio of TOF-PET images [107].

#### 2.2.6.2 Current trends

Currently, TOF is implemented in commercially state of the art PET scanners, such as Philips Gemini TF PET/CT ($\Delta t$ =585 ps) [108], Siemens mCT time-of-flight PET/CT ($\Delta t$ =527.5 ps) [109], GE PET/CT Discovery-690 ($\Delta t$ =544.3 ps) [110].

Several studies about the TOF benefits for both lesion estimation and detectability have been carried out [111, 112, 113]. The trade-off between TOF gain and number of counts was also studied, showing that the TOF gain can be used as a sensitivity amplifier [114], despite the limitations at very low counts [115]. The influence of TOF on the reconstruction speed has also been reported [102, 116]. In chapter 5, we will focus on the convergence speed of a reconstruction routine dedicated to human RPC-PET and on the detectability benefits provided by a TOF resolution of 300 ps FWHM.

### 2.2.7 Data correction

PET has since long been regarded as a quantitative imaging tool. That is, the voxel values of reconstructed images can be calibrated in absolute units of radioactivity con-

centration with reasonable accuracy and precision. To produce an image volume in which each voxel value represents the true tissue activity concentration, a number of corrections has to be applied to the raw data. These corrections provide a true reflection of the underlying physiology and enable the use of tracer kinetic methodology to model the time-varying distribution of a labelled compound in the body. In what concerns large AFOV PET systems covering the entire human length, such as human RPC-PET, kinetic tracing assumes an increased importance, since dynamic heart image data may provide some input function information in a dynamic function study of a tumor [117], with all tasks being performed in a single-bed examination [9].

The various sources of measurement error in PET and the methodological approaches to correct them will be summarized next. The ability to accurately measure or model these sources of error and correct for them, while minimizing the impact on signal-to-noise ratio, determines the accuracy and precision of PET images. We will follow the order in which the various corrections are typically applied: random coincidences; normalization; dead time; scatter; and attenuation.

**Random coincidences** result in additional events being recorded as LORs [118]. They arise because of the finite width of the electronic time window used to detect true coincidences. This finite width allows two uncorrelated single detection events occurring sufficiently close together in time to be mistakenly identified as a true coincidence event [119]. Without correction, these events: add a relatively uniform background across the reconstructed image, suppressing contrast; adversely affect quantification; and may produce significant image artifacts [2, 120]. The two main approaches to correct these errors result from the estimation of the singles counting rate for a given coincidence time window, or from the direct measure of the random coincidences, which can be achieved by adding a parallel coincidence circuit to the one measuring the prompt coincidences, but with the logic pulse from one of the two detectors delayed in time [2]. The first method for estimation of random coincidences is based on eq. 2.14. This method produces a statistically superior estimate of the number of random events with a smaller statistical noise level due the higher single events rate, which is typically of an order of magnitude greater than that of coincidence events. This method requires that each detector continuously monitors the rate at which is detecting single events [120]. The second method estimates the random coincidence by delaying the coincidence timing window by a time that is much greater than its width. For a typical coincidence

timing window of 4-12 ns, if the two photons arrive within this time interval, they are recorded as a valid coincidence. A coincidence 12 ns timing window delayed by 64 ns will just accept events with arrival times separated by between 64 and 76 ns. The trues and scattered events will not be detected in the delayed window, and the rate of random coincidences will be the same in the undelayed and delayed windows. Finally, the delayed window count is subtracted from the total number of coincidence events for the detector pair. As we will show in section 4.2.2, for small-animal RPC-PET, the removal of random events is performed in the digital pulse processing stage.

**Normalization** methods utilized in different PET scanners make use of models that decompose the detectors response in several components which are independent from each other [121]. These components characterize specific physical features which are defined by parameters that can be determined separately. The utilized model and the respective components depend on the features of the scanner. These components comprehend the crystal intrinsic efficiency, the detection rings efficiency, systematic efficiency variations due to the geometry of the detection system and dead-time effect. The first normalization techniques implemented in PET were based on the direct efficiency measurement for each LOR, by exposing each pair of detectors to a source of known activity for a certain period of time [85]. This is usually accomplished with a rod source (e.g., $^{68}$Ge) spanning the entire axial FOV and rotating it around the periphery of the FOV. One revolution of the rod source around the FOV would expose all detector pairs to the same number of photon pairs, and each detector pair would ideally record the same number of counts. In practice, some detector pairs record more counts and some record less counts because of efficiency variations [120]. After a normalization scan, the correction factor, $\mathrm{NF}_{ij}$, is calculated as the ratio between the average number of counts per LOR and the number of events in each LOR between detectors $i$ and $j$. During the patient scan, the normalized number of events are obtained from the multiplication of the raw number of events in the LOR between detectors $i$ and $j$ and the correction factor, $\mathrm{NF}_{ij}$ [122]. This approach, known as direct normalization [123], is very time-consuming for present PET scanners, due to their high number of LORs ($10^8$ in a modern PET scanner operating in 3D mode), leading to very long acquisitions ($\sim$55 hours) in order to obtain a reasonable number of counts per LOR and a good accuracy in the efficiency estimation. Therefore, the PET scanner normalization

is usually done at installation, then annually, or after major service, whenever deteriorating image quality requires a new normalization [122]. The normalization methods have evolved to a small number of determined parameters, by modeling the correlation among the LORs, thus providing a better estimation statistics for each parameter and a reduction of the acquisition time [121, 124, 125]. The model utilized to normalize the data should replicate as well as possible the LORs efficiency variation, making use of a small number of measurable parameters [85]. Scattered coincidences also require a different normalization [126]. Meanwhile, some iterative methods have been developed [127, 128], and the influence of the geometry of the sources has also been studied [129, 130].

**Dead time** influence on a PET system is highly dependent on its design and architecture. PET scanners may be regarded as a series of sub-systems, each of which requires a minimum amount of time to elapse between successive events for them to be registered as separate [119]. In an ideal system, the net true count rate of the system should increase linearly with increasing activity in the field of view. However, the different components in the detection chain will experience some level of dead time as the activity increases [2]. Since radioactive decay is a random process, there is always a finite probability that successive events will occur within dead time and, at high count-rates, the fraction of events falling in this category may become very significant. The main consequence of this phenomenon is to reduce the number of coincidence events counted by the PET scanner and, since the effect becomes stronger as the photon flux increases, the net result is that the linear response of the system is compromised at high count-rates [119]. In section 2.4.2, we will present the simulation results about the influence of dead time on the NEC in the human RPC-PET system.

**Scatter** correction is probably the most difficult correction that is required in PET, mainly because a scattered event is indistinguishable from a true one except on the basis of energy and TOF [2]. Scatter correction is always mandatory if an absolute PET quantification is required in 3D mode. In 2D mode, due to the lower scatter fraction, this correction may be ignored. The scatter correction involve the correct estimation of the form and amplitude of the scatter distribution. In single scatter simulation 1 (SSS1), this distribution is then subtracted from the total of detected events, mostly at the projection level and before the reconstruction [131]. It is also possible to apply the correction after data reconstruction (SSS2 method) [132].

Several methods were proposed to correct scattered radiation by Compton effect in PET, which are fully described by Bailey [133]. They are divided in three main categories: energy discrimination methods, convolution and deconvolution methods, and simulation and modeling methods.

Among the energy discrimination methods, the most utilized are the *Dual Energy Window* (DEW) [134] and the *Estimation of Trues Method* (ETM) [135]. There are additional methods just available in certain non-commercial PET systems, such as the *Triple Energy Window* (TEW) [136] and the *multispectral method* [137]. All these methods are based on the assumption that scattered photons have lower energy than the un-scattered ones. The energy resolution determines the effectiveness of such methods.

The deconvolution techniques allow recovering the un-scattered distribution from the measured one [138, 139, 140], while the convolution methods estimate the scattered distribution through the convolution of the real activity distribution with an adequate response function [141, 142]. Both methods are based on the premise that the spatial distribution of the scattered events varies slowly along the space, thus being obtained from the real activity distribution with an adequate filtering on the high-frequencies [85].

Since the physics of photon interactions in matter is well understood, it is possible to model these processes and estimate the scatter contribution to projections given an accurate map of attenuation coefficients in the scattering medium and an initial estimate of the scatter-free radioactivity distribution [2]. The analytical simulation methods assume that the scatter distribution can be calculated from the emission and transmission measurements. The proposed models [143, 144, 145] assume that only one of the annihilation photons forming a coincidence undergoes a Compton interaction, representing 75 to 80% of the total scattered coincidences [146, 147, 148]. The SSS method uses the preliminary images obtained from the emission and attenuation distributions, reconstructed with lower resolution, to estimate the scatters. A regular grid of points is then disposed over the attenuation image, typically spaced by 2.5 cm, and it is assumed that those *scatter points* locate the single Compton interaction that lead to the detection of the scatter coincidence by the detector pair. Then, those points are slightly and randomly displaced from their initial position to avoid artifacts resulting from the rotational asymmetry of a cartesian grid of points. The estimation of the scattered coincidence is done for a limited set of line coincidences and scattered

points. The complete calculation is fully described by Ferreira [85]. The Monte Carlo method [149] is a very accurate and practical approach to scatter correction in PET, but also more time consuming. However, dramatic improvements can be made in the computational efficiency of Monte Carlo simulation by making reasonable approximations and using implementation techniques without compromising the accuracy of scatter estimation [150, 151].

With the appearance of TOF-PET scanners, the SSS method, originally proposed by Watson, was conveniently implemented by the same author onto those TOF capable systems [152]. Meanwhile, other researchers have also implemented the TOF-based scatter correction into TOF list-mode PET reconstruction routines, with an improved uniformity of scatter correction over scaled non-TOF scatter correction [153].

Work aiming at a proper scatter correction in RPC-PET has already been deployed within our group [154, 155, 156]. It has been concluded that the SSS method is the most appropriate to be implemented in RPC-PET, since RPCs do not possess energy resolution and such tomographs will not provide the adequate data for a convolution method. Simulation studies pointed out that large AFOV tomographs, such as RPC-PET, have a *Single Compton Fraction* of $\sim$71.9%, which is in line with the values presented before. The integrated CT planned for RPC-PET system, besides providing multimodality imaging, will also supply the data necessary to estime the object-scattered events. A scatter correction combining the body-scattered and detector-scattered events is currently under study.

**Attenuation** and scatter are manifestations of the same physical process, apart from photoelectric interaction. A coincidence event requires the simultaneous detection of both photons arising from the annihilation of a positron. If either photon is absorbed within the body or scattered out of the field of view, a coincidence will not occur. Therefore, the probability of detection depends on the combined path of both photons. Correction involves removing scattered events from the LORs and the subsequent correction of each LOR for the fraction of events that were scattered, or attenuated, from that LOR.

Let us consider a point source located at an unknown depth $x$ in a uniform attenuating medium with attenuation coefficient $\mu$ (see fig. 2.14). The probability that the

annihilation photon 1 will escape the object is the result of equation 2.8:

$$p_1 = \frac{I(x)}{I_0} = e^{-\mu x}, \tag{2.21}$$

and for a thickness $D$ of the object along the LOR, the probability that annihilation photon 2 escapes is:

$$p_2 = \frac{I(D-x)}{I_0} = e^{-\mu(D-x)}. \tag{2.22}$$

The probability that both annihilation photons escape the object is the product of the former individual probabilities:

$$p1 \times p_2 = e^{-\mu D}. \tag{2.23}$$

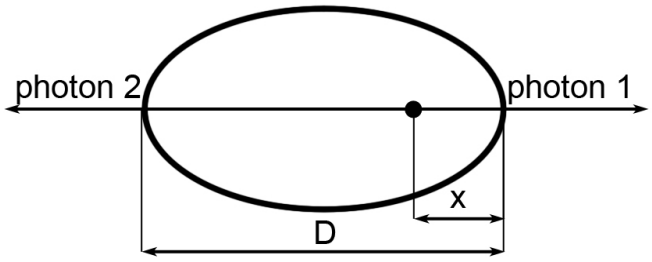


**Figure 2.14:** The photons emitted by a source located at an unknown depth $x$ in an uniform volume of thickness D may escape the object depending on its attenuation coefficient and on the thickness of the object along the LOR.

The attenuation correction factor, $f_{att_i}$, that need to be applied to the portion of LOR $i$ is given simply by the reciprocal of equation 2.23:

$$f_{att_i} = e^{\mu D_j}, \tag{2.24}$$

where $D_j$ is the 3D length of the portion of the LOR corresponding to the touched voxels. Equation 2.24 will be adopted for the attenuation correction presented in chapter 5.

The attenuation correction can be measured using coincidence or singles transmission data or can be directly calculated, which saves the time needed for transmission scans. However, with the advent of dual modality scanners capable of acquiring PET and CT data during the same imaging session, one can make use of CT data for PET

attenuation correction. The statistical quality and spatial resolution of CT data is far superior to conventional transmission data used in PET, and calculated attenuation correction is prone to bias when applied to most regions of the body, due to their non-uniform density. Additionally, nowadays we can have CT image in a few seconds, resulting in a much more comfortable solution. Nevertheless, the speed of the CT scanning in comparison to PET scanning is also a potential pitfall, once in CT a snapshot of respiratory motion is obtained, rather than a time-averaged image. Without due care, this can lead to substantial artifacts in the reconstructed images [157]. Artifacts are also caused by misregistration between the CT and PET data when the patient moves between scans. CT images are normally calibrated in Hounsfield units and must first be converted to $\mu$ values. This challenge can be addressed by segmenting the CT images into a discrete set of tissue types [158].

### 2.2.8 State of the art PET scanners

The main properties of the high-end clinical PET scanners from the three major manufacturers are summarized in table 2.2.

**Table 2.2:** Performance of different commercial PET systems.

| System | Detector | FOV Trans / Axial $\phi$(mm) /(mm) | $\Delta t$ / $\tau_{cw}$ (ns)* | Energy resolution (%) | CFOV and off-centre Spatial Resolution (mm) FWHM[0] | ACS (%) ($E_w$ (keV)) | Peak NEC (kcps)@ activity kBq/mL) | Ref. |
|---|---|---|---|---|---|---|---|---|
| Biograph® mCT TOF | *LSO* | 605 / 218 | 0.528/ 4.1 | 11.5 | $4.4 - 4.4 - 4.4^{2,1}$ | 1.0 $(435 - 650)^{2,1}$ | 180@28[3] | [109] |
| | | | | | $5.2 - 4.7 - 5.9^{2,4}$ | | | |
| Gemini® TF | *LYSO* | 576 / 180 | 0.585 / 6.0 | 11.5 | $4.8. - 4.8 - 4.8^{5,2}$ | 0.7 $(440 - 665)$ | 125@17[3] | [108] |
| | | | | | $5.2 - 5.2 - 4.8^{5,4}$ | | | |
| Discovery® 690 | *LYSO* | 700 / 153 | 0.544/4.9 | 12.4 | $4.7 - 4.7 - 5.6^{4}$ | 0.7 $(425 - 650)$ | 139@29[3] | [110, 159] |
| | | | | | $5.3 - 4.8 - 6.3^{4}$ | | | |

.*$\Delta t$ and $\tau_{cw}$ are the timing resolution and coincidence time window in ns.

.[0]Radial, tangential and axial spatial resolution.

.[1]10 mm radial offset.

.[2]Reconstructed with FORE and FBP, without attenuation or scatter correction. 100 mm radial offset.

.[3]Human-like phantom.

.[4]100 mm radial offset.

.[5]Reconstructed with 3D FBP after correction for random coincidences. 100 mm radial offset.

## 2.3 Resistive plate chambers in positron emission tomography

As in many other branches of applied science, high energy physics met the medical needs, making use of detectors originally designed for a different specific purpose, by adapting them to radiological and nuclear medicine diagnostic. The application of resistive plate chamber technology [3] to positron emission tomography (RPC-PET) [4] is a successful example. RPC-PET has been growing in two parallel research lines: for human imaging, being capable of performing a single-bed scan covering an axial field-of-view of 2.4 m, and assisted by time-of-flight capability down to an experimental coincidence timing resolution of 300 ps FWHM; for small-animal imaging, providing sub-millimeter spatial resolution down to a few hundreds of micrometer, and depth-of-interaction measurement, rendering images essentially paralax-free.

### 2.3.1 Historical introduction

A resistive plate chamber (RPC) consists of a gas gap delimited by two parallel electrodes one of which, at least, is mandatorily made of resistive material [50]. The current between the two parallel electrodes at a certain differential voltage, and for a small number of released electrons, was firstly measured by Townsend, in 1910 [160]. He observed an exponential growth of the electrons with an increasing voltage beyond a certain threshold, and explained these measurements as a consequence of the multiplication phenomenon. This occurs when the electrons originated in the primary ionization gain enough energy from the applied electric field to ionize the gas molecules. The secondary electrons produce further ionizations, thus developing an avalanche of electrons. Due to the large mobility of the electrons, they group near the head of the avalanche, whereas the ions with a slower drifting velocity tail behind, forming a liquid drop shape (see fig. 2.15). The signals produced by the avalanches developed in the gas are measured by different kind of detectors, including the RPCs. These are gaseous detectors and their primary conception is assigned to Santonico and Cardarelly, in 1981 [162]. Nevertheless, in 1971, Pestov [163] had already adopted a similar kind of detector to construct the so-called Pestov-counter, achieving a time resolution of 25 ps $\sigma$ [164].

At the beginning, RPCs were composed by one single gap operating in streamer mode, but soon a double-gap structure emerged [165] improving the detection efficiency

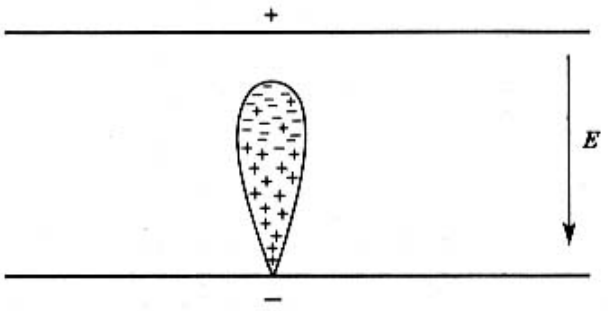


**Figure 2.15:** Electron avalanche. From [161].

while operating in avalanche mode [166]. A few years later, in 1996, another type of RPCs came along, the multigap RPC [167]. It was developed with the purpose of having a counter with more than one single gas gap. The characteristic design of these latter detectors includes resistive and electrically floating electrodes, thus forming several gas gaps inside the gas volume without further unnecessary conductive electrodes. According to its inventors, the steady-state requirement for a null total current on each of the dividing electrodes stabilizes their potential at a value that equalizes the currents flowing in and out by adjusting the gas gain in the neighboring gaps [164]. However, this design may have some inconvenience, since it requires large voltages, and thus increased dark counts that may influence the stability mechanism of the device.

Nowadays, we can classify RPCs into two main categories: large gap RPCs [162], mainly used as trigger devices, and narrow gap RPCs [3], achieving time resolutions of a few tens ps. Typically, the large gap RPCs are made of glass or Bakelite with gas gaps ranging from 1 to 3 mm. Their time resolution is about 1 ns and they provide a spatial resolution from a few mm to 1 cm. The narrow gap RPCs are made of glass, with gas gaps below 0.3 mm, and are operated in high-gain avalanche mode [168].

Large gap RPCs operated in "streamer" mode have successfully been used in several experiments, for instance, L3 [169], OPERA [170], BaBar [171], BELLE [172], and ARGO [173]. Figs. 2.16 and 2.17 present the single-gap and double-gap RPCs used in such experiments. The good performance of narrow multigap RPCs (see fig. 2.18) has been proved in HARP [174], STAR [175] and FOPI [176] experiments. Large gap RPCs were also successfully operated on an unprecedented scale at LHC [177, 178, 179, 180]. Multigap RPCs featuring a time resolution below 100 ps have also been reported in the

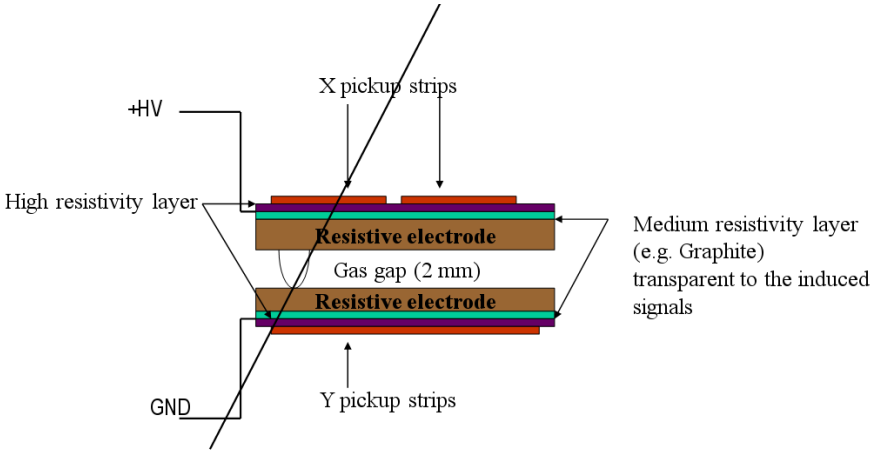


**Figure 2.16:** Single-gap streamer-mode RPC used by the BABAR experiment. From [164].

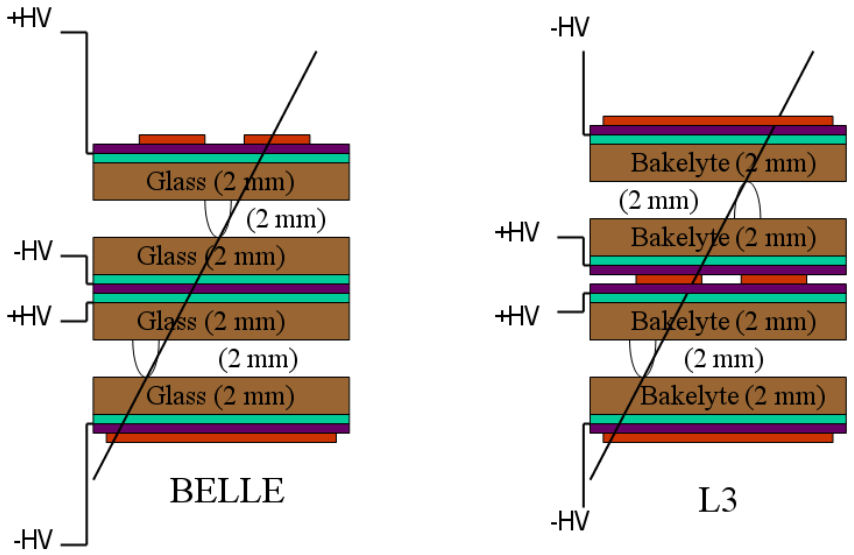


**Figure 2.17:** Schematic drawing of the double-gap RPCs used by L3 and Belle experiments. From [164].

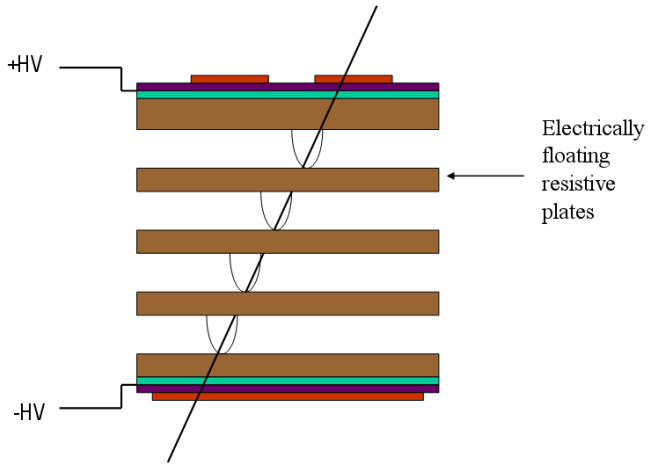


**Figure 2.18:** Schematic drawing of the multigap RPC first proposed in [167]. From [164].

HADES experiment [181].

In 2000, tRPCs [3] were developed, based on the combination of thin and precise gas gaps with fast front-end electronics (FEE). A time resolution at the level of 120 ps was achieved for an RPC with a gas gap of 0.3 mm operated in avalanche mode, and soon after, this value was pushed down to the level of 50 ps [182]. Despite the difference between minimum ionizing particles (MIPs) and photons, these achievements seemed particularly important for medical imaging, by providing to RPC-PET a sharp time-of-flight (TOF) capability. Fig. 2.19 relates TOF with the width of the gas gap, suggesting that, for charged particles, the timing resolution of thin-gap parallel geometry detectors depends mainly on that width [3].

Meanwhile, along the last decade, several configurations allowed improving counting rate capability and spatial resolution of RPC-based systems. Metallic and resistive electrodes were used [183], as well as low resistivity electrodes, plastic [184] and ceramic [185], extending the counting rate capability up to 35 kHz/cm$^2$ and 500 kHz/cm$^2$, respectively. Position sensitive RPCs have also been developed with sub-millimeter spatial resolution for very accurate systems [19, 186, 187]. A review on the current challenges for RPCs can be found in [188, 189].

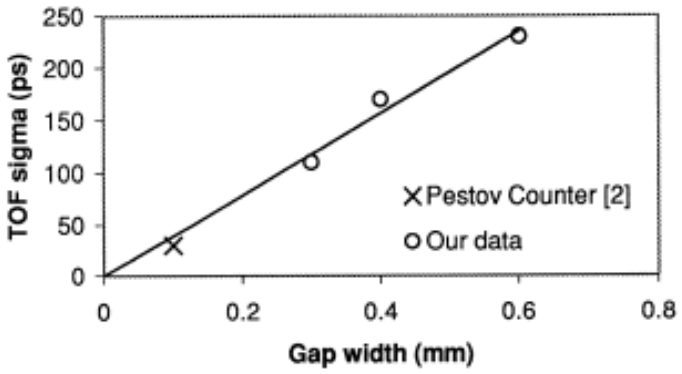


**Figure 2.19:** Charged particle tests performed with detectors featuring gas gaps of different widths suggest that the main contribution to the time jitter is associated to the amplification process in the gas. From [3].

### 2.3.2 Avalanche versus streamer mode of operation and the space-charge effect

As previously stated, an RPC faces an uniform electric field across its volume by means of a DC voltage applied to the electrodes. The particles that interact with the detector may liberate electron-ion pairs from the electrodes, which reach the gas gaps with a certain density. The electrons are subsequently accelerated in the direction of the anode developing an avalanche. In the presence of gamma radiation, the interaction probability must be increased. For this reason, a converter is used [190] with a specific thickness that depends on the balance between the interaction probability (increasing with thickness) and the electron extraction probability (decreasing with thickness).

In the multiplication process, the avalanche precedes the "streamer" discharge and corresponds to the generation of a Townsend avalanche in the gas gap. In a metallic counter, the discharge comprehends several sequential stages: avalanche, streamer, glow discharge, filamentary discharge, and finally ending up with a spark [191]. In RPCs, the sparks are avoided by using a high resistive electrode, and the discharge is quenched at the filamentary discharge stage [192, 193]. The glow discharge may be observed for electrode resistivities of the order of $4\times10^7$ $\Omega$ cm [194]. Fig 2.20 shows examples of pulses collected in avalanche mode (top, left) and in "streamer" mode (top, right). The streamer pulses are generally preceded by a small prepulse (fig. 2.20, bottom, left), this prepulse being an avalanche pulse which subsequently builds up enough charge

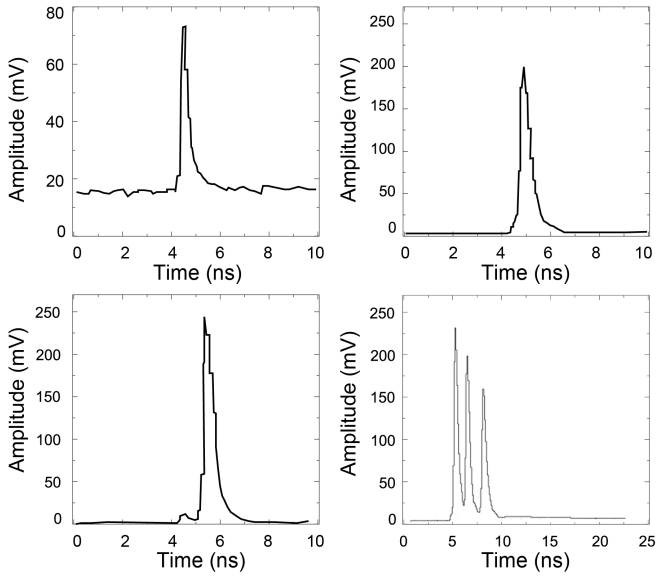


**Figure 2.20:** An avalanche pulse (top, left), a streamer pulse (top, right), a streamer preceded by a pre-pulse (bottom, left), and a multi-pulse (bottom, right). Adapted from [195].

to trigger the "streamer". Multi-pulses may also occur (fig. 2.20, bottom, right), and these become increasingly common as a chamber nears breakdown [195]. The charge signal ranges from a few pC for the fast (electron) component of the signal in avalanche mode to between 50 pC [196] and a few nC [197] in streamer mode.

Depending on the mode of operation, RPCs can achieve a rate capability, for the state-of-the-art designs, of around 300 Hz/cm$^2$ ("streamer") and 1-3 kHz/cm$^2$ (avalanche) [164]. Due to the lower charge release occurring in avalanche mode operation, charge amplifiers are required for proper readout [87]. Conversely, in the "streamer" mode, the read-out electronics needed are simpler. The avalanche mode operation also requires an electronegative gas to prevent excessive avalanche growth, thus limiting the space-charge effect and the evolution of the avalanche into a streamer [198, 199]. The space-charge effect, illustrated in fig. 2.21, consists of an electric field associated to the charge build up. In the figure, $E_0$ is the applied external field, and $E_1$, $E_2$, $E_3$ are the effective fields at the tip, center and tail of the avalanche, respectively. The multiplication is stronger in the regions where the total field is larger than the applied field immediately upstream and downstream from the avalanche region, at a given time point. Conversely, the multiplication is reduced at the center of the avalanche where

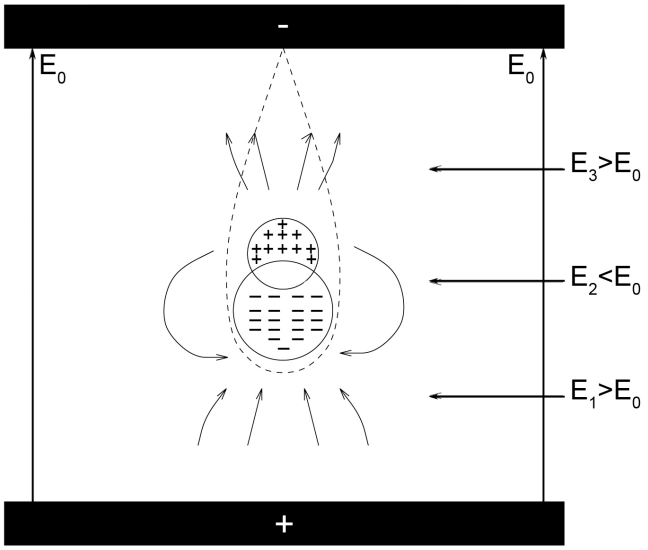


**Figure 2.21:** Space-charge effect. Adapted from [195].

the total field is lower than the applied field [50, 200]. This effect, which is fundamental to understand the behavior of RPCs, has been fully described by Lippmann [44, 201]. When the number of electrons in the advancing head of the avalanche approaches $10^8$ (the Raether limit [202]), the electrons are significantly restrained and the space-charge field in the middle of the avalanche is so increased as to practically cancel out the applied field. In the center of the charge cloud a radiative recombination occurs, with the emission of ultraviolet photons which may ionise the molecules outside the space-charge cloud. The electrons may drift back and multiply at the tip of the positive cone where the field is highest, thus generating the condition for the development of "streamers" advancing towards the electrodes. On arrival, the electrodes become connected by a low resistance conducting plasma of electrons and positive ions, and a high current flows between them [195]. By opposition, the lower field region causes the reduction of gas gain by the avalanche (resulting in a saturation effect [202]). Therefore,"streamer" development and avalanche saturation share a common physical origin and are in general simultaneously present [164]. The effect of strong avalanche saturation in RPCs has been confirmed experimentally and is of fundamental importance in the interpretation of the charge spectra and efficiency properties, both for millimeter [198, 203] and sub-millimeter [204, 205] gas gaps [164].

### 2.3.3 Computing the signal induced on the RPC electrodes

#### 2.3.3.1 Avalanche propagation

In the case of RPC-PET, the $\gamma$-rays that interact with the RPCs should be converted into electrons that eventually reach the gap. In the presence of a stationary and uniform electrical field, an avalanche may be developed by consequence of the multiplication, drifting and diffusion of these electrons [42, 206]. The continuity equation associated to the electron density is given by [207]:

$$\frac{\partial n_e(x,y,z,t)}{\partial t} = \alpha n_e |v_e| - \nabla(n_e v_e) + D_e \nabla^2 n_e, \tag{2.25}$$

where $n_e$ is the electron density, $\alpha$ is the first *Townsend* coefficient, $v_e$ is the electrons drift velocity, and $D_e$ is the electrons diffusion coefficient.

The first *Townsend* coefficient, $\alpha$, is the inverse of the mean free path $\lambda$ that an electron traverses before it ionizes an atom or molecule of the gas. It corresponds to the number of ionizing collisions per unit length caused by the drifting electrons under the applied field. The ionizing probability increases with an increasing $\alpha$ value, corresponding to a larger avalanche gain. The $\alpha$ value is in turn raised with the applied electric field, despite the requirement of a minimum applied field to endow the detectors with avalanche gain [87]. In the presence of electronegative components, the *Townsend* coefficient is replaced by the effective *Townsend* coefficient $\alpha_{eff} = \alpha - \eta$, where $\eta$ is the attachment coefficient.

In the simplest case where $n_0$ electrons are released at instant $t = 0$ from a certain point in the cathode, and assuming that the transversal and longitudinal diffusion coefficients are equal and $\alpha$ and $v_e$ are constant along the propagation, eq. 2.25 has the following solution

$$n_e(x,y,z,t) = n_0 e^{\alpha v_e t} \frac{1}{(4\pi D_e t)^{3/2}} e^{\left(-\frac{x^2+y^2+(z-v_e t)^2}{4D_e t}\right)}. \tag{2.26}$$

The avalanche process can thus be described by an exponential growth of charges diffusing in space. This electron component $n_e$ will have terms that express the diffusion of the electrons in the $x$, $y$, and $z$ directions, and one term expressing the growing number of electrons drifting under the applied external electric field.

#### 2.3.3.2 Electron current

Considering $n_0$ electrons being released from a certain point on the cathode surface with a constant drift velocity $v_e$ and subject to an applied electrical field $E = U/g$, where $U$ is the applied electric potential and $g$ is the gap width, the electron current $i_e$ flowing in the course of the electron transit time $T_e = g/v_e$ [202] is given by

$$i_e(t) = \frac{en_0}{T_e} = \frac{en_0 v_e}{g} \qquad 0 \leq t \leq T_e, \tag{2.27}$$

where $e$ is the electron charge [50]. As the distance $y$ from the initial $n_0$ electrons to the cathode increases, the number of electrons also grows due to the ionizing collisions in the avalanche process. The electron component thus becomes a function of time $t = y/v_e$,

$$i_e(t) = \frac{e_0 n_e(t) v_e}{g} \qquad 0 \leq t \leq T_e \tag{2.28}$$

Inserting eq. 2.26 into 2.28 results in the electronic current obtained due to the avalanche process in the gas gap,

$$\begin{aligned} i_e(t) &= \frac{en_0 v_e}{g} e^{\alpha v_e t} \qquad 0 \leq t \leq T_e, \\ i_e(t) &= 0 \qquad T_e < t, \end{aligned} \tag{2.29}$$

with eq. 2.29 not reflecting the negligible effect of electron diffusion term.

#### 2.3.3.3 Current due to positive ions

The positive ion current that moves to the cathode is given by

$$\begin{aligned} i_i(t) &= \frac{en_0 v_i}{g}(e^{\alpha v_e t} - e^{\alpha v_i t}) \qquad 0 \leq t \leq T_e, \\ i_i(t) &= \frac{en_0 v_i}{g}(e^{\alpha g} - e^{\alpha v_i t}) \qquad T_e \leq t \leq T_e + T_i, \end{aligned} \tag{2.30}$$

where $v_i$ represents the drift velocity of the positive ions under the applied electric field, being three orders of magnitude lower than $v_e$ [202]. The presence of electronegative components in the gas was here disregarded. However, since the gas attachment coefficient $\eta$ becomes important in the presence of electronegative gases, this leads to the substitution of the *Townsend* coefficient in eqs. 2.28 to 2.30 by $\alpha - \eta$. Fig 2.22 illustrates the current evolution with time, evaluated for the electronic (solid line) and

positive ion (dashed line) components[1]. The latter creates a much smaller current due to the small drift velocity of the positive ions, while the fast current created by the electrons breaks abruptly when they reach the anode.

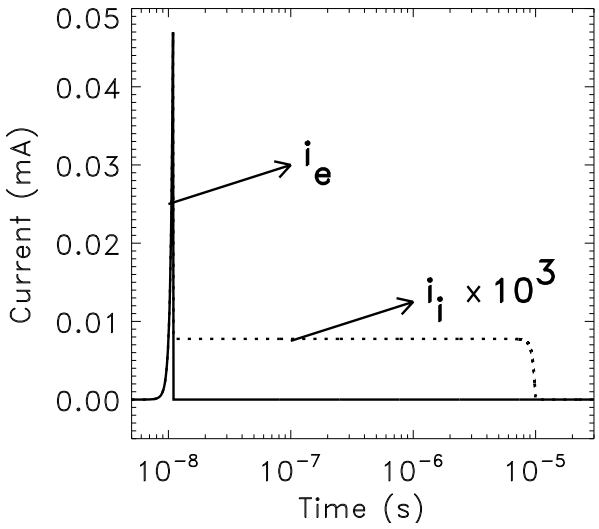


**Figure 2.22:** Electron and positive ion induced current evolution with time for an avalanche started by one electron ($n_0 = 1$). Further assumptions were $v_e = 1 \times 10^7$ cm/s, $v_i = 1 \times 10^4$ cm/s, $\alpha = 200\,\mathrm{cm}^{-1}$, and $g = 0.1$ cm. From [11] after [202].

An extensive survey of physical modeling in RPCs has been carried out by Fonte [208]. In this article, a full quantitative description of the diffusionless and diffusive cases for an arbitrary point of release of a single primary electron-ion pair was accomplished. The small avalanche approximation[2] has been considered there for the calculation of the current and total charges induced in a single flat cathode-side electrode.

#### 2.3.3.4 Current induced on the pickup electrodes and the theorem of Ramo

The theorem of Ramo provides the charge induced on the pickup electrodes due to the moving charges [87]. Only a fraction of the current created by the moving charges is induced in the pickup electrodes [50]. The current $i_{ind}(t)$ induced in a pickup electrode

[1]For a gap width of 0.35 mm, the ionic component time reduces to approximately 1 $\mu$s.

[2]The limit at which the electric field caused by the avalanches' own space-charge is negligible when compared to the applied field [208].

is given by the theorem of Ramo [209]:

$$I(t) = Q\boldsymbol{E}_W(\boldsymbol{r}(t)) \cdot \boldsymbol{v}(t), \tag{2.31}$$

where $Q$ is the charge and $\boldsymbol{v}(t)$ is the drifting velocity. Here, $\boldsymbol{E}_W(\boldsymbol{r}(t))$ is the weighting field corresponding to the application a unit voltage to the readout electrode, with all other electrodes and conductors grounded[1]. This is a key concept for the determination of the current induced on each pickup electrode, essential for achieving a fine positioning of the developed avalanches.

### 2.3.4 Converter plate principle

The converter plate principle illustrated in fig. 2.23 is utilized to detect electromagnetic radiation like X- or $\gamma$-rays with RPCs. This principle is valid as long as the gas mass remains insignificant in comparison with the converter plates mass. Because an

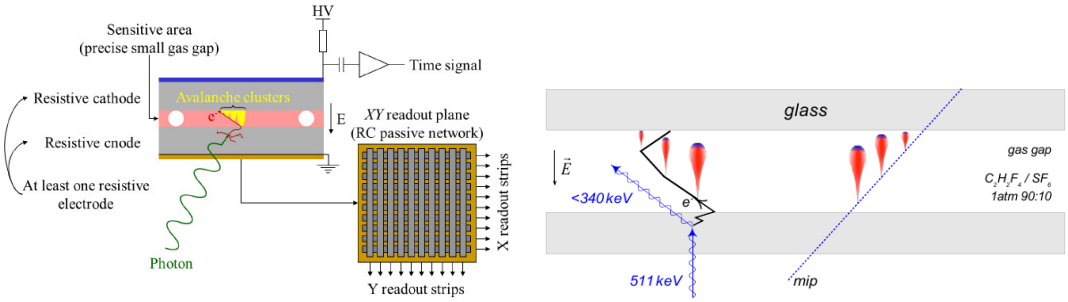


**Figure 2.23:** Converter principle of RPC detectors. The scheme shows a Compton interaction occurring in the glass converter medium. The electron, ejected in the forward (shown) or backward direction (not shown) with respect to the applied electric field, may not travel a long distance before changing direction. The electrodes may be adjacent to either the high voltage or the ground metallic plate by means of a resistive material. From [10] and [87].

electron needs enough kinetic energy to escape from the glass electrodes[2], we call them "converters" of the incoming photons. Any Compton or photoelectric interaction with the glass converter may eject an electron. Once the electron reaches the gas gap, if accelerated by the applied electric field that can go up to 10 MV/m, it may start an

[1] We will show in fig. 4.9 a representation of the simulated weighting field for a 4 mm pitch read-out strip of a RPC-PET detector module.

[2] The resistive electrodes may be made of comercial glass, bakelite, or even lead glass.

avalanche. The signal collected by the pickup electrodes, which are external to the resistive electrodes, will determine the position of the avalanche.

#### 2.3.4.1 Probability of extraction versus plate thickness

One way of increasing the detection efficiency with RPCs is to expand the number of thin stacked electrodes, thus incrementing the number of gas gaps. As stated above, in order to maximize the detection efficiency, a compromise has to be set between the probability of extraction of the electron from the electrode and the probability of interaction of the incoming photons with the electrode. Fig. 2.24 was obtained by means of GEANT4 simulations [7] and shows how the energy of the photons influences the optimum plate thickness. For a given number of stacked electrodes, the detection

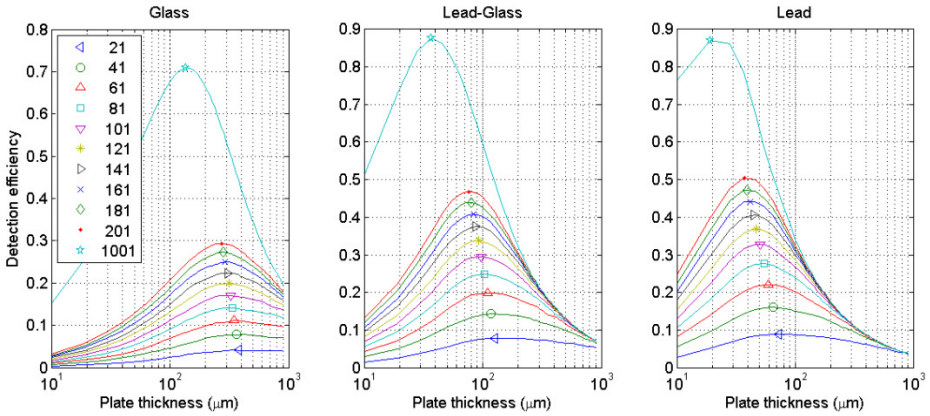


**Figure 2.24:** Gamma ray detection efficiency versus plate thickness, for different materials and different number of plates. From [210]

.

efficiency to 511 keV $\gamma$-rays raises with the thickness of the plates until it reaches a maximum, decreasing afterwards. Too thick plates prevent the electrons from escaping the electrode, thus avoiding the development of an avalanche. The results also show that an increasing number of plates requires a reduced plate thickness for optimum efficiency.

The dependence of the photon detection efficiency on the energy of the incoming photon is shown in fig. 2.25, and was also obtained through GEANT4 simulations [7]. We observe that the low-energy photons have a lower probability of starting an avalanche, since their energy is not enough to extract the electron from the converter plate. This fact configures a major advantage of RPC-PET, as we will see in

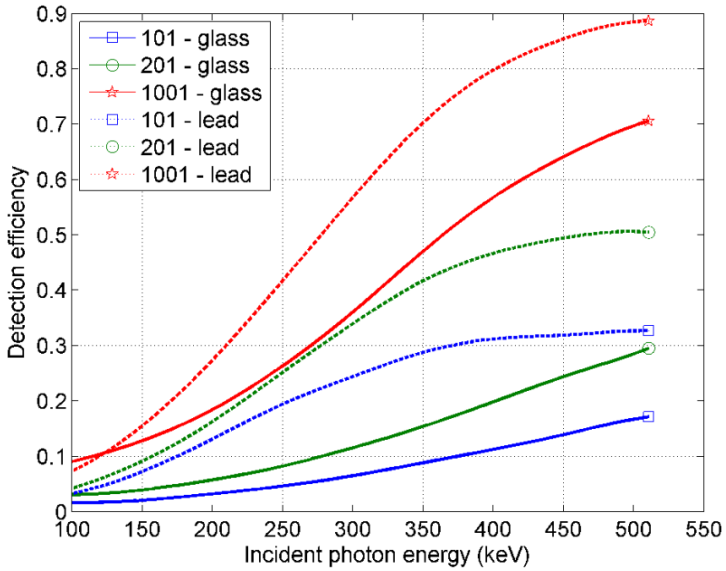


**Figure 2.25:** Efficiency versus energy for optimum plate thickness. From [210].

chapter 5. By rejecting the low-energy photons, we are removing from the acquisition those photons that have sufferd one or more Compton interactions in the object (patient), thus contributing to the increase in lesion detectability. The figure also confirms that increasing the converter plates results in a larger photon detection efficiency.

#### 2.3.4.2 Misidentified fraction

Compton scattering in the detectors may lead to the production of undesired and incorrect lines of response (LORs) that do not cross the annihilation point. The *misidentified fraction* (MIF) corresponds to the number of coincidence events where at least one of the detector interactions gives wrong spatial information. It is associated to photons deviated from their original path due to Compton interaction on one or more electrodes, providing an undesired scattered LOR. The point spread function (PSF)[1] resulting from the simulation of the interaction of $\gamma$-rays with an RPC detector with 201 plates is shown in fig. 2.26, for photons shot perpendicularly to either glass or lead plates. The MIF is given by the ratio between the number of events out of the central bin and the total number of events detected. In fig. 2.27 we observe that a decreasing width of the central bin leads to an increase of the MIF, because more events fall outside

[1]The point spread function may be characterized as the FWHM of the response of the system to a point source.

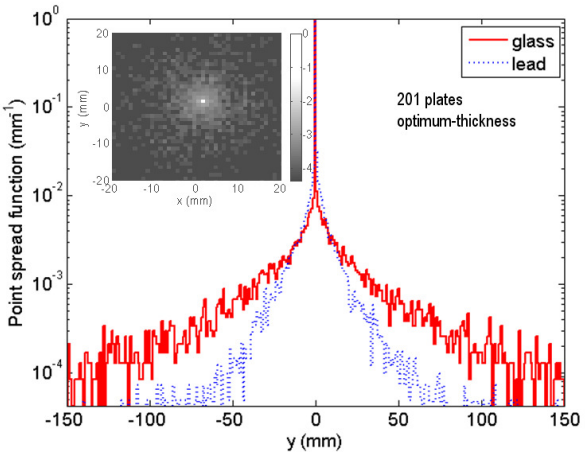


**Figure 2.26:** Point spread function resulting from GEANT4 simulations. From [210].

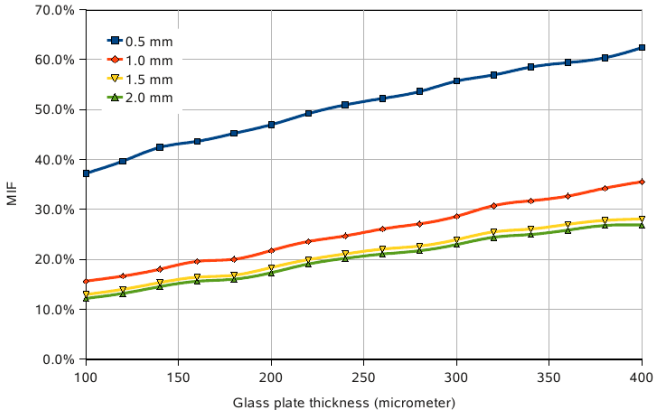


**Figure 2.27:** Misidentified fraction (MIF) as a function of central bin size, for different glass plate thicknesses.

the limits of the bin. Consequently, a trade-off between the chosen distances and the corresponding MIF has to be considered. Small distances between electrodes demand more instrumentation burden at the cost of a larger MIF, while larger distances have a significative impact on the spatial resolution.

### 2.3.5 Electronic read-out

In order to handle large detection areas, RPC-based detectors need an appropriate electronic read-out system to avoid an electronic channel for each read-out strip, which is too expensive. For this purpose, two pre-amplifiers are located at the left and right ends of a certain number of strips separated by resistive or capacitive charge division.

Each of the two pre-amplifiers receives a fraction of the total charge induced by the avalanche, and the relative position $\chi$ of one event occurring between two electrodes is given by

$$\chi = \frac{Q_L - Q_R}{Q_L + Q_R}, \qquad -1 \leq \chi \leq 1, \tag{2.32}$$

with $Q_L$ and $Q_R$ being the avalanche charge fraction collected by the left and right pre-amplifiers, respectively. For a division matrix with length $L$, the absolute position $x$ is then given by

$$x = (1 - \chi)\frac{L}{2}. \tag{2.33}$$

Both charge division configurations present their own advantages and disadvantages in what respects noise, linearity, and signal propagation [87, 211]. The resistive charge division features a good linearity in $\chi$, while the capacitive charge division provides a fast signal at reduced noise level. The characteristic nonlinearity in $\chi$ in the capacitive charge division can be corrected using proper software tools. The use of high capacitors may minimize the nonlinearity, nevertheless the trade-off between the nonlinearity and the signal-noise relationship should always be considered. The intrinsic capacity between strips favors the capacitive division approach. Fig. 2.28 depicts the electrical model of capacitive charge division applied to the small-animal and human RPC-PET prototypes. The charge read-out strips are separated by charge division capacitors and

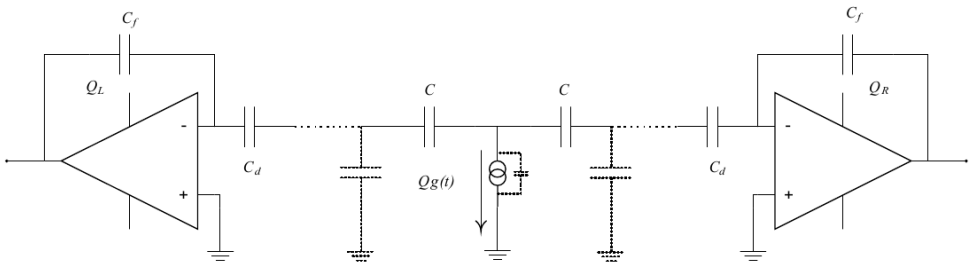


**Figure 2.28:** Positioning by means of charge division. Each detection element is composed by a capacity $C$ positioned between successive electrode strips, and by an intrinsic capacity to ground (dotted) for each strip. $C$ represents the equivalent capacity due to the capacitor positioned between electrodes for charge division readout together with the intrinsic capacity between neighboring parallel electrodes. The current signal may be modeled by $Qg(t)$, with $Q$ being the charge of the avalanche and $g(t)$ a unity function that models the charge collection mechanism. From [87].

the signal induced by the avalanche is collected by two charge amplifiers located at the end of the charge division chain. A possible configuration of a 2D strip and read-out electronics for the reading out the positioning of the hits in an RPC-detector is depicted in fig. 2.29.

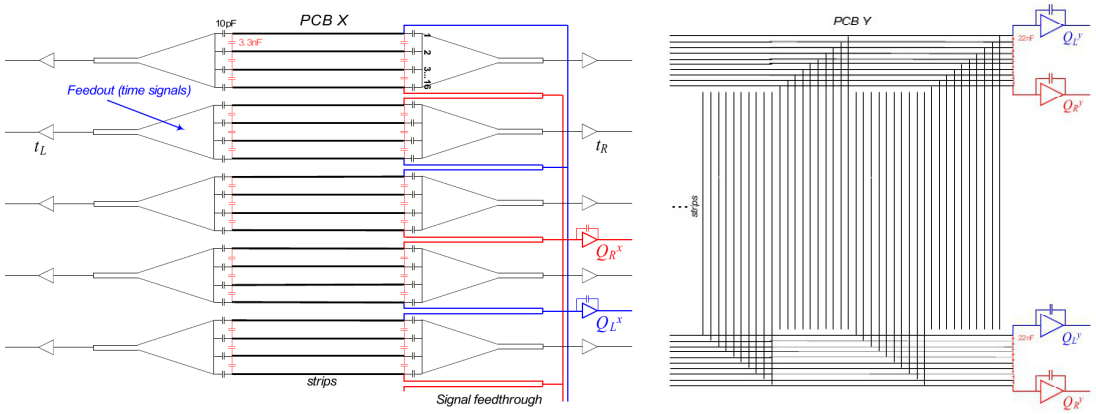


**Figure 2.29:** Left: example of electrode read-out with charge division implemented in the vertical axis $X$ for groups of 16 horizontal strips, with left and right charge signals denominated $Q_L$ and $Q_R$, respectively. Left-right coarse position $Y$ in the horizontal axis may be derived by means of the time difference between $t_L$ and $t_R$: $Y = (t_L - t_R) \cdot v/2$, with $v$ being the velocity of signal propagation along the strip ($\sim c/2$). Right: example of an electrode read-out with charge division implemented in the horizontal axis $Y$ (fine $Y$ positioning). From [87].

#### 2.3.5.1 Sub-millimeter electronic resolution

A measurement of the contribution of the charge-division read-out electronics to the spatial resolution was performed with a capacitive charge injector positioned in the four vertices of a square with 2 mm side. Fig. 2.30 shows the reconstructed image of each point in the square demonstrating sub-millimeter accuracy.

### 2.3.6 Experimental detection efficiency

The detector efficiency of two RPC-PET detectors was experimentally measured with a setup whose scheme is depicted in fig. 2.31 [87, 210]. Each detector was composed by five stacked 0.4 mm thick glass plates with an area of 30 × 30 cm$^2$, and separated from each other by 0.35 mm. The pickup electrodes were inserted between the detectors,

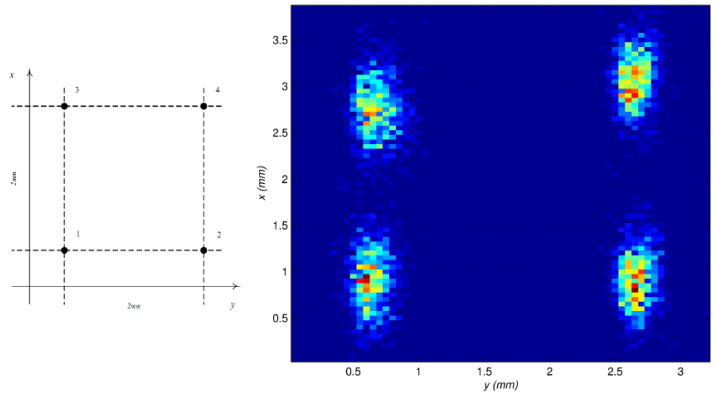


**Figure 2.30:** Example of sub-millimeter electronics read-out by means of a charge transient injected at the four vertices of a square with 2 mm side. The capability of the readout electronics to deliver positions with sub-millimeter accuracy is demonstrated. From [87].

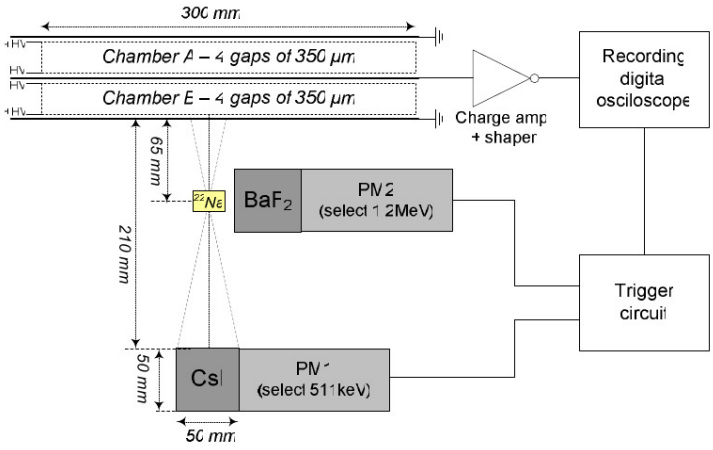


**Figure 2.31:** Setup utilized for determining experimentally the efficiency of a four-gap RPC detector for PET. From [210].

shunted, and converted to a single-charge sensitive amplifier read-out by a storage oscilloscope. This detector assembly was contained within an aluminium box flushed with 90% $C_2H_2F_4$ + 10% $SF_6$.

A $^{22}$Na radioactive source was positioned lateral to a $BaF_2$ detector and in line with a CsI crystal and the RPC-PET detectors. The coincidence of the 1.275 MeV photons detected by the $BaF_2$ scintillator with the 511 keV photons detected by the CsI scintillator served as a trigger for the detection of the two almost back-to-back 511 keV

photons. The ratio between the number of events detected by the RPC-PET detectors and the number of detected triggers yields the detection efficiency of the RPC-PET detectors to $\gamma$-rays of 511 keV. Baseline oscillations in the signals collected from the RPC-PET detectors can be corrected with a charge pre-amplifier and a spectroscopy amplifier. This permits to study the dependence of the detector efficiency even for very low charge thresholds, as shown in fig. 2.32.

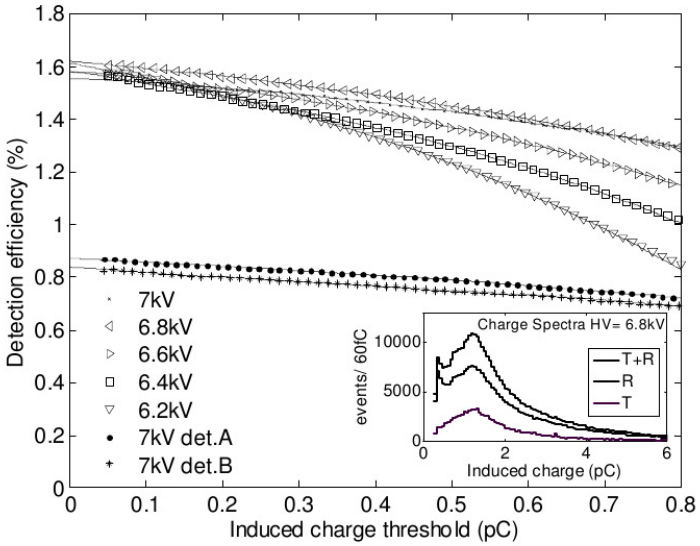


**Figure 2.32:** Efficiency results obtained with two four-gap RPC detectors for PET. From [210].

The high voltage applied on both chambers simultaneously or on each one individually ranged from $\pm 6.2$ to $\pm 7$ kV. The curves depicted in fig. 2.32 are rather flat and the error incurred on the extrapolation to zero charge is certainly small. All voltages yield essentially the same intrinsic efficiency, confirming that the result is quite independent on read-out effects. The results presented were corrected for the random events and the data were acquired at a trigger rate of approximately 200 Hz. Fig. 2.33 shows the time spectrum obtained from the difference between the time of the trigger logical signal and the time of the chamber charge signal. The number of true+random (T+R) and random (R) events were estimated by integrating the time spectrum over the windows shown in fig. 2.33. The influence of the random events was corrected for, thus providing

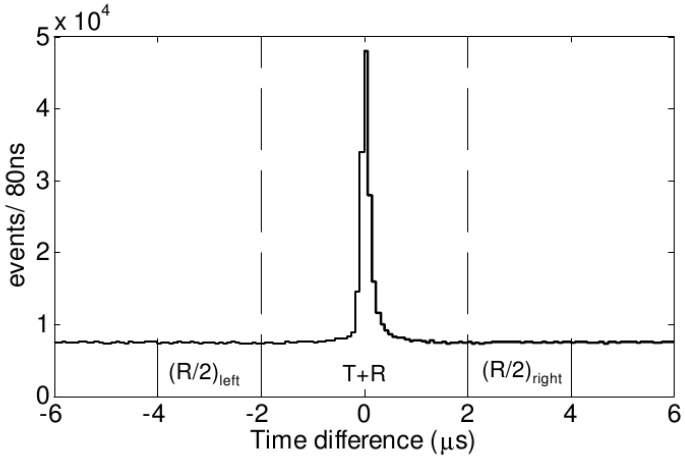


**Figure 2.33:** Data processing utilized for determining experimentally the efficiency of a four-gap RPC detector for PET. From [210].

the number of true events $T$,

$$T = (T + R) - (R/2)_{left} - (R/2)_{right}. \tag{2.34}$$

The efficiency is finally given by $\frac{T}{no.\ of\ triggers}$.

### 2.3.7 Experimental time resolution

The measurement of the time resolution of the tRPCs intended for a TOF-PET system has been carried out with dedicated read-out electronics [5]. Its performance has been evaluated with a pulse generator and with tRPCs. An almost linear correlation between the charge collected from the detectors and the one digitally measured with the electronics was observed. In order to determine the coincidence time resolution of the RPC-PET system, a setup with two 6-gap (200 $\mu$m each) detectors and a $^{22}$Na source between them was assembled . For an applied voltage of 6.5 kV, a coincidence time resolution of 126 ps $\sigma$ was obtained, which corresponds to 300 ps FWHM (see fig. 2.34). This result is the proof for the time-of-flight capabilities of RPC-PET that will be deeply analysed in chapter 5.

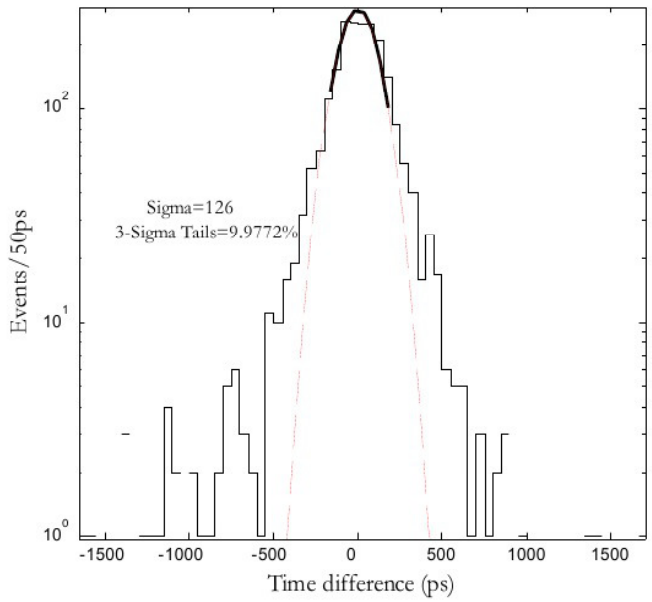


**Figure 2.34:** Experimental time resolution obtained between two RPC detectors with 6 gaps each for pair of 511 keV photons. Adapted from [5].

## 2.4 Whole-body PET

Applications of clinical PET oncology are driving scanner technology to further improve image quality for small lesion detection and reduce scanning time for faster patient throughput in the clinic. Such improvements will require higher sensitivity for shorter acquisition times and lower injected dose [212].

Single-bed whole-body positron emission tomography based on resistive plate chamber detectors has been proposed for human studies (RPC-PET) [4]. RPC-based detectors offer simple and economic construction, reliability of operation, and extremely good time and intrinsic position resolutions (300 ps FWHM for the coincidence [4], and 38 $\mu$m $\sigma$ for cosmic muons [19], respectively). These results make RPC detectors suitable for large AFOV PET systems assisted by TOF (TOF-PET). The DOI can also be accurately measured [6], rendering RPC-PET essentially parallax-free.

In current whole-body PET scanners, the AFOV is approximately 15-22 cm [109]. A long AFOV scanner capable of imaging the whole-body in a single scan would increase significantly the sensitivity. Simulated (NEMA NU2-1994 [66]) and experimental feasibility studies [7, 8] indicate that human RPC-PET, covering an AFOV of 2.4 m, can increase the absolute sensitivity over existing PET systems with 16-cm AFOV by a factor up to 20, if the TOF benefit is taken into account [9]. Based on the NEMA NU2-1994 protocol, the absolute sensitivity for RPC-PET without TOF is still 4.5 times larger than that of the Advance PET scanner from General Electric Medical Systems [7] (GE).

In the last decade, several authors have devoted work to studying the feasibility of extended-AFOV crystal-based PET scanners [117, 213, 214, 215]. However, the high cost of such systems and the slow performance of the reconstruction algorithms still remains a major concern.

There are clear advantages for large AFOV systems covering the entire human length. Whole-body parametric imaging becomes feasible, with the possibility of examining simultaneously multiple volumes of interest, such as a tumor and the heart. It may also provide a substitute for arterial blood sampling in the generation of time-activity curves and plasma input function parameters [216]. The determination of pharmacokinetic parameters for multiple organs could also enhance the study of side-effects for drug development.

Fig. 2.35 illustrates a planned RPC-PET system integrated with a CT machine. Detailed transverse and longitudinal views of this RPC-PET system and its detector

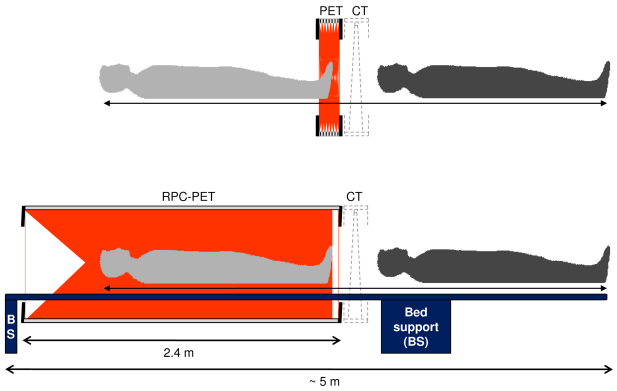


**Figure 2.35:** Scheme of the planned RPC-PET system integrated with a CT machine. Detailed transverse and longitudinal views of this RPC-PET system and its detector layout have been presented by Couceiro et al. [73]. The full system length is well within typical dimensions of current PET-CT rooms utilized for clinical scans. The PET-CT center of the University of Coimbra, for example, has two rooms each with a total length superior to 7 m.

layout have been presented by Couceiro *et al.* [73]. The full system length is well within typical dimensions of current PET-CT rooms utilized for clinical scans. The PET-CT center of the University of Coimbra, ICNAS, for example, has two rooms each with a total length of over 7 m. Besides supporting multimodality imaging capabilities, the CT will also provide the data, on a patient-to-patient basis, necessary to estimate by simulation the attenuated and object-scattered events, and introduce that correction into the PET reconstruction [9].

### 2.4.1 Planar sensitivity

The planar (slice) trues sensitivity of a PET system dictates the exposure time necessary to obtain a good enough statistics to detect a lesion [117]. This quantity is currently measured using a NEMA NU 2-2001 line-source phantom [217]. However, such phantom is not tailored for large AFOV PET systems, due to its length of 70 cm, thus being necessary to extend the phantom axial length.

An exhaustive Monte Carlo study on the sensitivities of several PET scanners has been carried out by Crespo et al. [9]. It included both the NEMA NU 2-2001 phantom

and the extended one, with an axial length of 2.4 m. The considered scanners were: the BGO-based Advance (15.2 cm AFOV) in 3D-mode, from General Electric Medical Systems; the LSO-based Biograph TruePoint (16.2 cm AFOV) and Biograph TruePoint TrueV (22 cm AFOV), from Siemens Medical Solutions; an LSO-based scanner simulated with 196 cm axial length (and decreased crystal depth); and an RPC-PET system with 2.4 m AFOV made of detectors with 120 gas gaps.

#### 2.4.1.1 Simulation with a spherical source of 1 cm diameter

The very oblique LORs accepted by a whole-body single-bed RPC-PET system contribute to a higher sensitivity because of the increasing acceptance. However, this has the drawback of increasing the attenuation due to the longer path through matter. In order to study these competing effects, the trues sensitivity, $\eta_T$, and the noise equivalent sensitivity, (NES) [1], are evaluated by means of Monte Carlo simulations of a spherical source with a diameter of 1 cm immersed both in air and in water phantoms of different diameters $\phi$. The results presented in table 2.3 (see also fig. 2.36) show that an RPC-PET tomograph performs better than the Advance PET scanner for more than one bed, especially for a spherical source surrounded by air.

[1] The noise equivalent sensitivity NES is defined as

$$\mathrm{NES} = \frac{\mathrm{T}^2/(\mathrm{T}+\mathrm{S})}{\text{events started}}. \tag{2.35}$$

Here, $T$ and $S$ are the rates of true and scattered events, respectively. A scanner NES is the slope of its noise-equivalent count rate (NECR) curve at low activity, where system dead-time and random events are negligible. It is therefore constant and independent of object activity. Therefore, the NES provides an estimate of the net sensitivity at low activities of a PET scanner with the negative impact of the scatter events taken into account [218].

**Table 2.3:** Comparison of trues sensitivity and NES for a spherical source with 1 cm diameter scanned in air or immersed in water phantoms of different diameters $\phi$. The TOF advantage of RPC–PET is not taken into consideration at this stage. An energy-dependent detection efficiency according to fig. 2.36 (left) has been taken into account for computing the sensitivities associated with the Advance PET scanner from General Electric. For RPC-PET the detection efficiency followed the curve shown in fig. 2.36 (right). From [9].

| | Scanner | | | | Ratio $\eta_T$ | | | |
|---|---|---|---|---|---|---|---|---|
| Diameter of | GE Advance | | RPC-PET ($\theta \leq 45°$) | | $^{\text{Advance}}/_{\text{RPC-PET}}$ | | | |
| water phantom | $\eta_T$ (%) | NES (%) | $\eta_T$ (%) | NES (%) | 1 bed | 7 beds | 14 beds | 20 beds* |
| 0 cm (air) | 4.35 | – | 2.57 | – | $^{1.7}/_{1}$ | $^{1}/_{4.1}$ | $^{1}/_{8.2}$ | $^{1}/_{11.8}$ |
| $\phi = 27$ cm | 0.33 | 0.180 | 0.155 | 0.044 | $^{2.1}/_{1}$ | $^{1}/_{3.3}$ | $^{1}/_{6.7}$ | $^{1}/_{9.5}$ |
| $\phi = 35$ cm | 0.20 | 0.086 | 0.068 | 0.013 | $^{2.9}/_{1}$ | $^{1}/_{2.4}$ | $^{1}/_{4.8}$ | $^{1}/_{6.9}$ |

$\theta$ = angle formed between a LOR and the transaxial plane of the tomograph.

$\eta_T$ = trues sensitivity; NES = noise equivalent sensitivity.

7 beds* $\simeq$ scan from head to beginning of thighs (e.g. [219]); 14 beds* $\simeq$ scan from head to mid-legs.

* The PET-scan protocol at the PET center of the University of Coimbra, equipped with a Philips Allegro™ PET/CT with an axial field of view of 18 cm, consists of 11 bed positions for a scan from top of the head to mid thighs, and 20 beds for a full whole-body scan (top of the head to feet, included).

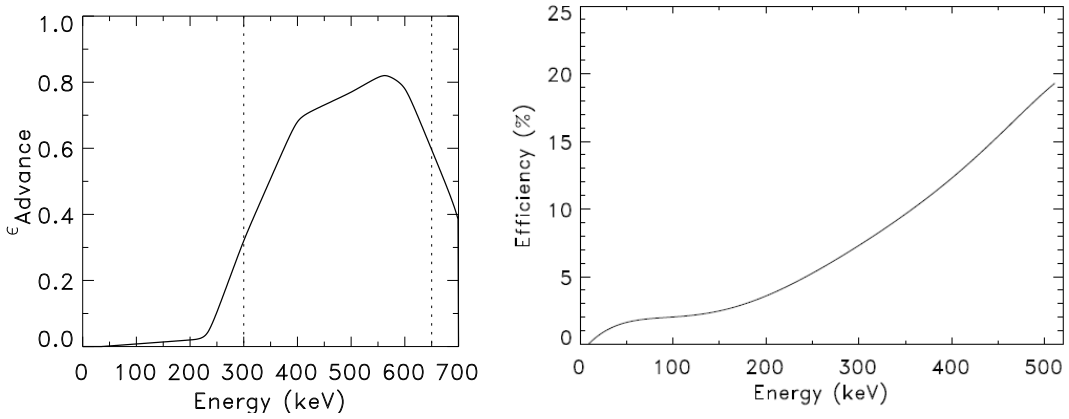


**Figure 2.36:** Left: detection efficiency as a function of photon energy for the BGO block-detector of the GE Advance PET scanner (from [9] after, [220]). Right: simulated efficiency of an RPC-PET detector with 121 glass plates (120 gas gaps). From [9].

#### 2.4.1.2 Simulation with the NEMA NU2-2001 protocol

The planar (slice) sensitivity, $\eta_S$, has the same definition as the absolute sensitivity, $\eta_a$, (see section 2.2.5.2), except that, for $\eta_s$, the events are started in a given slice of the scanner. Such $\eta_s$ can therefore be represented as a profile along the longitudinal axis of the tomograph, with its maximum value taken to be $\eta_a$. Following the NEMA NU2-2001 protocol, we define planar sensitivity $\eta_s$, and the axial sensitivity as

$$\eta_s[\%] = \frac{\text{Rate events detected from center slice}}{\text{Source activity contained in slice}}, \tag{2.36}$$

$$\eta_{axial}(i)[\%] = \frac{\text{Rate events detected from slice } i}{\text{Source activity contained in slice}}. \tag{2.37}$$

The meaning of these equations is illustrated in fig. 2.37 for the current whole-body scanners (left), and for the extended AFOV PET scanners.

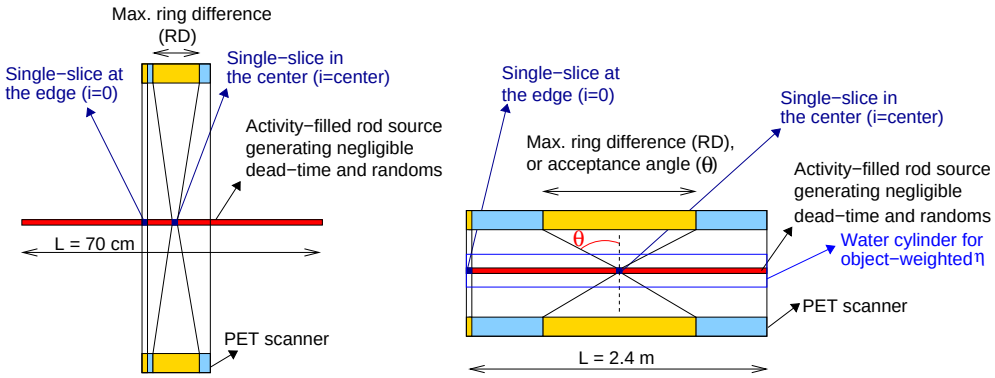


**Figure 2.37:** Left: setup for computing, by simulation, the sensitivities for NEMA NU-2 2001: absolute, $\eta_a$, slice, $\eta_s$, and axial sensitivity, $\eta_{axial}$. Details respecting each scanner are summarized in rows 1 to 6 of table 2.4. Right: absolute, $\eta_a$, and slice sensitivity, $\eta_s$, simulated for scanners with extended AFOV (196-cm LSO-based, and RPC-PET) corresponding to an extended NEMA NU-2 2001 protocol. Details respecting the scanners are summarized in columns 5 and 6 of table 2.4. From [9].

The simulated trues sensitivity performance of several commercial PET scanners together with the RPC-PET system performance are presented in table 2.4.

These results assumed a bed measuring time of 1.5 minutes (lines 10 and 19) for the Siemens TruePoint TrueV PET scanner [117]. For the remaining scanners the measuring time per bed was computed according to the ratios of planar (slice) sensitivities $\eta_s$ (lines 9 and 18).

**Table 2.4:** Trues sensitivity performance of several PET scanners simulated with GEANT4. From[9].

| | PET scanner | Biograph[a] TruePoint | Biograph[a] TruePoint TrueV | GE[b] Advance (3D-mode) | 196-cm AFOV LSO-based | RPC-PET | |
|---|---|---|---|---|---|---|---|
| Line − source (LS) only | Nb. of block-rings | 3[c] | 4[c] | 3[d] | 35[c] | n.a. | 1 |
| | AFOV (cm) | 16.2 | 22 | 15.2 | 196 | 240 | 2 |
| | Ring difference | 27 | 38 | 11 | 162 | $\theta \leq 45°$ [e] | 3 |
| | Packing fraction | 0.86 | 0.86 | 0.844 | 0.86 | 1.0 | 4 |
| | Crystal depth (cm) | 2.0 | 2.0 | 3.0 | 0.43 | n.a. | 5 |
| | Singles efficiency at 511 keV | 0.7 | 0.7 | 0.78[f] | 0.194 | 0.194 | 6 |
| | Absolute sensitivity, $\eta_a$ | | | | | | |
| | 70-cm line source (cps/kBq[g], (%[h])) | 4.19[i] (0.43) | 7.60[j] (0.79) | 6.4[k] (0.66) | 13.07 (1.35) | 24.9 (2.57) | 7 |
| | 1.5-m line source (cps/kBq, (%)) | 1.96 (0.20) | 3.55 (0.37) | 2.99 (0.31) | 12.5 (1.30) | 24.9 (2.57) | 8 |
| | Planar (or slice) sensitivity[l], $\eta_s$ | | | | | | |
| | (% per 2-mm slice thickness) | 3.06 | 4.22 | 4.35 | 1.45 | 2.57 | 9 |
| | Time for equal slice | | | | | | |
| | quality[m] (min:sec) | 2:04 [117] | 1:30 [117] | 1:27 | 4:22 | 2:28 | 10 |
| | Scan of 70-cm length object | | | | | | |
| | Nb. of bed steps | 7 | 5 | 7 | 1 | 1 | 11 |
| | Total scan time (min:sec) | 14:28 | 7:30 | 10:09 | 4:22 | 2:28 | 12 |
| | **Relative gain (no TOF)**[n] | **1.0** | **1.9** | **1.4** | **3.3** | **5.8** | 13 |
| | Scan of 1.5-m length object | | | | | | |
| | Nb. of bed steps | 14 | 11 | 14 | 1 | 1 | 14 |
| | Total scan time (min:sec) | 28:56 | 16:30 | 20:18 | 4:22 | 2:28 | 15 |
| | **Relative gain (no TOF)**[n] | **1.0** | **1.8** | **1.4** | **6.6** | **11.7** | 16 |
| LS in water phantom[o] | Absolute sensitivity, $\eta_a$ | | | | | | |
| | 1.5-m line source (%) | 0.013 | 0.023 | 0.019 | 0.066 | 0.172 | 17 |
| | Planar sensitivity[l], $\eta_s$ | | | | | | |
| | (% per 2-mm slice thickness) | 0.239 | 0.327 | 0.342 | 0.079 | 0.158 | 18 |
| | Time for equal image | | | | | | |
| | quality[m] (min:sec) | 2:04 [117] | 1:30 [117] | 1:27 | 6:15 | 3:08 | 19 |
| | Scan of 1.5-m length object | | | | | | |
| | Nb. of bed steps | 14 | 11 | 14 | 1 | 1 | 20 |
| | Total scan time (min:sec) | 28:56 | 16:30 | 20:18 | 6:15 | 3:08 | 21 |
| | **Relative gain (no TOF, TruePoint = 1)**[n] | **1.0**[p] | **1.8**[p] | **1.4** | **4.6**[p] | **9.2**[q] | 22 |
| | **Relative gain (no TOF, TrueV = 1)**[n] | **0.6**[p] | **1.0**[p] | **0.8** | **2.6**[p] | **5.3**[q] | 23 |

n.a. = not applicable
[a] from Siemens Medical Solutions.
[b] from General Electric.
[c] 5.6×5.6 cm$^2$ front face[117].
[d] 5.0×2.45 cm$^2$ front face[221].
[e] $\theta$ = inverse polar angle.
[f] cf. Fig. 2.36.
[g] NEMA NU 2-2001 [8, 9].
[h] events detected / annihilations started.
[i] 4.2 cps/kBq measured by manufacturer [9].
[j] 7.6 cps/kBq measured by manufacturer [9].
[k] 6.41 cps/kBq measured in [222] (375–650 keV).
[l] $\eta_s$ = maximum of $\eta_{axial}$ in fig. 2.38.
[m] Neglecting scatter fraction.
[n] For same scan time.
[o] Phantom with 27-cm diameter.
[p] $\Delta$t = 600 ps FWHM (not considered).
[q] $\Delta$t = 300 ps FWHM (not considered).

The NEMA NU2-2001 protocol does not consider the extended rod source, nor the surrounding water cylinder. These additional elements were included to assess quantitatively, in terms of sensitivity, two competing effects: 1) the larger solid angle acceptance for PET systems with extended AFOV, increasing system sensitivity, and

2) the increased scatter fraction expected for inclined LORs, due to the larger photon path in the patient/phantom surrounding the source, which decreases sensitivity.

The axial sensitivity trues profiles obtained for several scanners are shown in fig. 2.38 (left). Despite the slightly inferior axial sensitivity of the RPC-PET system, it remains

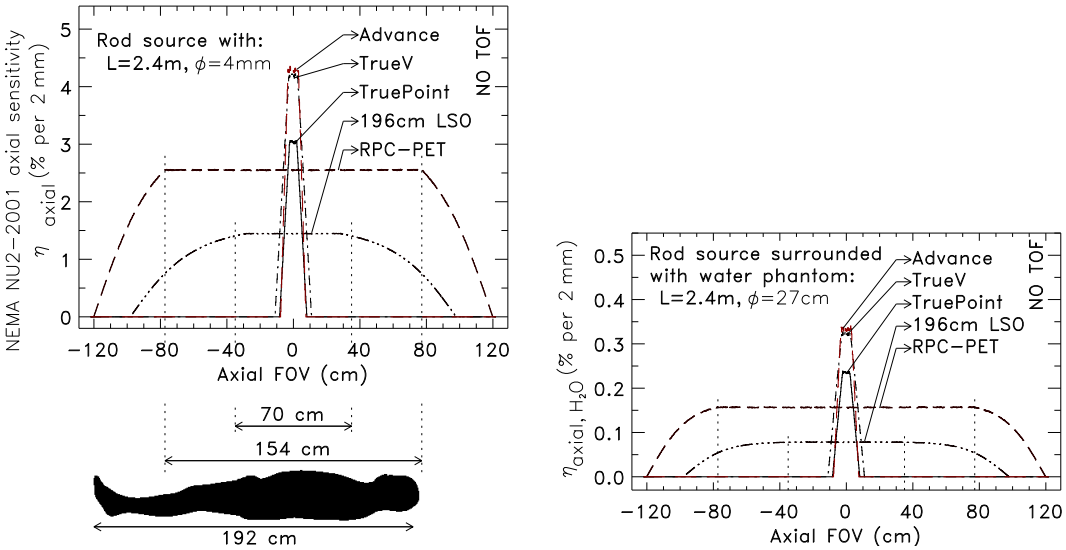


**Figure 2.38:** Left: axial sensitivity, $\eta_{axial}$, simulated for scanners with different AFOV. Details respecting the various PET scanners are given in table 2.4. The sagittal contour at the bottom, corresponding to a human figure with 1.92 m height illustrates the imaging potential of the whole-body RPC-PET system under study: a single bed can collect events from head to mid-legs with uniform longitudinal sensitivity. Right: axial trues sensitivities simulated with the line source immersed in a water cylinder with 27 cm diameter. From [9].

constant along the longitudinal direction in one-single exposure, and must be multiplied by the number of beds that a scintillator-based PET scanner would require to cover a 2.4 m AFOV. Fig. 2.38 (right) shows the axial sensitivity results considering a line source positioned inside a water phantom with 27 cm diameter. The increased sensitivity gain ranging from 5.3 to 9.2 (lines 22 and 23, table 2.4) makes of RPC-PET a well-positioned candidate to penetrate the PET segment[1].

Axial trues sensitivity and scatter fraction profiles obtained with the anthropomorphic phantom NCAT are shown in fig. 2.39. The collected scatter fraction and the trues sensitivity at each axial location for the RPC-PET system are compared to those

[1]An additional sensitivity gain, by a factor 4 to 5 in respect to non-TOF scanners, is expected when the 300 ps FWHM TOF resolution of RPC-PET is taken into account.

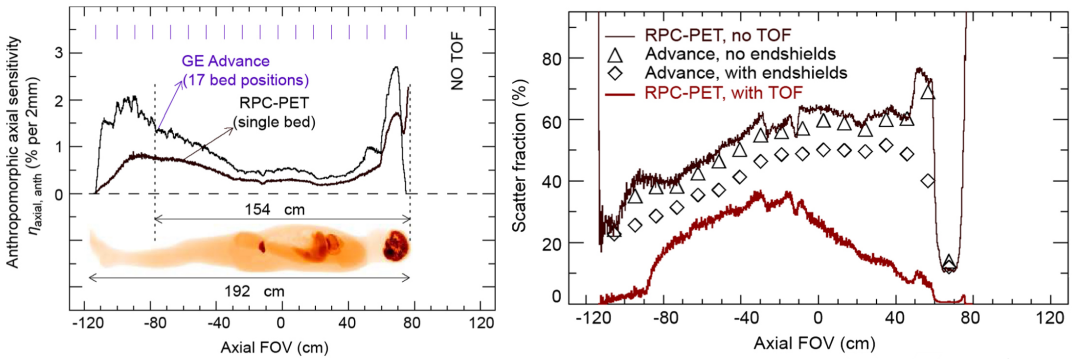


**Figure 2.39:** Left: Anthropomorphic axial trues sensitivities similar to fig. 2.38 (right), but simulated with an anthropomorphic phantom adapted to GEANT4 (both positron emission and photon attenuation were considered). Right: axial scatter fraction profiles obtained for the 2.4-m-long RPC-PET system, and for a 17-bed scan with the GE Advance with and without the lead end-shields described in [223]. From [9].

obtained with the conventional PET system (GE Advance, 3D mode). The vertical dashes displayed in fig. 2.39 (left) represent the margins of each bed step considered with the GE Advance. The scatter fraction profile for the GE Advance with its lead end-shields [223] is show in fig. 2.39 (right). The figure also shows that RPC-PET further benefits if its 300 ps FWHM TOF information is utilized to exclude scatter events occurring outside the anthropomorphic phantom [9].

### 2.4.2 Noise-equivalent count rate with the NEMA NU2-2001 protocol

The scatter fraction (SF), count rates and noise equivalent count rate (NECR) of an RPC TOF-PET system with 2.4m length AFOV have been addressed by detailed simulations performed in GEANT4, in which several factors influencing those quantities were considered [10]. An efficient first level trigger was proposed, which reduces the raw data to be transmitted for a post processing dedicated cluster. A multiple time window coincidence sorter with acceptance of all possible coincidence pairs along with LOR rejection based on TOF information was found to give higher NECR than those of state of the art PET scanners (see fig. 2.40).

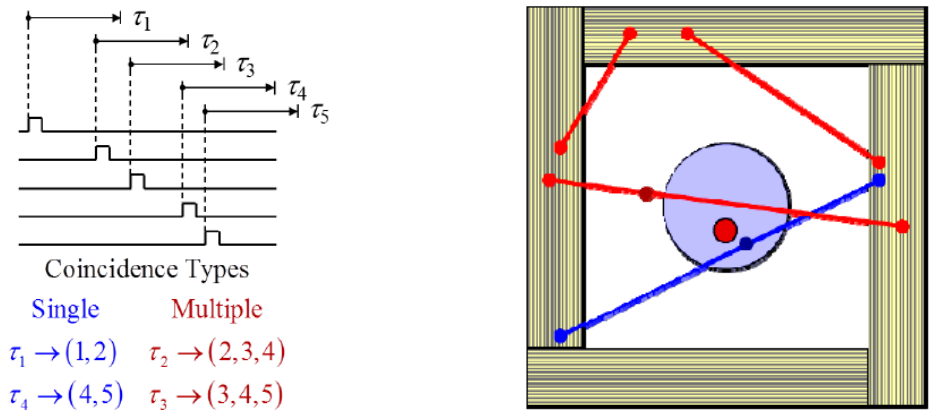


**Figure 2.40:** Left: coincidence sorter scheme with examples of produced coincidences based on a multiple time window (MTW). Right: TOF-based scatter rejection principle applied to the NEMA NU2-2001 protocol. Dots in the scanner walls represent the readout detection points. Red and blue lines correspond to rejected and accepted LORs, respectively. Dots in the bore represent direct TOF reconstructed points. From [10].

#### 2.4.2.1 Scanner geometry

The scanner geometry implemented in GEANT4 [224, 225] is depicted in fig. 2.41 (left). The scanner consisted of four detection walls forming a hollow cuboid, with 1151.6 mm outer width, 2408 mm axial outer length and 864.4 mm square bore width. Each detection wall consisted of a 1 mm thick aluminum case with outer dimensions of 143.6 mm, 1008 mm and 2408 mm in the radial, transaxial and axial directions, respectively. Each detection wall contained a stack of 20 RPC detectors, each with 6.88 mm thickness (radial direction), 1 m width (transaxial direction) and 2.4 m length (axial direction).

Fig. 2.41 (right) depicts the readout scheme of each RPC detector. Both outer axial electrodes (fig. 2.41 (left)) have transaxially aligned strips with 2 mm pitch, while the middle axial electrode has 2 mm pitch axially aligned strips. This scheme allows to distinguish between each detector module, providing a 3.44 mm DOI binning to the module center, which corresponds to a 1.22 mm maximum DOI parallax error at the center of the image space.

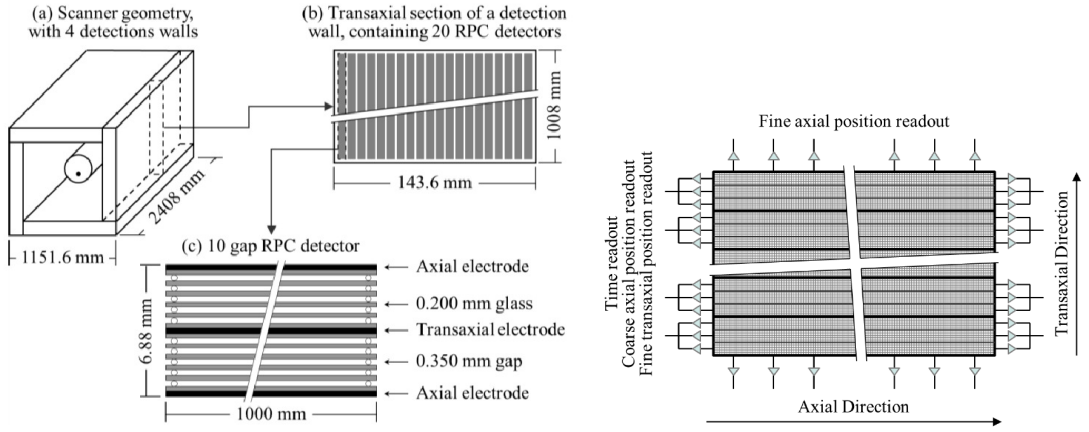


**Figure 2.41:** Left: sketch of the RPC TOF-PET system: (a) Scanner, consisting of four detection walls, with the NEMA NU2-2001 [65] phantom centered in its field of view; (b) Structure of each detection wall; (c) Internal structure of each RPC detector. Right: readout scheme for RPC detectors. Fine mesh represents 2 mm pitch strips. Large transaxial sections containing a set of axially aligned strips, placed on the middle transaxial electrode, represent independent readout sections, used for time, coarse axial position (1 cm $\sigma$ Gaussian distribution) and fine transaxial positions readout. These are further subdivided into 3 equal width subsections for coarse transaxial position readout, binned to the subsection center. Transaxially aligned strips on the outer axial electrodes, used for fine axial position readout, allow to distinguish between the two detection modules, providing a 3.44 mm DOI binning to the module center, which corresponds to a maximum DOI parallax error of 1.22 mm at the center of the image space. From [10].

#### 2.4.2.2 Simulated results of noise equivalent count rates

Fig. 2.42 depicts the computed NECR for a simulated RPC TOF-PET system (solid lines, left Y-axis) for a standard 70 cm length NEMA NU2-2001 phantom (left) and a 180 cm axially extended phantom (right). The NECR profile of the Philips Gemini TF scanner [108] (solid black line, left Y-axis) is also included in the images, as well as the NECR gains (dashed lines, right Y-axis). All data correspond to a multiple time window acquisition strategy.

We observed that, for a dead time in the reading of the position signal $\tau_{ps} = 3.0$ $\mu$s (present value without dedicated efforts in speeding up the electronics), the NECR has a peak value of $\sim$167 kcps at 7.6 kBq/cm$^3$, representing a 2.0 NECR increase in respect to published data for the Philips Gemini TF scanner [108]. For $\tau_{ps} = 1.0$ $\mu$s, the NECR increases up to 349 kcps at 7.6kBq/cm$^3$.

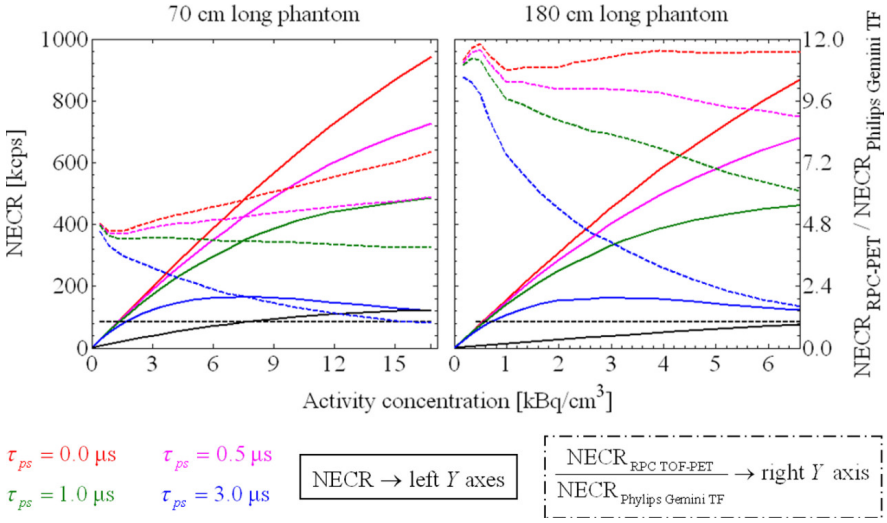


**Figure 2.42:** NECR (solid lines, left Y axes) using TOF rejection for a data set with all accepted coincidence pairs, along with Philips Gemini TF published data [108]. Left: Results for the 70 cm length strict NEMA NU2-2001 [65] phantom. Right: Results for an axially extended phantom with 180 cm length. Also presented is the ratio between computed NECR and that of the Philips Gemini TF scanner (dashed lines, right Y axes). From [10].

Considering the 180 cm length extended phantom with the same total phantom activity, there is a 0.39 (70/180) factor reduction in activity concentrations, thus resulting in a peak NECR, for $\tau_{ps} = 3.0$ $\mu$s, of 164 kcps at 3 kBq/cm$^3$. This represents a 5.5 gain relative to the Philips Gemini TF at the same activity concentration [108].

### 2.4.3 Clinical Applications

The applications of PET/CT are fundamentally concentrated in the oncologic medical field. The term whole-body used in PET/CT is misleading because the most commonly used FOV (160 cm) covers only the base of the skull to the upper tights [226]. Therefore, it became necessary to include the term "true whole-body" for a scan range from the top of the head to bottom of feet (193cm) [227, 228].

Compared to the limited FOV imaging, the true whole-body imaging may increase the staging accuracy, modify the treatment planning, and help on the selection of more accessible biopsy locations, thus avoiding the need of unnecessary surgical and imaging procedures. It may also provide an overview of the extension of the disease, once a considerable number of metastases occur outside the limited FOV [229]. A deeper

analysis of the benefits and trade-offs of a true whole-body imaging is presented in appendix A, where some medical cases and several studies on large populations are reported.

For instance, a study on the sensitivity and specificity [1] of the PET imaging for the detection of brain metastases showed that from 40 patients, MRI detected 16 patients with brain metastases and PET identified 12 true positives, 4 false negatives, 20 true negatives and 4 false positives. Thus, the calculated sensitivity and specificity of the PET imaging was 75% and 83%, respectively. The main reason for the lower lesion detectability of the PET system was related with the size of the lesions [230]. The RPC-PET system may provide an increasing lesion detectability as we will show in chapter 5, thus eventually increasing the RPC-PET sensitivity and specificity.

The acquisition and reconstruction times can be dramatically reduced with an RPC-PET system covering an AFOV of 2.4 m. In old PET/CT scanners, emission data were acquired for 12-13 bed positions (coaxial scan range of 193 cm), at 3 minutes per bed position, resulting in a total scan time of 36-39 mins. Nowadays, for instance, at ICNAS, the acquisition takes ∼20 minutes and the reconstruction needs approximately 15 minutes do display the image. The time required for true whole-body acquisitions and processing will continue to decrease and the co-axial scan range will continue to expand. It is therefore expected that RPC-PET will contribute to push even further the acquisition and reconstruction times (see chapter 5).

[1] Sensitivity measures the proportion of actual positives which are correctly identified as such, i.e., the ratio between the number of true positives and the total number of sick individuals. Specificity measures the proportion of negatives which are correctly identified as such, i.e., the ratio between the number of true negatives and the total number of well individuals.

## 2.5 Small-animal PET

Small-animal or preclinical PET imaging constitutes a way of assessing biological structures and function in vivo by non-invasive means, allowing the collection of quantitative information, both in health and disease states [231]. It also provides a very useful way of performing longitudinal studies of the entire disease process, from disease onset to progression and therapy monitoring.

An ideal PET scanner designed for small-animal imaging would have the following features: high spatial resolution (sub-millimeter range), high sensitivity, detector ring with a FOV optimized to the specific targeted animal size range, good timing resolution, and multimodality imaging capability [232].

### 2.5.1 System performance

In recent years, huge developments in small-animal PET imaging have occurred, that permitted to achieve, concurrently, better spatial resolution and sensitivity. Fig. 2.43 shows the performance of several PET and PET-MRI systems. The specifications

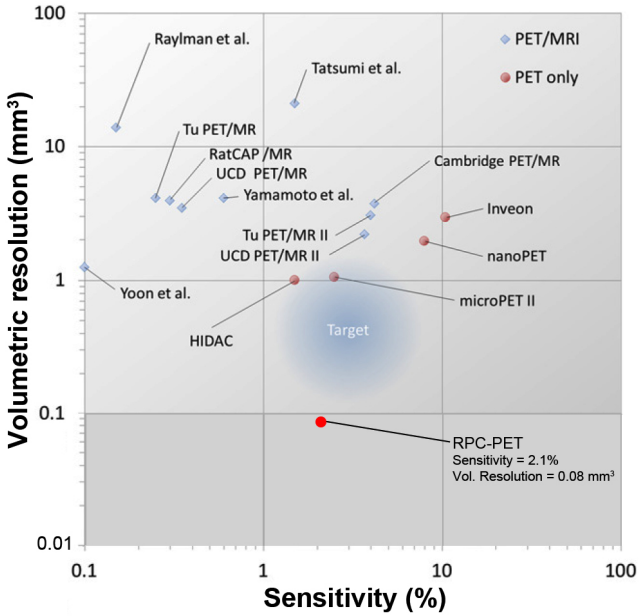


**Figure 2.43:** The performance of small-animal PET/MRI systems (blue, diamond) and stand-alone small-animal PET systems (red, circle). Adapted from [233].

of commercial systems and the small-animal RPC-PET are summarized in table 2.5. Most of these commercial systems have been compared following the NEMA NU 4 standards [234, 249]. This protocol was published due to the need for standardized

**Table 2.5:** Performance of different commercial preclinical PET systems and the small-animal RPC-PET under construction.

| System | Detector | AFOV (mm) | $\tau_{cw}$ (ns) | Reconstruction | CFOV (radial offset = 5 mm) Spatial Resolution (mm) FWHM[0] |
|---|---|---|---|---|---|
| microPET P4® | LSO | 78 | 6 | FORE + 2D FBP | $2.29 - 2.18 - 2.20^{1,2}$ |
| microPET R4® | LSO | 78 | 6 | FORE + 2D FBP | $2.13 - 2.21 - 2.72^{1,2}$ |
| microPET Focus 220® | LSO | 76 | 6 | FORE + 2D FBP | $1.92 - 1.66 - 1.90^{1,2}$ |
| microPET Focus 120® | LSO | 76 | 6 | FORE + 2D FBP | $1.75 - 1.80 - 1.70^{1,2}$ |
| Inveon® | LSO | 127 | 3.4 | FORE + 2D FBP | $1.63 - 1.62 - 2.45^{1,2}$ |
| Mosaic HP® | LYSO | 119 | 7 | 3D FRP | $2.32 - 2.32 - 2.64^{1,2}$ |
| ClearPET® | LYSO/LuYAP | 110 | 12 | 3D FBP | $1.94 - 2.00 - 3.24^{1,2}$ |
| Argus® | LYSO/GSO | 48 | 7 | 2D FBP | $1.63 - 1.65 -^{1,2}$ |
| VrPET® | LYSO | 45.6 | 3.8 | SSRB + 2D FBP | $1.52 - 1.62 - 2.66^{1,2}$ |
| LabPET 8® | LYSO/LGSO | 75 | 20 | SSRB + 2D FBP | $1.65 - 1.70 - 1.4^{1,2}$ |
| LabPET12® | LYSO/LGSO | 112.5 | 20 | SSRB + 2D FBP | $1.65 - 1.70 - 1.40^{1,2}$ |
| HIDAC® | MWPC | 280 | 40 | FBP | $1.08 - 1.08 - 1.10$ |
| NanoPET/CT® | LYSO | 95 | 5 | SSRB/FBP | $1.18 - 1.03 - 0.98^{1,2}$ |
| NanoPET/MRI® | LYSO | 94 | 5 | SSRB/FBP | $1.5 - 1.32 - 0.91^{1,2}$ |
| ALBIRA® | LYSO/PSPMT | 40 | 5 | - | $< 1.3$ |
| ClearPEM-Sonic®[4] | LYSO/APD | 160[5] | 4 | OSEM | 1.3 |
| RPC-PET | RPC | 100 | 1 | FBP | $0.43 - 0.43 -^{2}$ |

·[0]Radial, tangential and axial spatial resolution. ·[1]Radial offset = 5 mm. ·[2]Performance parameters assessed by means of the NEMA NU 4 standards [234]. ·[3]Axial not measured but should be uniform within the entire FOV for all three components. ·[4]Dual-head positron emission mammography exploited at ICNAS for small-animal imaging. ·[5]Two detector plates (16× 18 cm$^2$ FOV).

| | | **Mouse phantom** | | **Rat phantom** | | | |
|---|---|---|---|---|---|---|---|
| System | ACS (%) ($E_w$ (keV)) | Peak NECR (kcps)@ activity (MBq) | NECR @ 3.7 MBq | Peak NECR (kcps)@ activity (MBq) | NECR @ 10 MBq | Equip. cost (k€) | Ref. |
| microPET P4® | 2.25 (250-750) | 601@174 | 22.1 | 173@254 | 19.2 | | [235] |
| microPET R4® | 4.36 (250-750) | 618@156 | 37.2 | 164@137 | 30.5 | | [236] |
| microPET Focus 220® | 3.4 (250-750) | 897@103 | 66.5 | 267@129 | 50.9 | 850 | [237] |
| microPET Focus 120® | 7 (250-750) | 763@89 | 47.3 | 359@162 | 51.8 | | [238] |
| Inveon® | 9.3 (250-625) | 1670@131 | 129.0 | 593@110 | 137.8 | 650 | [239] |
| Mosaic HP® | 3.6 (250-665) | 555@92 | 59.6 | 244@87 | 65.2 | 600 | [240] |
| ClearPET® | 4.7 (250-750) | 73@18 | 29.3 | - | - | | [241] |
| Argus® | 4 (250-700) | 117@50 | 18.7 | 40@41 | 20.4 | 700 | [242] |
| VrPET® | 2.2 (100-700) | 74@22 | - | 31@34 | - | | [243] |
| LabPET 8® | 2.6 (250-650) | 279@82 | 23.5 | 94@91 | 19.4 | | [244] |
| LabPET12® | 4.3 (250-650) | 362@81 | 38.9 | 156@83 | 40.5 | | [244] |
| HIDAC® | 1.5 (-) | 67@209 | - | 52@96 | - | 500 | [245] |
| NanoPET/CT® | 7.7 (250-750) | 430@36 | - | 130@27 | - | | [246] |
| NanoPET/MRI® | 8.4 (250-750) | 406[0] | - | 392[1] | - | | [16] |
| ALBIRA® | 2 (350-650) | - | - | - | - | - | [247] |
| ClearPEM-Sonic® | 1.5[2] | - | - | - | - | - | [248] |
| RPC-PET | 2.1[3] | 320@88[4] | 125[5] | - | - | 100[5] | [50] |

·[0]@0.847 MBq/mL. ·[1]@0.125 MBq/mL. ·[2]Detector efficiency in the center of the plates at a distance of 100 mm. ·[3]Simulated, 15% RPC detection efficiency. ·[4]Simulated. ·[5]Estimated.

methods of performance evaluation that facilitate acceptance testing and routine monitoring, while providing comparison between systems from different vendors. Research prototypes features are outlined in table 2.6.

**Table 2.6:** Performance of different experimental preclinical PET systems.

| System | Detector | AFOV (mm) | $\tau_{cw}$ (ns) | Reconstruction | CFOV Spatial Resolution (mm) FWHM[0] | ACS (%) | Ref. |
|---|---|---|---|---|---|---|---|
| FSI-PET[1] | CdTe | 26 | 20 | FBP | $< 1 - 0.74 -$ | 4.0 | [14] |
| RatCAP | LSO | 18 | 40 | FBP | $2.1 - 2.1 -$ | 0.7 | [250] |
| SAI-UTSW[2] | BCF-10 | 135 | 18 | MLEM | $\sim 2$ | 1.3 | [251] |
| LWS-PET[3] | LWS[6] | 50 | 15 | MLEM | $1 - 1 - 1$ | 7.8 | [252, 253] |
| cMICE | LYSO | 120 | - | FBP | $1.05 - 0.99 - 1.24$ | - | [254, 255] |
| CZT[4] | CZT | 80 | - | MAP[5] | $1 - 1 -$ | 15-30 | [256, 257] |
| SBDIS[6] | LYSO-PSAPD | 80 | 20 | FBP | $0.62 - 0.83 -$ | - | [15, 257] |
| Yamamoto[7] | LYSO-SiPM | 10.4 | 16 | FBP | $0.75 - 0.71 -$ | 0.24 | [258] |

[0]Radial, tangential and axial spatial resolution. [1]Fine Structure Imaging. [2]Lead-Walled Straw. Price (approx.) = $325,000. [3]Small Animal Imager (SAI) - University of Texas Southwestern Medical Center (UTWS). [4]Cadmium Zinc Telluride. [5]Bayesian reconstruction based on MAP [259] [6]Stanford Breast Dedicated Imaging System. It is used for small-animal imaging, or organ-specific (breast) clinical imagers [257]. [7]Author's name.

#### 2.5.1.1 Spatial Resolution

Contrary to human PET, small-animal PET deals with very low-mass objects. Imaging a 20-30 g mouse as compared with a 75 kg average-size adult, represents a downscale by a factor 3,000 in weight and 15 in size. For a 300 g rat, the downscale is respectively 250 and 6. To visualize the same level of detail in a mouse, when compared with a human, the small-animal PET system needs to have a spatial resolution 15 times better than a human PET system. Given that state-of-the-art human PET systems achieve a spatial resolution of 4-5 mm FWHM, small-animal PET would need to have a spatial resolution of 0.33 mm for mouse imaging and 0.83 mm for rat imaging to distinguish the same level of structural detail in the images [260]. The best resolution reported so far for comercial preclinical PET systems, according to NEMA standards, approached 1 mm FWHM, both in the axial and radial directions [246]. However, because of the statistical nature of PET imaging, detailed detector models of modern iterative reconstruction algorithms enable extraction of more information from the collected datasets than does filtered backprojection used in NEMA standards. The nanoScan PET-MRI system tests on a micro-Derenzo phantom filled with 9.34 MBq of 18-fluorodeoxyglucose ($^{18}$F-FDG), for a 4 h acquisition time, binned with a 400-600-keV energy window and a 5 ns time

window, and reconstructed with maximum a posteriori maximum-likelihood (MAP) algorithm with the total variation as regularization term, yielded a 0.8 mm spatial resolution (i.e., enabled 0.8 mm rods of the Derenzo phantom to be resolved) [16]. The reconstruction was performed with scatter, attenuation, and positron range modeling enabled, on a matrix of 0.2 $mm^3$ voxels.

#### 2.5.1.2 Sensitivity

The sensitivity in small-animal PET should be as high as possible to achieve an acceptable signal-to-noise ratio (SNR) for high spatial resolution reconstructed images. Better statistical quality of the data also enhances the ability to differentiate and quantify a subtle signal in the presence of significant background counts [261]. The highest reported absolute sensitivity at the center of the FOV for state of the art small-animal PET systems was approximately 10%, which is about 3 times higher than for a conventional human PET scanner [260]. This is largely due to the improvement in geometric efficiency resulting from the reduction of the system diameter, which essentially brings the detector system closer to the detector source. However, this causes substantial parallax positioning error and associated spatial resolution loss. The arrangement that provides the highest sensitivity of all possible detector geometries is a four-sided polygon. This geometry has smaller gaps through which scattered photons can escape. Habte proposed a box-shaped system built from semi-conductor CZT detectors that would boost center point source photon sensitivity to 19% for a very narrow energy window [262]. This is a very similar geometry to the one adopted by an RPC-PET system. An advantage of the four-sided system is the introduction of moving heads that can bring the detectors closer to the subject and accomodate subjects of different sizes (see fig. 2.44). Having sufficient sensitivity is a particularly important requirement

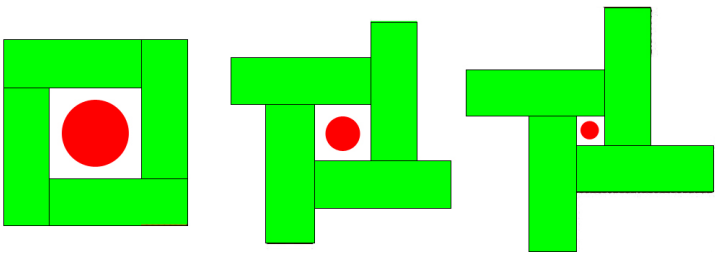

**Figure 2.44:** Proposed box system geometry with fixed FOV and adjustable transaxial FOV. Adapted from [262].

because it is necessary to collect a sufficient number of counts in a reasonable amount of

time and for a reasonable injected dose, while ensuring that only trace amounts of the radiolabeled compound are injected to avoid saturation of the biological target under study [233].

#### 2.5.1.3 Image quality and quantification

The ability to differentiate and quantify one focal region of probe accumulation from the background (contrast) or two adjacent regions of focal probe accumulation with slightly different concentrations (contrast resolution) depends strongly on the level of background present [261]. The quantities spillover ratio (cold cylinder regions) and contrast recovery (hot rod regions) are calculated to assess image quality. Besides the influence of the physiology of the subject and the biology of the target, contrast also depends on photon scatter (on tissue or detectors), random coincidences and partial volume effect.

To take full advantage of the quantitative capabilities of PET imaging, data normalization, object-specific correction of background and the correction of physical degrading factors such as attenuation, scatter, partial volume, and motion, must be performed before reconstruction or incorporated within iterative image reconstruction techniques.

Quantification provides the direct relationship between the activity concentration measured *in vivo* in organs/tissues and the underlying physiologic or pharmacokinetic processes occurring in the structure of interest [263].

To address image quantification, many aspects need to be considered, namely, animal handling and preparation, mode and type of anesthesia utilized, and mass of injected tracer. Typically, certain devices are used to hold the animals in selected positions, mainly in longitudinal studies. Anesthesia is preferably performed through masking the animal with a mixture of isoflurane and oxygen gases. The tracer mass injected must not interfere with natural physiological state of the animal. The adopted conventions imply a maximal receptor occupancy of 1% and the injection volume should be less than 10% of the animal's total blood volume, which is 30 and 2.5 mL, for rats and mice, respectively.

Absolute quantification generally requires accurate measurement of activity concentrations in arterial blood, which provides the input function to the kinetic model using more advanced blood sampling devices [264]. The ultimate goal is the production

of quantitative regional estimates of physiologic or pharmacokinetic parameters from dynamic radiotracer studies.

### 2.5.2 Applications

The three primary disease fields of application in small-animal PET are oncology, cardiology, and neurology. Other areas, with less expression, but yet very relevant, like infection and inflammation, are also object of study by PET. In appendix B, a thumbnail description of such applications is given.

### 2.5.3 Current trends

Multimodality devices are now commonly used in clinical and preclinical environment. The most common are combinations between high sensitivity and functional modalities, such as PET and single photon emission computed tomography (SPECT), with high spatial resolution and "morphological" techniques, such as CT and MRI[1]. Generally, when combined, these modalities feature lower performance due to the needs of avoiding interference between the corresponding devices. Multimodal imaging can be performed in each device separately, and then fused later with powerful software (co-registration), or acquired simultaneously in the same imaging device. Commercially available systems include the combination of PET/CT, PET/MRI, SPECT/CT, and SPECT/MRI. There are already trimodality systems combining PET/SPECT/CT. PET/MRI is the only physically available modality where image acquisition is truly simultaneous.

Micro-MRI provides images with excellent contrast and spatial resolution (100$\mu$m), as well as information regarding tissue composition, perfusion, oxygenation, tissue elasticity, metabolism, and detection of molecular probes, within a single session and no exposure to ionizing radiation [265]. Small-animal MRI scanners should be at least 4.7 T or, ideally, higher than 7.0 T. In fact, dedicated small-bore MR devices can operate between 4.7 and 21 T. For high-energy positron emitters, these strong magnetic fields reduce the positron range improving image resolution, as discussed in section 2.2.2. MRI is preferred over CT for combination with PET, particularly in brain imaging, because it provides a better soft tissue contrast (important in neuroimaging, as well as in abdominal and pelvic regions), it does not contribute with additional ionizing

[1] Of course MRI can also be used to study function.

radiation (important for longitudinal studies), and it has the ability of providing supplementary functional information (perfusion and tissue oxygenation). In fig. 2.45, we present a schematic example of workflows for combined PET/MRI. These workflows

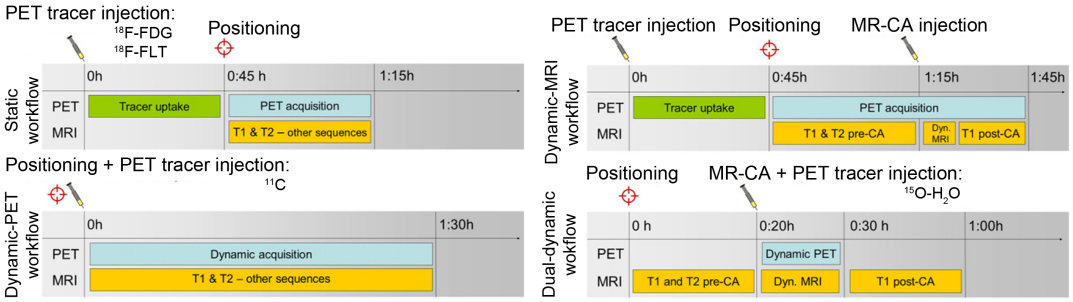


**Figure 2.45:** Schematic workflows for combined PET/MRI acquisitions. Adapted from [233].

can be accomplished with a substantial reduction in total examination time compared with sequential measurements, reducing the time under anesthesia for the animals and the anesthesia-related side effects, thus improving animal health in longitudinal studies [233].

In fig. 2.46, we present the comparison of PET and functional MRI (fMRI) activation. PET is an excellent tool for elucidating the metabolic basis of the fMRI signal and providing complementary information. In the case of $^{18}$F-FDG, glucose metabolism in the brain can be assessed and quantified as cerebral metabolic rate of glucose (CMRG) [266]. In reference [266], the response to stimulus in the brain was assessed simultaneously using PET/MRI, which traces changes in glucose metabolism on a slow time scale, and fMRI, which determines the fast vascular and oxygenation changes during activation. The author identified seven glucose metabolism-related networks.

### 2.5.4 Final considerations

Small-animal PET is now ranked as the third most used single preclinical imaging technique, representing 20% of the preclinical imaging applications, only behind optical imaging (OI) (with 28% for the bioluminescence techniques) and MRI (23% share) [267].

PET is highly dependent on the availability of an "on site solution" for radiopharmaceutical production. Due to the short half-lives of most positron emitters (from

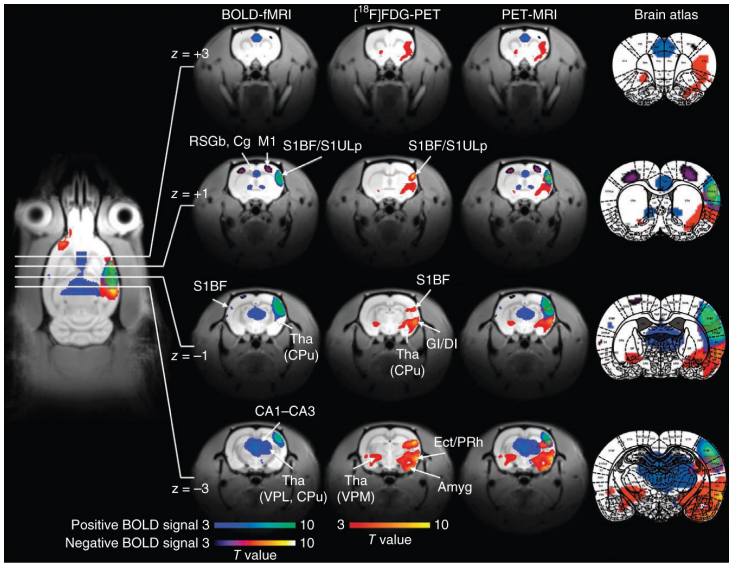


**Figure 2.46:** Comparison of activated areas of a whisker rat by simultaneous PET/MRI. From [266].

seconds to a few hours), the use of this imaging modality may require *in situ* radioisotope production and compound labeling. In fact, a huge number of radiotracers can only be used if locally produced. The existence at close distance of a multidisciplinary highly skilled and specialized team, with knowledge from distinct scientific areas is also fundamental [232]. In Coimbra, we have such conditions at ICNAS.

The price for small-animal PET systems ranges between $325,000 and $1,200,000. Siemens Preclinical Imaging owns more than 50% of the world's market share [260]. The overall small-animal imaging (*in vivo*) market was valued at $790 million in 2012. A recent report estimates an annual growth rate for the preclinical imaging market of about 14.5% over the next 5 years, reaching the value of $1.55 billion in 2017 [268]. The market growth is driven by factors such as increasing number of pharmaceutical companies and research institutions, rising application of functional imaging, growing adoption rate for small-animal imaging and technological advancements. However, high device cost and technological limitations are the factors hindering the market growth. We believe that RPC-PET will potentialize the small-animal imaging market, offering a cutting-edge PET performance at significantly lower cost.

## 2.6 Image reconstruction

Image reconstruction is a linear inverse problem. If we have a vector $\mathbf{x}$ corresponding to an unknown image and a set of projections combined in a vector $\mathbf{y}$, the imaging process can be modeled as

$$\mathbf{y} = \mathbf{A}\mathbf{x}. \tag{2.38}$$

The vector $\mathbf{y}$ is a discrete representation of projections of a continuous object and is commonly represented by 2D or 3D image elements (pixels or voxels). The matrix $\mathbf{A}$ is called imaging matrix, or system matrix, and models the behaviour of the imaging system.

Analytic reconstruction methods are based on the assumption that PET data are deterministic and contain no statistical noise, thus leading to fast reconstruction techniques. However, PET data have an inherent stochastic nature. The physical properties of PET introduce uncertainties that can be modeled to produce more precise reconstucted images. Among these uncertainties are the positron decay, the photon detection processes, and the effects associated to attenuation, scattered and random events [269]. Consequently, the average behaviour of the imaging system usually requires a statistical formulation.

We consider that the inverse problem $\mathbf{y} = \mathbf{A}\mathbf{x}$ is well-posed if: (i) there exists a solution $x_i$ for any $y_i$ in $\mathbf{y}$; (ii) the solution is unique in $\mathbf{x}$; (iii) it depends continuously on the data $\mathbf{y}$ [270]. In general the solution $\mathbf{y} = \mathbf{A}\mathbf{x}$ does not exist and/or is not unique and we are in the presence of an ill-posed problem. For instance, this happens in a discrete-discrete 3D PET model with $N_{coincidence\ channels} >> M_{voxels}$. In this case $\mathbf{y} = \mathbf{A}\mathbf{x}$ has no solution, because it is extremely under-determined. The finite number of unknowns to estimate is given by

$$E(y_j) = \sum_i a_{ij} x_i, \tag{2.39}$$

with $x_i$ being the activity of the $i^{th}$ voxel that contributes with weight $a_{ij}$ to the $j^{th}$ coincidence channel [102].

### 2.6.1 Analytic image reconstruction

As mentioned above, analytic reconstruction methods do not include noise in PET data. They seek for a mathematical solution for the image through the measured projections. The central section theorem is in the basis of tomographic analytic reconstruction. It states that the 1D Fourier transform of a projection at angle $\phi$ is equivalent to a section at the same angle through the center of the 2D Fourier transform of the object. The projection data is related to the object activity distribution by [271]

$$P(\nu_s, \phi) = F(\nu_x = \nu cos\phi, \nu_y = \nu sin\phi), \tag{2.40}$$

where $F(\nu_x, \nu_y)$ is the 2D Fourier transform of the object distribution $f(x, y)$ ($x$ here denotes a cartesian coordinate), and $P(\nu_s, \phi)$ is the 1D Fourier transform of projection $p(s, \phi)$,

$$P(\nu_S, \phi) = \int_{\mathbb{R}} ds\ p(s, \phi) e^{-2\pi s\nu} \tag{2.41}$$

and $\nu$ is the frequency associated to the radial variable $s$.

The direct Fourier reconstruction takes the 1D Fourier transform of each projection, and interpolates and sums the results on a 2D rectangular grid in Fourier domain. Then, the inverse 2D Fourier transform is performed to obtain the image. This algorithm is numerically efficient because the discretized 2D transform can be calculated with the fast Fourier transform (FFT) algorithm. A more detailed description of the analytic algorithms, e.g., transformation of data from 3D tomographs into 2D datasets, is carried out in appendix C.

#### 2.6.1.1 Filtered backprojection

Filtered backprojection (FBP) is the most used algorithm in analytic image reconstruction and combines accuracy, speed and simplicity of implementation [269]. The term backprojection refers to the backprojection of the counts from a detector pair into an image array along the LOR connecting that detector pair. After repeating this process for all detector pairs, occurs a linear superposition of backprojections, that reflects the true activity distribution. The 2D Fourier transform of the backprojection will provide the 2D Fourier transform of the object weighted by the inverse distance from the origin [272]. This has the drawback of producing blurred images, since this weighting

term will amplify low frequencies and attenuate high frequencies. To compensate for the blurring in direct backprojection, the projection must be first filtered in Fourier domain, after taking the 1D Fourier transform of the projection. Then, the FBP algorithm takes the inverse Fourier transform to obtain the filtered projection and project it back into the image. The ramp filter is an option, but it amplifies high-frequency components producing noisy reconstructions. It may be replaced by apodizing filters with a reduced amplitude at high frequencies, such as Hann or Shepp-Logan filters [273]. This affects the spatial resolution, therefore a trade-off must be achieved to control the noise in reconstructed images at the expense of resolution.

Analytic reconstruction algorithms, despite their speed and easiness of implementation, suffer from the inability to model the degrading factors in PET, such as positron range and non-collinearity. Modeling the statistical noise of PET may provide a better performance, despite the increase in complexity of the reconstruction algorithm.

### 2.6.2 Iterative image reconstruction

Iterative reconstruction methods consider a starting initial estimate of the object activity distribution, which can be either a homogeneous image or a direct backprojection of the data. Then, the estimated projection is calculated by forward projecting the initial estimate. By comparison between estimated and measured projections, the initial estimate is adjusted following a certain criterion. This "forward project, compare, backproject, update" process is repeated until the best image estimate is found [269] (see fig. 2.47).

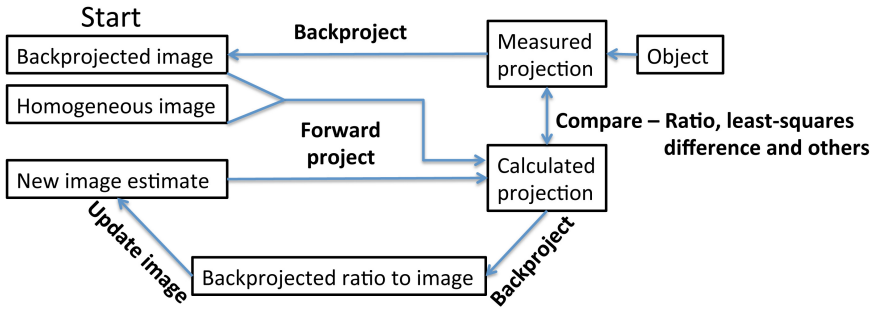


**Figure 2.47:** Flowchart for iterative reconstruction. Starting with a homogeneous image or a backprojection of the data, in the upper left, the algorithm iteratively updates those images based on the comparison between the measured and calculated projections and is stopped after reaching a hypothetical best image estimate.

Iterative methods generally obey to two main components: design of an optimization criterion and development of efficient algorithms. The first component defines the best image estimate, by measuring, when possible, the similarity between that image and the image estimate. This criterion is represented as a cost function being the maximum likelihood (ML) usually the chosen one. There is still the least squares approach, that measures the difference between measured and estimated projections using Euclidean distance. The second component determines the way of image estimate update at each iteration and requires a numerical algorithm. The expectation-maximization (EM) algorithm is generally used to find the ML estimate.

The most widely used iterative algorithms in PET are the maximum likelihood expectation-maximization (MLEM) algorithm and its accelerated version, ordered subset EM (OSEM). We will focus on those algorithms, despite the large range of iterative reconstruction methods. They depend mainly on: the image representation (i.e., pixels, voxels, blobs,); the system matrix $\mathbf{A}$ that can include other physical effects, besides the geometrical mapping from the object to the data, such as attenuation and detector blurring; and the statistical model that describes the uncertainty of PET data, that is usually poissonian, since photon detection is Poisson distributed.

#### 2.6.2.1 MLEM

The MLEM method was introduced by Dempster et al in 1977 [274] and first applied to PET by Shepp and Vardi [275] and Lange and Carson [276]. For an image reconstruction with a Poisson likelihood cost function, the MLEM algorithm is given by the iterative equation [271]

$$x_i^{n+1} = \frac{x_i^n}{\sum_{j'}^{N_{LOR}} a_{j'i}} \sum_{j=1}^{N_{LOR}} a_{ji} \frac{y_j}{\sum_{k=1}^{P} a_{jk} x_k^n}, \tag{2.42}$$

where $x_i^n$ is the image estimate for voxel $i$ at iteration $n$, $N_{LOR}$ are the number of detector pairs in coincidence, and $P$ are the number of voxels. The flowchart of the algorithm is shown in fig. 2.47. The first estimate, usually a uniform distribution $x_i^1 = 1$ is forward projected into the projection domain (denominator of the second term in the right hand side of equation 2.42). Then, the comparison between estimated and measured projections is determined by calculating their ratio. This ratio is backprojected to the image domain and properly weighted, providing a correction factor. The

denominator in the first term is equal to the sensitivity of the scanner, for a certain voxel $i$. Finally, the current image estimate $x^n$ is multiplied by the correction term, generating the new estimate $x^{n+1}$. This process is repeated and the image estimate converges to the ML solution [102, 271].

This algorithm produces very noise images due to the ill-conditioning of the problem. One solution is stopping the algorithm before convergence, and several stopping rules were proposed [277, 278]. In what concerns whole-body RPC-PET reconstruction, we stopped the reconstruction at iteration 20, when the root mean squared error (RMSE) between the simulated NCAT image and the reconstructed image reached a minimum. Concerning the spatial resolution of the small-animal RPC-PET prototype, we mostly stopped the algorithm at the iteration that minimized the FWHM of the profiles taken through the maximum intensity region.

Another way of reducing the image noise is by applying a smoothing pos-filter to the reconstructed image. However, this leads to a degradation of the spatial resolution, which depends on the filter type [279, 280, 281]. Likewise, sieves [282] (an operation that suppresses high frequency noise) can be applied to the image estimate after each iteration to impose smoothness and reconstruction stability. For this reason, we introduced a median filter between MLEM iterations in our reconstructions routines.

A major drawback of MLEM is its slow convergence. It usually takes 20-100 iterations to achieve the desired image. The MLEM algorithm requires considerably more computation time than FBP. However, several efforts are constantly being put forward in order to enhance convergence speed issues. With the advent of parallel computing, iterative algorithms have practically replaced analytical solutions.

### 2.6.3 OSEM

To overcome the slow convergence of the MLEM algorithm, the update equation was rearranged to boost the image change at each iteration. The OSEM algorithm [283] partitions the projection data into $B$ subsets (typically mutually exclusive) and uses only one subset of data $S_b$ for each update. The iterative equation thus becomes

$$x_i^{n+1} = \frac{x_i^n}{\sum_{j' \in S_b} a_{j'i}} \sum_{j \in S_b} a_{ji} \frac{y_j}{\sum_{k=1}^{P} a_{jk} x_k^n}, \tag{2.43}$$

where $b$ is the index for the subset. OSEM convergence speed usually improves by a factor $B$ compared to MLEM, but the convergence to the ML solution is not guaranteed.

Due to the increasing noise level with iterations, the algorithm is ended early and/or the reconstruction is post-smoothed. Other variants of OSEM include re-scaled block-iterative EM (RBI-EMML) [284] and the row-action ML (RAMLA) [285] algorithms, which converge to the ML solution under certain circumstances. OSEM is currently the most widely used iterative reconstruction algorithm.

### 2.6.4 AW-MLEM and AW-OSEM

Contrary to analytical algorithms, where data is corrected before reconstruction, MLEM and OSEM algorithms may destroy the Poisson characteristics of data and introduce a bias in the reconstruction, if that data is pre-corrected. This means that the MLEM and OSEM algorithms should be applied to raw data and attenuation correction should be included in the system matrix. The attenuation weighting of the MLEM algorithm (AW-MLEM) is multiplicative and has been formulated by Hebert and Leahy [286],

$$x_i^{n+1} = \frac{x_i^n}{\sum_{j'}^{N_{LOR}} a_{j'i}/\alpha_{j'}} \sum_{j=1}^{N_{LOR}} a_{ji} \frac{y_j}{\sum_{k=1}^{P} a_{jk} x_k^n}, \tag{2.44}$$

where $y_j$ are the data corrected for all effects except attenuation, $\alpha_j$ is the pre-computed attenuation correction factor for LOR $j$, typically the ratio between the blank and transmission scans. This algorithm is easily extended to the attenuation-weighted OSEM algorithm [287]. In chapter 5, we will present a direct-TOF implementation of the MLEM and OSEM algorithms applied to pre-corrected list-mode data, which seems to preserve the Poisson characteristics of the data despite the considerations mentioned above.

### 2.6.5 Other algorithms and current trends

There is a broad range of image reconstruction algorithms that are continuously being created and improved to meet the specific needs of each imaging modality. In fig. 2.48 some of the most popular methods utilized in PET/SPECT/CT imaging are summarized[1]. In appendix C, we present a broad range of reconstruction algorithms and their

[1]Backprojection of filtered projections (BFP); multiplicative algebraic reconstruction technique (MART); simultaneous MART (SMART); conjugate gradient (CG); coordinate descent (CD); image space reconstruction algorithm (ISRA); space-alternating generalized EM (SAGE); interior point (Int. Point); grouped-coordinate ascent (GCA); paraboloidal surrogates coordinate descent (PSCD); functional substitution coordinate descent (FSCD).

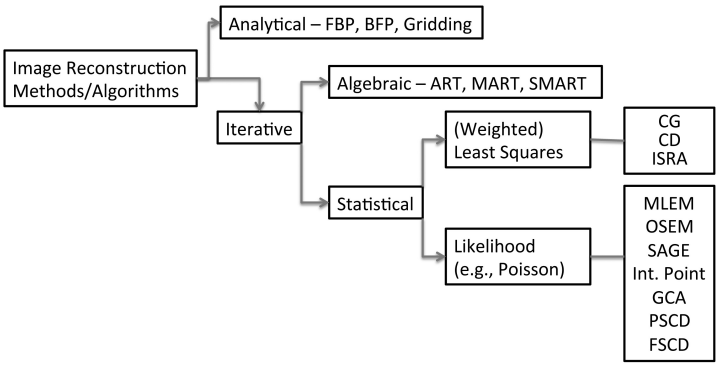


**Figure 2.48:** Classification and examples of some image reconstruction algorithms utilized in PET/SPECT/CT. Adapted from [288]

applicability to the different tasks required by state of the art PET imaging systems.

In conclusion, for the purpose of this work, we can state that the iterative reconstruction approach has several key advantages over the analytical approach. Iterative methods may present improved spatial resolution, since they replace the simple line integral approximation measured by the imaging system with a model that reflects the probability that a $\gamma$-ray emitted at a certain location in the object is detected in a given projection element [2]. Generally, iterative methods can produce better signal-to-noise ratios in regions of low tracer uptake at a given spatial resolution, leading to improvements by a factor two over FBP, which is equivalent to a fourfold increase in the effective sensitivity of the scanner. Another perspective is that the same quality image could be obtained with iterative methods using just one quarter of the injected dose or in one quarter of the imaging time. Iterative algorithms also provide a better visibility of the contours of the body and produce reduced streak artifacts [271]. The disadvantages of iterative reconstruction related to computational complexity and reconstruction times are being overcome with faster iterative algorithms that make use of parallel computing. The option to use MLEM and OSEM algorithms is now found on many commercial PET scanners and has been also our choice for the image reconstruction of whole-body RPC-PET data.

# Part I

# Small-Animal RPC-PET (Experimental Results)

# 3

# Experimental Setup and Hardware

An experiment with RPC-PET detectors was carried out in order to determine the spatial resolution of a small-animal RPC-PET prototype. The detector construction is fully described in section 3.1. In section 3.2, we describe the structure of a $^{22}$Na needle-like source surrounded by a stainless steel cylinder. A setup has been assembled to image several radioactive sources. In section 3.3, we characterize the main components of this setup, exposing the features of a custom-made read-out electronics. A brief summary of the attributes of the data acquisition system, developed by the HADES DAQ group, and its adaption to RPC-PET needs is explored in section 3.4. Several tests of performance and stability of the elements of the complete system are analysed in section 3.5. These measurements are made on an ongoing basis. The ones here presented intend to assure the proper operation of the detectors and front-end electronics with high levels of reliability. This is a fundamental requirement to comprehend the reconstructed images and spatial resolution results that will be presented in the next chapter. Relative activity of the different sources utilized in this work are estimated in section 3.6.

## 3.1 Detector construction

The detector construction here described was developed and refined along several months to produce the 5 gaps RPC-PET detector modules needed for the full assembly

of an small-animal RPC-PET prototype. The final purpose was to produce 40 detection modules, 10 for each of the 4 heads of the scanner. The Computer-Aided Design (CAD) view of the scanner architecture under construction and the full 10-detectors head under tests are shown in fig. 3.1.

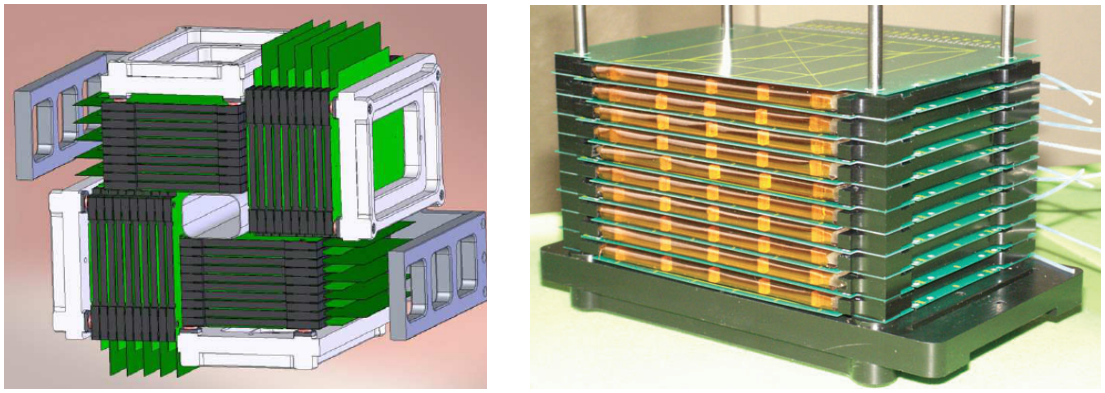

**Figure 3.1:** Small animal RPC–PET prototype consisting of four heads (presently under commissioning). Left: CAD design of the whole system. Right: photograph showing one head with ten fully instrumented detectors.

The illustration of a single detector is depicted in fig. 3.2. Supported by pictures, we present a detailed description of the steps towards the conclusion of a detector ready for electrical tests.

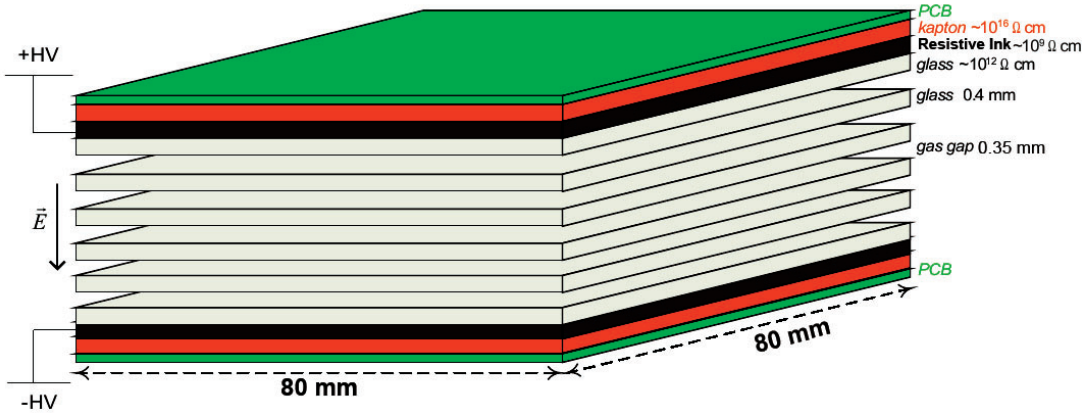


**Figure 3.2:** Small animal RPC–PET detector consisting of 6 stacked glass electrodes and defining 0.35 mm gas gaps. The high voltage is applied on resistive ink painted on the outer electrodes, while the others are left ellectrically-floating.

The first three main steps in the detector construction must be accomplished in three different days, while the last one can be done once on a large set of detectors. These steps comprehend: i) glass cleaning; ii) detector assembly; iii) setup disassembly; iv) painting and insulation.

- Glass Cleaning
  - This step is done at LIP's mechanical workshop. We start by sanding 102 glass plates ($80 \times 80 \times 0.4$ mm$^3$). A sandpaper with a coarse grain (220) is used to adjust the width of the glass plates, since it varies between 80 and 81 mm. This step is very delicate, since the force (applied with the fingers) must be correctly balanced along the plate edge to avoid glass shattering. A softer sandpaper (800) is then employed to smooth the edges roughness, thus eliminating spots where discharges can be triggered.
  - Once sanded, the glass plates are displaced as depicted in fig. 3.3 1). Before being cleaned in an ultrasound bath of water and soap, several paper layers are inserted between glass plates for surface protection, as the contact could originate scratches. This cleaning in the ultrasound bath lasts one night.
  - The next day, each glass plate is cleaned with water and rubbed by hand, with latex gloves on. They are immediately dried with compressed air to remove water droplets. This must be done carefully to avoid glass break. Afterwards, they are also placed between paper layers, as shown in fig. 3.3 1), and taken into the clean chamber.
- Detector Assembly
  - The detectors are constructed using a custom-made tool, shown in fig. 3.3 2). This ancillary mounting tool is made of aluminium and *teflon*, the latter being immune to the resin used to hold the detector elements.
  - We roll the fishing line of 0.35 mm diameter that defines the gap between the glass plates around the polyvinyl chloride (PVC) tool, shown in fig. 3.3 3). The fishing line is subsequently cut with a sharp blade. This task requires two persons, one to hold the PVC tool and stretch the fishing line and another one to cut it. Five cut fishing lines pass through the holes on the

flat surface of each of the five spacers (see fig. 3.3 4)) and are tied with a knot. On the opposite face of the spacer, there is a cavity to fill with resin for fixing the fishing lines to the spacer. Each spacer has the dimensions of $3.85 \times 2.5 \times 1.85$ mm$^3$ and they are separated from each other by 19.5 mm. The tied phishing lines are gently screwed against the aluminium structure with the concern of leaving the outer phishing lines closer to the center of the structure.

- One by one, the glass plates are cleaned from dust with air flow and piled up in the mounting structure. After the positioning of the first glass plate, the mounting procedure follows with the stretching of five bottom fishing lines, as presented in fig. 3.3 5). The next procedure is to put another glass plate over the fishing lines and stretch other 5 fishing lines, and so on, until we reach the last glass plate. At the end, we have 6 glass plates and 5 gaps, utilizing 5 fishing lines to define each gap. The fishing lines are then stretched and joined together with a common adhesive tape.
- The top part that compresses the glass plates is set just above the top glass plate. A part with 15 nylon screws and 8 metal screws (see fig. 3.3 2)) is then attached to the mounting structure. First, we check that the nylon screws are unscrewed. Then, the metal screws are screwed to the mounting structure. Next, the nylon screws are gently screwed from the center to the edges until they touch the part that compresses the glass plates, applying a slight pressure on it.
- The 25 fishing lines sticking out from the right side are then inserted in 5 spacers. The 10 spacers are then gently pressed against the glass plates with a toothpick, as depicted in fig. 3.3 6).
- The first row of 3 nylon screws are unscrewed and the corresponding fishing line is stretched and wrapped around the right metal screw, in the same way we did with the left metal screws. Two persons are needed to perform this step: one to stretch and wrap the fishing line with pliers and another one to screw and attach the fishing line to the aluminium structure. The unscrewed nylon screws are screwed again, and we repeat the process for the next four rows of nylon fishing lines. The first person who controls the strain in the

fishing lines should keep the outer fishing lines more strained, since the glass plates tolerate more tension on that region and, additionally, that blocks the resin flow into the detector. The inner fishing lines should be kept more relieved. This is a key point to prevent the top glass from breaking along the middle fishing line. Most of the unsuccessful detectors broke there due to an over-stretching, but we only realized it afterwards.

- In order to insert the acrylic part that supports the detector inside the drawer (see fig.3.3 7)), the first row of nylon screws is unscrewed and the *teflon* part removed. The corners of these acrylic parts must be sanded and rounded off. Each acrylic part has the dimensions of $80 \times 9.5 \times 3.8$ mm$^3$. The holes inside the acrylic part have to be well cleaned to favor the resin drain, at a later stage. After the correct placement of the acrylic part, the top nylon screws must be screwed again tightly.
- Aside, we prepare the epoxy adhesive *ARALDITE*® Standard that takes 14 hours to attain full strength. We insert it in a syringe by the top and push the piston. With the green needle (see fig. 3.3 7)) we start inserting the resin by the middle of the acrylic part, (say, hole number 3), while compressing the piston very slowly. We follow the fluid flow between the fishing lines and the acrylic part in both directions. Once it reaches the next hole, we move the needle to that hole and keep injecting the resin, repeating the procedure till the last hole (number 5). In the last hole, we inject the resin till it reaches the spacer, at the same time ensuring that the spacer does not move. We then repeat the procedure for holes number 2 and number 1. We keep the pressure of the acrylic part against the detector with the previously removed *teflon* part, by screwing it again to the aluminium structure.
- The last two procedures are repeated for the opposite detector side. Once finished the sticking of the acrylic parts, we change the needle to the red one in order to stick the 10 spacers to the fishing lines. The mounted structure at this stage can be seen in fig. 3.3 8). Once the spacers cavities are filled with resin, we lay the mounting structure aside with the fishing lines pointing upwards, and wait for the next day to remove the detector module.

- Setup disassembly
  - We start removing the detector module by cutting the fishing lines with a sharp blade.
  - The nylon screws are unscrewed as well as the metal screws in order to remove the top part which keeps the pressure on the detector.
  - The lateral *teflon* parts which hold the spacers are gently removed with the help of a screwdriver utilized as a lever that pivots about one screw. The force is equally applied on each side of the part and the resin surplus in the spacers cavities removed with a X-Acto-knife. The left parts and the mounted detector are depicted in fig. 3.3 9). The two remaining *teflon* parts are easily removed. We finally make use of a screwdriver to remove the detector very carefully from the bottom *teflon* part while supporting the tool on the aluminium mounting structure.
- Painting and Insulation
  - After removing the resin surplus with a X-Acto-knife, one small copper strap is sticked to each detector wall, as depicted in fig. 3.4 10), for feeding the high-voltage electrodes.
  - We utilized two types of high-voltage electrodes: a thin electrode made of a thin *SEMITRON*® plate epoxied to the outer glasses and a resistive ink developed by Eng. Luís Lopes, used to paint both detector walls, as depicted in fig. 3.4 11). Before painting, the detectors must be protected from contamination of the gas gaps with a common adhesive tape, as shown in fig. 3.4 10). The first measurements were made utilizing the *SEMITRON* electrodes. However, the resistive ink performed better for long times, it is cheaper and easier to handle, so it was adopted since its development. A high conductive ink ring is painted around the detector equally distributing the high voltage to the whole surface.
  - We insulate the detector high voltage with several layers of Kapton® insulator with resistivity of $\rho = 10^{16}$ $\Omega$ cm. The detector walls, as well as the copper straps and the faces where the spacers are located must be carefully

insulated, since any faulty insulation can lead to a discharge, which may damage the detector or the read-out electronics.

– Finally, each detector module is fully closed, apart from four small openings near the corners, which let the gas in and out of the module (see arrows in fig. 3.4 12).

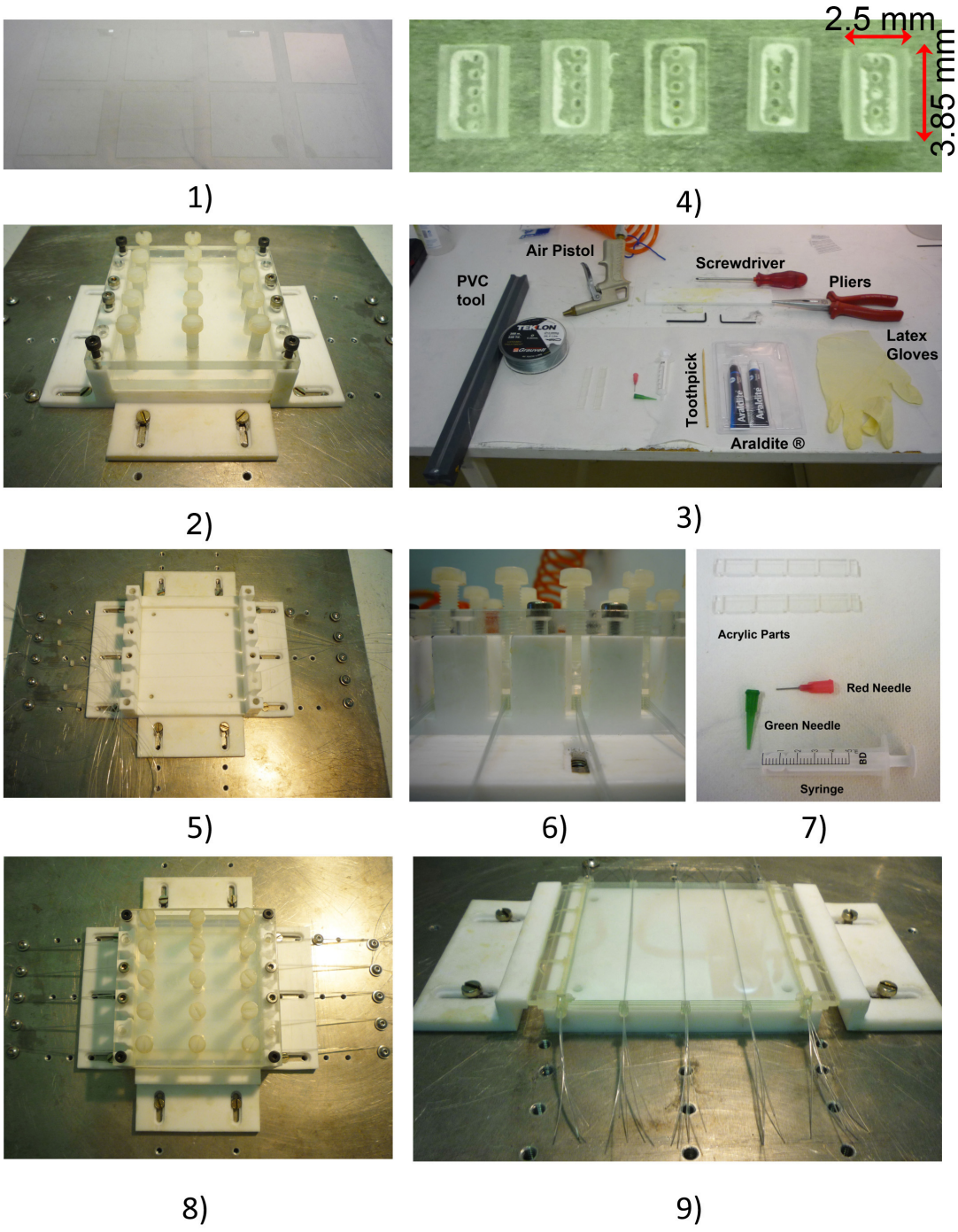


**Figure 3.3:** Construction of RPC-PET detectors: assembly and disassembly.

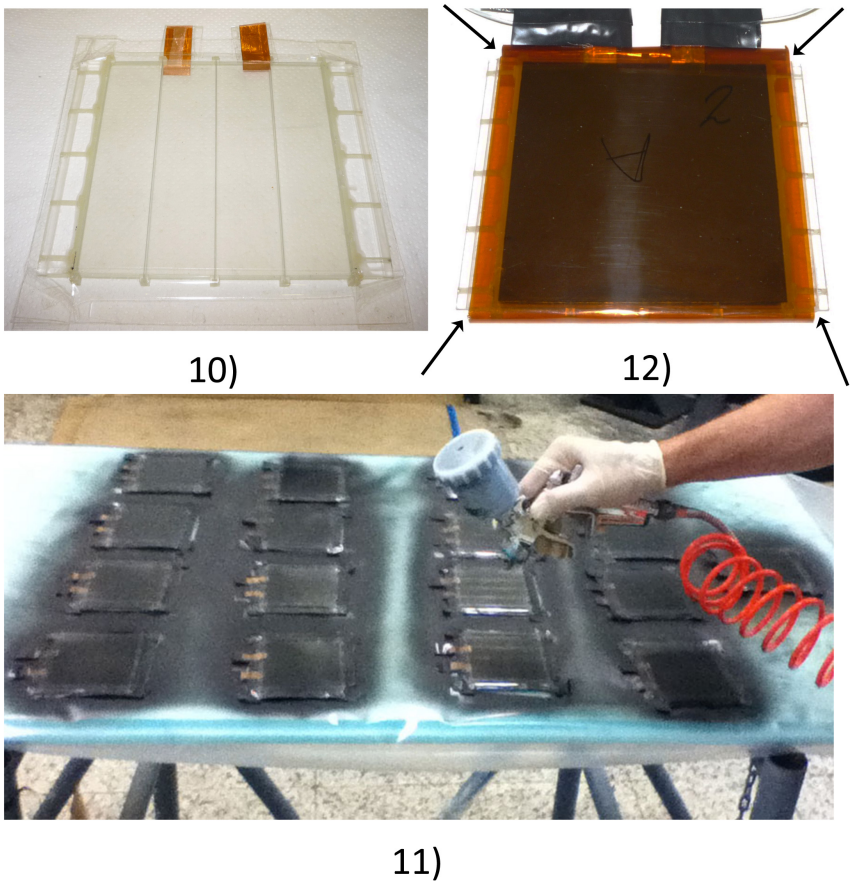


**Figure 3.4:** Construction of RPC-PET detectors: painting and insulation.

## 3.2 Construction of a needle-like $^{22}$Na source

To evaluate the system spatial resolution, a technique was purposed which consisted on inserting a $^{22}$Na source in a hollow cylinder (inner diameter - 250$\mu$m; outer diameter - 500$\mu$m) made of stainless steel (see fig. 3.5). The source itself consists of a solution of

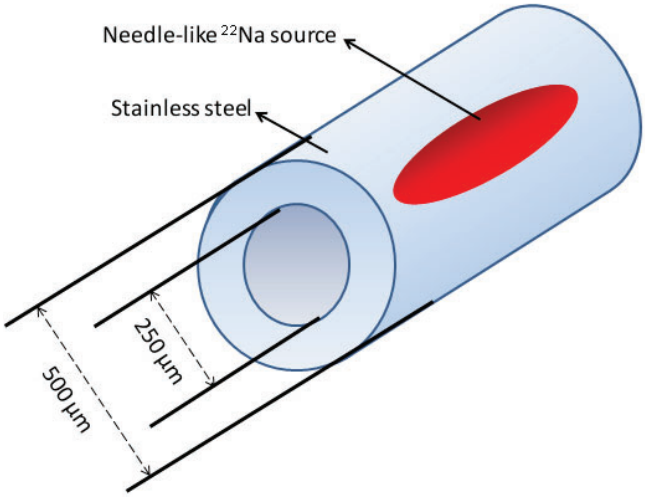


**Figure 3.5:** Scheme of the $^{22}$Na needle-like source immersed into a hollow cylinder, the latter made of stainless steel

NaCl (with $^{22}$Na isotope) deposited on a short piece of cotton thread and evaporated. Then, the thread was moved into the stainless steel needle.

The stopping profile of energetic positrons emitted by a radioactive source can be described by

$$P(z) = \alpha e^{-\alpha z}, \tag{3.1}$$

where $P(z)$[1] represents the probability of positron penetration to the depth $z$, with

[1]Brandt & Paulin [289] have described the implantation profiles of positrons from $^{64}$Cu sources, with maximum kinetic energy 0.65 MeV, in 14 different solids, ranging in density from 0.9 to 9 g/cm$^3$ by $P_+(x) = e^{-\frac{x}{R^+}}$. Derenzo [51] questioned whether the exponential relationship between positron transmission and absorber thickness was still valid for surrounding media. Therefore, an experiment using very thin sources deposited on mylar foils and surrounded by low density polyurethane foam was carried out. He measured the positron range distributions (PRDs) for $^{18}$F, $^{11}$C,$^{68}$Ga, and $^{82}$Rb sources. The same sources were also surrounded by aluminium to measure all broadening effects other than positron range. He came along with an empirical PSF that includes the positron range effects only, $q(r) = Ae^{-\frac{r}{r1}} + (1-A)e^{-\frac{r}{r2}}$, and determined the best fit values of $A$, $r_1$, and $r_2$. The observed PSF, $p(r)$, is a convolution of $q(r)$ and the PSF in metal $f(r)$.

the absorption coefficient $\alpha$ being given by

$$\alpha = 16\frac{\rho}{E_{max}^{1.4}}[cm^{-1}], \tag{3.2}$$

where $\rho$ is the material density and $E_{max}$ is the maximal energy of the emitted positrons [290]. For positrons emitted by a $^{22}$Na source (maximum beta energy = 0.546 MeV) and for a stainless steel density, $\rho = 8$ g/cm$^3$, the characteristic penetration, $1/\alpha$, is 33 $\mu$m. Given the geometry of the stainless steel cylinder, the wall absorbs 99.95% of the positrons emitted radially. Additionally, most of them actually annihilate inside the hollow cylinder, more precisely, in the thread where the radioactive solution is deposited.

Figs. 3.6 and 3.7 show the setup used to construct the needle-like $^{22}$Na source and the preparation tests with a $^{23}$NaCl solution, respectively.

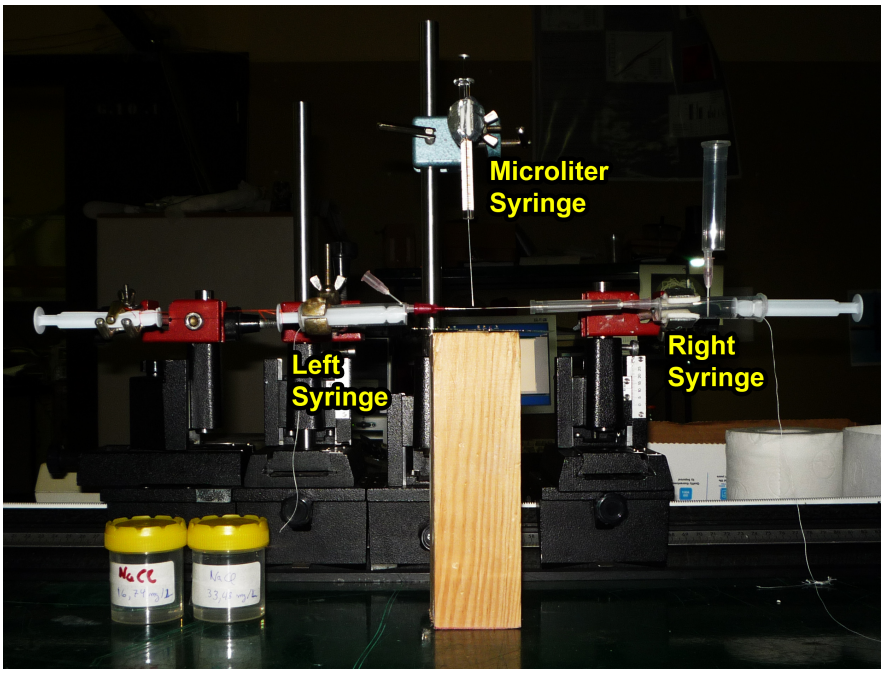


**Figure 3.6:** Setup mounted to construct a $^{22}$Na needle-like source.

The resulting source (see fig. 3.8) was achieved with the participation of ICNAS, and colleagues from Physics Department and LIP[1].

[1] Dr. Paulo Gordo, Dra. Fátima Ferreira Marques, Dr. Alberto Blanco, and Dr. Francisco Alves.

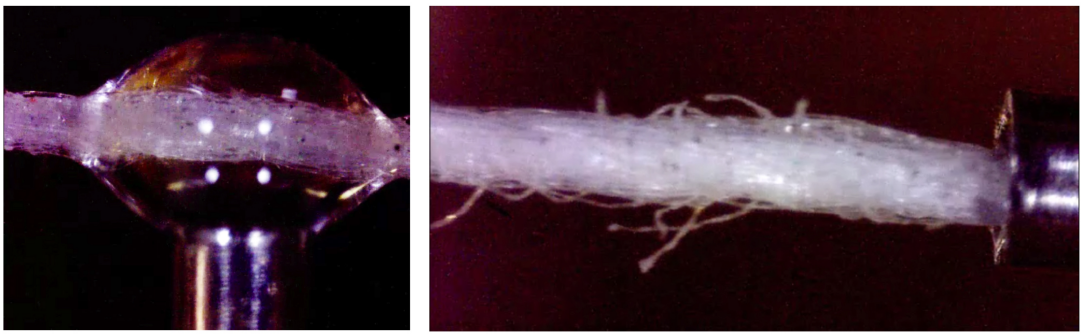

**Figure 3.7:** Snapshots of two movies made with a digital microscope for the simulation of the radioactive solution deposition on a cotton thread (left) and its displacement into the stainless steel hollow cylinder (right).

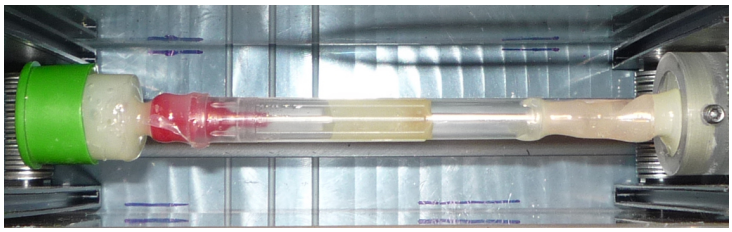

**Figure 3.8:** $^{22}$Na needle-like source.

## 3.3 Experimental setup and electronics

A setup with two parallel RPC-PET detectors ($a$ and $b$ in fig. 3.9) was assembled in order to determine the contribution of the detectors with the full read-out electronics and data processing to the spatial resolution of the system under construction.

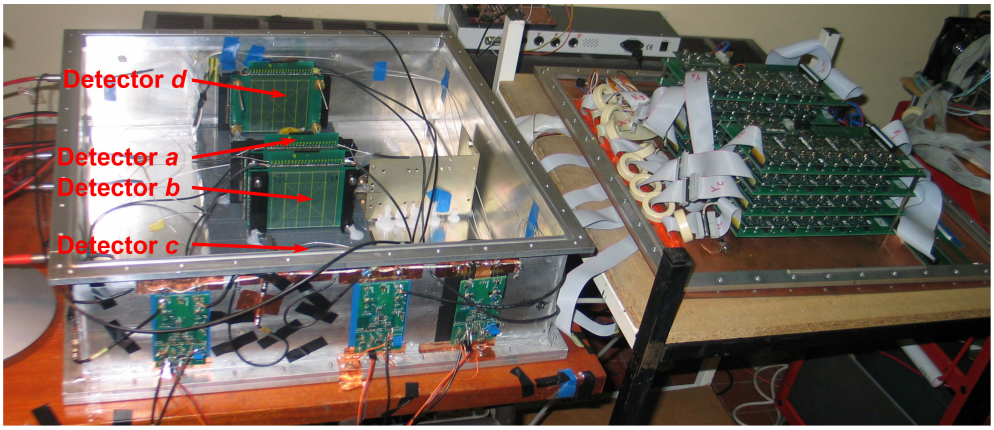


**Figure 3.9:** Experimental setup with 4 assembled detectors and front-end electronics.

Other two detectors ($c$ and $d$ in fig. 3.9), separated by 45 cm and aligned with the inner detectors, were additionally mounted to study the contribution of the non-collinearity effect to the system spatial resolution. These distant detectors were epoxied with *SEMITRON*, while the inner detectors were painted with resistive ink.

The two inner detectors were disposed parallel to each other, separated by 4 cm, and mounted on a small-animal RPC-PET head structure (see fig. 3.10, left). This structure was fixed to a PVC base, and the radioactive sources placed equally distant to both detectors. The movement of the needle-like source, in steps of 0.2 mm is achieved with the help of a remotely controlled step-motor. Additionally, two acrylic plates abut the $X$ and $Y$ read-out PCB electrodes to preserve the distance from these pick-up electrodes to the detector module, which is essential to the measurement of the position of the photon hits. A sheet of clear acetate film was inserted between the read-out printed circuit board (PCB) electrodes and the detector to insulate the high voltage (HV) from the PCB electrode ground (see fig. 3.10, right).

The setup was fixed to an aluminium box container fed with a gas mixture of 90% $C_2H_2F_4$ + 10% $SF_6$ under continuous flow. The HV was supplied by a 2 CAEN High Voltage Power Supply N471A ($\pm$ 8kV/8$\mu$A, 1 nA resolution). An HV splitter was used

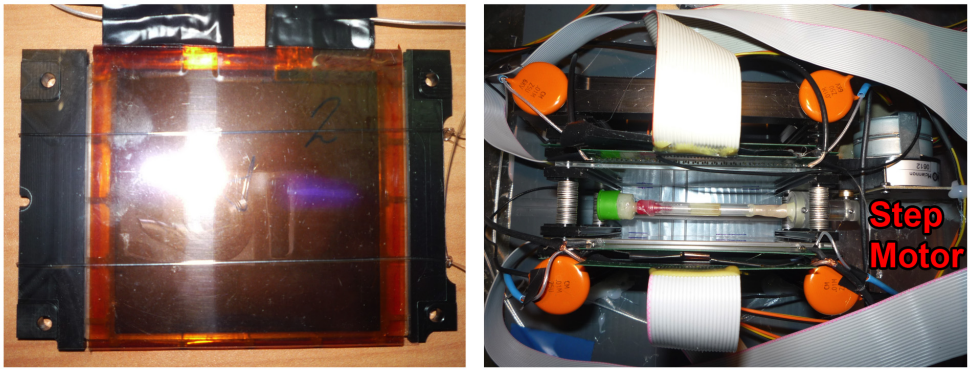


**Figure 3.10:** Concluded detector inserted in a drawer (left) that fits in the scanner head (right). A step motor moves the source in the vertical direction by remote control.

to perform measurements on different detectors and to test a full 10-detectors head. Capacitors of 6 kV and 10 nF in series with a 1MΩ resistor are used to uncouple the HV from the charge signal. The aluminium box container was sealed and any gas leakage verified (see fig. 3.11).

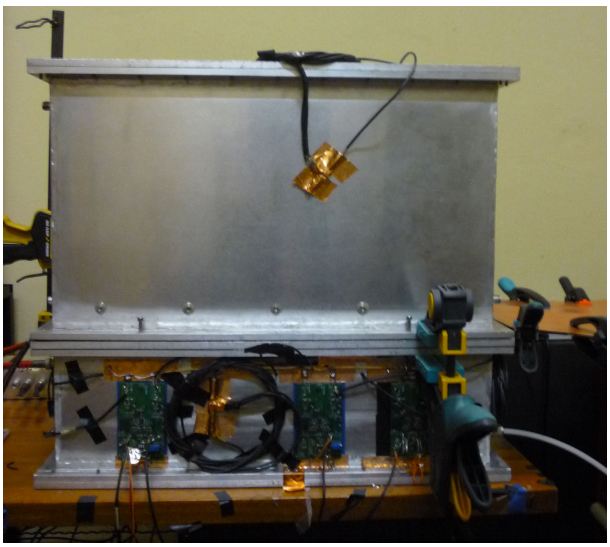

**Figure 3.11:** The aluminium box container, sealed against gas leakage, constitutes a *Faraday cage* to avoid environment RF noise from reaching the charge amplifiers.

Each of the two detectors utilized in this work had an effective front face of 8 × 8 $cm^2$ and consisted of 5 gas gaps with a total thickness of 5 mm. The full detector area covers the LORs inclined up to an angle of 58°. The $Z$ axis is perpendicular to the

plane defined by each of the two detectors (i.e., it crosses the detector planes), whereas the X axis defines the longitudinal direction of the source (see fig. 3.12). The $X$ and

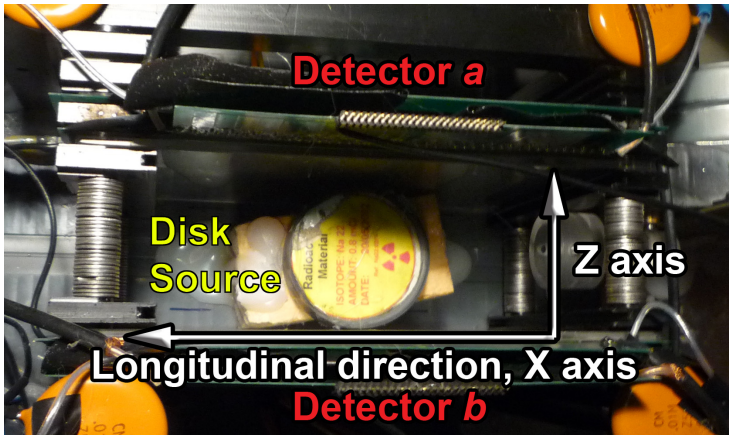


**Figure 3.12:** Two parallel small-animal RPC-PET detectors separated by 4 cm were used to scan a $^{22}$Na disk source. The $Z$ axis is perpendicular to the plane of the detectors.

$Y$ coordinates are measured by collecting the charge signals induced on twenty four pickup strips, 4-mm-pitch, on the outer printed circuit boards (see fig. 3.13).

Each $X$-strip delivers some of the induced charge to a common PCB track via a 40 pF capacitor and the remainder to a charge amplifier via a choke (MURATA BLM21BB201SH1). The common track is connected to a custom timing amplifier and a comparator partially similar to [291] via two equal length cables. This arrangement directs the high-frequency signal components towards the timing amplifiers and the low frequencies towards the charge amplifiers. The 24 $Y$-strips are arranged in the perpendicular direction similarly to the $X$-strips, except that here the common track is split in two, one each side of the $Y$-strips, connected via 20pF capacitors. The shielding of the cables leading to the timing amplifiers is connected to these tracks [19].

The timing electronics depicted in fig. 3.14 is composed of two channels. Each channel has a low noise monolithic microwave integrated circuit (MMIC) amplifier (LNA), commonly used to amplify very weak signals.

Both channels of the LNA connect to a ultra-high-speed comparator (MAXIM MAX9601), which features extremely low propagation delay (500 ps). The dual-channel positive emitter-coupled logic (PECL) output comparator incorporates latch enable and hysteresis [5]. A slow and noisy input signal can trigger several times the discrimination

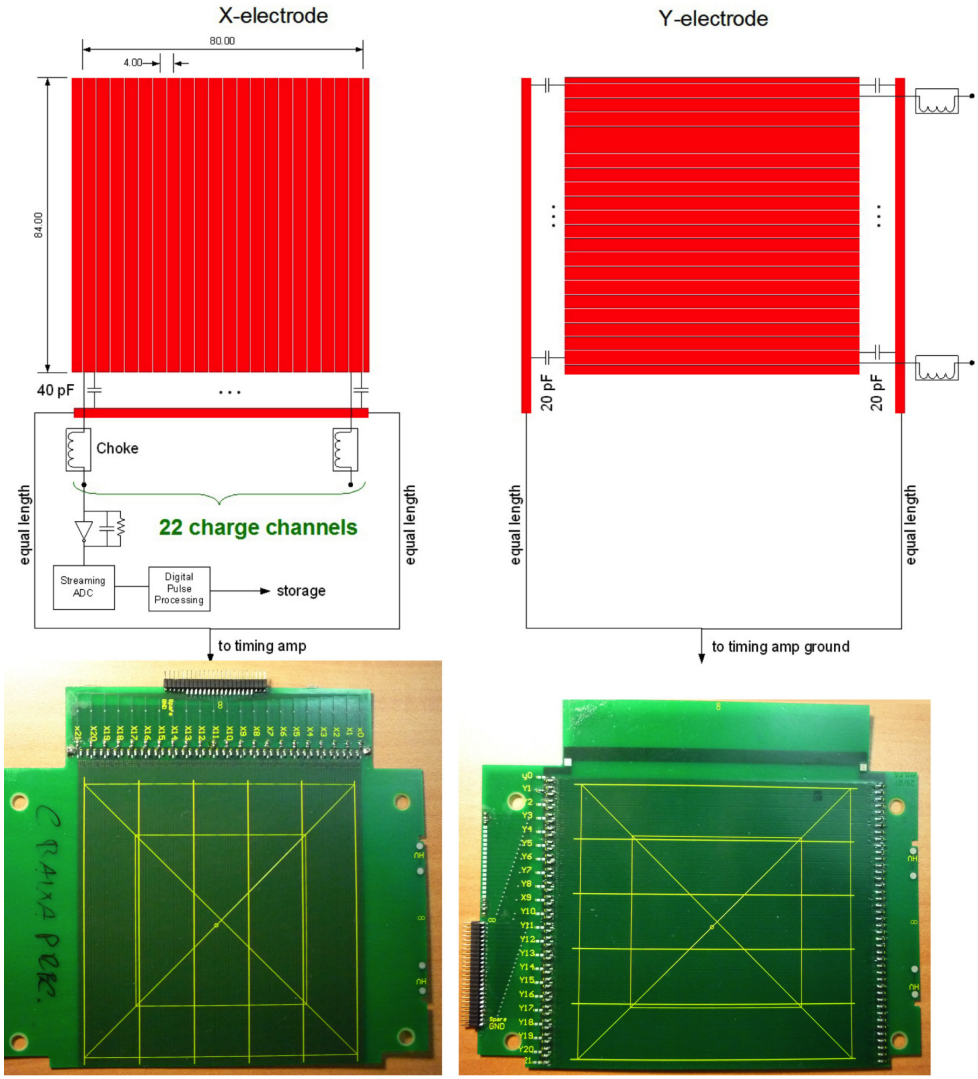


**Figure 3.13:** Schematic representation and photography of the read-out PCB electrodes and the readout circuit. From [19].

hysteresis prevents such oscillations. The latch-enable control permits tracking or sampling mode of operation, the circuit having two stable states, thus allowing to block a component in the required one. The threshold voltage is controlled via a potentiometer.

The output signal sends a low-voltage differential signaling (LVDS) with time information to the data acquisition (DAQ) time to digital converter (TDC) channels and a trigger signal to a discriminator (Octal Discriminator PS Mod.705). The LVDS cables must be kept away from the front-end electronics (FEE) input, since they create

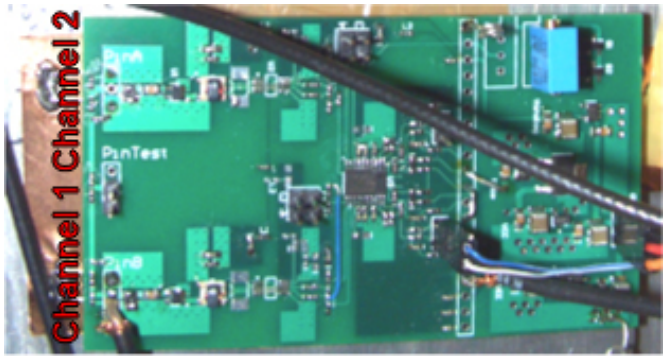


**Figure 3.14:** Timing electronics is composed of two channels with two custom timing amplifiers, a dual discriminator, and a comparator. The connection output to the time to digital converter (TDC) channels is made by low-voltage differential signaling (LVDS) cables.

electromagnetic noise.

The coincidence triggers are given by a threshold set on the sum of the discriminator output signals. The coincidence time window is defined in this unit, as well as the coincidence discrimination threshold voltage. The coincidence discrimination method is described in fig. 3.15. The output signal is sent to the input trigger of a gate/delay

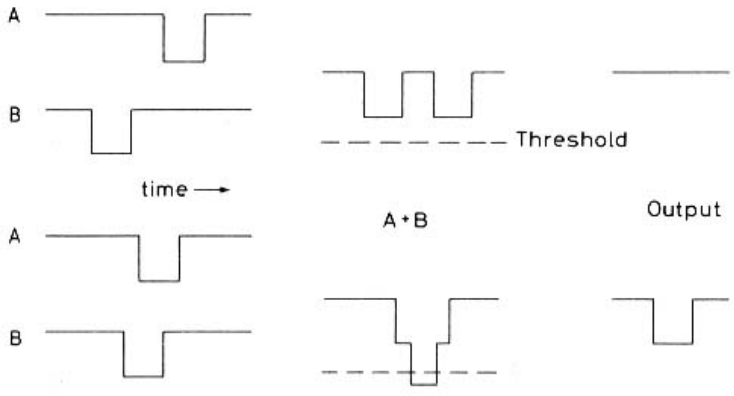


**Figure 3.15:** Method for the determination of a coincidence based on the sum of two of the discriminator output signals. The coincidence discrimination threshold voltage is set slightly below the output signals sum [292].

generator (Quad Gate/Delay Generator PS Mod. 794). A gate of 1 $\mu$s is generated inhibiting all discriminator channels through the Veto. A transistor-transistor logic

(TTL) signal is sent to the DAQ trigger input, via a converter, thus informing that a coincidence took place and triggering the DAQ to store the charge and time signals sent by the FEE.

The charge signals are amplified in 8 mother-boards, depicted in fig. 3.16, which

a) b)

**Figure 3.16:** a) 24 channel charge amplifier mother-boards. Each readout electrode needs one such board. The 8 boards are capable of reading each coordinate of each small-animal PET head. From those boards an output of 192 channels connect to the 24 ADCs present in the DAQ system; b) 4 channel daughter-board.

are capable of reading each channel of each small-animal RPC-PET head. The charge amplifiers with 10$\mu$s integration time feed 40MHz streaming analog to digital converters (ADCs) (ADC specifications presented in next section). Each mother-board has 6 daughter-boards, each of them capable of amplifying the signal of 4 strips of the corresponding read-out PCB electrode. A problem of this present electronics is the power dissipation; at 6.25 V the whole system consumes approximately 8 A.

One major problem that affected our acquisitions was the digital noise coming from the DAQ. To deal with it, appropriated filters were placed between the charge amplifying mother-boards and the DAQ. Additionally, the DAQ and the experiment box container were laboriously grounded. A *Faraday cage* covering the charge amplifiers was attached to the box container and three notch filters, tuned to the main noise bandwidth, were placed between the feedthrough that carry the detector time signals to the time FEE LNA.

The inner detectors were placed with the cathode electrode closer to the source, once the avalanche develops from the cathode to the anode. Consequently, in this

arrangement the gain is higher, thus making detectable the small charge events.

Preliminary tests with a full 10-detectors head were accomplished with the goal of identifying the triggered detector (see fig. 3.17).

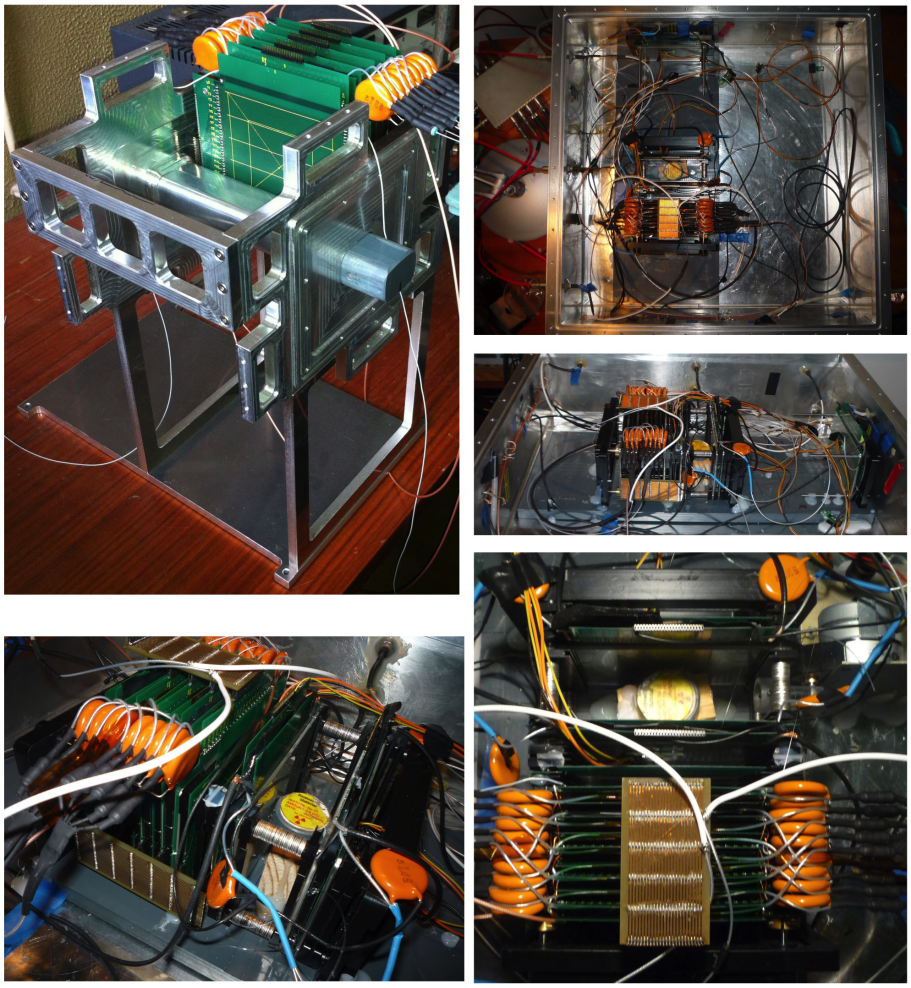

**Figure 3.17:** Top left: Full 10-detectors head mounted on the small-animal RPC-PET structure. Other Photo show several views of a trial experiment with the 10-detectors head in line with the inner detectors aiming at a higher sensitivity.

## 3.4 DAQ system

The DAQ system was primarily conceived to cope with the requirements of the high acceptance di-electron spectrometer (HADES) detector. Meanwhile, this system has

been re-designed to meet the needs of experiments with heavy ions and higher beam energies, where data rate was of special concern, the aim of the upgraded HADES DAQ being to reach a trigger rate of 100 kHz. This clearly meets the needs of small-animal RPC-PET, where we expect a trigger rate of 15kHz for an activity in mice of 100$\mu$Ci. However, in our experiment, we are just dealing with one single sub-system, while in the HADES experiment several such sub-systems must be connected through a common network setup for reading out 80,000 individual detector cells.

All electronics of the DAQ system are based on platforms equipped with field programmable gate arrays (FPGAs) and optical links, and all data links run a dedicated network protocol, TrbNet. The time signal is sent to the HADES TDC read-out board (TRB) and the amplified charge signal to an Addon to this board (see fig. 3.18). According to [18], each TRB2 TDC platform uses four high precision time to digi-

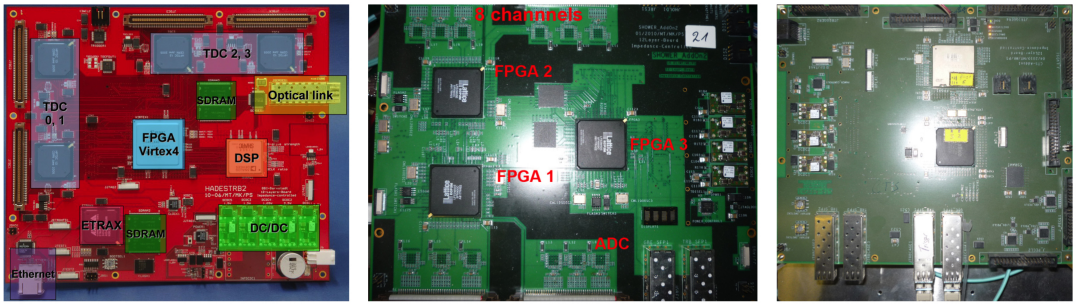


a) b) c)

**Figure 3.18:** Main DAQ boards: a) TDC Read-out Board, from [293]; b) Addon; c) Central Trigger System.

tal converters (HPTDCs), which allows monitoring 128 channels with a time resolution of 40 ps (rms) in regular mode or of 32 channels in high-precision mode, with a time resolution of 16 ps (rms). The TRB2 is now used world-wide in many different applications, and a next-generation TDC board is being built, the TRB3. It uses FPGA-based TDC circuits with a time resolution of 10 ps, and a high rate capability of 20 MHz per channel [294]. In total, the board is being designed to house 256 TDC channels allowing a good integration in experiments with high channel count, which is the case of RPC-PET.

The Addon consists of 3 Lattice ECP2M FPGAs, two of them containing 96 ADC channels with 40 MSPS and 10 bit resolution, and the third provides the connectivity

via optical links running TrbNet protocol and bi-directional Gigabit Ethernet for read-out and slow-control process. Both the trigger and the read-out processes are controlled by the central trigger system (CTS). The Trb network is described in fig. 3.19.

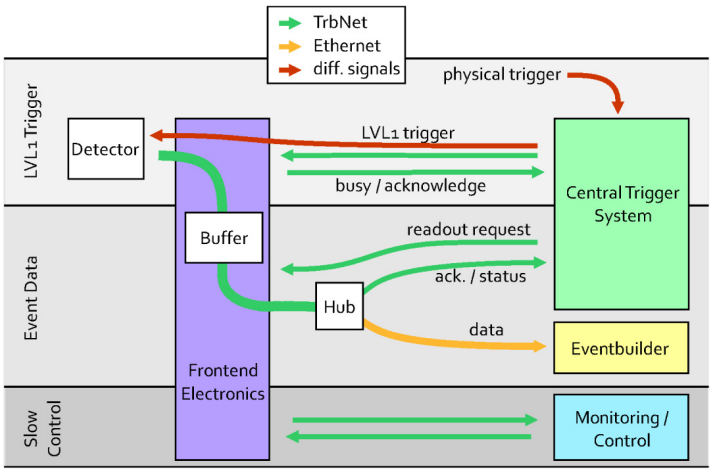


**Figure 3.19:** The TrbNet network is divided into three channels. The first one handles sending triggers from the Central Trigger System to the front-ends and busy-release information in the return path. Data are stored in the front-ends until a read-out request is received on the second channel. Data is then forwarded to hubs and converted to Gigabit Ethernet. The third channel handles all slow-control accesses. From [18].

There is a network hub through which data are extracted from TrbNet (optical network) and sent to the server ("the event-builder") via commercial Ethernet switch. The gigabit ethernet standard (GbE) was chosen because it supports routing of data to different server nodes, it can be built with off-the-shelf components and the integration to common hardware platforms is provided. Optical links run at 2.5 Gb/s and the Gigabit Ethernet interfaces can send up to 100MB/s each to the event-builder.

So far, the acquisitions have been performed with a desktop PC with 4 CPU cores, 3 hard-disks (3 TB) and 4GB RAM memory. The event-builder receives the data stream from our system and assembles the event. Data are then written to local disk storage.

## 3.5 Hardware measurements

### 3.5.1 Comparing high-voltage electrodes of *SEMITRON* and resistive ink

A major cause to look for an alternative to *SEMITRON* electrodes was the difficulty to manage this material and the effect of charge depletion with time. In fig 3.20 we can see that detectors $c$ and $d$, whose electrodes are made of *SEMITRON*, suffer from a charge drift to right channels[1] in the $Y$ electrodes with time. This means that the region closer to the copper straps looses charge along the time. This issue is overcome with the use of resistive ink (detector $a$ and $b$).

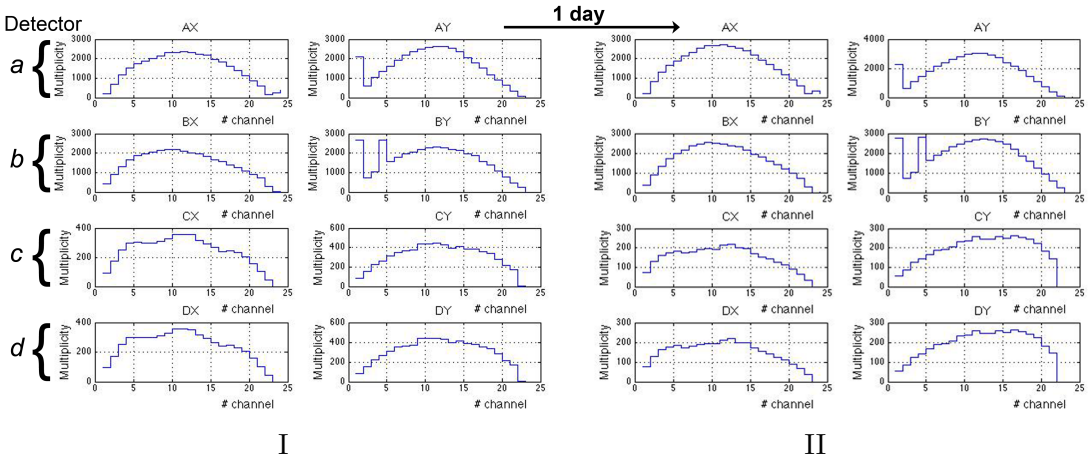


**Figure 3.20:** Multiplicity in the 24 channels of each electrode at a given time point (I) and after one day of continuous operation (II). Detectors $a$ and $b$ were painted with resistive ink, while detectors $c$ and $d$ were epoxied with *SEMITRON*. A drift to the right channels is clearly observed in the $Y$ electrodes of detectors $c$ and $d$.

In fig. 3.21, we compare signals directly induced with a small pad ($\sim$5 mm$^2$) fed by pulse generator on a glass detector, on a detector coated with *SEMITRON*, and on a detector painted with resistive ink. They all agree, but to achieve this goal, a big effort has been made to obtain the ideal resistivity. In many previous attempts, a large dispersion of charges was observed for different mixtures (different resistivities) of the ink. Concerning stability, we measured a resistivity of $6.4\times10^{10}$ $\Omega$ cm on 12/06/29 and

[1] After one day of continuous operation, an increase in the multiplicity of the right channels is observed. Multiplicity is the number of events per channel whose charge is above a given threshold.

a very similar resistivity of $6.9{\times}10^{10}$ $\Omega$ cm on 12/07/06, keeping the detector under a constant applied voltage of 14 kV and consuming 20 nA with a $^{60}$Co source.

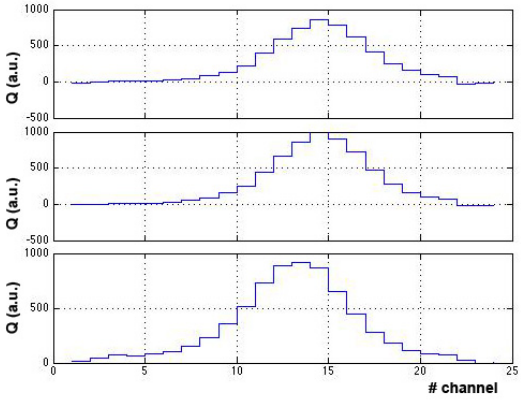


**Figure 3.21:** Induced signal on a: glass detector (top); detector coated with *SEMITRON* (middle); detector painted with resistive ink.

### 3.5.2 Checking the integrity of the read-out channels

Some channels could not read the charge induced on the strips because they were interrupted somewhere along the path from the read-out electrodes to the ADCs. Furthermore, when any daughter board of the amplifying mother-boards was not working properly, or a bad connection happened in the connectors, or even a problem emerged from the read-out PCB electrodes, this could result in a dead channel, whose cause had to be identified. If the problem was downstream the mother-boards, we injected a signal with a pulse generator through a capacitor in every flat-cable, one by one, at the entry of each mother-board and checked if all the ADC channels read that signal. Conversely, if the problem was upstream the mother-boards, somewhere inside the aluminium box container, we disconnected the flat-cable connecting the mother-board to a certain $X$ or $Y$ read-out PCB electrode and injected a signal on this flat-cable. By capacitive coupling, the corresponding $X$ or $Y$ electrode should collect charge and be read by the ADC channels. Such example is shown in fig. 3.22, where a signal is injected on a flat-cable that goes to electrode $Y$ and couples capacitively to every channel of electrode $X$.

One fast way to look for dead channels is by plotting the coefficients of correlation of each of the 88 channels (spare channels not included) with each other. This is visible

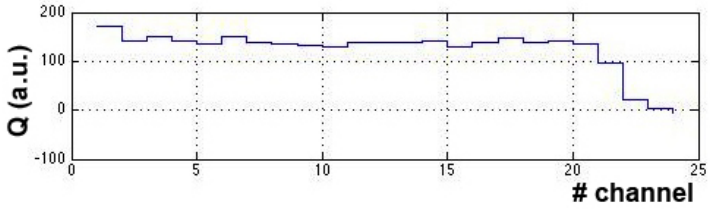


**Figure 3.22:** Signal conduction test between the channels of the read-out PCB electrodes and the ADC channels. All channels seem operational.

in fig. 3.23 a), where channel 17 of electrode $X$ of detector $a$ seems to have a problem which has to be identified. Figs. 3.23 a) and b) show the coefficients of correlation between channels of detectors $c$, 45 cm away. We can see a correlation between the channels of electrodes $X$ and electrodes $Y$ of both detector pairs, signaling the origin of the almost collinear photons.

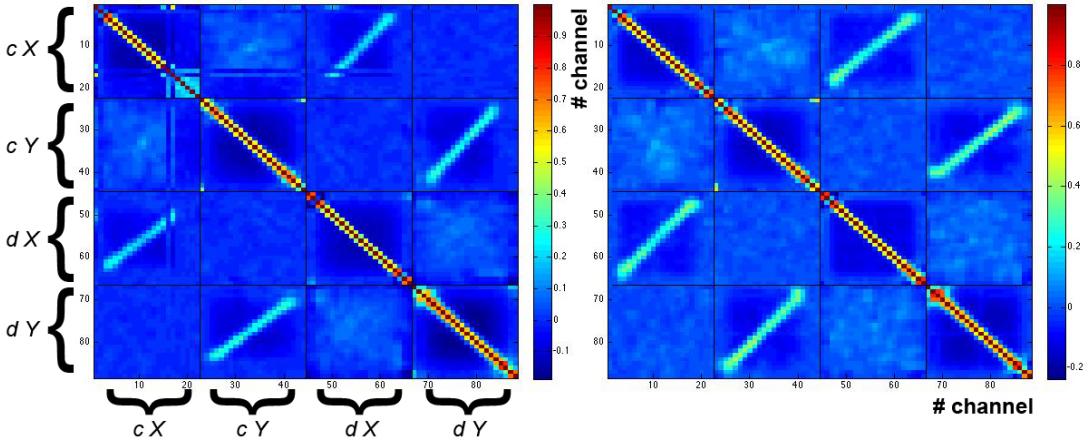


**Figure 3.23:** Coefficients of correlation for the 88 detector channels for detectors $c$ and $d$ before (a) and after (b) repairing channel 17 of electrode $X$.

An additional method to find any problem in the read-out PCB electrodes, once the box is sealed and under gas flux, is by measuring the capacitance between consecutive wires in the flat-cable. Such measurements have been made and are shown in fig. 3.24. Because the measurements are made on a pair of wires, we do not know which of the two has a problem. The figure suggests that the channel 2 of electrode $cX$ and the channels 15 and 16 of electrode $cY$ have problems. Fortunately, this time-consuming method

was not frequently adopted, since such problems rarely appeared on the read-out PCB electrodes.

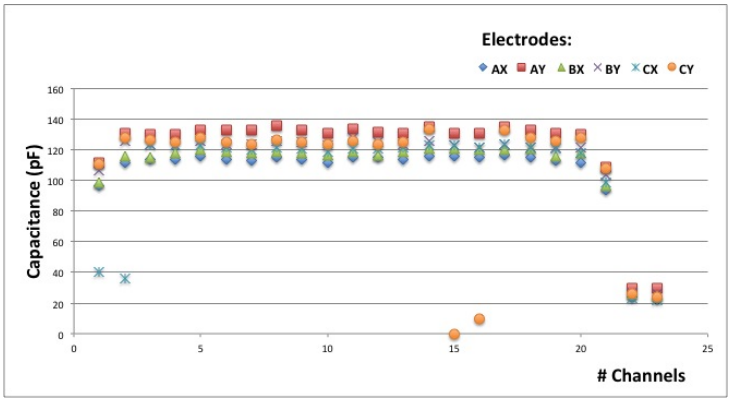


**Figure 3.24:** Capacitance between each pair of consecutive wires in the flat-cables that connect the read-out PCB electrode strips to the charge amplifying FEE.

### 3.5.3 Counting rate, electric current and stability measurements

We have tested the background counting rate and the electric current with increasing applied voltage for detectors epoxied with *SEMITRON* and painted with resistive ink (see fig. 3.25). While the *SEMITRON* detectors change their behavior along time,

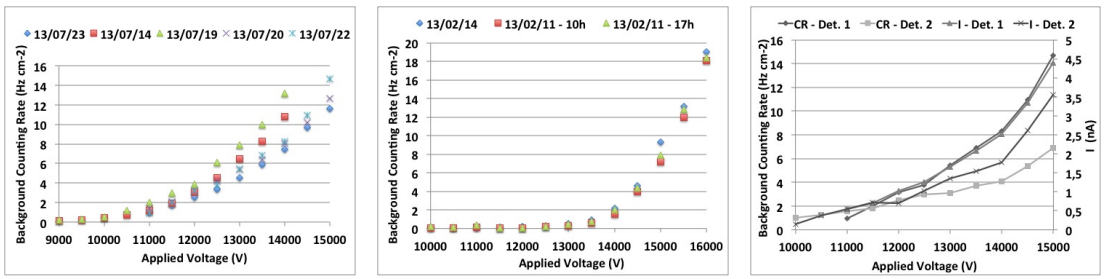


a) b) c)

**Figure 3.25:** Background counting rate for: a) *SEMITRON* detectors; b) Resistive Ink detectors. c) Background counting rate and electric current for two *SEMITRON* detectors.

painted detectors show a more stable behavior. Fig. 3.25 c) compare two *SEMITRON* detectors. Detector 2 has a higher counting rate and consumes higher electric current. That may depend on the temperature and humidity conditions at the moment of the measurements and on the elapsed time since high-voltage application. The same

behavior is observed in the presence of a source (see fig. 3.27, b).

When we bring a source close to the detector the counting rate increases substantially, as observed in fig. 3.26 a). The behavior of the consumed electric current in the

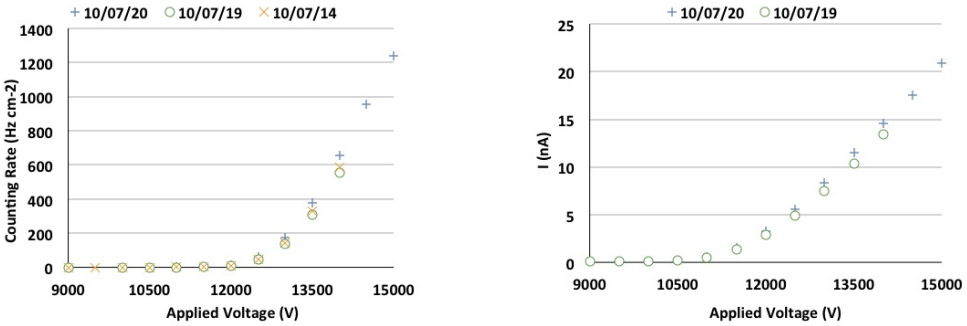


a) b)

**Figure 3.26:** a) Counting Rate and b) electric current in the presence of a source for *SEMITRON* detectors.

presence of a source is show in fig. 3.26 b).

In figs. 3.27 we address the response of a *SEMITRON* detector to different sources (a), the behavior of two *SEMITRON* detectors to the same source (b) and the influence of temperature on the counting rate (c). The red squares of fig. 3.27 c) represent

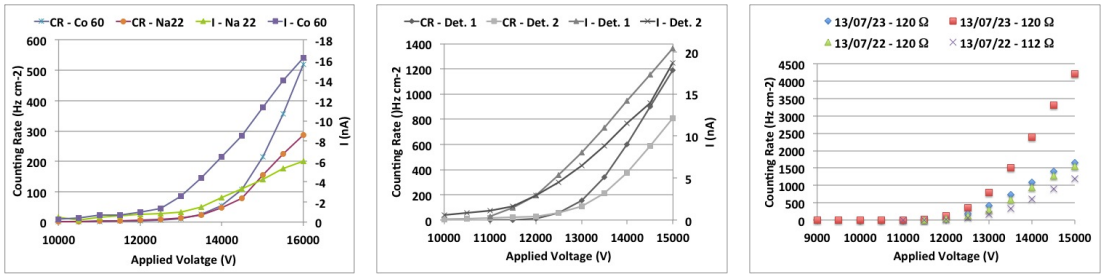


a) b) c)

**Figure 3.27:** a) Comparison of the counting rate and electric current in the presence of two different sources for one *SEMITRON* detector; b) Comparison of the counting rate and the electric current of two *SEMITRON* detectors in the presence of one source; c) Effect of the chamber temperature on the counting rate. Red squares correspond to the source positioned closer to the detector.

a warmed chamber with the source closer to the RPC detector. The increase in the counting rate is substantial. In all the measurements, the detectors started increasing their gain above 12 kV. The electric current has a linear dependence with the applied

voltage, while the counting rate varies exponentially. These tests to the detector modules were carried out in order to verify their proper operation and readiness to be mounted in the scanner head. RPC performance tests may take several weeks or even years [295], and consequently are out of the scope of this work.

A measurement of the valid coincidence counting rate is show in fig. 3.28. The

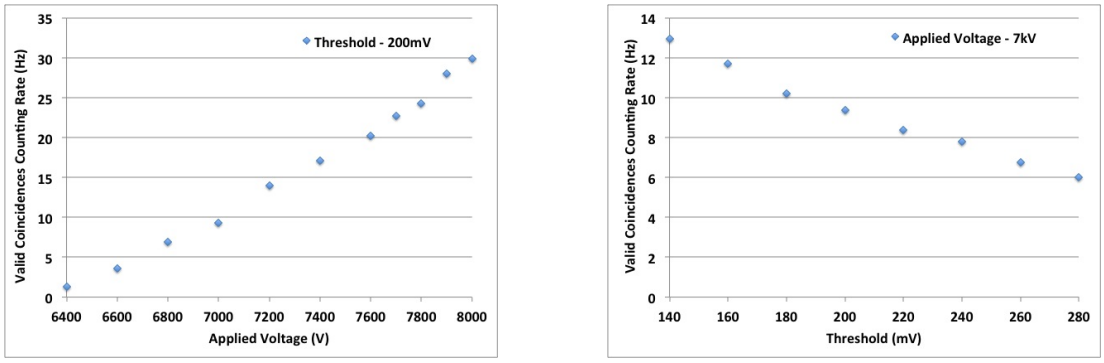


a) b)

**Figure 3.28:** Evolution of the valid coincidence counting rate for: a) an increasing applied voltage with a threshold set at 200mV; b) an increasing threshold with an applied voltage of 7kV. It was not possible at the time of these measurements to set the threshold below 140mV.

data, for two *SEMITRON* detectors in coincidence, with a source between them, show a rough linear dependence of the counting rate on both the applied voltage and the threshold. We believed at the time of the measurements that we might achieve higher rates with the notch filter at the entrance of the time FEE and working with resistive ink detectors. More recent data have confirmed this expectation.

Fig. 3.29 presents the evolution of the rate of events crossing the source with the applied voltage. This represents approximately 33% of the total events (signal). The remainder events come essentially from coincidences with (Compton of) the "$3^{rd}$ photon"[1] (background). These measurements were made with the needle-like source and the adopted high-voltage was 7900V, since it seems not to compromise the efficiency.

A test on the stability of the current consumed by a full 10-detectors head is shown in fig. 3.30. An increasing current due to the warm up of the aluminium box con-

[1]The $^{22}$Na source decays essentially by positron emission (90.6%) and electron capture (9.4%) with the subsequent emission of two 511 keV photons and one 1.275 MeV photon (the "$3^{rd}$ photon") originated from the $\gamma$-decay of the resulting excited nucleus.

tainer is observed at the beginning. The sealed box is warmed up by the 8 charge amplifiers placed on top within the *Faraday cage*. A transient to a stable current is observed, despite the oscillations at the end, alerting for a high-voltage leakage, which was immediately fixed.

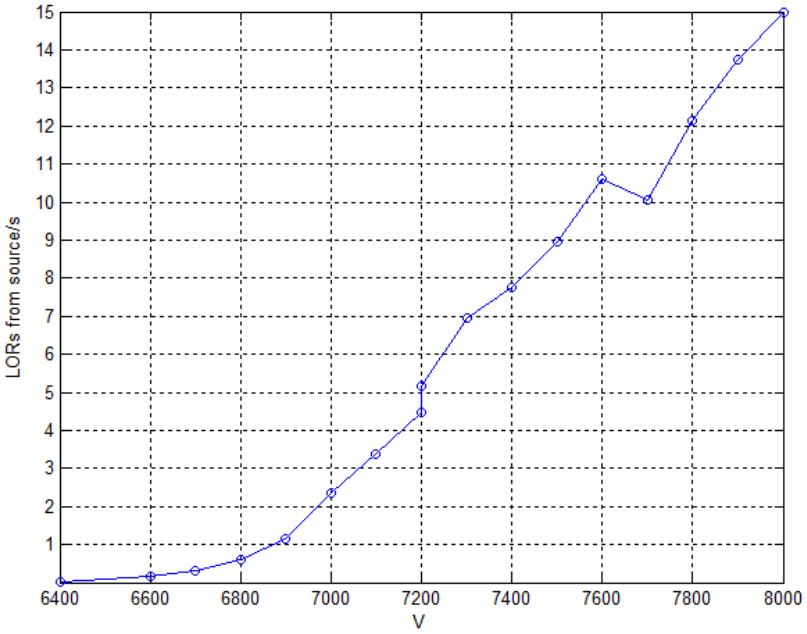


**Figure 3.29:** Rate of events crossing the needle-like source as a function of the applied voltage.

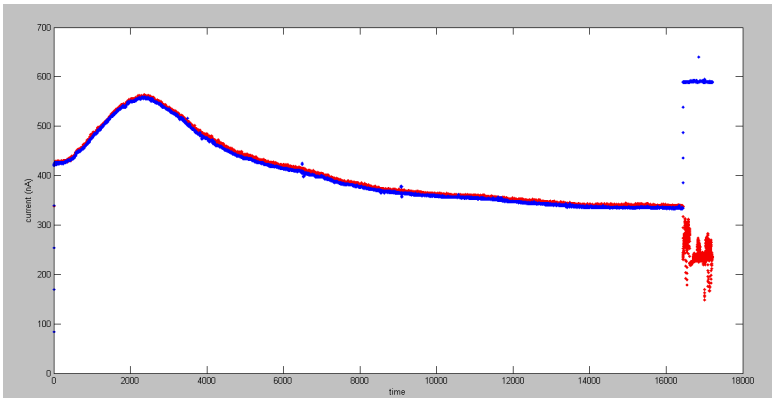


**Figure 3.30:** Evolution of the current consumed by a full 10-detectors head with time.

## 3.6 Relative activity measurements

If we have a source of known activity $\alpha_k$, the unknown activity $\alpha_u$ of another source of the same isotope can be determined from the ratio between the count rates of the unknown $R_u$ and of the known $R_k$, measured under the same conditions (geometry and electronics),

$$\alpha_u = \alpha_k \frac{R_u}{R_k}. \tag{3.3}$$

For this purpose, we used a system composed of a NaI scintillator crystal coupled to a PMT. The PMT signals pass through a converter and spectroscopy chain (pre-amplifier and linear amplifier) and feed a multi-channel analyser (MCA). We analysed the spectra of 5 different $^{22}$Na sources. From those, we knew the fabrication date of 3 disk sources and their original activity: 0.8 mCi and 0.08 mCi (2002/05/20); 26.5$\mu$Ci (2005/10/15). The activity of the needle-like and $W$ sources were unknown. The measurements were made with the sources set 22.6 cm apart from the NaI, to avoid pile-up causing a strong dead-time contribution. Fig. 3.31 shows the gamma-ray spectra for the needle-like source and the 0.8 mCi disk-source, both obtained from a 600 s acquisition, the two distinct peaks corresponding to 511 keV and 1.275 MeV photons.

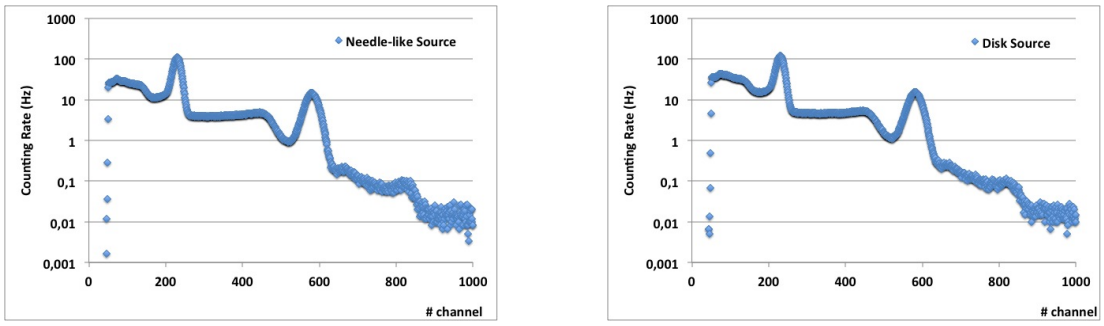


a) b)

**Figure 3.31:** Gamma-ray spectra of $^{22}$Na for the: a) needle-like source; b) 0.8 mCi disk source.

From the expected activity for the 3 know sources, we estimate from equation 3.3 the activity of the unknown sources. The ratio $\frac{R_u}{R_k}$ is obtained by dividing the integrals of the corresponding peak areas. The results are presented in table 3.1.

| **511 keV** | **Known Sources** | | |
|---|---|---|---|
| Unknown Sources | 0.08 mCi | 0.8 mCi | 26.5$\mu$Ci |
| 0.08 mCi | 5.0 | 5.6 | 4.5 |
| 0.8 mCi | 45.0 | 50.1 | 40.5 |
| 26.5 $\mu$Ci | 4.6 | 5.1 | 4.1 |
| Needle-like | **39.2** | **43.7** | 35.2 |
| W-source | **6.2** | **7.0** | 5.6 |

| **1275 keV** | **Known Sources** | | |
|---|---|---|---|
| Unknown Sources | 0.08 mCi | 0.8 mCi | 26.5$\mu$Ci |
| 0.08 mCi | 5.0 | 5.6 | 4.5 |
| 0.8 mCi | 45.2 | 50.1 | 40.7 |
| 26.5 $\mu$Ci | 4.6 | 5.1 | 4.1 |
| Needle-like | **41.1** | **45.6** | 37.0 |
| W-source | **6.3** | **7.0** | 5.7 |

**Table 3.1:** Estimated activies of the needle-like and $W$ sources based on the known source activities.

The summed activities of the needle-like and $W$ sources divided by the deposited solution volume of 7.5 $\mu$L should approximate the expected activity concentration of 10.85 $\mu$Ci/$\mu$L, but the results are below the expectation for both measurements. The needle-like source measurements suggest an activity of 44.6 $\pm$ 0.1 $\mu$Ci.

# 4

# Data Processing

The data provided by our experimental setup followed a processing chain with the ultimate goal of imaging radioactive sources and evaluating the spatial resolution of our system. The process of decoding the raw data provided by the DAQ system (see section 3.4) should be fast, as well as the digital processing of the decoded data. In sections 4.1 and 4.2, we describe in detail both processes and the time consumed which evolved in a most promising way[1]. At the end, we were able to filter the different types of coincidences between the pairs of detectors. The next step involved the data analysis which dealt with several issues fully explained in section 4.3. A crucial achievement concerns the identification of the gap where the avalanche developed, allowing a precise depth of interaction (DOI) measurement, thus overcoming the limitations of the parallax associated to other kind of detectors used in PET. A method for the determination of the position distribution of the triggered events on the detectors is exploited, in accordance with the results presented by Fonte *et al.* [19]. In section 4.5, we introduce a custom-made reconstruction routine based on the MLEM algorithm and we evaluate its reliability with simulated data generated by a custom-made event generator. We show reconstructed images of experimental data obtained from the imaging of three different sources. In section 4.6, we assess the spatial resolution of the system. Finally, in section 4.7, with detectors separated by 45 cm, we attempt to measure the photon non-collinearity contribution to the spatial

[1]We made efforts to process the data with reasonable computing resources and within a short time. The data acquisition and decoding processes were carried out in the lab, while the digital processing was accomplished on the GRID. Thus, the presented system processing chain was not primarily conceived to deal with the final prototype requirements, which will be drawn up on a standalone computing basis.

resolution and validate the results with simulated data. A brief summary of the work in progress is addressed at the end of the chapter.

## 4.1 Decoding raw data

The acquisition chain stores the data in the raw HADES list-mode data (HLD) format written in a local hard disk. The user defines the maximum size for each HLD file, according to the trigger rate and computing capabilities. As depicted in fig. 4.1, each file stored in the hard disk has a file header containing the time and date of its creation, allowing the evaluation of the temporal evolution of the run.

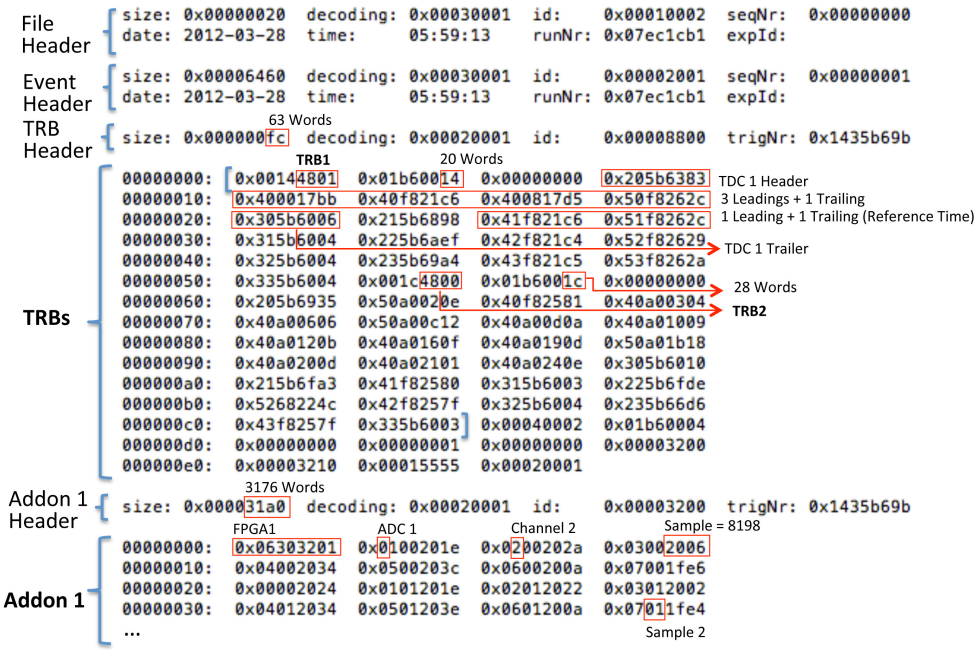


**Figure 4.1:** Event coding including the time and charge measurements recorded by the TRBSs and the Addons, respectively.

The HADES TDC read-out boards (TRBs) are able to store the timing measurements of 128 channels. The TRB header indicates the number of words supplied for the event, including leadings and trailings measurements. The data read-out from the time to digital converter (TDC) is contained in 32 bit data packets. The packet format is described in fig. 4.2. The first four bits of each packet define the type of data packet. Converting to decimal format, the leading measurements start with number 4, while trailing measurements start with number 5. The following four bits identify the TDC

**TDC header**: Event header from TDC

| 31 | 30 | 29 | 28 | 27 | 26 | 25 | 24 | 23 | 22 | 21 | 20 | 19 | 18 | 17 | 16 | 15 | 14 | 13 | 12 | 11 | 10 | 9 | 8 | 7 | 6 | 5 | 4 | 3 | 2 | 1 | 0 |
|---|---|---|---|---|---|---|---|---|---|---|---|---|---|---|---|---|---|---|---|---|---|---|---|---|---|---|---|---|---|---|---|
| 0 | 0 | 1 | 0 | TDC | | | | Event ID | | | | | | | | | | | | Bunch ID | | | | | | | | | | | |

**TDC trailer**: Event trailer from TDC

| 31 | 30 | 29 | 28 | 27 | 26 | 25 | 24 | 23 | 22 | 21 | 20 | 19 | 18 | 17 | 16 | 15 | 14 | 13 | 12 | 11 | 10 | 9 | 8 | 7 | 6 | 5 | 4 | 3 | 2 | 1 | 0 |
|---|---|---|---|---|---|---|---|---|---|---|---|---|---|---|---|---|---|---|---|---|---|---|---|---|---|---|---|---|---|---|---|
| 0 | 0 | 1 | 1 | TDC | | | | Event ID | | | | | | | | | | | | Word count | | | | | | | | | | | |

**Leading measurement**:

| 31 | 30 | 29 | 28 | 27 | 26 | 25 | 24 | 23 | 22 | 21 | 20 | 19 | 18 | 17 | 16 | 15 | 14 | 13 | 12 | 11 | 10 | 9 | 8 | 7 | 6 | 5 | 4 | 3 | 2 | 1 | 0 |
|---|---|---|---|---|---|---|---|---|---|---|---|---|---|---|---|---|---|---|---|---|---|---|---|---|---|---|---|---|---|---|---|
| 0 | 1 | 0 | 0 | TDC | | | | Channel | | | | | Leading time | | | | | | | | | | | | | | | | | | |

**Trailing measurement**:

| 31 | 30 | 29 | 28 | 27 | 26 | 25 | 24 | 23 | 22 | 21 | 20 | 19 | 18 | 17 | 16 | 15 | 14 | 13 | 12 | 11 | 10 | 9 | 8 | 7 | 6 | 5 | 4 | 3 | 2 | 1 | 0 |
|---|---|---|---|---|---|---|---|---|---|---|---|---|---|---|---|---|---|---|---|---|---|---|---|---|---|---|---|---|---|---|---|
| 0 | 1 | 0 | 1 | TDC | | | | Channel | | | | | Trailing time | | | | | | | | | | | | | | | | | | |

**Figure 4.2:** Packet format of the read-out data acquired by the TDCs. From [296].

chip which converts the data. In the event shown in fig. 4.1, the 4 TDCs of TRB1 generate 20 words. Time events are just generated by TDC 1, in its first and second channel, complemented by the reference times. Incidentally, TRB2 registered several measurements on channel 20 of TDC1, associated to some kind of noise on this channel.

The first Addon stores the charge for each of the 96 channels and writes 3176 words per event. Excluding the four words from the header and the two words denoting which field programmable gate array (FPGA) it corresponds to, it ends up with 1584 words per FPGA. This value corresponds to the words associated to each of the 33 sums of samples[1] recorded by the 8 channels of each of the 12 analog to digital converters (ADCs). The first four bits identify the ADC, followed by the next four bits indicating the channel and the next 8 bits indicating the sample number. The last 16 bits correspond to the sampled value.

Although the number of words for the Addons are constant, the number of words of the TRBs are variable, which renders the decoder code used for this purpose non-parallelizable. Nevertheless, we can adapt the size of the HLD file to meet the computational needs depending on the trigger rate. For higher trigger rates, we decided to set the HLD file size to 500MB (corresponding to roughly 20k events), write it to one

[1]The ADCs sample the charge signal through sums of 16 10-bit samples. From now on, for ease of reading, we will refer to these sums as samples.

hard drive and transfer it to the shared memory, where a ramdisk stores the HLD file to be decoded. This avoids the time spent loading the data into the global memory, this being the major bottleneck on the decoding process. While the decoder processes a HLD file, another HLD file is already being transfered to the ramdisk. The output is written to another hard drive, preventing I/O data transfer limitations. The output is written to binary files which are then compressed with QuickLZ® and piped via secure shell (SSH) to the nodes inside the Grid computing cluster (GRID). The QuickLZ compressor shows the best throughput and tradeoff between speed and compressing capability [297, 298], reaching 308 MB/s per core. The task of decoding the HLD file and compressing the output takes a few seconds, the bottleneck being the transfer speed from the DAQ machine to the GRID, which in our case was limited to 100MBits/s. In the GRID user interface machine, there is a script running permanently that submits an array of jobs each time it receives a bunch of decoded HLD files. These jobs send up to 24 simultaneous digital pulse processes – detailed in the following section – to the available cores, but can be scaled when more computer resources are available. Our goal is to process the data on the fly for later reconstruction.

## 4.2 Signals processing

### 4.2.1 Towards optimum measurement of the charge released by the detector

Digital signal processing (DSP) is widely used in nuclear spectrometry in order to produce digital signals describing the properties of radiation, such as the energy of radiation. The energy is absorbed in solid state, proportional or scintillation detectors, and converted into an electrical charge, which is usually contaminated with noise as it passes through non-ideal front-end electronics (FEE) components. In RPC-PET, we are concerned with an accurate measurement of the charge signal. Therefore, it is important to process correctly the signal and remove the several sources of noise, such as junction gate field-effect transistors (JFETs) and preamplifiers (series noise), and the detector itself and its dark currents (parallel noise).

Signal processing methods different from the optimum one result in the loss of signal-to-noise ratio. The problem of the optimum signal processing in the measurement of the charge $Q$ delivered by a detector can be presented as a search of a network which

allows the best least-squares measurement of $Q$ in the presence of the several sources of noise [299].

Baldinger and Franzen [300] synthesized the best processing of detector signals in the time domain, while Radeka and Karlovac [301] extended to the nuclear case the theory of the matched filter with a frequency domain approach. Gatti and Manfreddi [299] integrated these two approaches on optimum processing to make an analytically demonstration of the optimum signal-to-noise ratio. They move forward with the calculation of the signal-to-noise ratio of some analog processors. In the class of the time-invariant shapers, they present the trapezoidal shaping, used in nuclear radiation detectors. There are networks that respond to a $\delta$-impulse shaped detector current with signals different from the triangle, like the inclusion of a flat-topped trapezoidal response, used for instance to reduce the ballistic errors [302]. Flat-topped pulses $v_\delta(t)$ of suitable duration are also required for the cancellation of induction and cross-talk signals.

Since the emergence of fast ADCs, FPGAs and DSPs, digital technology has evolved quickly, thus replacing most of the classical analog components. The FPGA can handle the readout, trigger decisions, and simple to medium levels of complexity of signal processing [303]. DSP systems can perform more complex calculations and are being continuously upgraded into very compact digital systems, mostly as standalone units, thus comprising preamplifier and digital pulse processor all in one.

In our tests, we developed basic digital processing to remove noise from charge signals. Fig. 4.3 shows a typical pulse processing scheme for charge estimation. The

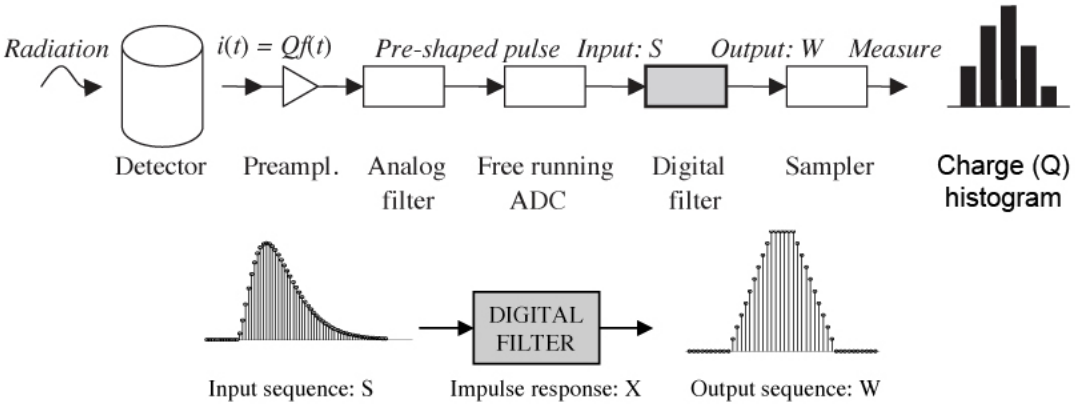


**Figure 4.3:** Generic pulse processing scheme for charge estimation. Adapted from [304].

input sequence $S$ is convoluted with a filter impulse response $X$, giving an output sequence $W$ [304]. In what concerns the charge measurements in RPC-PET, we focused on the employment of filtering techniques and optimized filters for a best estimation of the signal to noise ratio. We had to set constraints in time domain for optimum filter synthesis, such as a flat top equal or longer than the detector maximum charge collection time.

### 4.2.2 Digital pulse processing in small-animal RPC-PET

The experimental setup composed by four detectors and eight pickup electrodes delivers charge through 24 channels per electrode to the 24 8-channel ADCs (described in section 3.4). This charge is digitally filtered in the time domain by a trapezoidal shaper with time constants $2\mu$s, $1\mu$s, $2\mu$s (leading, top-flat, trailing) (see fig. 4.4). For the es-

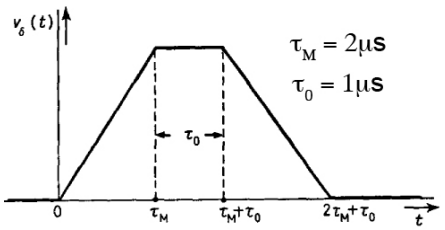


**Figure 4.4:** Trapezoidal shaping.

timation of the voltage step in the presence of white noise, we convolute the measured voltage step signal with a digital filter with a trapezoidal weighting function. Both the voltage step and the trapezoidal filter output (TFO) are depicted in fig. 4.5. In this case, we have a coincidence between the detectors $a$ and $c$, and a delayed random signal in detector $b$.

A first processor calculated the signal for each pick-up electrode as the average charge in the strip with largest signal and in its six closest neighbors (three left and three right). By means of a vote, depending on wether the average charge was above a defined threshold in two of the four detectors, the processor accepted the event as a valid coincidence. Because this processor allowed random events being accepted as valid coincidences, an optimization on the chosen reference sample was reconsidered. In order to quantify the charge collected by each ADC channel, some constraints have

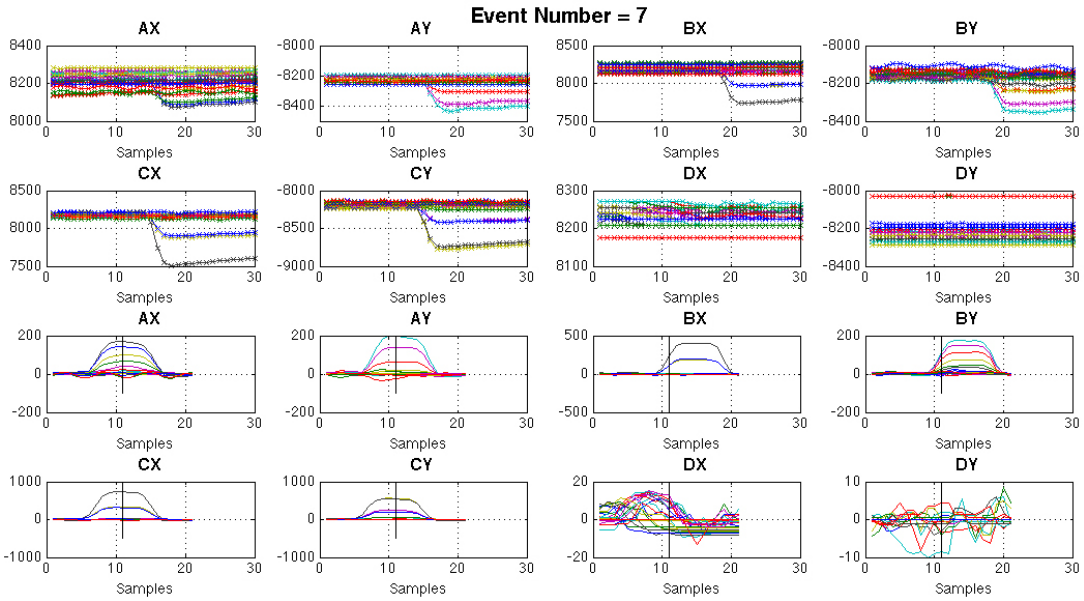


**Figure 4.5:** Voltage steps (top) and the corresponding trapezoidal filter output (bottom) relative to the 24 channels of each signal pickup electrode $X$ and $Y$, enclosing the detectors $a$, $b$, $c$, and $d$.

to be set and the reference sample must be calculated[1].

A second version of the processor envisaged a more efficient identification of the detectors that produce valid coincidences. A starting lower cut on the charge collected by each ADC channel allowed removing some baseline noise. For each channel, a condition was set on the first and last three samples requiring those values to be below 20% of the maximum charge sampled on that channel. This condition avoided most of the random events. An interpolation at half maximum on the leading and falling edge of the TFO allowed determining the center of the TFO, and thus the reference sample. An additional constraint consisted on only accepting the TFOs whose reference sample was the same or next to the one obtained from the channel with larger signal. This process can be visualized in fig. 4.6 where we have the TFOs corresponding to each channel before (top) and after (bottom) getting through the imposed constraints.

In order to accept an event as a valid coincidence, we need to have at least one TFO and the respective channel triggered in all the four read-out electrodes of two detectors. The average of the reference samples rounded to the nearest integer is depicted on the

[1]As a first approach, we defined the $11^{th}$ sample as the reference which we still use for hardware debugging.

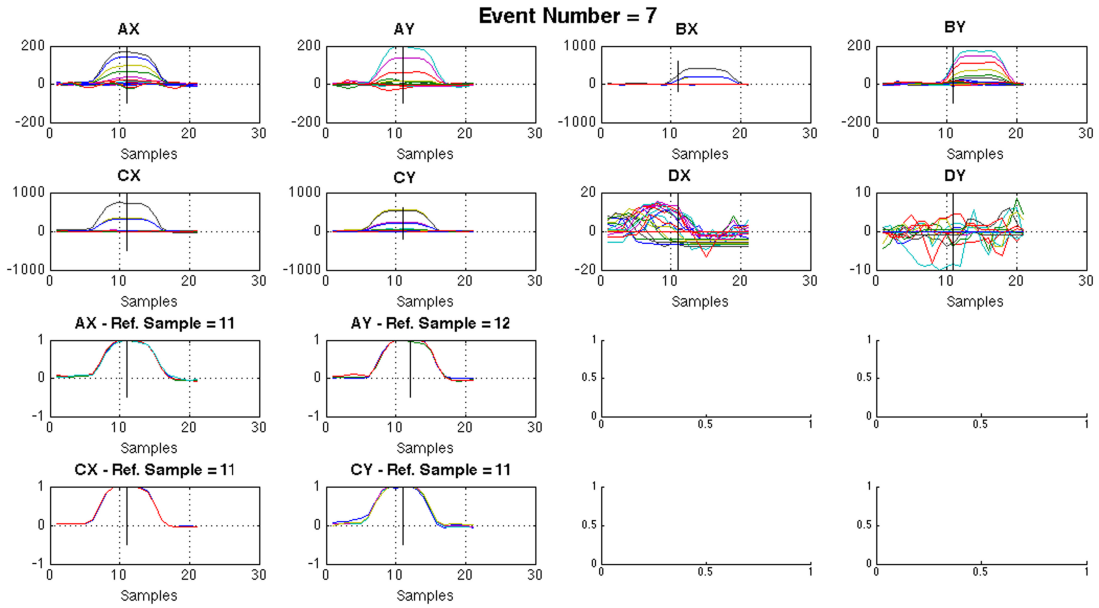


**Figure 4.6:** Coincidence between the detectors $a$ and $c$. TFOs relative to the 24 channels of each signal pickup electrode $X$ and $Y$, enclosing the detectors $a$, $b$, $c$, and $d$ (top) and the ones that got through the imposed constraints (bottom).

top of each plot of figs. 4.6 and 4.7. The absolute difference between these average values for the four electrodes must be less than 2 ($\Delta t_{max} \simeq 800$ ns). Otherwise, the double coincidence depicted in fig. 4.7 would be considered as a unique coincidence. This double coincidence verifies all the constraints imposed so far. Consequently, we identify a coincidence between detector $a$ and $b$, and another coincidence between detector $c$ and $d$.

The integration of the processor on the decoder, all in C language, avoids writing the output of the decoder on the hard drive, thus saving space and time. The resulting output for 20k triggered events amounts to 2MB instead of the 100MB occupied by the decoder output or the 500MB occupied by the HLD. We reached a maximum trigger efficiency[1] of 30%. The running time of the decoder, together with the processor is less than 30 s for the 20k triggered events. This goal was pursued for higher trigger rates and for future scans with mice. However, for the results presented in this work, we kept the output of the decoder in order to optimize the processor and to keep the raw

[1] In this case, trigger efficiency corresponds to the ratio between the number of triggered coincidences processed as valid and the number of triggers reaching the DAQ.

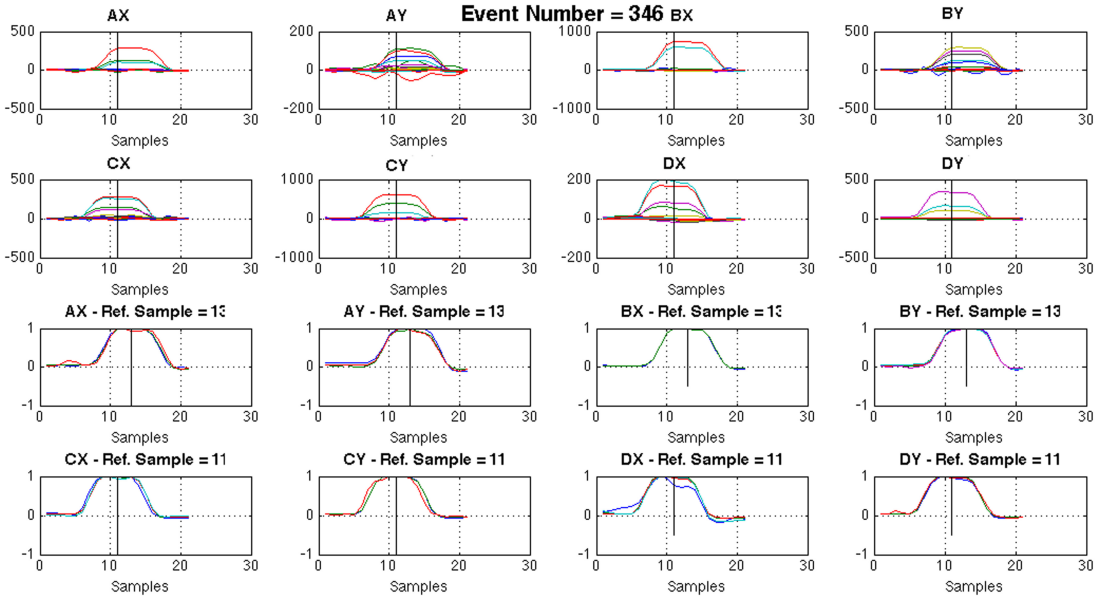


**Figure 4.7:** Double coincidence between detectors $a$ and $b$, and $c$ and $d$. The average reference samples matches for each coincidence.

data for other studies, such as the inefficiency of the trigger and the reduction of the number of sums of samples.

The reliability of the method was verified by improving the processor with timing filtering and pole-zero cancelation, producing similar results. (see fig. 4.8 and explanation in the figure caption).

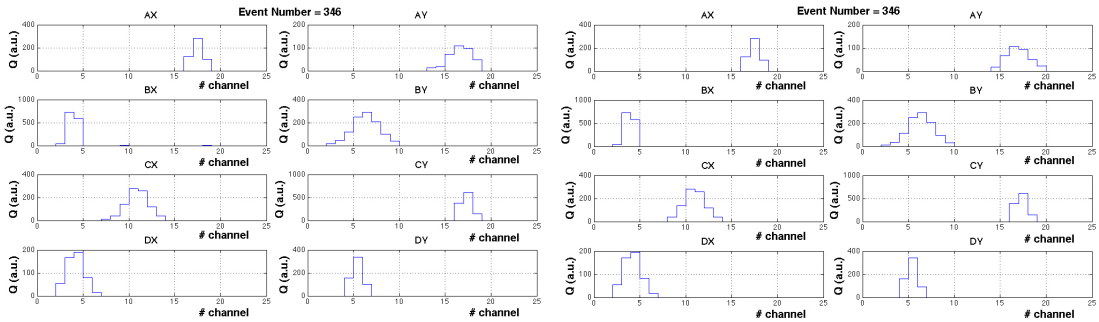


**Figure 4.8:** Processed charge distribution along the channels of each electrode for the double coincidence. The match between the output of two different processing methods (left and right) ensure their reliability.

As stated before, a running script hosted in a user interface machine of the GRID waits permanently for the incoming data sent by the DAQ machine. Once it gets some

data, it submits a job for each decoded HLD it receives. This script waits for the submitted jobs to run, to submit another array of jobs and process the new data. This way, it was possible, in one month, to acquire and process, automatically and without interruptions, approximately 250M events ($\sim$ 50k HLDs) resulting from the imaging of the planar source.

## 4.3 Event analysis

### 4.3.1 The *k*-means clustering technique

The so-called "$k$-means algorithm" was first used by MacQueen [305]. The purpose of $k$-means clustering consists of achieving qualitative and quantitative insight into large multivariate data sets. Like other data clustering techniques, $k$-means is a descriptive data analysis technique and it is used to form clusters by evaluating similarities and dissimilarities of intrinsic characteristics between different data points [306]. It belongs to partitional clustering techniques and it is based on the iterative relocation of data points between clusters. The goal is to produce groups of data points with a high degree of similarity within each group and a low degree of similarity between groups [307]. It is an algorithm of simple implementation, computationally efficient and with low memory requirements. On the opposite side are the hierarchical clustering techniques, such as "linkage", that require large computational resources.

The first step of $k$-means algorithm is to choose the $k$ initial centroids. In our work, we knew previously the number of expected clusters corresponding to each gap (which is 5). Because this algorithm has a bias to create clusters of equal size, we were in good conditions to use it, with the clusters presenting a globular shape and similar size and data densities.

### 4.3.2 Principal component analysis

Principal component analysis (PCA), one of the oldest multivariate statistical techniques, is used by almost every scientific disciplin [308]. Initially conceptualized by Galton [309] and Pearson [310], its modern implementation was formalized by Hotelling [311]. The central idea of PCA is to reduce the dimensionality of a data set consisting of a large number of interrelated variables, while retaining as much as possible of the variation present in the data set. This is achieved by transforming to a new set of variables, the principal components (PCs), which are orthogonal, and thus uncorrelated, and which are ordered so that the first few retain most of the variation present in all of the original variables [312]. PCA usually analyzes a data table representing observations described by several dependent variables, which are, in general, inter-correlated. PCA also represents the pattern of similarity of the observations and the variables by displaying them as points in maps [308].

In this work, we use the PCA to identify the gap between glass electrodes where the avalanche developed. Together with the aforementioned $k$-means clustering technique, this allows measuring the DOI, rendering RPC-PET essentially parallax-free.

A more detailed review of both aforementioned statistical tools is presented in appendices D and E.

### 4.3.3 Application on gap identification

A simulation has been performed to evaluate the "propagation" of the electric weighting field along the detector [19]. The detector cross section, along with the weighting field (e.g. [313]) map for a 4 mm pitch strip is represented in fig. 4.9, left. The intensity of the vertical weighting field for a generic strip as a function of the avalanche distance in each gap is shown in fig. 4.9, right (vertical axis). The charge sharing between several strips can be deduced from these curves by considering the different avalanche-strip distances.

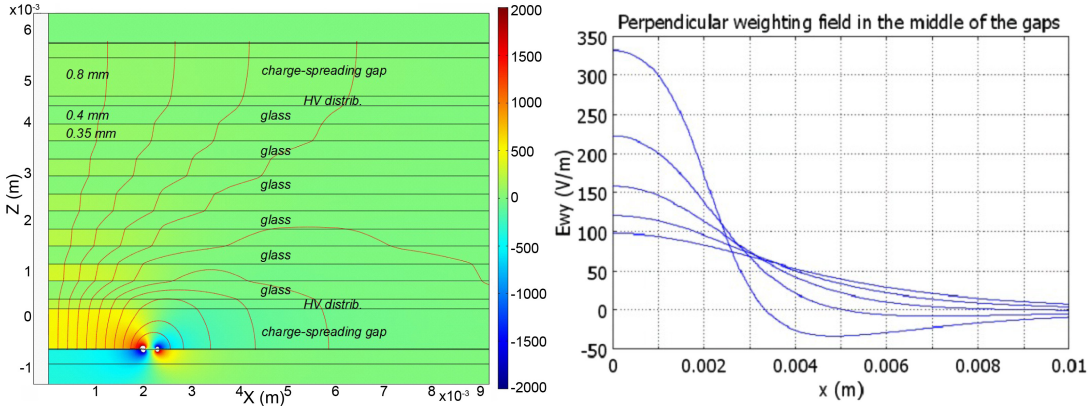


**Figure 4.9:** Representation of the detector cross-section (in meter) and of the weighting field for a 4 mm pitch strip (left). The red lines are the electric field lines and the colors map the intensity of the vertical component of the weighting field (in V/m). The intensity of the weighting field for each gap as a function of the distance between the avalanche and the centre of the strip is shown on the right. The x $< 0$ region was omitted owing to reflection symmetry. From [19].

To identify the gap where the avalanche took place, an algorithm based on the induced charge pattern was developed [19]. From the charge in the 3 strips with larger signal, $Q_{-1}$, $Q_0$, $Q_1$, we started by forming the following quantities: $Q = Q_{-1}+Q_0+Q_1$, $q_{-1} = Q_{_1}/Q$, $q_0 = Q_0/Q$, and $q_1 = Q_1/Q$. After applying the PCA to the induced

charge on 3 contiguous strips ($q_{-1}$, $q_0$, $q_1$), both on the simulated and experimental data, we obtain the PC scores depicted in fig. 4.10. They share a very similar pattern, and from its visualisation, it is possible to distinguish the 5 gaps where the avalanches developed.

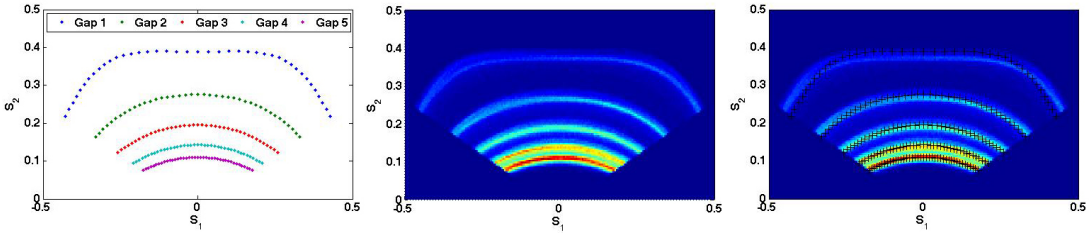


**Figure 4.10:** Histogram of PC scores $S_1$ and $S_2$ defining the 5 gaps. Left: results from electrostatic simulation. Middle: results from experimental data. Right: overlap of simulated and experimental data demonstrating the agreement between both.

A PCA of the simulated data corresponding to gap 1 extracts three principal components with eigenvalues of 1.98, 1.02, and 0, respectively. The other gaps behave similarly with the eigenvalues converging to 2 and 1, respectively, with increasing gap number. The component 1 explains 66% of the total variance, while the component 2 accounts for the remaining 34%. The squared loadings depicted in Table 4.1 produce the proportion of variance of each variable explained by each of the first two components, since component 3 does not contribute at all, thus being redundant. From

| | **Loadings ($\boldsymbol{L}$)** | | | **Squared Loadings ($\boldsymbol{L^2}$)** | | | $\boldsymbol{A'_\Sigma}$ | | | $\boldsymbol{A'_R}$ | | |
|---|---|---|---|---|---|---|---|---|---|---|---|---|
| PC | $q_{-1}$ | $q_0$ | $q_1$ | $q_{-1}$ | $q_0$ | $q_1$ | $q_{-1}$ | $q_0$ | $q_1$ | $q_{-1}$ | $q_0$ | $q_1$ |
| 1 | 0.994 | 0 | -0.994 | 0.988 | 0 | 0.988 | -0.707 | 0 | 0.707 | 0.707 | 0 | -0.707 |
| 2 | -0.112 | 1 | -0.112 | 0.013 | 1 | 0.013 | -0.408 | 0.817 | -0.408 | -0.110 | 0.988 | -0.110 |
| 3 | 0 | 0 | 0 | 0 | 0 | 0 | -0.577 | -0.577 | -0.577 | -0.699 | -0.156 | -0.699 |
| $\Sigma$ | | | | 1 | 1 | 1 | | | | | | |

**Table 4.1:** Component loadings from simulated data for gap 1. The elements of matrix $\boldsymbol{A'}$ are also provided.

matrix $\boldsymbol{L^2}$, we conclude that variables $q_{-1}$ and $q_1$ are almost completely explained by component 1, while variable $q_0$ is totally explained by component 2. For component 1, there is a common but negative association (note the signs in matrix $\boldsymbol{L}$) between vari-

able $q_{-1}$ and $q_1$. The matrix $\boldsymbol{A'_\Sigma}$ and $\boldsymbol{A'_R}$, which define the component scores depicted in fig. 4.10, differ mainly on the second component, thus reflecting in the amplitude of the stripes. Moreover, the signs of the component 1 are inverted for both matrices, consequently the scores along the $S_1$ axis become symmetrically inverted.

The results of the PCA applied to experimental data are shown in table 4.2. As

| | **Loadings ($\boldsymbol{L}$)** | | | **Squared Loadings ($\boldsymbol{L^2}$)** | | | $\boldsymbol{A'_\Sigma}$ | | | $\boldsymbol{A'_R}$ | | |
|---|---|---|---|---|---|---|---|---|---|---|---|---|
| PC | $q_{-1}$ | $q_0$ | $q_1$ | $q_{-1}$ | $q_0$ | $q_1$ | $q_{-1}$ | $q_0$ | $q_1$ | $q_{-1}$ | $q_0$ | $q_1$ |
| 1 | 0.968 | -0.018 | -0.962 | 0.937 | 0 | 0.926 | -0.709 | 0.004 | 0.705 | 0.709 | -0.013 | -0.705 |
| 2 | 0.252 | -1 | 0.272 | 0.063 | 1 | 0.074 | -0.404 | 0.817 | -0.411 | 0.236 | -0.938 | 0.255 |
| 3 | 0 .009 | 0.005 | 0.009 | 0 | 0 | 0 | -0.578 | -0.577 | -0.578 | 0.662 | 0.347 | 0.664 |
| $\Sigma$ | | | | 1 | 1 | 1 | | | | | | |

**Table 4.2:** Component loadings from experimental data for electrode $X$ of detector $a$. The elements of matrix $\boldsymbol{A'}$ are also provided.

stated before, the agreement with simulated data is very notorious, as shown in fig. 4.10. The eigenvalues for the three principal components, sorted in decreasing order, are respectively: $\lambda_1 = 1.86$, $\tau_1 = 62\%$; $\lambda_2 = 1.14$, $\tau_2 = 38\%$; $\lambda_3 = 0$, $\tau_3 = 0\%$. We notice a small difference on component 2, which accounts for 7% of the variance of variables $q_{-1}$ and $q_1$. The other values confirm the results obtained from simulated data. Matrix $\boldsymbol{A'_R}$ has also small disagreement concerning component 2, which reflects only on the amplitude of the stripes. By this reason, we chose to work with the matrix of the eigenvectors obtained from the covariance matrix, $\boldsymbol{A'_\Sigma}$, which indicates more reliable data. We state in appendix D that an advantage of covariance matrices holds in the special case when all the variables are measured in the same units, which is the case. Standardizing the variables to give correlations is equivalent to making an arbitrary choice of measurement units. Nevertheless, when the variables have widely differing variances, the first few PCs usually contain little information apart from the relative sizes of variances, and the correlation matrix is preferable. However, this seems not to be the case.

To proceed with gap identification, we need to define the angle between the PC

scores $S_1$ and $S_2$ as well as the amplitude. Thus, the following quantities were formed

$$\alpha = -arctan\left(\frac{S2}{S1}\right), \tag{4.1}$$

$$G = S_1^2 + S_2^2 \tag{4.2}$$

If we assume the quantities $G$ and $\alpha$ as being the polar coordinates $r$ and $\phi$, respectively, we can convert them to the cartesian coordinates $U = r\ \cos(a\ \phi)$, and $V = r\ \sin(a\ \phi)$. An histogram relating the $U_x$ and $U_y$ coordinates corresponding respectively to the electrodes $X$ and $Y$ of one detector is presented in fig. 4.11, left. The scalar $a$ in $u$ ranges between 0.6 and 1 for a maximum intensity in the histogram, ensuring that the clusters are compact. The 5 gaps are perfectly distinguishable. By means of the

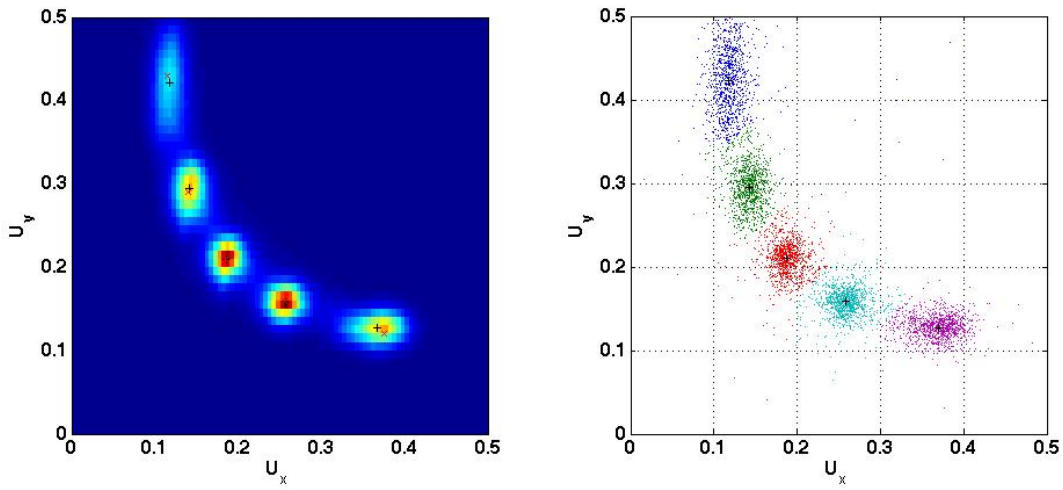


**Figure 4.11:** Method of gap identification: histogram of the variables $U_x$ and $U_y$, obtained from the defined variables $\alpha$ and $G$ (left); scatter plot dividing the experimental data into 5 clusters corresponding to the 5 gaps where the avalanches developed (right).

statistical clustering tool, *kmeans*, it is possible to partition the data into 5 clusters. The *kmeans* separates the data points into 5 different sets, corresponding respectively to the 5 gaps, ordered from the first to the fifth gap, as depicted in fig. 4.11, right. Each color corresponds to a cluster, consequently, to a certain gap[1]. The results show that the middle gap has more statistics followed by the second and fourth gap, and ultimately, by the first and the fifth gap.

[1] An alternative tool, *linkage*, creates a tree of hierarchical clusters using Euclidean distances between the observations, and produces similar results. Once it is computationally heavier and the clusters are formed in a hierarchical way, it becomes difficult to identify the order of the gaps.

### 4.3.4 Hits position determination

Bencze *et al.* and Fonte *et al.* indicate a relationship between the avalanche position relative to the center of the strip with largest charge and the above calculated quantity $\alpha$ [19, 314]. By simulation, we obtain for each gap 41 points whose coordinates are determined by this relationship, as shown in fig. 4.12, left. By doing an interpolation

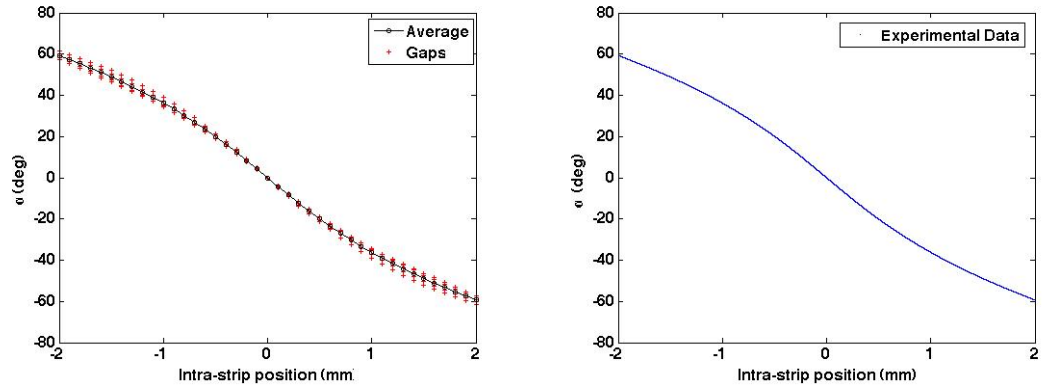


**Figure 4.12:** Relation between the defined variable $\alpha$ and the avalanche position for 4 mm strips. Left: simulated data for each gap and the corresponding average curve. The agreement with the experimental data (right) is good.

on the average curve, it is possible to determine the position coordinates of each event. Fig. 4.12, right, shows the corresponding curve obtained from experimental measurements of $\alpha$, from which the determination of the fine position of the hit on the detector is done.

Fig. 4.13 shows the position distribution (hit map) on detector $a$ (left) and $b$ (right), respectively. The shadowed vertical lines correspond to the 0.35 mm spacers used to define the gap width.

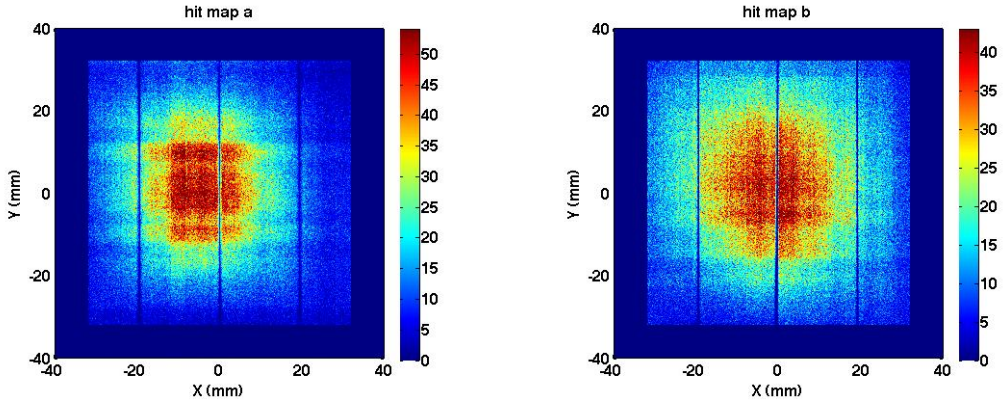


**Figure 4.13:** Hit map in a) detector $a$, and in b) detector $b$. The shadowed vertical lines correspond to the 0.35 mm spacers used to define the gap width.

#### 4.3.4.1 Advanced methods for hits position determination

In more recent runs, we had to deal with an issue that arose when we histogrammed the PC scores. As we can see from fig. 4.14, when we histogramme the PC scores, considering the events whose largest signal pertains to two or more distinct strips, the stripes do not fully overlap. As a consequence, they mix with each other, becoming

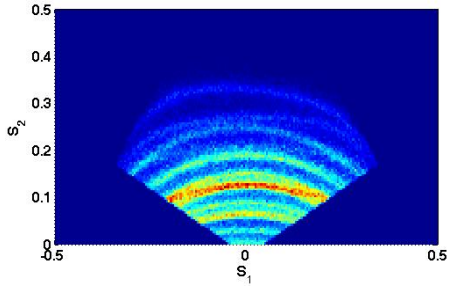


**Figure 4.14:** Overlap of the PC scores corresponding to the events with largest charge on three adjacent middle strips.

difficult to identify the gap. On the other hand, if only the events whose largest signal belongs to a given strip, are histogrammed, they present the regular pattern that we have shown before (fig. 4.10). In fig. 4.15, we see that the charge collected on the strips 7 (top left) and 16 (bottom right ) are influenced by the spacers. The histograms differ mostly on their "amplitude" $G$ (see eq. 4.2) and thus, when different classes of events are histogrammed, they do not superimpose. Consequently, the events have to be analysed on classes based on the strip with largest charge signal. Those classes

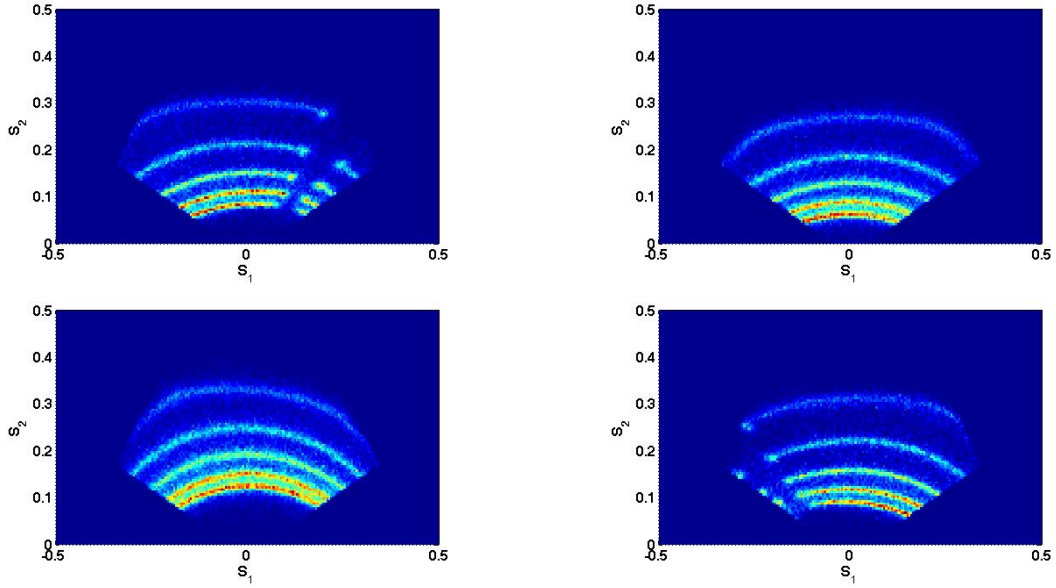


**Figure 4.15:** PC scores histograms considering the events whose largest signal pertains to strips 7 (top left), 8 (top right), 9 (bottom left), and 16 (bottom right).

can also be used to histogram the variables defined above, $U_x$ and $U_y$ (fig. 4.16, left and middle), although these quantities are less sensitive to class mixture. Just for illustration, we present the histogram of $U_x$ and $U_y$ considering all events together, mixing all strips (fig. 4.16, right).

When comparing the identified gaps from a strip-to-strip approach to an overall gap identification, considering all strips together, the differences amount to 13.6% for detector $a$ and to 3.8% for detector $b$. Actually, as shown along this chapter, we observe that detector $a$ does not exhibit a smooth behavior. A problem in strip number 10 of electrode $X$ was detected, possibly emerging from the read-out PCB electrode. This problem became evident in a first attempt of determining the position of the hits on detector $a$ (fig. 4.17, left). The position distribution of the triggered events for detector $b$ is also depicted in fig. 4.17, right.

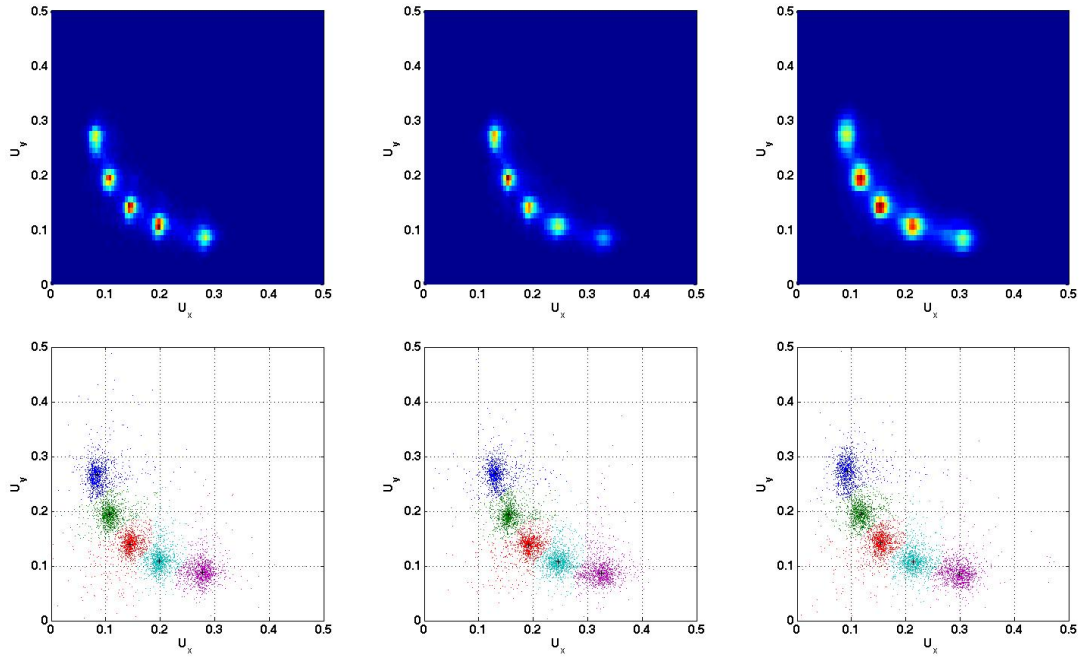


**Figure 4.16:** Histogram of the variables $U_x$ and $U_y$ and corresponding scatter plots for strips 5 (left) and 9 (middle). Right: mixed strips.

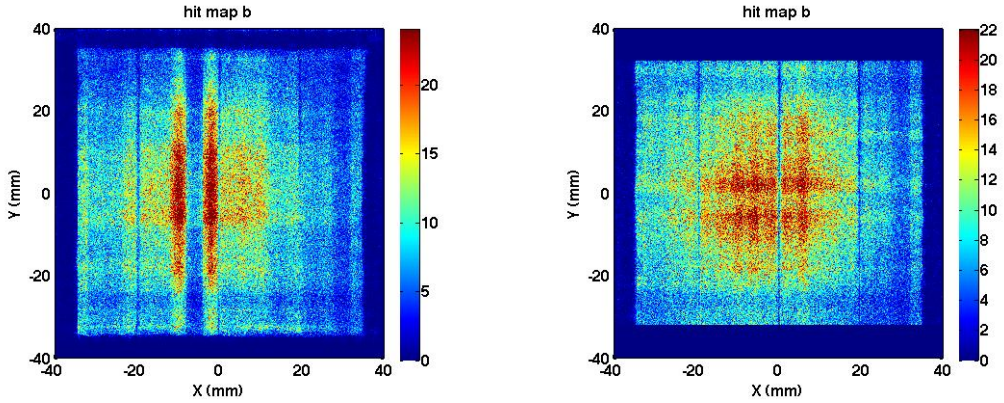


**Figure 4.17:** First attempt of a hit map in detector $a$ (left), and $b$ (right), based on the interpolation of the hits coordinates for the calculated $\alpha$ values. The data was obtained from the imaging of the needle-like source.

#### 4.3.4.2 Calculation of the induction functions

A way of converging to a fine positioning is by calculating the induction functions generated by the induced charge on the read-out strips[1]. These functions are calculated empirically, aiming to reproduce the simulated functions of fig. 4.9. We can estimate the approximated position coordinates of each event, $X_{i0}$, in the hit map (see fig. 4.17), based on the aforementioned interpolation depicted in fig. 4.12. The next step is to normalize the five largest charge signals of each event, $q_{il} = \frac{Q_{il}}{\sum_l Q_{il}}$, where $l = -2, ..., 2$, being $l = 0$ the strip with larger signal and the others, the two left and right neighboring strips . We proceed with the calculation of the induction functions for each of the five gaps, once we know in which of the five gaps the events occurred. Being the events associated to each gap, we choose, for each of them, a reasonable set of 20k events to build the induction functions. For each strip, we find the events whose maximum charge in on that strip or on its two neighboring strips. To each event with maximum charge located on one of the five strips considered, we attribute the value of the normalized charge, $q_l$, located on the symmetric strip. For each event, the induced charge, $F_{ls}$, on the strip $s = 0$ with largest charge signal and their two left and right neighboring strips, where $s = -2, ..., 2$, will correspond the normalized charge $q_l$, where $l = 2, ..., -2$. For each strip we will have an induction function $F_l$. For instance, we show the induction function corresponding to strip 11 (fig. 4.18, left). The calculated induction functions

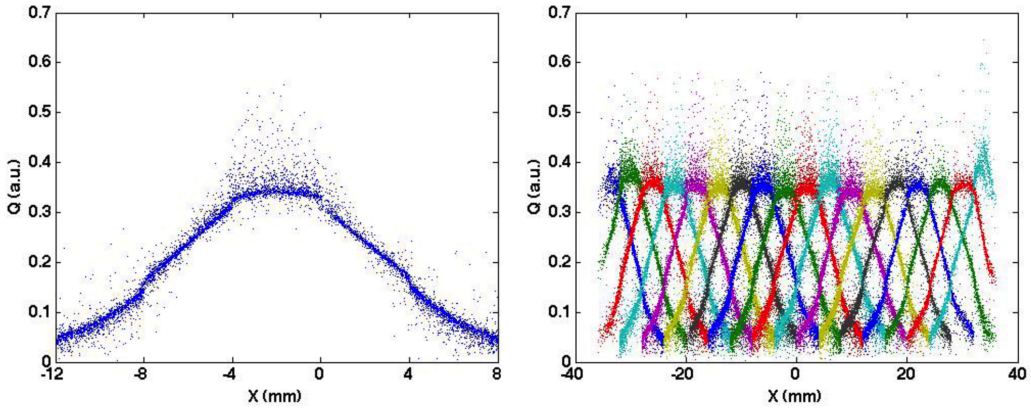


**Figure 4.18:** Left:induction function for strip 11. Right: induction functions for the 18 strips taken into account.

[1]This approach was inspired by the work of Solovov *et al.* [21].

for the 18 strips are presented in fig. 4.18, right. The 4 outer strips were left apart, because they are not all equal, and a dedicated algorithm for that specific purpose will be needed.

A polinomial of $6^{th}$ degree that fits to each of the induction functions is presented in fig. 4.19. Each fit curve is composed of 400 elements spaced by 0.05 mm comprising a range of ±10 mm from the center of each strip. At the end, we will have, for each of

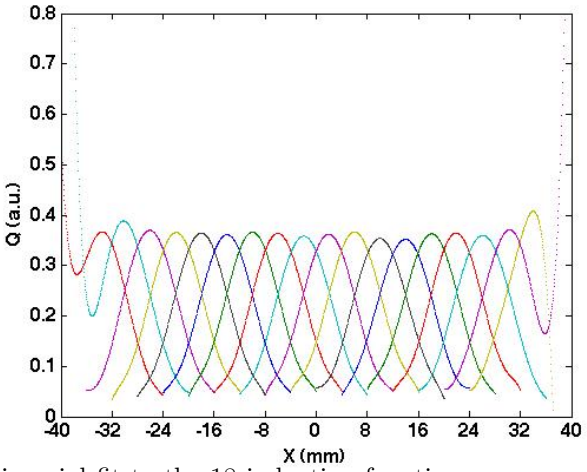


**Figure 4.19:** Polinomial fit to the 18 induction functions corresponding to the 18 strips taken into account.

the 5 gaps, a set of 1765 elements ranging from -44.1 mm to 44.1 mm, for each of the 18 induction functions.

#### 4.3.4.3 Fine positioning

To begin with, we consider data from the sample of 20k events mentioned in 4.3.4.2. To calculate the fine coordinate position of the avalanche we follow the least-squares method, an approach partially similar to the one described by Morozov *et al.* and Solovov *et al.* [20, 21]. The best solution minimizes the sum of the squares of the errors, determined by equation 4.3. For each event, the error derives from the difference between the fit to the induction functions of the 3 strips with larger signal (fig. 4.20, left) and the normalized charge of those strips, $q_l$. The most likely coordinate position of the hit for each event is obtained by minimizing the following expression:

$$v(X_i) = \sum_{l=-1}^{1} (F_{il} - q_{il})^2. \tag{4.3}$$

Fig. 4.20, right, shows a parabola whose minimum value gives the most probable position for the hit, $X_i$. The algorithm thus iterates three times, utilizing the obtained

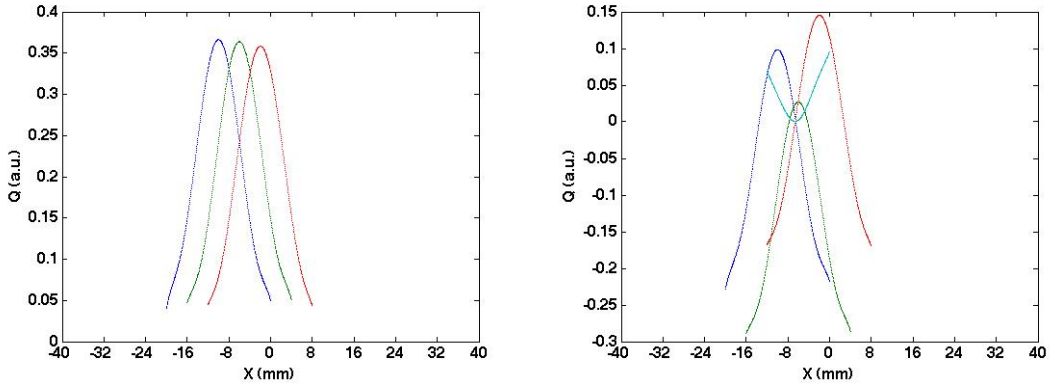


**Figure 4.20:** Left: polinomial fit to the induction functions corresponding to the 3 strips with larger charge signal, in this case, the strips 10, 11, and 12. Right: the parabola with positive concavity (cyan) represents the function $v$, whose minimum gives the most probable position for the hit.

coordinate positions to generate a new set of induction functions, in order to minimize the residuals of the least-squares fit. After the 3 iterations, the induction functions converge, as depicted in fig. 4.23, where those functions and the corresponding fits are plotted for the first 4 gaps of electrode $X$ of detector $b$.

In order to extrapolate for any data, we proceed as follows: for each event we have 3 induction functions corresponding to the 3 strips with larger signal, as depicted in 4.20, left. We apply the PCA to the induction functions, thus extracting the angle $\alpha$ between the PC scores $S_1$ and $S_2$. Then, we perform a linear interpolation to extrapolate the experimental coordinate positions, $X_p$, from all events, based on the calculated $\alpha$ values. These are obtained from the relation between $X_i$ and $\alpha_i$, variables that were obtained with the induction functions. Fig. 4.21 shows the distribution of the calculated $\alpha$ values as a function of the experimental coordinate positions, $X_p$. For each strip, there are 5 curves corresponding to the 5 gaps that allow having a precise positioning of the hit.

The position distribution of the triggered events in detector $a$ and $b$, obtained from the presented method, is depicted in fig. 4.22. They exhibit some differential non-linearity (DNL)[1]. The effect of the spacers, producing shadowed vertical lines, also

[1]Differential non-linearity is an important parameter of an ADC that quantifies its precision. It corresponds to the maximum deviation from one least significant bit (LSB) between two consecutive levels, over the entire transfer function [39].

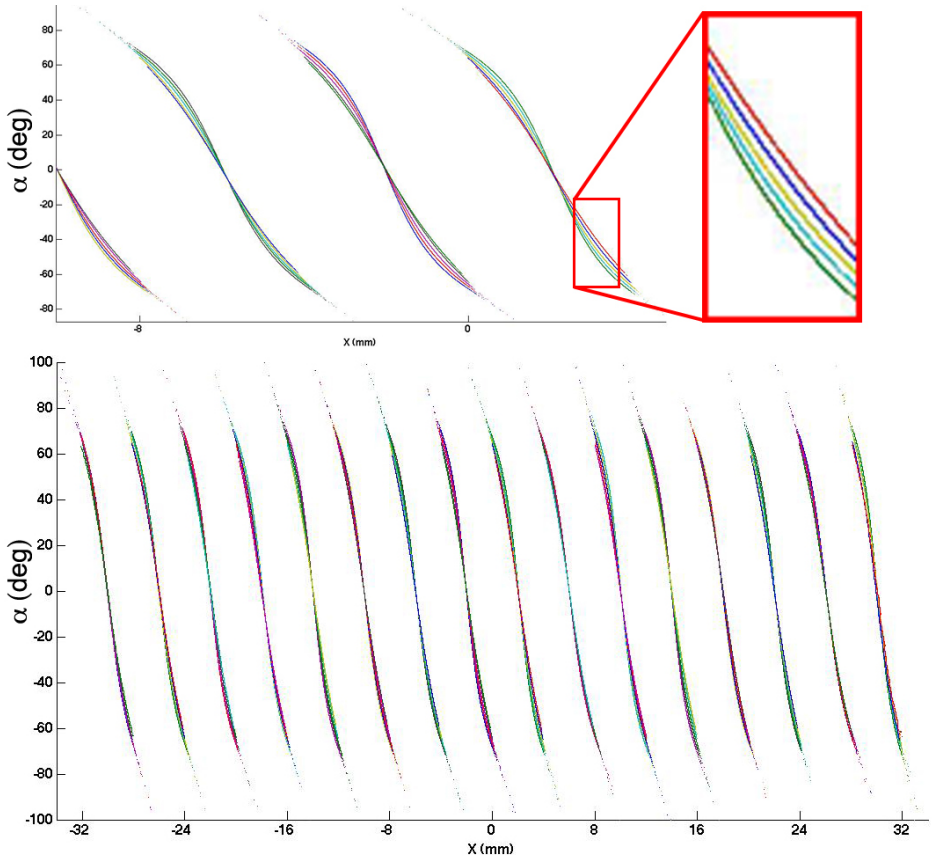


**Figure 4.21:** Relation between the calculated $\alpha$ values and the experimentally determined avalanche positions for the 18 strips (bottom). The magnified images (top) permit to distinguish the 5 gaps inside each $\alpha$ curve.

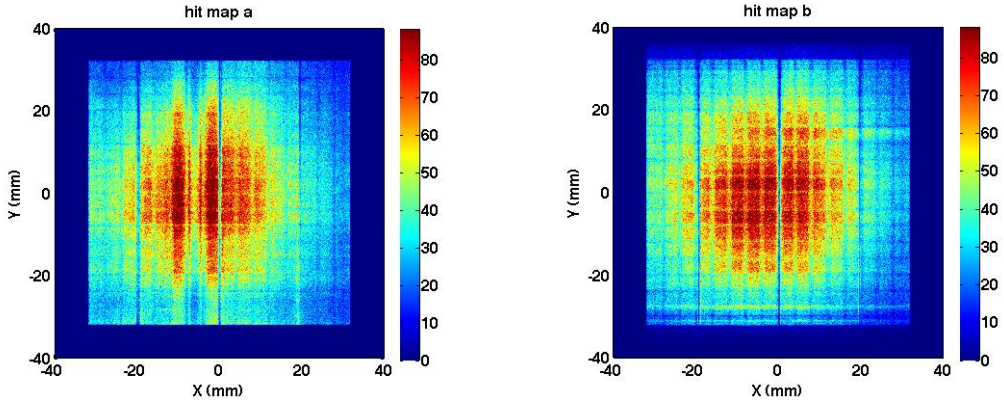


**Figure 4.22:** Hit map in detector $a$ (left), and $b$ (right), resulting from the proposed method described in this section. Some DNL appears in the $X$ and $Y$ coordinates of both detectors.

remains visible. It is clear that these images feature an improvement in comparison with fig. 4.17.

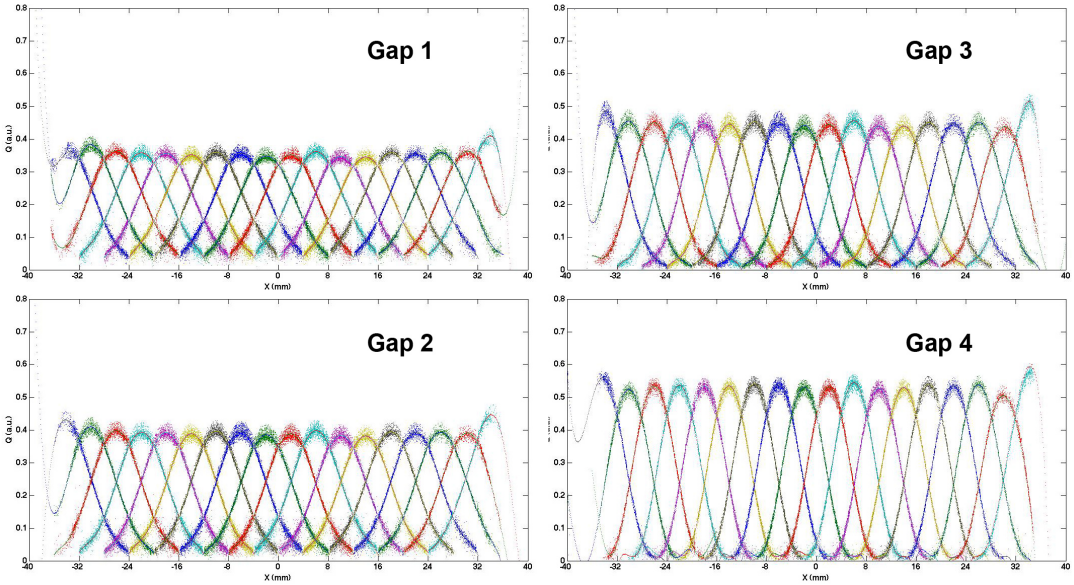


**Figure 4.23:** Induction functions and the correponding polinomial fit for the 18 strips of electrode $X$ of detector $b$.

## 4.4 Event cuts and detection features

From the imaging of the needle-like source, approximately five million events were digitally processed as valid coincidences. We take from each event the average charge collected in the channel with higher charge and their three left and right neighbouring channels from the $X$ and $Y$ electrodes of detectors $a$ and $b$. We perform charge cuts on the charge spectra to avoid very-low charge signals, highly contaminated by electronic noise. Fig. 4.24 presents the charge spectra for detectors $a$ and $b$, after performing those charge cuts. The curve in red represents the charge resolution of each detector, which is given by the charge difference in the $X$ and $Y$ electrodes of each detector. Fig. 4.25

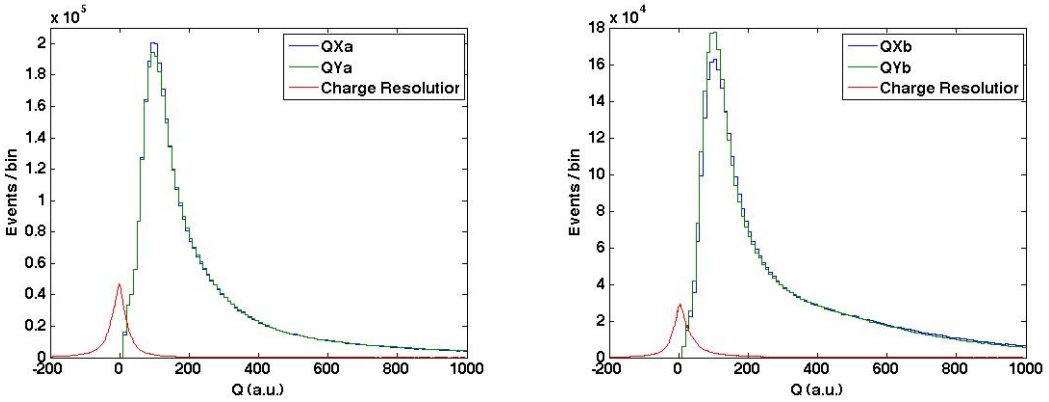


**Figure 4.24:** Charge spectra in the electrodes $X$ and $Y$ of detector $a$ (left), and $b$ (right). The spectra present a good agreement. The curve in red represents the charge resolution (on a different vertical scale). These results were obtained after charge cuts for very-low charge signals.

confirms a fairly good charge correlation between electrodes.

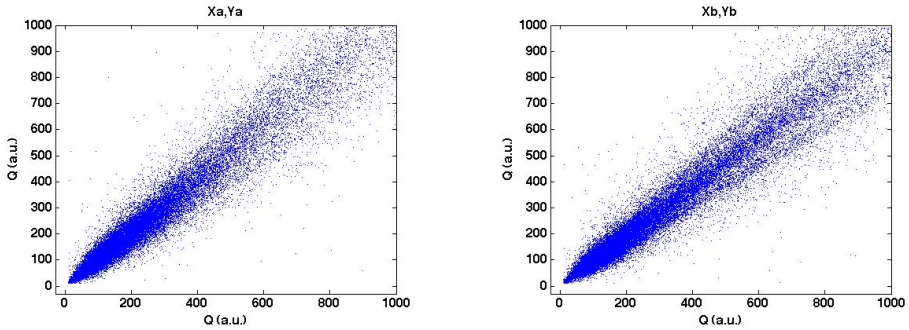


**Figure 4.25:** Charge correlation between $X$ and $Y$ electrodes of the same detector. A fairly good correlation is observed.

The fine position distribution along the $X$ and $Y$ electrodes of detectors $a$ and $b$ is shown in fig. 4.26. The lack of events on the strips of electrode $X$ next to the 0.35 mm spacers is notorious and the DNL is patent.

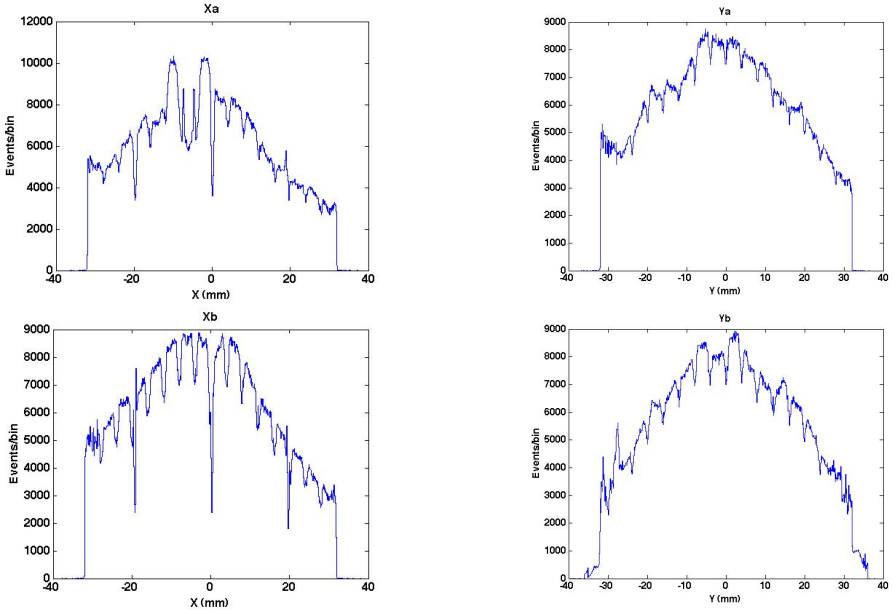


**Figure 4.26:** Position distribution of the events along $X$ and $Y$ coordinates of detectors $a$ and $b$. Both detectors exhibit some differential non-linearity as already observed before.

Fig. 4.27, left, presents the sagittal view of the needle-like source resulting from projecting on a plane perpendicular to $Z$-axis (see fig. 3.12) the intersection of that plane with the LORs emerging from the source.

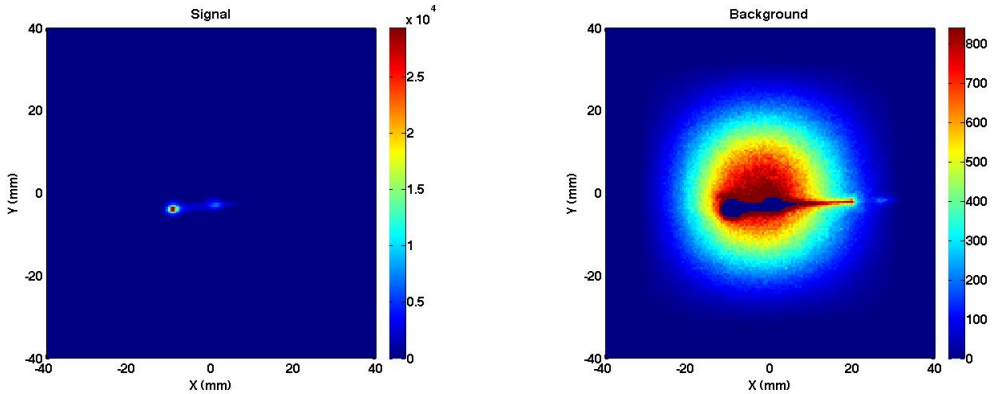


**Figure 4.27:** Sagittal view of the needle-like source, obtained by the intersection of a plane parallel to the detectors with the accepted LORs in the voxel of maximum intensity. The signal (left) represents 20% of total events, while the background (right) mops up the remaining 80%.

The remaining LORs composing the background, and mainly contaminated by the third photon (defined in section 3.5.3), are projected on the same plane, as depicted in fig. 4.27, right. The background contributes with 80% of the events, while the LORs that are part of the signal amount to 800k, and will be the ones utilized for image reconstruction.

## 4.5 Image reconstruction

### 4.5.1 Reconstruction routine

A custom-made maximum likelihood expectation-maximization (MLEM) algorithm was implemented into a reconstruction routine in order to reconstruct the data and validade the spatial resolution of the system. This routine operates on the list-mode data with a ray-driven approach for navigation in the image space. The reconstruction starts by backprojecting the data into the image space. A scan along the $Y$ and $X$ axes is accomplished with the respective coincidence line projection on the $Y_0$ and $X_0$ voxel planes. This allows identifying the voxels that were crossed by the line coincidence and extract the respective index in the image space. Each backprojected event is weighted by the number of voxels crossed by the LOR, so the sum of the total activity in the crossed voxels equals one. The MLEM algorithm forward-projects the starting backprojected image into the data space, and then compares and updates the image estimate by backprojecting the calculated projection data. The starting backprojected image is multiplied by the image estimate, whose resulting image feeds the next iteration of the MLEM algorithm. The reconstruction routine stops when the reconstructed image converges. This actually never occurs in practice, because of noise in the data. Therefore, we decided to stop the algorithm when the root mean squared error (RMSE) reaches a minimum. An ordered subsets expectation-maximization (OSEM) algorithm has also been implemented, which can be used for large data sets, once it converges faster than MLEM. The routine is fully parallelizable and a comparison between the speed of a reconstruction utilizing a single-thread CPU and a 16-threads CPU will be presented. Efforts to convert the code to the CUDA language, in order to run in GPUs, will be accomplished in a near future. A MLEM-based reconstruction developed in MATLAB code has also been implemented for the sake of comparison and validation, and the resulting images will be presented in coming sections.

### 4.5.2 Reconstruction of simulated data

A Monte-Carlo simulation based on MATLAB code has been developed to validate the reconstruction routine. This code has been adapted from another one[1] which performs a Monte Carlo (MC) calculation of the solid angle subtended by a target circular area at a source circular area. The adapted code is able to provide the LORs emitted by a three-dimensional (3D) simulated phantom which interact with two parallel planes placed at equal distance from the phantom. This simulation intends to reproduce the developed experimental setup. Consequently, we defined two phantoms, a cylinder with a diamater of 0.25 mm and 1 mm long, reproducing the needle-like source, and a cylinder with a diameter of 2 mm and 0.4 mm thick, reproducing the disk source. The $80 \times 80$ mm$^2$ square planes were set at a distance of 20 mm from the phantoms.

First, we give some introductory considerations about the geometrical features of the simulation. The requirement for an isotropic distribution is

$$\frac{dN}{d\Omega} = \frac{dN}{sin(\theta)d\theta d\varphi} = \frac{dN}{d(cos(\theta))d\varphi} = constant. \tag{4.4}$$

This distribution is generated from the inverse cumulative distribution $\mathbb{F} = arccos(\mathbb{U})$, where $\mathbb{U}$ is a random variable sampled in the interval [-1,1] and $\mathbb{F}$ is a random variable with a distribution $f(\theta) \propto sin(\theta)$. Two random probabilities, $P_i,\ i = 1, 2,\ 0 \leq P_i \leq 1$, are used to generate the isotropic distribution:

$$\theta = arccos(2P_1 - 1), \tag{4.5}$$

$$\varphi = P_2 \times 2\pi \tag{4.6}$$

The polar angle covers from 0 to $\pi$ and the azimuthal angle covers from 0 to $2\pi$, as shown in fig. 4.28. The $\theta$ distribution, as expected, is sinus distributed. The algorithm was validated by standard methods.

For the needle-like phantom we generated 1 million annihilations, out of which approximately 600k events were detected. For the disk-shaped phantom, due its larger size, 5 million annihilations were generated, being detected approximately 2.9M events. Fig. 4.29 shows the hit map in one of the detectors for both simulated phantoms. A 3D visualization of a sample of LORs emitted by the needle-like phantom is displayed in fig. 4.30.

[1] Kindly provided by M.Sc. Luís Pereira.

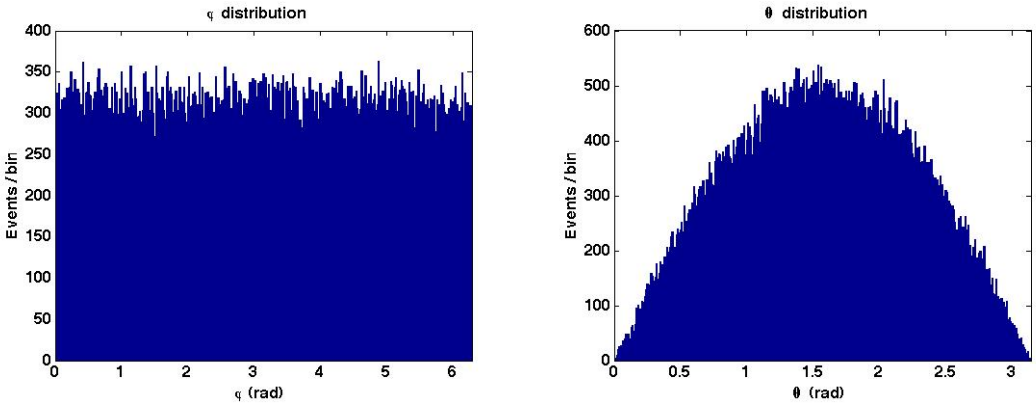


**Figure 4.28:** Azimuthal (left) and polar (right) angle distributions. The $\theta$ distribution is sinus distributed.

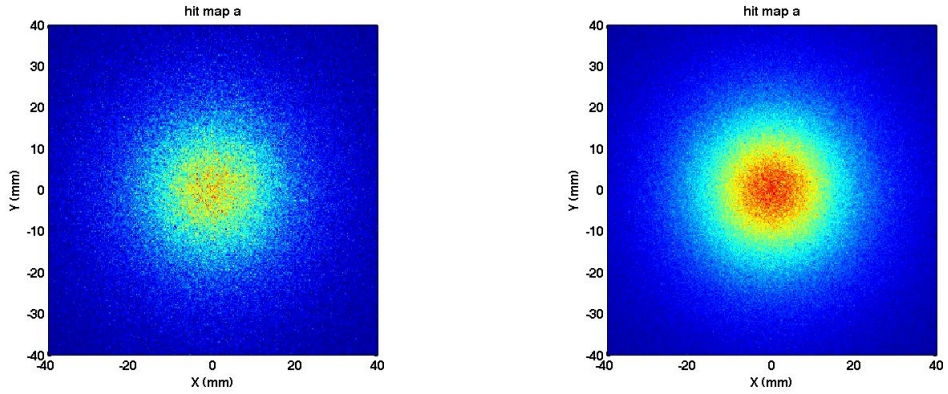


**Figure 4.29:** Position distribution of simulated events emitted by a needle-like phantom (left) and a disk-shaped phantom (right). Right image has more events concentrated at the center due to the larger statistics.

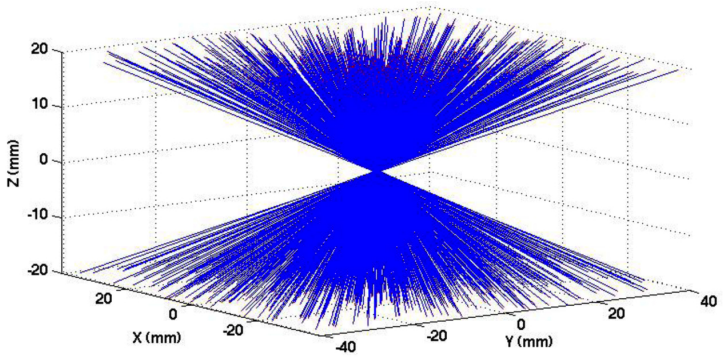


**Figure 4.30:** Simulated LORs sample emitted by the needle-like phantom.

Fig. 4.31 presents the RMSE evolution for the MLEM reconstruction along 200 iterations for the needle-like phantom and along 500 iterations for the disk-shaped phantom. The RMSE was calculated between the original annihilation points image and the reconstructed image. Concerning the needle-like phantom, RMSE reaches a minimum at iteration 46, diverging afterwards, as expected for a MLEM-based reconstruction. For the disk-shaped phantom, the RMSE behavior is similar, although the convergence is slower, reaching a minimum just at iteration 297. The reconstructed images presented hereafter correspond to the MLEM iteration which minimizes the RMSE.

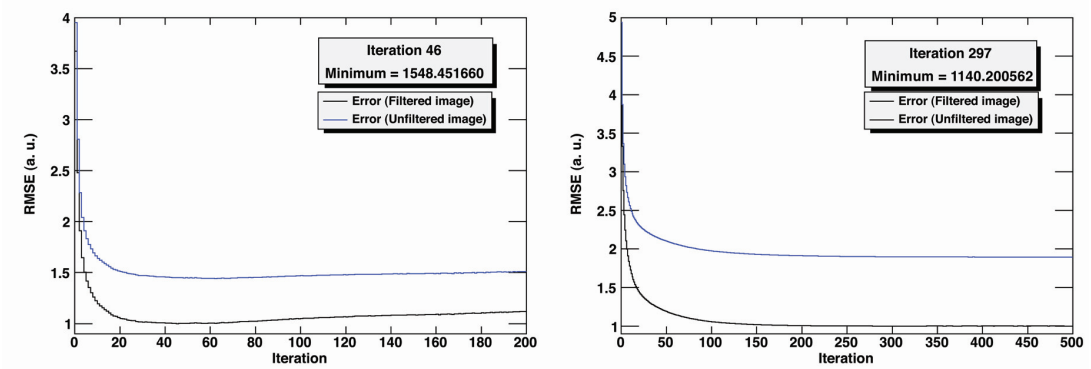


**Figure 4.31:** Graph of the evolution of the RMSE of the reconstructed images of the simulated needle-like (left) and disk-shaped (right) phantoms.

Fig. 4.32 shows the sagittal and axial views of the image of the needle-like phantom obtained from the annihilation points, before and after applying a median filter. It illustrates the influence of the median filter on the reduction of the "salt-and-pepper" noise, as well as the effect of rounding the edges, which results from the lack of activity in the surrounding voxels. These images serve as an appropriate basis for comparison with the reconstructed ones.

Figs. 4.33 and 4.34 show the reconstructed images of the simulated data, resulting from the imaging of the needle-like phantom and the disk-shaped phantom, respectively.

A 3D representation (isosurface along the $50^{th}$ percentile) of the reconstructed images of simulated data is depicted in fig. 4.35. A comparison with the original annihilation points image, before and after passing the median filter, validate the reliability of the reconstruction algorithm. It is perceptible that the median filter rounds the edges, although it plays a crucial role in the stabilization of the reconstruction routine.

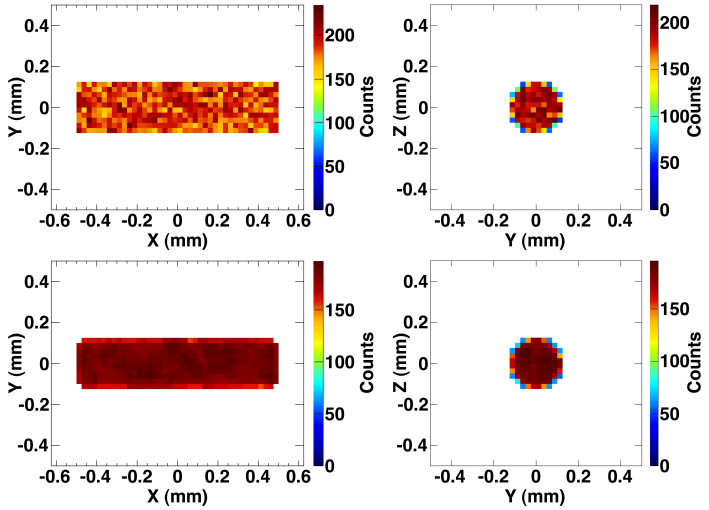


**Figure 4.32:** Sagittal (left) and axial (right) views of the images of the needle-like source containing the original annihilation points, before (top) and after (bottom) passing through a median filter.

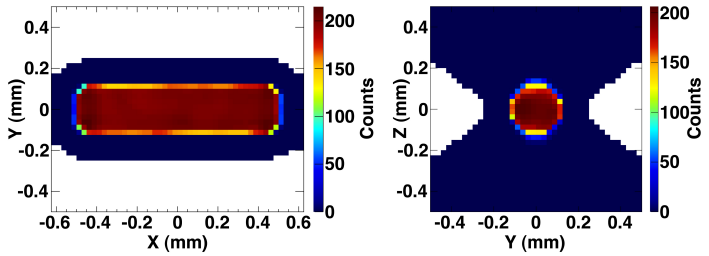


**Figure 4.33:** Results of the MLEM reconstruction applied to the simulated data of the needle-like phantom. Sagittal (left) and axial (right) views correspond to 25 $\mu$m thick slices.

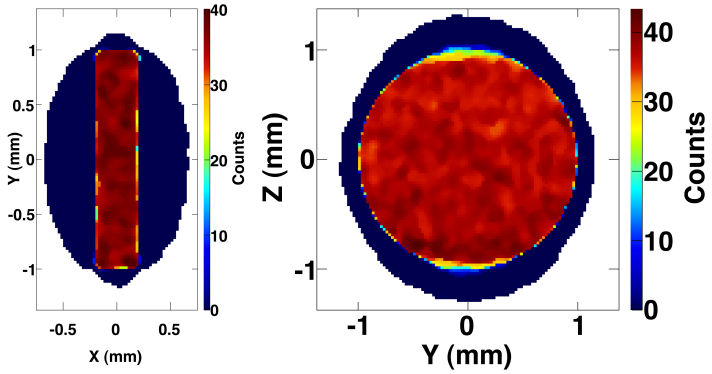


**Figure 4.34:** Results of the MLEM reconstruction applied to the simulated data of the disk-shaped phantom. Sagittal (left) and axial (right) views correspond to 25 $\mu$m thick slices.

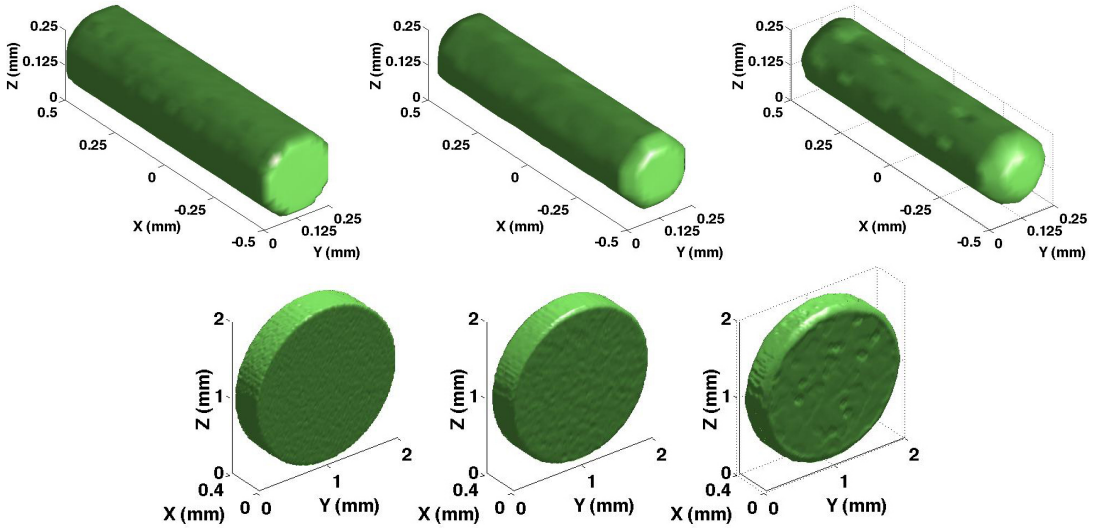


**Figure 4.35:** 3D representation of the reconstructed images of simulated data of the needle-like phantom (top right) and the disk-shaped phantom (bottom right). The corresponding original annihilation points, before (left) and after (middle) passing through the median filter, are also represented for the sake of comparison.

### 4.5.3 Reconstruction of experimental data

Since our first tests, several runs have been taken to study and improve spatial resolution and produce reliable reconstructed images. We will focus in three main runs, which correspond to the imaging of three different sources.

In the first run, a low-activity disk-shaped source ($\sim 5$ $\mu$Ci) was imaged for a long time. Five million events were digitally processed as valid coincidences. The charge cuts left 3 million events to be analysed and reconstructed by a MLEM-based algorithm. Fig. 4.36 presents the RMSE between images of two consecutive iterations. The image stabilizes with increasing iteration number, diverging from iteration 146 onwards, as expected for a MLEM-based reconstruction. The three views of the reconstructed disk-shaped source at iteration 10 for the full area, covering all LOR angles, are presented in fig. 4.37. A 3D representation of the reconstructed disk-shaped source is shown in fig. 4.38. This run was taken using detectors epoxied with $SEMITRON^{®}$, whose construction was described in chapter 3.

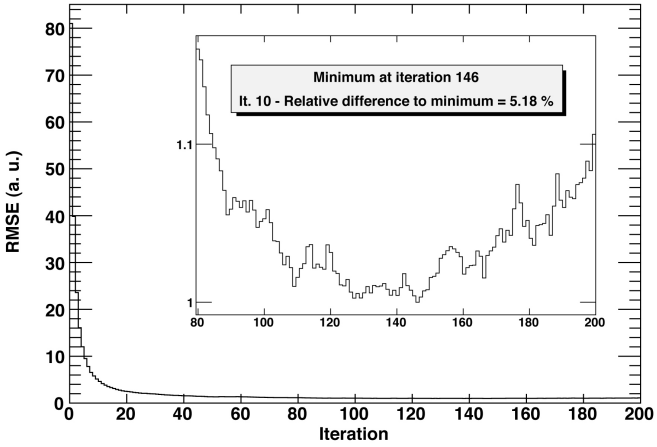


**Figure 4.36:** Evolution of the RMSE between two consecutive images along 200 iterations.

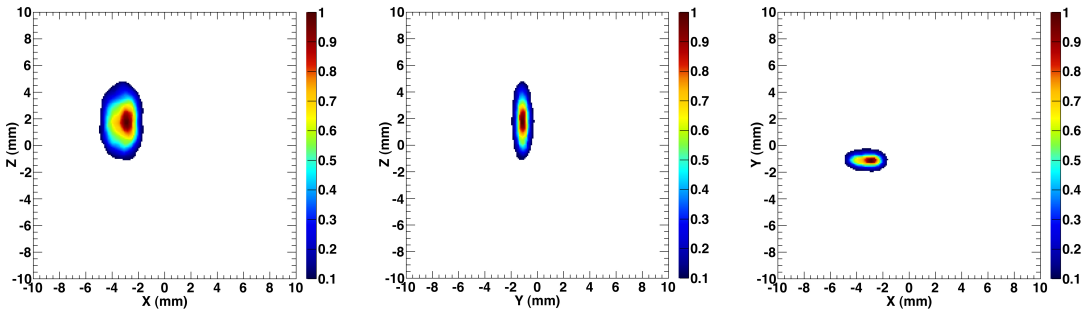


**Figure 4.37:** Reconstructed views of the disk-shaped source. All views correspond to 100$\mu$m thick slices. The disk shape of the source is confirmed by the three views.

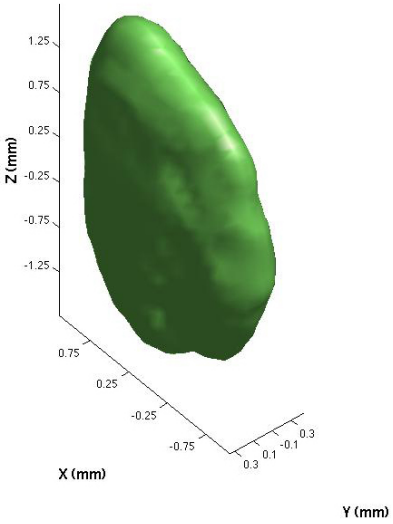


**Figure 4.38:** Three-dimensional representation of the disk-shaped source showing the isosurface along the 50th percentile.

To improve the image resolution, detectors painted with resistive ink have been utilized with the cathode surface of both detectors placed on the source side. Meanwhile, the trigger rate was largely increased and the digital pulse processing was upgraded (see section 4.2.2) to become capable of filtering the noise more efficiently. As mentioned in section 4.3.4.1, the software analysis tools were also improved to give a more precise hit positioning. Fig. 4.39 shows the reconstructed images obtained from the custom-made needle-like source, with the aforementioned upgrades implemented.

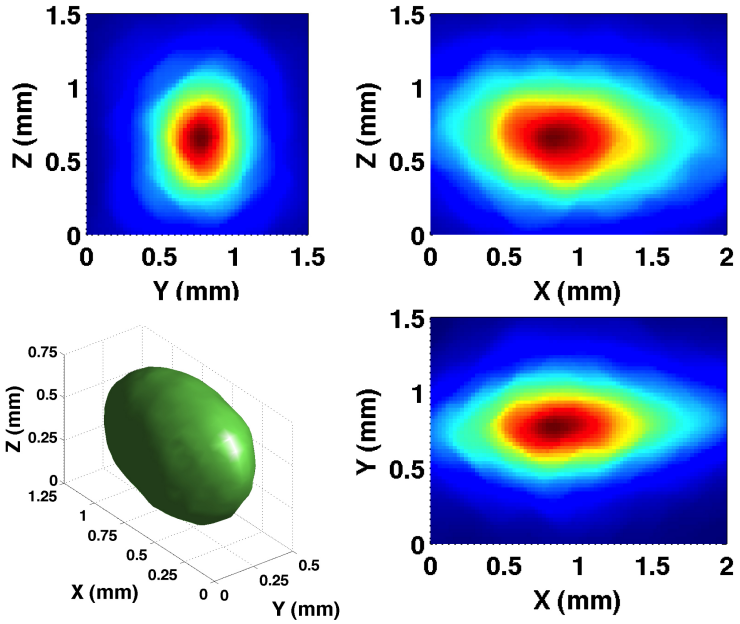


**Figure 4.39:** Results of the MLEM reconstruction applied to the experimental data obtained from the needle-like source. The three cuts along the reconstructed image pass through the point of maximum intensity. A 3D representation (isosurface along the 50th percentile) of the reconstructed needle-like source is also presented.

From the 4.8 million events that were digitally processed as valid coincidences, the vast majority corresponded to background, leaving only approximately 773k events for the reconstruction. Cuts for very-low charge signals and on the events with unidentified gaps were also applied.

A second run consisted on moving the source by 1 mm in order to prove that the system is able to distinguish two close-by source positions, demonstrating sub-millimeter resolution. A visual analysis of the reconstructed images of the data of the two combined source positions (see fig. 4.40) allows us to conclude that the spatial resolution of the system is well below 1 mm.

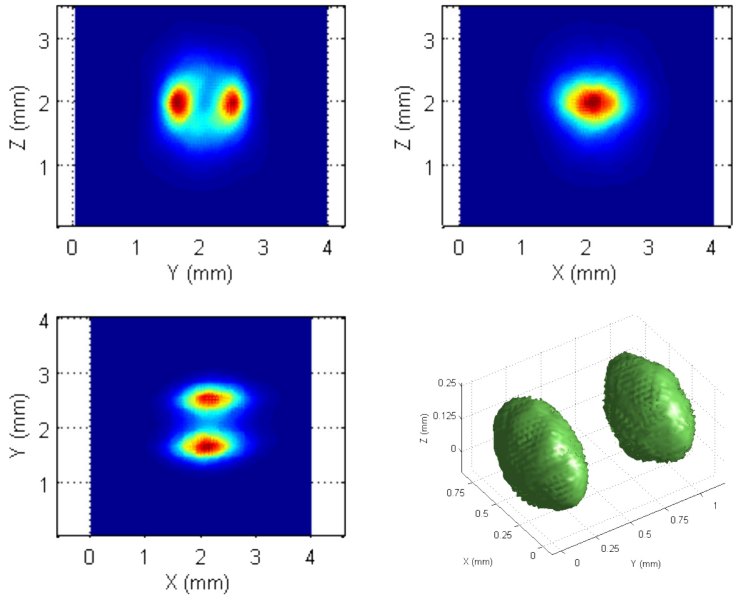


**Figure 4.40:** Reconstructed images from the needle-like source in two different positions, 1 mm appart.

From a comparison with the images from MLEM reconstruction of the data without the DOI information (fig. 4.41), we observe that there is a distortion of the shape of the source in the $Z$ direction, despite the small influence on the other coordinates.

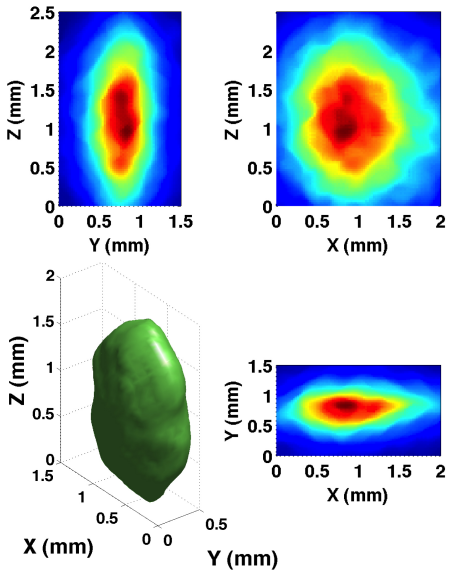


**Figure 4.41:** Reconstructed images obtained from the needle-like source without DOI information.

Finally, a very long run of approximately one month was taken. It permitted to image the planar source, which had an activity of approximately 44 $\mu$Ci. The experimental setup was similar to the one utilized for the needle-like source. Nevertheless, automatic self-consistant routines were created to decode and process the data without human intervention. In that way, we succeeded in acquiring 250 million coincidences during this period. These data were subsequently analysed. Like in the previous run, cuts on the low-charge signals and on the events with unidentified gaps were performed and the background was removed. At the end, we ended-up with 23 million events to be reconstructed. Figs. 4.42, left and right, show the corresponding reconstructed images with voxel sizes of $25 \times 25 \times 25$ $\mu$m$^3$ and $50 \times 50 \times 50$ $\mu$m$^3$, respectively. The

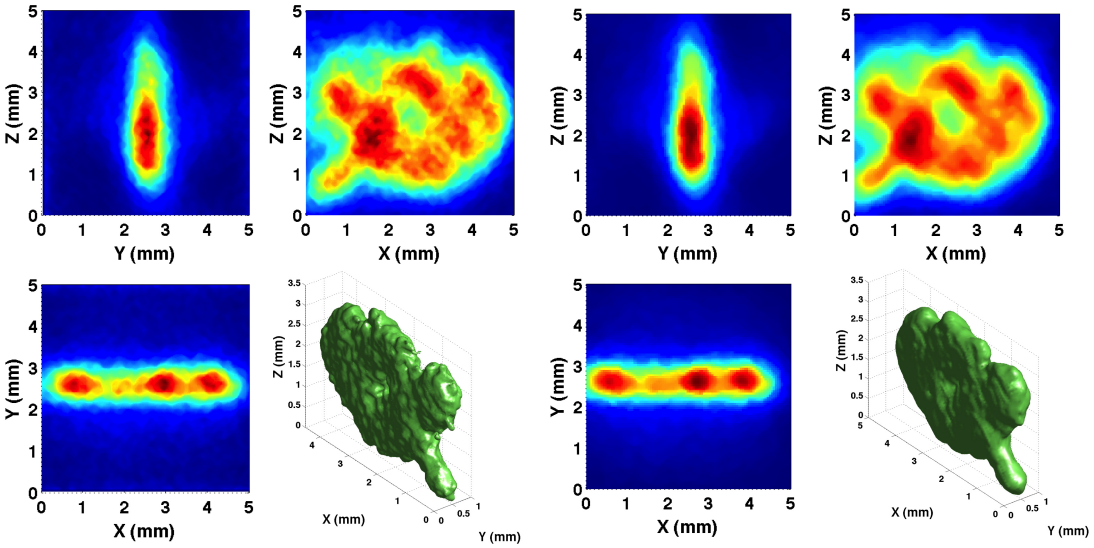


**Figure 4.42:** Reconstructed images obtained from the planar source. The left and right images have voxels of $25 \times 25 \times 25$ $\mu$m$^3$ and $50 \times 50 \times 50$ $\mu$m$^3$, respectively.

voxel size seems to have an influence on the spatial resolution, as pointed out by Thoen *et al.* [80], despite the increasing image noise due to the reduced statistics. Since we reduced the voxel size by a factor 8, we should have an increase in the same proportion on the number of reconstructed events, which was not the case.

As mentioned before, we are still dealing with the differential non-linearity on the position distribution of the hits, since it seems to have a strong influence on the spatial resolution. Consequently, we performed a cut, accepting just the events whose distance to the center of the strips in the $Y$ electrode was below 1 mm. The reconstructed images of such events are shown in fig. 4.43. We observe a change in the shape of the

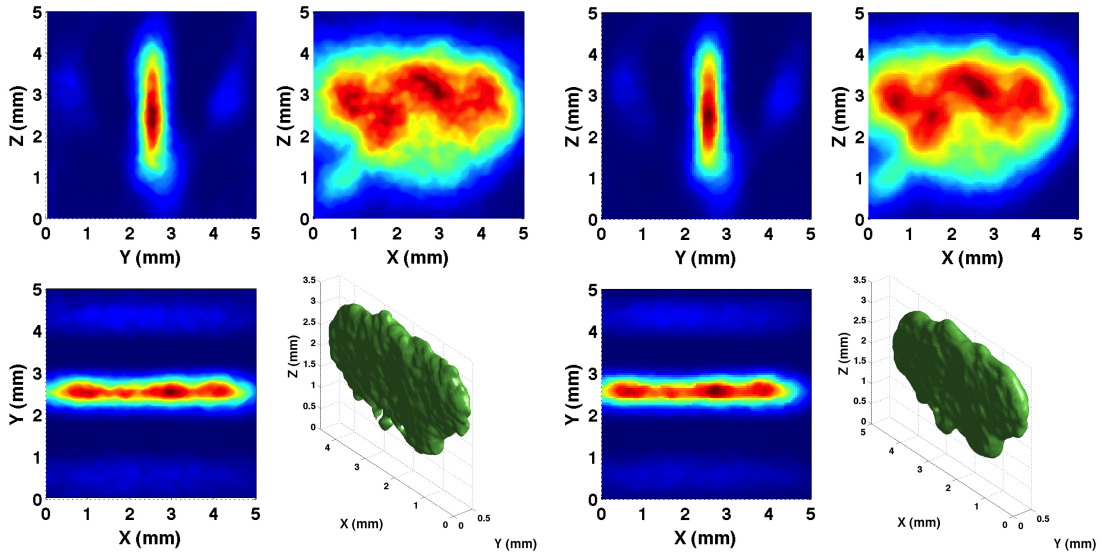


**Figure 4.43:** Results of the MLEM reconstruction applied to the experimental data obtained from the planar source. These data was restricted to the hits whose distance to the closest strip center was inferior to 1 mm. The left and right images have voxels of $25 \times 25 \times 25$ $\mu$m$^3$ and $50 \times 50 \times 50$ $\mu$m$^3$, respectively.

hottest regions of the image, which becomes more concentrated, while the general shape is preserved. The thickness of the source in the $Y$ direction is reduced, suggesting a possible improvement of the spatial resolution of the system with the solution of the differential non-linearity issue.

Since it was impossible to move the source inside the aluminium box container, we obtained the planar source positions, depicted in fig. 4.44, by mathematically displacing half of the available LORs 1 mm along the $Y$ coordinate. Once again, it is possible to distinguish the two source positions in the respective images. Although noisier, those obtained with a reconstruction binning of 25 $\mu$m seem to provide a better spatial resolution.

In what concerns the convergence speed of the reconstruction algorithm, a comparison was made between the speed of the routine running on a single-thread CPU and a fully parallelized code, supporting the capability of 16-threads CPUs to reconstruct large data sets. A speed test was performed, comparing the reconstruction time of 23 million events acquired with the planar source of 44 $\mu$Ci. The parallelized code allows each processor to reconstruct a chunk of data, producing several images, which are summed at the end of each iteration. Since we utilize a median filter to stabilize the

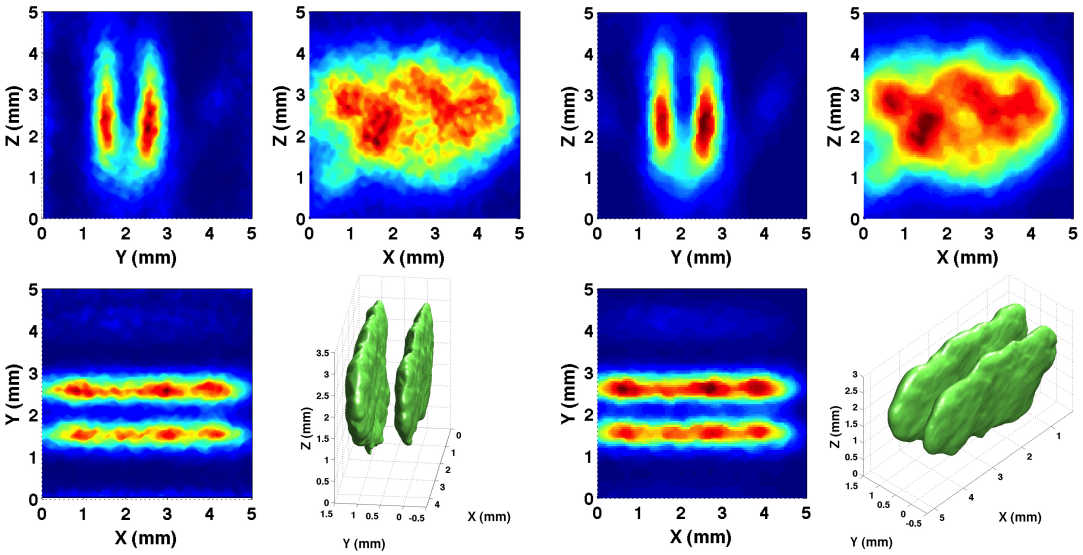


**Figure 4.44:** Results of the MLEM reconstruction applied to the experimental data obtained from the planar source in two different positions mathematically separated by 1 mm. The left and right images have a voxel size of $25 \times 25 \times 25$ $\mu$m$^3$ and $50 \times 50 \times 50$ $\mu$m$^3$, respectively.

routine and remove "salt-and-pepper noise", the bigger the image is, the slower the routine becomes, setting a bottle-neck on the reconstruction speed. A way of increasing the speed consists of dividing the image in 16 different images, and applying the median filter to each of them on each of the 16-CPU cores. The parallelization of the code achieved a reconstructed image after 20 iterations in 16 minutes, against the 47 minutes needed by a single-thread CPU, thus representing an improvement by a factor 3 in image convergence speed. Although not perfectly equal, the images obtained from a parallelized code and a single-thread code are virtually identical in view of floating point issues.

## 4.6 Spatial resolution

One of the main goals of this work was to determine the spatial resolution of the small-animal RPC-PET system. In this section, we present values of the spatial resolution full width at half maximum (FWHM) for all the three imaged sources. Fig. 4.45, right, shows the parallel profiles taken along the $Y$ coordinate in the sagittal $(X - Y)$ and axial $(Y - Z)$ views of the reconstructed image resulting from the imaging of the disk-

shaped source with an activity of ∼5 $\mu$Ci. We chose the image corresponding to the iteration 146 (see fig. 4.36). The 18 profiles in the sagittal view and the 27 profiles in the axial view demonstrate an average spatial resolution of 0.8 mm FWHM. The upper value of 808 $\mu$m (mentioned in fig. 4.36, right top) is the FWHM of the average profile, while the value of 797 $\mu$m (right) represents the average of the FWHM values for each profile. The average profile is represented by a black dashed curve superimposed on the 45 profiles.

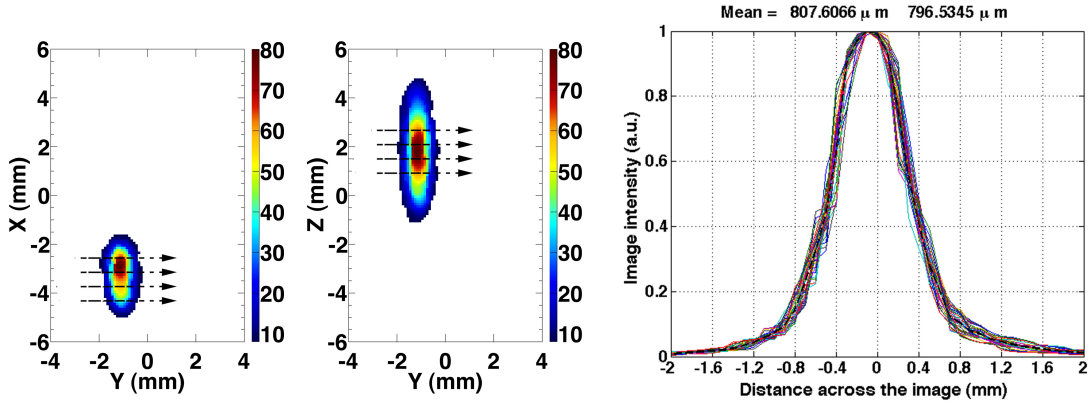


**Figure 4.45:** The profiles taken along the Y coordinate on the sagittal and axial view of the reconstructed image of the disk-shaped source, at iteration 146, demonstrated an average spatial resolution of 0.8 mm FWHM.

The chosen planes (sagittal, axial, and coronal) to take the profiles are the ones that cross the maximum intensity voxel. From now on, in what concerns experimental results from the imaging of disk-shaped or planar sources, this method will be adopted to extract the spatial resolution along the $Y$ coordinate. In regard to the experimental results of the imaging of the needle-like source, the profiles along the $Y$ coordinate are taken perpendicular to the coronal $(X - Z)$ plane that crosses the maximum intensity voxel. The considered profiles include the one that crosses the maximum intensity voxel and the ones crossing the surrounding 8 voxels in that plane.

To validate this method, we deduced the FWHM of the profiles taken along the $X$ coordinate for the reconstructed images of the simulated disk-shaped phantom and along the $Y$ and $Z$ coordinates for the reconstructed images of the needle-like phantom. We chose, for both cases, the images corresponding to the iterations that minimize the RMSE curves, depicted in fig. 4.31. The profiles taken along the $X$ and $Y$ coordinates of the disk-shaped and needle-like phantom images (figs. 4.33 and 4.34), respectively,

are depicted in fig. 4.46, left and middle. They agree with the diameter of the needle and with the thickness of the disk. The profile taken along the $Z$ coordinate of the needle-like image (fig. 4.46, right) has longer tails, a geometrical effect that results from the perpendicularity between the plane of the detectors and the $Z$ direction. We will show in the next section that this effect becomes more prominent with increasing distance between detectors, i.e., smaller LOR angles.

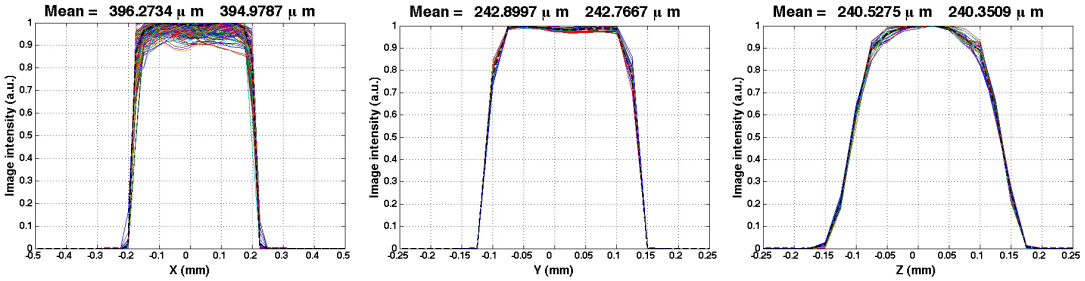


**Figure 4.46:** Profiles taken along the $X$ coordinate for the simulated disk-shaped phantom (left), and along the $Y$ (middle) and $Z$ coordinate for the simulated needle-like phantom.

The following profiles, taken along the images obtained from experimental data, correspond to the iteration that minimizes the FWHM. The curves of the evolution of the FWHM with increasing iterations are also displayed.

We see from fig. 4.47 that for the imaging of the needle-like source (fig. 4.39), a minimum value of 0.42 mm FWHM of the average profile taken along the $Y$ coordinate is reached at iteration 4 with a voxel binning of 25$\mu$m. For a voxel binning of 50 $\mu$m, the results are slightly worse, showing 0.5 mm FWHM. The average profile taken along the $Z$ coordinate exhibit 0.54 mm FWHM.

Concerning the reconstructed images without DOI information (fig. 4.41), the image noise affects the profiles, contributing also to a wider FWHM (fig. 4.48). The profiles taken along the $Z$ coordinate are especially affected (parallax error).

The profiles taken along the $Y$ coordinate in the sagittal and axial views of the reconstructed image of the planar source (fig. 4.42) are shown in fig. 4.49. The curves of the evolution of the FWHM along 20 iterations are also displayed. The FWHM of the average profile is 0.84 mm and 0.86 mm (fig. 4.49, top left and right), considering a voxel binning of 25 $\mu$m and 50 $\mu$m, respectively. These values are strongly affected by the differential non-linearity effect. As we can see in fig. 4.49, bottom left and right, if we just accept the events that hit the detectors at a distance inferior to 1 mm to

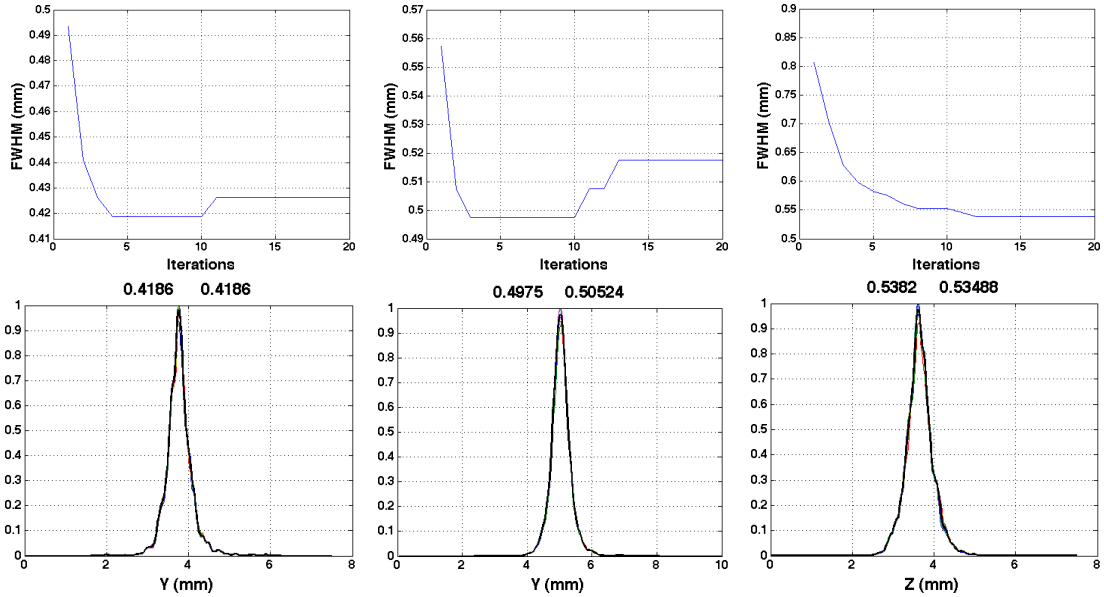


**Figure 4.47:** Line profiles through the point of maximum intensity in the images of the needle-like source (bottom). The images were reconstructed with a voxel binning of: 25 $\mu$m (left); 50 $\mu$m (middle); 25 $\mu$m (right). The evolution of the FWHM along 20 iterations is also shown (top).

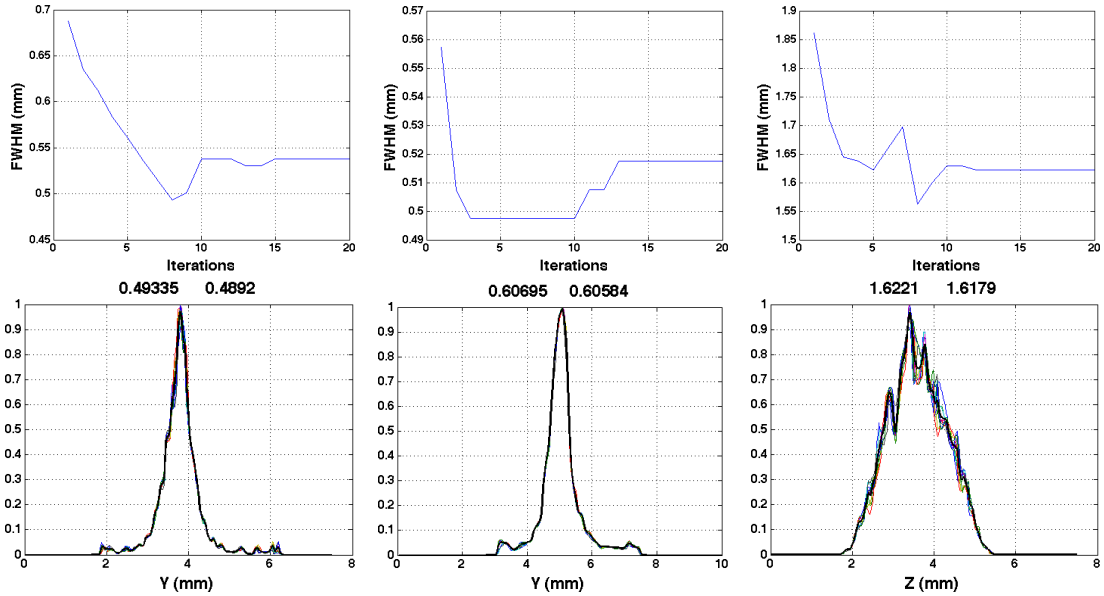


**Figure 4.48:** Line profiles through the point of maximum intensity in the images of the needle-like source without DOI information. The images were reconstructed with a voxel binning of: 25 $\mu$m (left); 50 $\mu$m (middle); 25 $\mu$m (right). The evolution of the FWHM along 20 iterations is also shown (top).

the closest strip center, the FWHM of the average profile has a substantial decrease to 0.49 mm and 0.56 mm, considering a voxel binning of 25 $\mu$m and 50 $\mu$m, respectively.

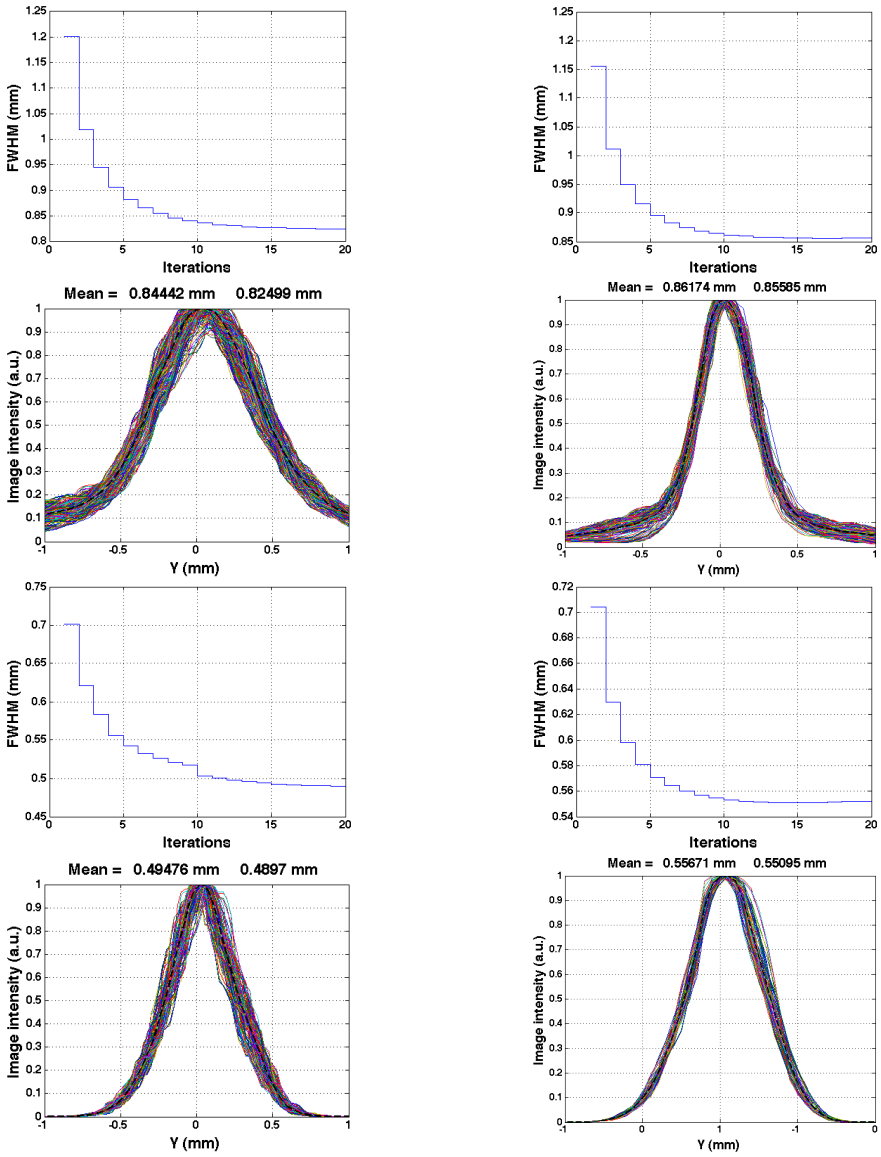


**Figure 4.49:** Curve of the evolution of the FWHM of the average profile taken along the $Y$ coordinate in the sagittal and axial views of the reconstructed image of the planar source (top). We used a voxel binning of 25 $\mu$m (left) and 50 $\mu$m (right) to reconstruct the images. A cut on the position of the hits was considered to overcome the differential non-linearity contribution to the FWHM (bottom).

Finally, in fig. 4.50, we present the activity profiles along the $Y$ coordinate through the maximum intensity voxel of the images depicted in figs. 4.40 and 4.44. The signal

was subtracted from background and the obtained profiles exhibit a 0.4 and 0.5 FWHM spatial resolution for the needle-like and planar sources, respectively.

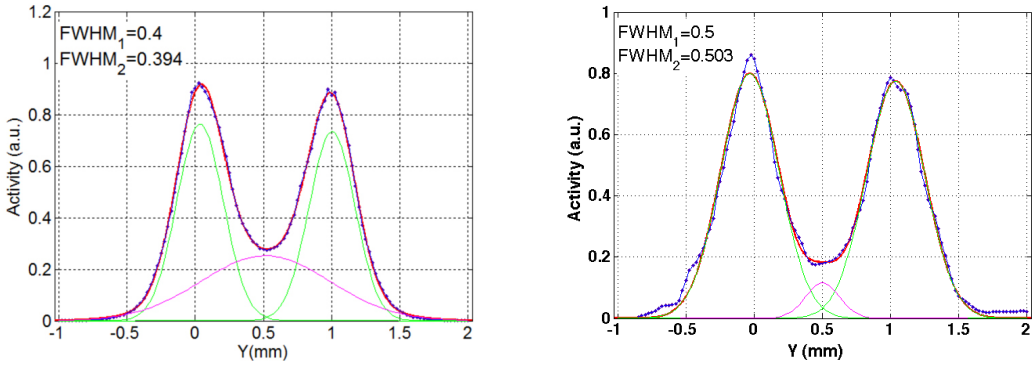


**Figure 4.50:** Activity profiles along the $Y$ coordinate through the maximum intensity voxel. The signal (blue) was subtracted from background (magenta) and the obtained profiles (green) exhibit a 0.4 and 0.5 FWHM spatial resolution for the needle-like (left) and planar (right) sources, respectively. Note that the needle-like source was effectively displaced by 1 mm, whereas the planar source was just mathematically moved by the same amount.

## 4.7 Annihilation photons non-collinearity

We proposed to investigate the contribution of the non-collinearity effect to the spatial resolution of the system. Therefore, we prepared the experiment to image a source with two detectors, parallel, aligned, and placed 4 cm apart and with other two detectors, also parallel and aligned with the first, but placed 45 cm apart. Concerning the closer detectors, the results have been presented so far, yielding a spatial resolution of 0.4 mm FWHM for the needle-like source and 0.5 mm FWHM for the planar source. In this section, we will present the results from the Monte-Carlo simulations of detectors separated by 0.5 m, with and without the contribution of non-collinearity. Then, experimental results will be presented and compared with the latter.

As stated before, it is commonly accepted that the non-collinearity effect on the annihilation photons degrades the spatial resolution. This results from the fact that the annihilation photons are not emitted in exactly collinear opposite directions (see section 2.2.2). According to DeBenedetti *et al.* [60], there is a gaussian distribution of non-collinearity around the polar angle $\theta$, centered in 180°, and with a FWHM of

approximately 0.5° ($\sigma = 37$ mrad). The photon non-collinearity contribution has been included in a simulation software widely used by medical physicists, GEANT4 application for tomographic emission (GATE)[1] [315]. The simulation of the contribution of non-collinearity effect to the spatial resolution of a human wide AFOV RPC-PET system has been studied by Couceiro [73]. From his simulation results and from ours, we observe that the obtained image PSF is far from being Gaussian shaped. The full width at tenth maximum (FWTM) is strongly affected, but the FWHM is well below the expected value of 1.1 mm for a 0.5 m diameter scanner[2]. Several authors have observed a Gaussian blurring in the planar distribution associated to the angular uncertainty in the emitted annihilation photons [58, 60]. We will also present our results for sake of comparison and validation of the theory. Because GATE simulations point out for a non-Gaussian PSF, two questions may arise: (i) the polar angular uncertainty is effectively Gaussian, as assumed by GATE, and has little impact in the image spatial resolution (FWHM); therefore, the experiments have not yet been sufficiently accurate to isolate the non-collinearity effect from other contributions; (ii) the experiments measured correctly the non-collinearity effect, but the polar angular uncertainty may not be Gaussian and should be modeled with a different function.

### 4.7.1 Simulation results

We simulated 50 million events corresponding to the photons emitted by a needle-like phantom with a diameter of 0.25 mm and a length of 1 cm. From the original events, approximately 800 k events hit the detectors with an area of $80 \times 80$ mm$^2$ and both separated from the phantom by 25 cm. Fig. 4.51 shows the coronal, axial and sagittal views, and the 3D representation of the reconstructed image, at iteration 2, 6 and 100. We see, from the profiles taken on the sagittal view (fig. 4.52) that the FWHM starts diverging with increasing iterations, with an initial value of approximately 200 $\mu$m, and from the $6^{th}$ iteration onwards, stabilizing around 215 $\mu$m. The lower angles of the emitted photons contribute to a decrease in the FWHM along the $Y$ coordinate (remember the needle diameter is 250 $\mu$m). On the other hand, the FWHM along the

[1] In GATE, the photon non-collinearity is modelled as a Gaussian blur in the polar angle with 0.58° FWHM, corresponding to the values measured in water.

[2] This value does not take into account the detectors and positron range contributions. $R_{180^\circ} = \frac{0.5^\circ \times \pi}{180^\circ \times 4} \times D \simeq 0.0022 \times D$, where D is the diameter of the scanner

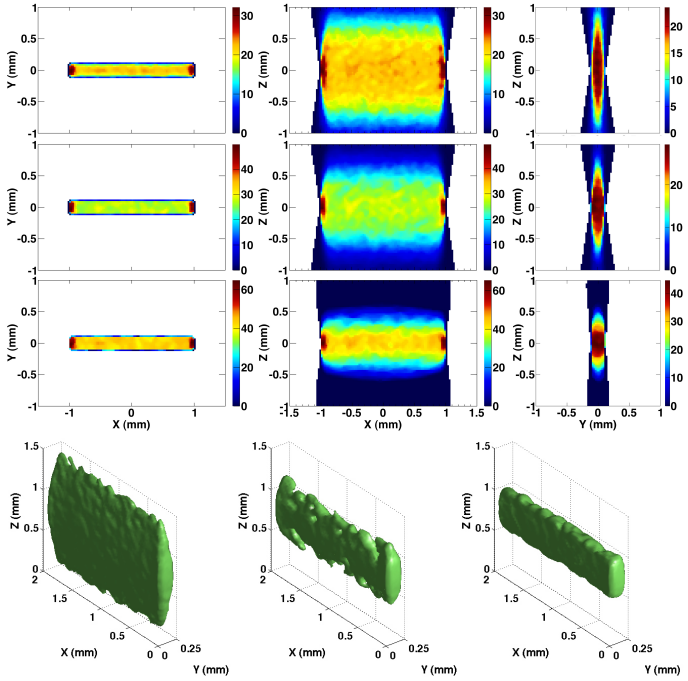


**Figure 4.51:** Sagittal, coronal and axial views of the reconstructed image of the needle-like simulated phantom placed at a distance of 25 cm from the detectors, at iterations 2 (top), 6 (middle), and 100 (bottom). The corresponding 3D representations are also shown.

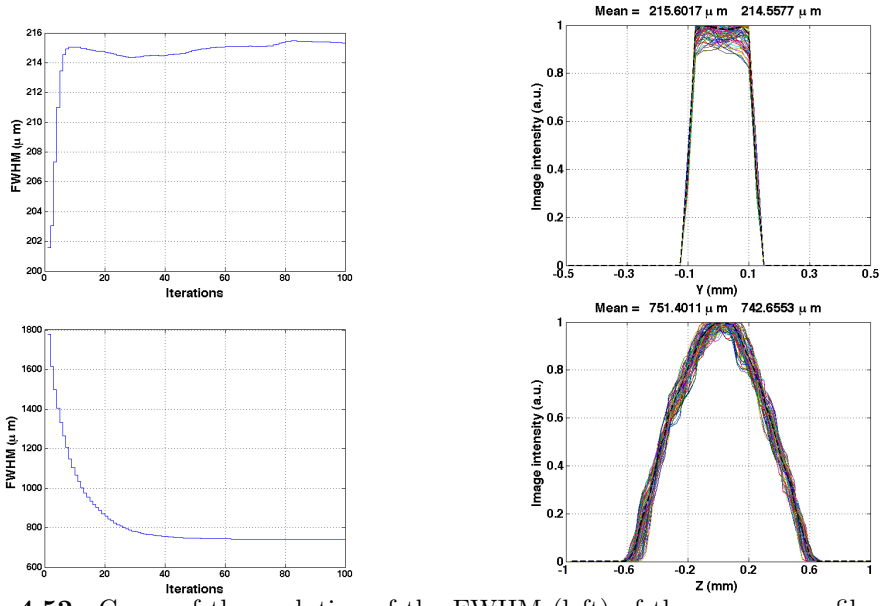


**Figure 4.52:** Curve of the evolution of the FWHM (left) of the average profile (right), taken along the $Y$ (top) and $Z$ (bottom) coordinates of the reconstructed images of the simulated needle-like phantom placed at a distance of 25 cm from the two detectors.

$Z$ coordinate has an opposite behavior, with to a very poor resolution in $Z$ for few iterations, but with a decreasing FWHM, converging to 750 $\mu$m after 100 iterations.

If we introduce a deviation of 0.5° on the second photon (adequate for data taken at room temperature), gaussian distributed, the images become noisier (see fig. 4.53).. We can observe in fig. 4.54 the appearance of tails on the profiles along the $Y$ coordinate, with the profiles becoming wider. Nevertheless, the FWHM converges to a minimum at iteration 23. This value is very close to the one obtained from the reconstructed image without the inclusion of the non-collinearity effect. But even so, the non-collinearity effect increases the tails and the standard deviation of the average profile.

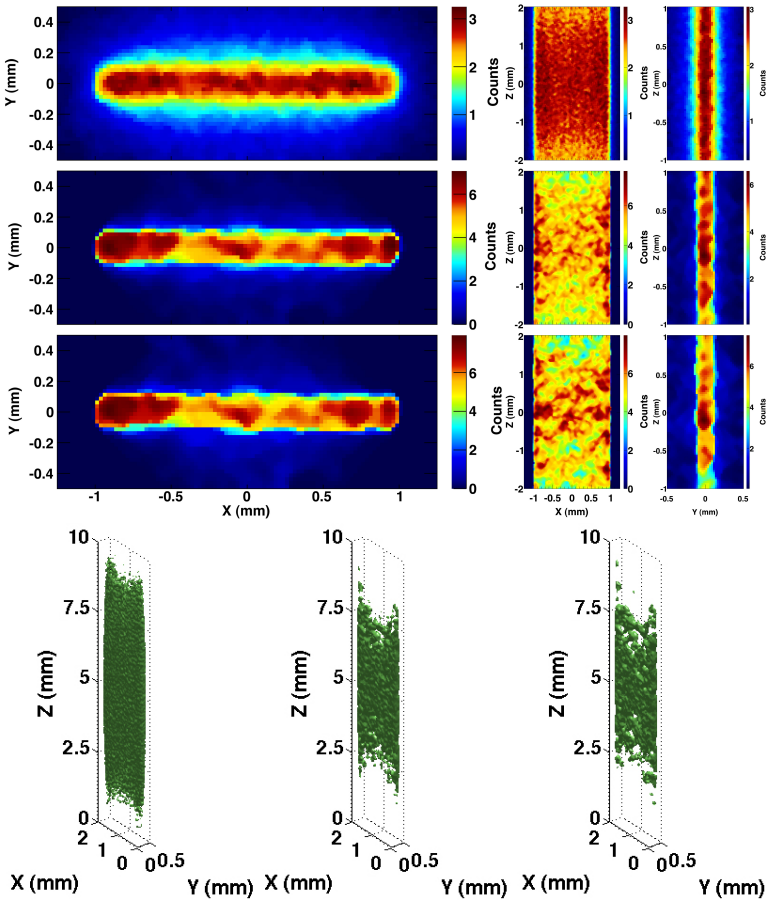


**Figure 4.53:** Sagittal, coronal and axial views of the reconstructed image at iterations 1 (top), 23 (middle), and 84 (bottom). They result from simulated data obtained the needle-like phantom with two detectors placed at a distance of 0.5 m from each other, and with the contribution of the non-collinearity effect. The corresponding 3D representations of the images at iteration 1 (left), 23 (middle), 84 (right) are also displayed.

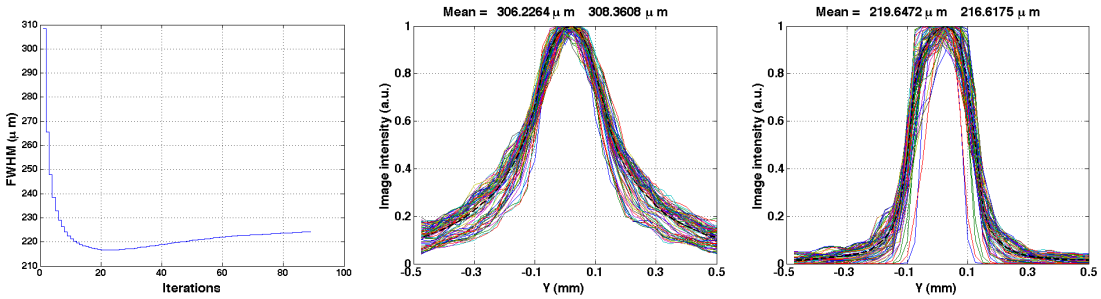


**Figure 4.54:** Curve of the evolution of the FWHM (left) of the average profile taken along the $Y$ coordinate of the reconstructed images, at iteration 1 (middle) and 23 (right). Those images correspond to the simulated needle-like phantom located at a distance of 25 cm from the two detectors, including the contribution of the non-collinearity effect.

### 4.7.2 Experimental results

We analysed and reconstructed 400k events corresponding to the imaging of the needle-like source with detectors placed at a distance of 225 mm. Fig. 4.55 shows the sagittal, coronal and axial views of the reconstructed image after 6 and 100 iterations. These

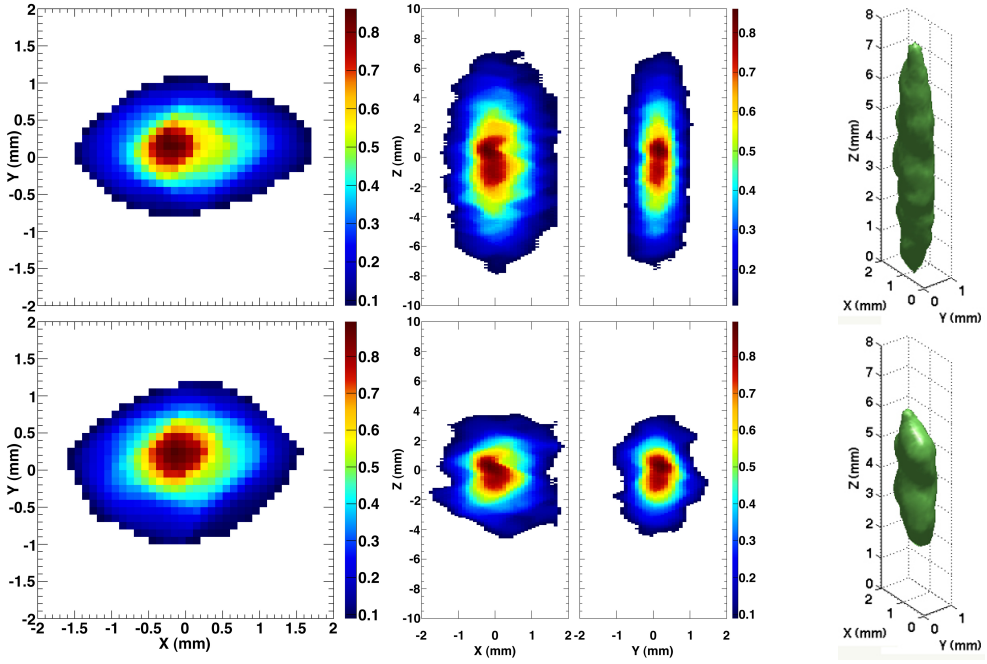


**Figure 4.55:** Sagittal, coronal and axial views of the reconstructed image at iterations 6 (top) and 100 (bottom). They result from experimental data obtained from the needle-like source with two detectors placed at a distance of 45 cm from each other with the source in the middle. The corresponding 3D representations of the images at iteration 6 (top) and 100 (bottom) are also displayed.

iterations correspond, respectively, to the minimum in the FWHM of the average profile along the $Y$ coordinate (see fig. 4.56) and the minimum in the RMSE between consecutive images obtained from each iteration of MLEM reconstruction.

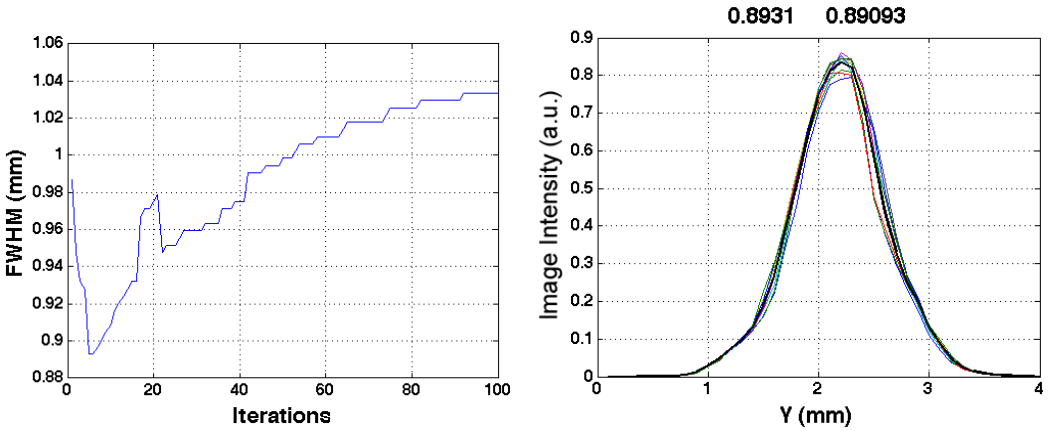


**Figure 4.56:** Curve of the evolution of the FWHM of the average profile, taken along the $Y$ coordinate of the reconstructed image (left). The profiles obtained at iteration 6 (right), demonstrate a spatial resolution of 0.89 mm. These results correspond to the experimental data obtained from the needle-like source placed at a distance of 25 cm from both detectors.

The low resolution in $Z$ coordinate was expected, agreeing with simulations. A spatial resolution of 0.89 mm FWHM is obtained from the profiles taken along the $Y$ coordinate of the reconstructed image at iteration 6 (fig. 4.56). These results demonstrate a loss of spatial resolution, when compared with the detectores placed at a distance of 20 mm from the source.

Fig. 4.57 shows the reconstructed images of the planar source obtained from the data collected by two detectors separated by 41 cm (left) and 45 cm(right). The top images correspond to the iteration whose FWHM of the average profile reaches a minimum and the bottom are obtained at iteration 68 (left) and 99 (right), when the RMSE between consecutive images obtained from MLEM reconstruction achieves a minimum.

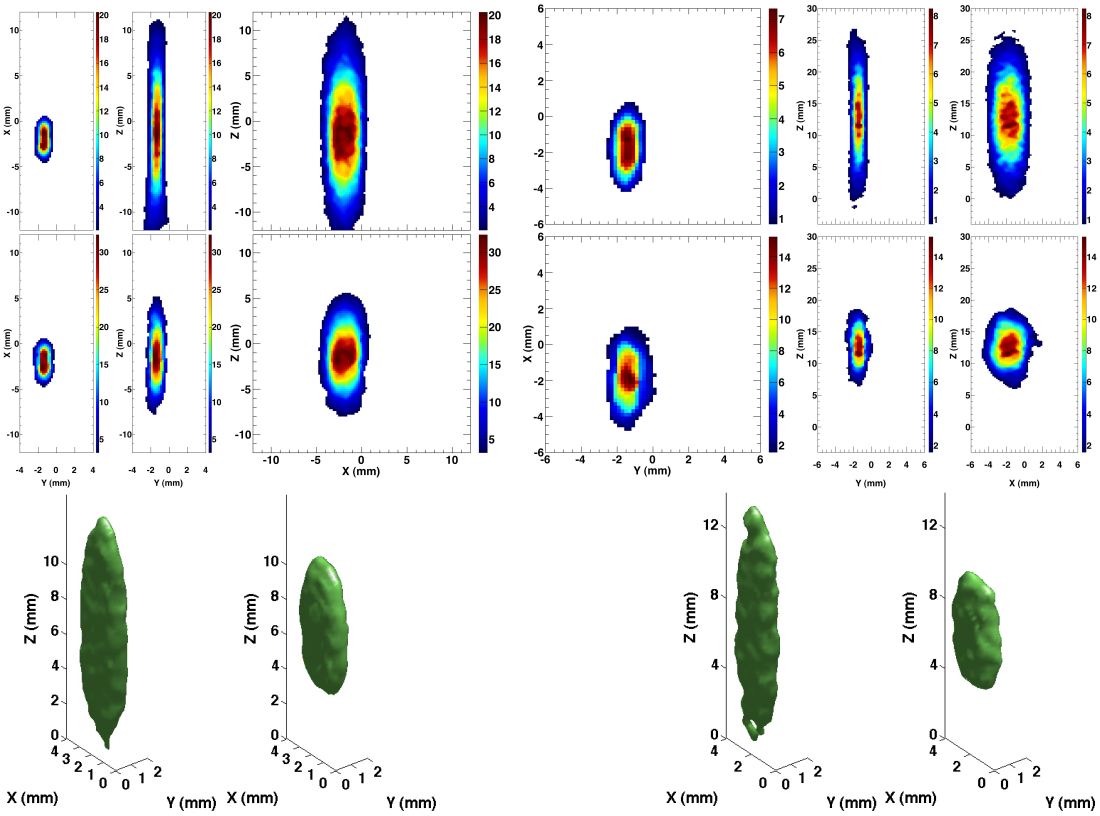
X (mm)
Z (mm)
Y (mm)
X (mm)
Z (mm)
Y (mm)
X (mm)
Z (mm)
Y (mm)

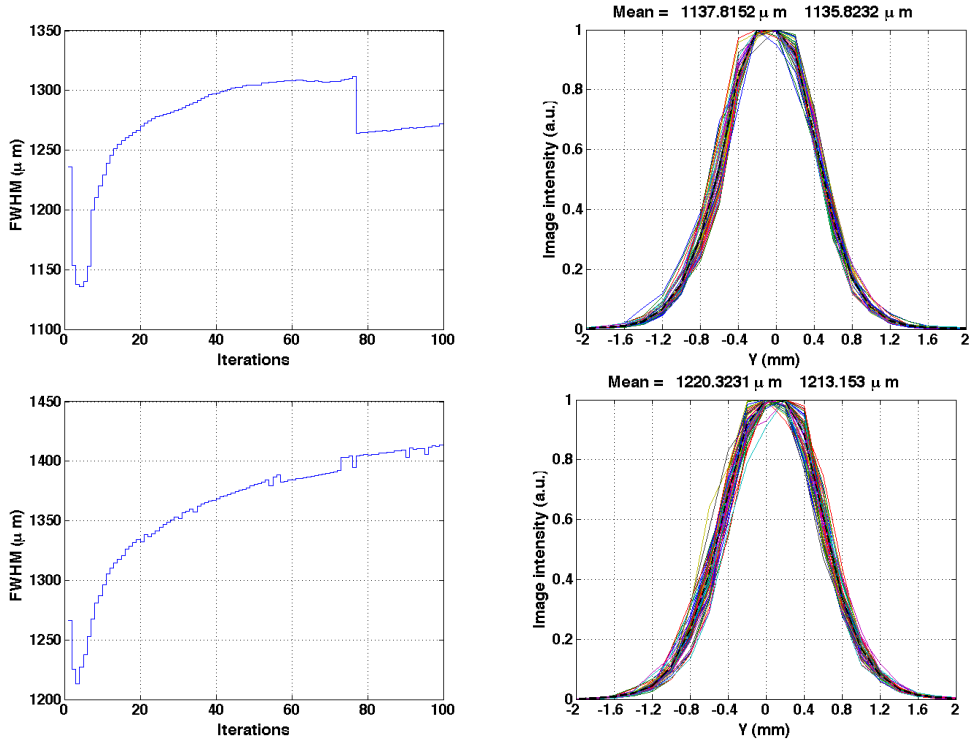


**Figure 4.58:** Curve of the evolution of the FWHM of the mean of the line profiles, taken along the $Y$ coordinate of the reconstructed images for detectors placed at a distance of 41 cm from each other (top left) and at a distance of 45 cm from each other (bottom left). The corresponding line profiles obtained at iteration 4 (top right), and

The results presented above are not conclusive about the Gaussian blurring contribution from non-collinearity effect to the system spatial resolution. They seem to suggest that such effect is well described in the literature and its implementation in GATE should be reviewed, perhaps by modeling the polar angular uncertainty with other function. Nevertheless, the different kind of detectors used for the measurements with the detectors placed closer to the source and with the detectors located at a larger distance does not allow making a direct comparison of the results. We observed that the detectors painted with resistive ink have a better performance than the ones epoxied with *SEMITRON*. A measurement in similar conditions, other than the distance between the detectors, should be considered. An experiment with detectors painted with resistive ink located at a distance from the source far enough to experience the effect of non-collinearity, thus permitting to compare those results with the results from the inner detectors, will be accomplished in the near future.

## 4.8 Ongoing work

A factor that contributes to the degradation of the spatial resolution of the system is the differential non-linearity on the position distribution of the hits on the detectors. This kind of discontinuity in the distribution of the hits between neighboring strips may be related to the number of strips considered for computing the position. We are just considering the strip with largest signal and their two neighbors to compute the PC scores, thus affecting the calculated angle $\alpha$ that determines the position of the hit. An alternative approach is proposed, based on considering the charges on four strips, instead of just three. As depicted in fig 4.59, the charge of the first event (top left) is shared between the strip 11 and 12. Consequently, it makes sense to consider the charge

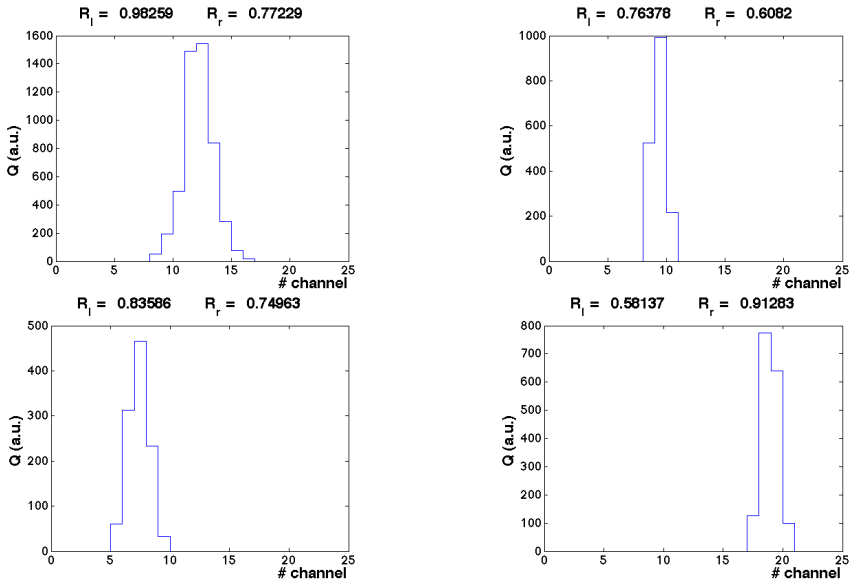


**Figure 4.59:** Charge distribution along the 22 channels for four independent events. The first (top left) and the fourth (bottom right) events share the charge between two strips, while the second (top right) and the third (bottom left) events have its charge concentrated on one strip.

on these strips and their two neighbors, instead of just taking into account the three strips with larger signal. The second (top right) and third (bottom left) events belong to the type of events whose criteria of considering the three strips with largest signal may be correct, while the first and the fourth event (bottom right) belong to the other class of events whose charge in the four strips should be taken into account. To realize how much this last kind of events contribute to the general statistics we defined the

variables: $R_l = (Q_{-1} + Q_0)/2Q_0$, and $R_r = (Q_1 + Q_0)/2Q_0$. Then, we set a threshold of 0.9 on both ratios, to distinguish the two kind of events. The first and the fourth event have one of these defined ratios above the threshold, while the second and the fourth event have both ratios below the threshold. Considering a large sample of 200k events, depending on the electrodes, approximately 35-40% of the events which benefit from considering the four strips with largest signal. The remaining can be handled in the way we have done so far.

A PCA analysis of the experimental data, considering the four strips with largest charge, produces the results shown in table 4.3. The eigenvalues for the four PCs, sorted

| | **Loadings ($L$)** | | | | **Squared Loadings ($L^2$)** | | | |
|---|---|---|---|---|---|---|---|---|
| Component | $q_{-1}$ | $q_{0l}$ | $q_{0r}$ | $q_1$ | $q_{-1}$ | $q_{0l}$ | $q_{0r}$ | $q_1$ |
| 1 | 0.7611 | 0.8446 | -0.8453 | -0.7644 | 0.5792 | 0.7134 | 0.7145 | 0.5843 |
| 2 | 0.5990 | -0.4862 | -0.4841 | 0.5944 | 0.3588 | 0.2364 | 0.2343 | 0.3534 |
| 3 | -0.2489 | 0.2239 | -0.2262 | 0.2498 | 0.0619 | 0.0501 | 0.0512 | 0.0624 |
| 4 | 0 | 0 | 0 | 0 | 0 | 0 | 0 | 0 |
| $\Sigma$ | | | | | 1 | 1 | 1 | 1 |
| | $A'_\Sigma$ | | | | $A'_R$ | | | |
| Component | $q_{-1}$ | $q_{0l}$ | $q_{0r}$ | $q_1$ | $q_{-1}$ | $q_{0l}$ | $q_{0r}$ | $q_1$ |
| 1 | -0.4053 | -0.5803 | 0.5747 | 0.4108 | 0.4728 | 0.5247 | -0.5251 | -0.4748 |
| 2 | 0.5044 | -0.4983 | -0.5017 | 0.4955 | 0.5507 | -0.4471 | -0.4451 | 0.5466 |
| 3 | -0.5756 | 0.4062 | -0.4100 | 0.5794 | -0.5240 | 0.4714 | -0.4762 | 0.5258 |
| 4 | 0.5 | 0.5 | 0.5 | 0.5 | 0.4457 | 0.5501 | 0.5472 | 0.4465 |

**Table 4.3:** Component loadings from experimental data for electrode $X$ of detector $a$, when considering the four strips with larger signal. The elements of matrix $A'$ are also provided.

in decreasing order, are respectively: $\lambda_1 = 2.59, \tau_1 = 64.8\%$; $\lambda_2 = 1.18, \tau_2 = 29.6\%$; $\lambda_3 = 0.23, \tau_3 = 5.6\%$; $\lambda_4 = 0, \tau_4 = 0\%$. The variables $q_{0l}$ and $q_{0r}$ are the normalized charges that correspond, respectively, to the strip on the left and the one on the right, from the two strips with largest signal,. For instance, concerning the first event of fig. 4.59, these variables correspond, respectively, to strip 11 and 12, while on the fourth event, they correspond to the strip 18 and 19, respectively. The variables $q_{-1}$

and $q_1$ are, respectively, the normalized charges of the left neighboring strip to the strip with normalized charge $q_{0l}$, and the right neighboring strip to the strip with normalized charge $q_{0r}$. As mentioned in appendix D, the matrix $\boldsymbol{L^2}$ represents the proportion of the variance of each variable explained by each of the first four components. The central variables $q_{0l}$ and $q_{0r}$ share the same proportion explained by the first three components, being mostly explained by component 1 (71%), followed by component 2 (23%). Component 3, accounting for 5% of the total variance, simply figures the residue from component 1 and 2. The same behavior is observed with their neighboring strip charges $q_{-1}$ and $q_1$, although the variance on these variables are more equally distributed between component 1 and 2, with a proportion of 58% for component 1 and 35% for component 2. In what concerns component 1, there is a common but negative association between the variables $q_{0l}$ and $q_{0r}$ and the variables $q_{-1}$ and $q_1$. In respect to component 2, there is a complete association between the variables $q_{0l}$ and $q_{0r}$ and the variables $q_{-1}$ and $q_1$. The matrices $\boldsymbol{A'_\Sigma}$ and $\boldsymbol{A'_R}$ return similar values, however for the sake of coherence, we will adopt the matrix $\boldsymbol{A'_\Sigma}$ to estimate the PC scores, depicted in fig. 4.60, left. It is possible to distinguish five stripes corresponding to the five gaps.

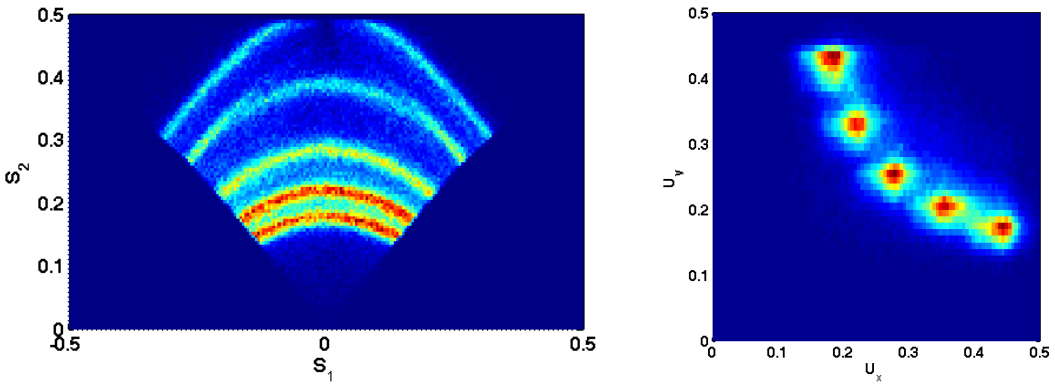


**Figure 4.60:** Histogram of PC scores S1 and S2, thus defining the 5 gaps (left). Histogram of the variables $U_x$ and $U_y$ (right). All the strips were considered.

This time, the contribution of all strips is included, showing a correct superposition. An histogram relating the coordinates $U_x$ and $U_y$ obtained from the transformation of the variables $\alpha$ and $G$ for the electrodes X and Y of the same detector, is presented in fig. 4.60 (right). It is, thus, possible through the statistical clustering tool, *kmeans*, to partition the data into 5 clusters, thus identifying each of the 5 gaps where the avalanche developed.

A strategy to determine the position of the hits will be addressed in the near future, with the goal of minimizing the contribution of the DNL on the position distribution of the hits. It should be noted that the five clusters present in fig. 4.60 (right) are more homogeneously distributed than the ones shown in figs. 4.11 and 4.16. It seems to be an advantage of this approach that all clusters have a similar intensity, despite the apparent lower compactness. Table 4.4 compares the distribution of the events in the five gaps for both approaches.

| | **Gaps** | | | | |
|---|---|---|---|---|---|
| **Approach** | 1 | 2 | 3 | 4 | 5 |
| 3 Strips | 16.9 | 22.1 | 23.2 | 22.5 | 15.3 |
| 4 Strips | 19.7 | 20.6 | 20.3 | 21.3 | 18.1 |

**Table 4.4:** Event distribution in the five gaps considering the analysis of 3 or 4 strips (%).

There is no good reason for the higher intensity of the middle gaps in figs. 4.11 and 4.16. This information suggests that this effect may be associated to data processing rather than to physical phenomena.

# Part II

# Human RPC-PET (Simulation Results)

# 5

# A Direct Time-of-Flight Reconstruction for Whole-Body Single-Bed RPC-PET

In this chapter, we present results connected to the challenge of providing a reconstruction routine tailored to the potentialities of RPC-PET. Such a routine must cope with data from the whole axial field-of-view (AFOV) of the system, rather than from one bed at a time as is the case with scintillator-based tomographs. In addition, the same routine must be able to incorporate the time-of-flight (TOF) advantage provided by RPC detectors and, at the same time, it must also be fast enough to cope with the imaging speed that an RPC-PET system may provide due to its increased sensitivity.

The first two aforementioned reconstruction challenges, incoming data from the whole AFOV and capability of TOF processing, were tackled by choosing an iterative algorithm capable of processing data in list mode format: the TOF-weighted maximum likelihood expectation-maximization (MLEM) and the TOF-weighted ordered subsets expectation-maximization (OSEM). Both were coupled to an attenuation correction procedure developed to allow the observation of events from the patient whole-body (WB).

A TOF-based scatter rejection method applied to the anthropomorphic NURBS-based cardiac-torso (NCAT) phantom is presented, demonstrating that by means of a 300 ps full width at half maximum (FWHM) whole-body RPC-PET, it is possible to reject 63% of the scattered events originated in the body, increasing lesion detectability.

Reconstructed images are shown, demonstrating the capabilities of this method.

A reconstruction method based on the division of the data through different regions of the body is presented. Such implementation allows us to perform independent reconstructions running simultaneously, and consequently increasing the image convergence speed. A comparison of performance between multi-core CPUs and GPU-based implementations of the reconstruction routine is shown. We made use of graphical processing units (GPUs) and 16-threads central processing units (CPUs) to implement a fully parallelized routine that is capable of processing, in less than 4 minutes, the simulated data corresponding to an acquisition time of 7 minutes, with a patient injected activity of 2 mCi.

## 5.1 Materials and methods

The reconstructed images presented in this article result from the application of the RPC-PET reconstruction algorithm to GEANT4 simulated data (version 9.02 and 9.03). The software-based anthropomorphic phantom NCAT [28] was adapted to Geant4 [9], including whole-body activity distribution and attenuated photon emission from the human body, taking into consideration different tissues and densities. The activity concentrations implemented at the anthropomorphic phantom NCAT are shown in Table 5.1. They are based on values published by Rodrigues et al. [316], Trindade et al. [317], and Reis [154], corresponding to activity concentrations existing in the human body one hour post-injection of 37 MBq (1 mCi) of 18-fluorodeoxyglucose ($^{18}$F-FDG). In the brain, a grey-to-white matter uptake ratio of 4:1 [318] was assumed in the simulation.

Reconstruction was processed with self-designed C, C++ and compute unified device architecture (CUDA) routines. The phantom used in the reconstruction was placed on a body-centered parallelepiped image and final images were interpolated to 2-mm $\times$ 2-mm $\times$ 2-mm voxels. Output images were analyzed and processed with ROOT (version 5.34.00).

**Table 5.1:** Organ and tissue activity concentrations implemented at the anthropomorphic phantom NCAT utilized throughout this study. Adapted from [9].

| Tissue / organ | Activity concentration (kBq/mL) |
|---|---|
| Body | 0.212 |
| Liver | 0.918 |
| Gallbladder | 2.190 |
| Lung | 0.197 |
| Stomach wall | 0.982 |
| Stomach cavity | 0.982 |
| Kidney | 0.858 |
| Spleen | 0.622 |
| Vertebral bone (head) | 0.212 |
| Vertebral bone (process) | 0.212 |
| Pelvic bone | 0.212 |
| Rib | 0.212 |
| Cartilage | 0.212 |
| Abdomen artery | 0.212 |
| Abdomen vein | 0.212 |
| Bladder | 4.000 |
| Prostate | 0.212 |
| Colon | 0.212 |
| Colon (air) | 0.000 |
| Rectum | 0.212 |
| Rectum (air) | 0.000 |
| Seminal vesicles | 0.212 |
| Deferent vessels | 0.212 |
| Testes | 0.212 |
| Ureter | 0.212 |
| Urethra | 0.212 |
| Lymph (normal) | 0.212 |
| Lymph (abnormal) | 0.212 |
| Myocardium | 2.190 |
| Ventricles | 0.701 |
| Atria | 0.701 |
| Brain (grey matter) | 3.260 |
| Brain (white matter) | 0.815 |

### 5.1.1 Simulated activity

#### 5.1.1.1 Six spheres in homogeneous background

A study of lesions in homogeneous background took into consideration six simulated spherical sources placed in a homogeneous background, with a signal-to-background activity ratio of 6:1. The phantom is 1.1 m long and has a diameter of 35 cm (volume = 105 L). Assuming $^{18}$F-FDG as the decaying solution, and a typical body background activity concentration of 2.12 kBq/mL [9], this corresponds to a scan time of 88s and

20 billion decays. The analyzed list-mode outputs were constructed for an RPC-PET system with 120 gaps and a singles detection efficiency to 511 keV perpendicular gamma rays of 19.4% (see fig. 2.36, right). From 142 M detected events, 41 M were true events and the scatter fraction after the scatter rejection by a 300 ps FWHM TOF resolution was 45.4%, which is explained by the large diameter of the cylinder which in turn corresponds to a patient with a large body mass index (BMI). After performing the cuts on the detector geometry (acceptance angle $< 45°$), 36 M true events were left to be reconstructed.

#### 5.1.1.2 NCAT anthropomorphic phantom

To study the NCAT anthropomorphic phantom, 16 billion decays were considered. This corresponds to 440 s of acquisition time at 2 mCi of injected dose [319]. The RPC-PET system detected 146 M coincidence events. After performing the cuts on the detector geometry (acceptance angle $< 45°$, and displacement of the NCAT phantom by 256 mm in the direction from head to feet) and rejecting the scattered events by a 300 ps FWHM TOF resolution, the scatter fraction was 33% for a total of 49 M true events.

#### 5.1.1.3 Six lesions in anthropomorphic phantom

Datasets of lesions with a diameter of 10 mm each were inserted by simulation in the anthropomorphic phantom with a lesion to background activity ratio of 10:1 [261], and placed in the following regions: cervical, sub-clavicular, axillary, inguinal, knee and foot [261]. To determine the events to be simulated in each lesion and detected by the RPC-PET system, we calculated the time-integrated activity density of the background phantom tissue. This tissue contributes with 60% of total body activity and occupies a volume of 82 L, therefore, it has a time-integrated activity density of 4.4 cts $mm^{-3}$. Consequently, 20.8 k events were simulated for each lesion.

### 5.1.2 TOF-based scatter rejection of anthropomorphic events

A method to increase lesion detectability based on the rejection of scattered events by means of its TOF information is investigated. Fig. 5.1 illustrates this method by which the annihilation point determined along the scatter line of response (LOR) has a certain probability of being inside the human body, according to the TOF resolution. The limits of rejection were estimated at 95% confidence level.

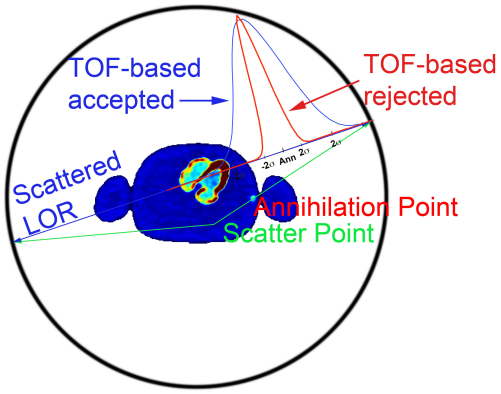


**Figure 5.1:** Scheme of the scatters rejection method. The calculated annihilation point located in the scatter LOR has a certain probability of being inside the human body, depending on the TOF resolution. Poorer TOF resolutions (curve in blue) increase the probability of the annihilation point being within the human body, resulting in a TOF-based accepted event. Better TOF resolutions reject a higher fraction of scatter events. The limits of rejection were estimated at 95% confidence level.

### 5.1.3 Attenuation correction

The attenuation correction performed was based on the NCAT attenuation phantom [28]. NCAT 3D navigation was calculated on the fly, based on the ray tracing technique only for attenuation correction. In equation 5.1, $\lambda_j$ corresponds to the mean free path in each voxel of the attenuation image that was crossed by the LOR, and $L_{LOR}$ to the 3D length of the portion of the LOR corresponding to the touched voxels. The symbol $f_{att}$ denotes the coefficient factor that is multiplied by the measurement associated to the voxels touched in the corresponding LOR whose activity has been attenuated,

$$f_{att_i} = e^{\sum_j \frac{1}{\lambda_j} L_{LOR}}, \tag{5.1}$$

as discussed further in section 5.1.5.

### 5.1.4 TOF kernel and image statistics

In this reconstruction, the TOF kernel was modeled as a Gaussian with a kernel of 300 ps FWHM - measured coincidence time resolution, as shown by experimental results with RPC-PET detectors for human PET [4]. This modeling was based on the direct technique for voxel filling [320]. In fig. 5.2 (left), the Gaussian kernel is filled

with 1 million samples centered in the coincidence time difference of the first two annihilation photons detected. Fig. 5.2 (right) shows the backprojected LOR for that first event. The integral of the curve corresponds to the weight given to that LOR by the attenuation correction. In the reconstruction algorithm, the filling of the Gaussian

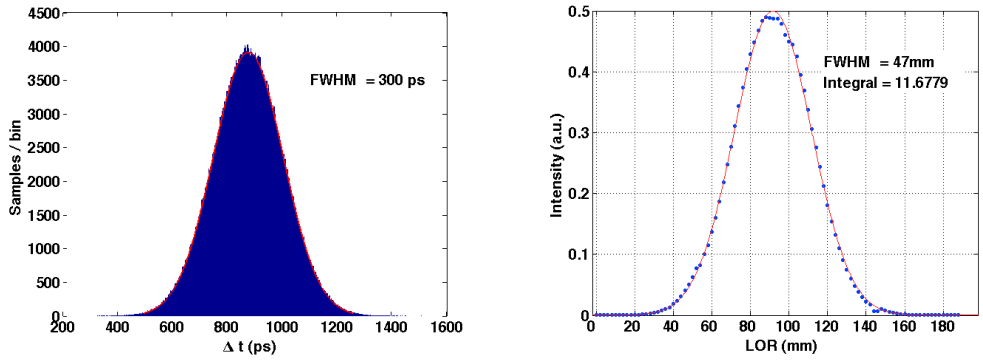


**Figure 5.2:** Left: Gaussian kernel of 300 ps filled with 1 million samples and centered in the coincidence time difference of the first two annihilation photons detected. Right: backprojection of the first event TOF-weighted with 1 million samples. Both the FWHM and the integral agree with the expectations (FWHM calculated: 45 mm versus FWHM from backprojection: 47 mm; attenuation coefficient calculated: 11.49 versus integral from backprojection: 11.68).

kernel was studied between 1 and 50 samples inside the Gaussian. Considering image improvement stabilization, a TOF kernel with 30 samples inside the Gaussian was taken into account. When reconstructing with a 600 ps FWHM TOF kernel, in order to compare with the 300 ps FWHM case, a kernel filling of 60 samples was implemented, to avoid statistical losses in the filling due the wider width of the gaussian. To evaluate the influence of image statistics, a reconstruction with half of the detected events was performed.

### 5.1.5 MLEM and OSEM mathematical implementation

The list-mode data was reconstructed with MLEM and OSEM, including a TOF probability density function. Fig. 5.3 depicts the flowchart of the reconstruction algorithm. Equation 5.2 presents the MLEM algorithm, in its matrix form, adapted to the TOF-based reconstruction, and including attenuation correction. The attenuation correction is incorporated neither in the form it is in attenuation weighted (AW)-MLEM [286] nor in AW-OSEM [287], but rather applied to pre-corrected list-mode data, as discussed in chapter 2. In order to find the activity distribution corresponding to iteration

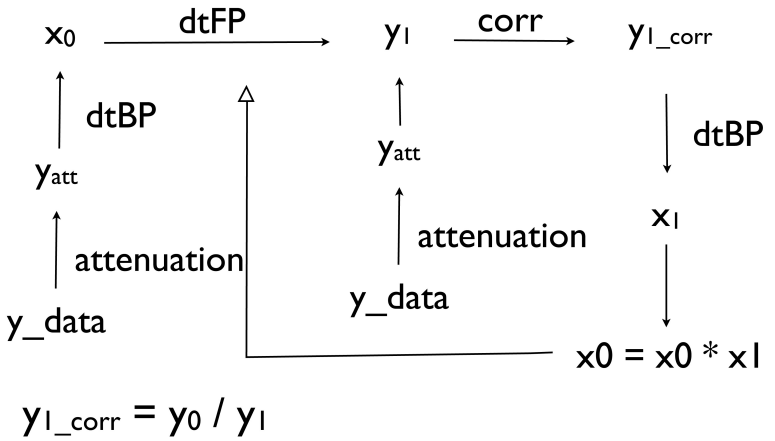


**Figure 5.3:** Flowchart of the direct TOF-based reconstruction algorithm implemented in this study. The abbreviation dtBP stands for direct-TOF backprojection, whereas dtFP stands for direct-TOF forward projection.

(n + 1), $X^{(n+1)}$, the backprojected image $X^{(n)}$ is forward-projected and TOF-weighted by weight $G$ (represented in equation 5.3 in index notation), as given by $AGX^{(n)}$, with $A$ being the system matrix, *i.e.* the matrix that makes the correspondence between the image space $X$ and the data space $Y$ . The simulated projected data ($Y^{(0)}$) was previously corrected by the attenuation correction factor $F$ ($f_{att_i}$ in index notation) and is divided by $AGX^{(n)}$. This corrected data fraction is then backprojected and TOF-weighted, by multiplying itself by $A^{-1}G$. The algorithm then multiplies this image by the image of the previous iteration, $X^{(n)}$, repeatedly through iterations,

$$X^{(n+1)} = X^{(n)} A^{-1} G \frac{Y^{(0)} F}{AGX^{(n)}} \tag{5.2}$$

$$g_i = \frac{1}{\sqrt{2\pi}\sigma_i c} e^{-\frac{(s_t - <s>)^2}{2\sigma_i^2 c^2}} \tag{5.3}$$

The OSEM algorithm in its index notation form is presented in eq. (5.4), where $g_i$ is defined by eq. (5.3), with $< s >$ defined by eq. (5.5), and $\sigma_i$ = 128ps (300 ps FWHM). The constant $c$ corresponds to the speed of light.

$$x_j^{(n+1)} = x_j^{(n)} \sum_{i \in S_N} a_{ij} g_i \frac{y_i f_{att_i}}{\sum_t a_{it} g_i x_t^{(n)}} \tag{5.4}$$

$$< s >= s_{middle,LOR} + \frac{\sigma_i c}{2} \tag{5.5}$$

### 5.1.6 Multi-threaded GPU-based parallelization reconstruction strategy

The method proposed to increase the performance of the reconstruction routine consists in reconstructing independently nine different regions of the body. For example, in fig. 5.4, we see that 40% of *LOR 1* is assigned to image region number 5, while 60% of the same LOR is assigned to image region number 6. However, *LOR 2* is totally assigned to image region number 7. In order to consider the events laying outside the

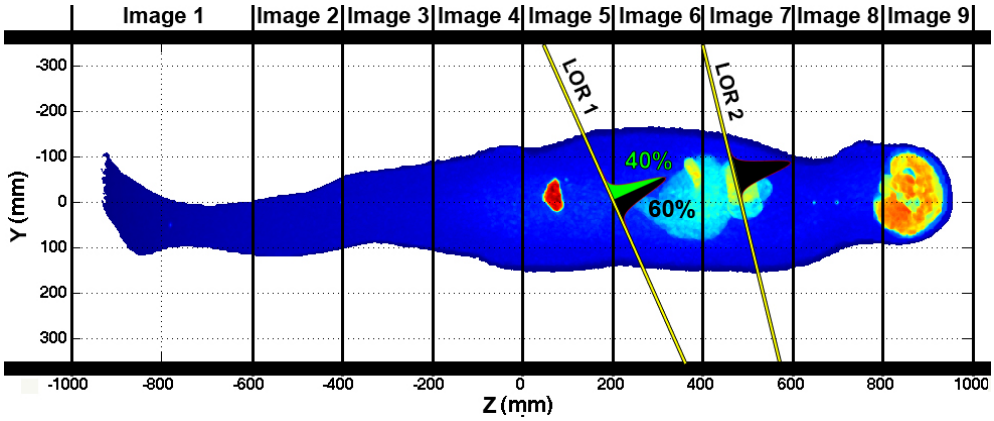


**Figure 5.4:** TOF-assisted data division into nine different body regions.

divided images while iterating on the TOF-kernel, a margin of $3\sigma$ in the space variable was taken in consideration. The nine different images are then summed, resulting in a single volume similar to the whole-body reconstructed one.

A complementary reconstruction technique to increase further the reconstruction speed consists in considering a certain number of dots equally spaced inside the 300 ps FWHM TOF gaussian and giving them the equivalent gaussian weight, so the sum of the weights equals one. Fig. 5.5 shows the equally spaced dots with their corresponding weight. The more points we consider, the lower is their individual weight. For the 16-threads CPUs implementation, 15 dots were considered while for the GPU implementation, 32 dots were contemplated without loss of reconstruction speed and image quality. To increase the compute-to-memory access ratio, this configures the suitable scenario for the use of the GPU constant memory. To overtake the inefficiency of cache entries, resulting from having the TOF uncertainties along the space variable and their corresponding weights stored in separate arrays, the solution arose from storing the elements of these arrays as a struct, known as an array of structs [321], [322]. In this approach, instead of giving an equal weight to each sample of the TOF-kernel, which is

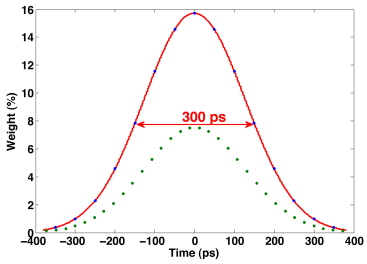


**Figure 5.5:** Distribution of the time uncertainty associated to a 300 ps FWHM TOF resolution. The TOF uncertainty along the space variable and its respective weight is distributed along 15 and 32 dots respectively used for the 16-threads CPUs and GPU routine implementations. This approach allows for an increase of 31% in reconstruction speed, since these values are accessed through a look-up-table (LUT).

done randomly, consuming undesired computing time capabilities, we access the 300 ps FWHM gaussian dots through a look-up-table (LUT) containing the TOF uncertainties along the space variable and their respective weights. This approach generates always an identical reconstructed image.

A LUT has also been done for the random TOF kernel filling to speed-up the reconstruction. By generating 1M uncertainty time samples to fill the TOF-kernel of a first set of events and using the same LUT for the next set of events, this shortened the time needed in the generation of a time uncertainty for each sample of each event. On each MLEM iteration, a new uncertainty time table was generated. Therefore, we end up always with a different image in each iteration. The final image can be correlated with another independent reconstruction to suppress statistical noise and increase system specificity.

The reconstruction routines were both implemented on an NVIDIA Tesla C2075 GPU assisted by a double Intel Xeon E5620 2.4GHz CPU with 16 threads, versus the 16-threads CPUs alone.

### 5.1.7 Contrast recovery coefficient calculation

Following the strategy adopted by [116] to determine the local contrast recovery coefficient (CRC) values, independent reconstructions were performed both on the NCAT simulated data without the inserted lesions assumed as background, and after inserting the lesions by simulation, the latter representing the signal. The volumes of interest

(VOIs) were drawn for each lesion with the respective diameter on both images and the CRC was calculated as

$$CRC = (H/B - 1)/(a - 1), \tag{5.6}$$

where $\boldsymbol{H}$ is the average intensity in the lesion VOI, $\boldsymbol{B}$ is the average intensity in the corresponding background VOI, and $\boldsymbol{a}$ is the simulated lesion to background activity ratio of 6:1 for the six spheres in homogeneous background and of 10:1 for the lesions inserted in the anthropomorphic phantom.

## 5.2 Results

### 5.2.1 Six spheres in homogeneous background

#### 5.2.1.1 Qualitative analysis

Fig. 5.6 shows six simulated sources immersed in a homogeneous background. This

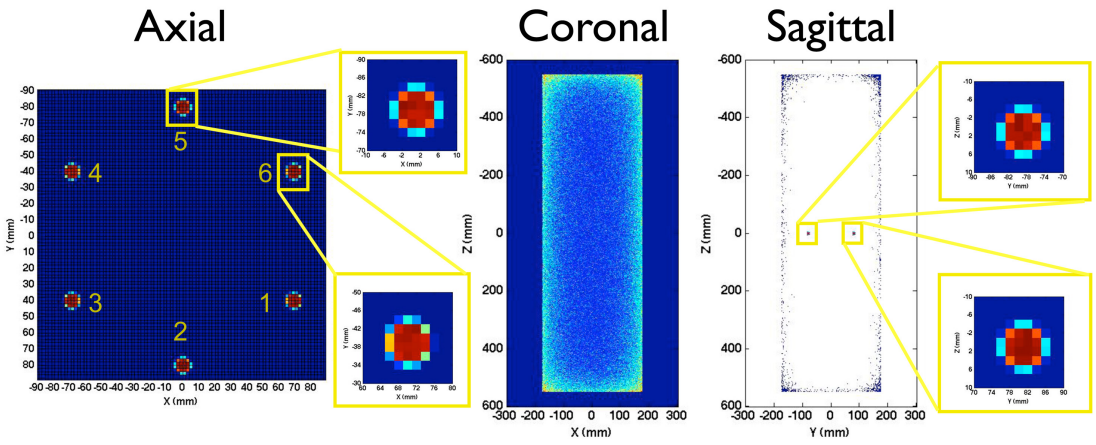


**Figure 5.6:** Original annihilation points corresponding to the simulated data of six spheres immersed in a homogeneous background. Coronal and sagittal views have higher intensity in the outer regions of the phantom due to the photon attenuation effect. The same is also visible in the axial view, where spheres 1, 3, 4 and 6 have less intensity on the voxels closer to the axis of the phantom (orange) than the ones closer to the phantom surface (red).

image corresponds to the annihilation points from where the photons that reached the detectors were emitted. In the axial view, spheres 1, 3, 4 and 6 have less activity on the voxels closer to the center of the cylinder. This is a consequence of the attenuation

of the emitted photons which are more attenuated when the annihilation process takes place in these inner regions. This effect is even more visible in the coronal view (see fig. 5.6, middle), which clearly lacks on attenuation correction. Additionally, this effect is even increased considering the efficiency curve presented in fig. 2.36 (right), which mostly rejects the low-energy scattered events in favor of the acceptance of the true events. In the sagittal view (see fig. 5.6, right), spheres 2 and 5 maintain their original shape, as it will be explained next.

As can be seen in fig. 5.7 left, the indicated *LOR 1* corresponds to the track of two opposite photons that cross more matter than the photons corresponding to *LOR 2*. This can be seen in detail in figs. 5.7 middle and right. The spheres get elongated

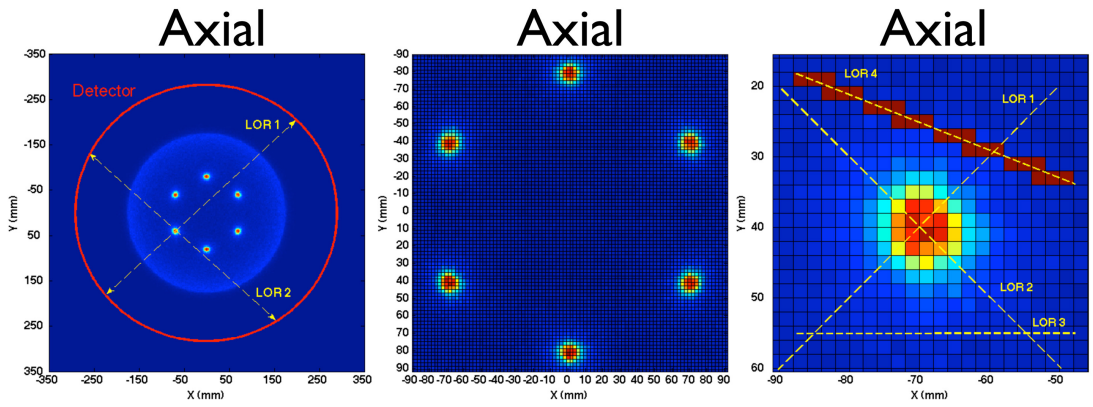


**Figure 5.7:** Depiction of the elongation effect of spheres 1, 3, 4 and 5 caused by the attenuation effect. Left: *LOR 1* traverses more matter than *LOR 1* leading to the elongation of the spheres observed in the zoomed image (middle). The closer observation of sphere 5 shown in right image confirms that voxels crossed by *LOR 2* have more intensity than the ones crossed by *LOR 1*.

along the track of *LOR 2*, because more photons are escaping from the phantom due to the closer position to the borders of the phantom on that specific direction. In fig. 5.7 right, voxels crossed by *LOR 2* have clearly more intensity than those crossed by *LOR 1*. Comparing *LOR 3* and *LOR 4*, it is shown that the TOF-based LOR filling of inclined LORs occurs in a larger number of voxels than for horizontal LORs, contributing to the elongation of the sphere. These images correspond to the backprojection of the detected trues events without attenuation correction.

After performing the attenuation correction the reconstructed image becomes homogeneous, as shown in fig. 5.8 (right).

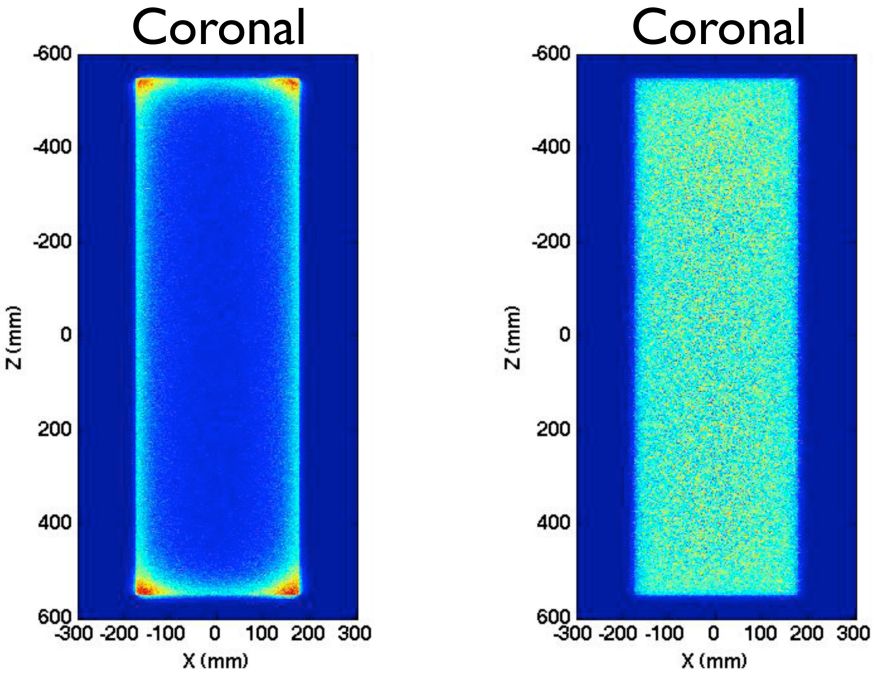


**Figure 5.8:** Backprojection of the background data without (left) and with (right) attenuation correction.

In order to understand the difference between the shape of spheres 2 or 5 in respect to all others, in fig. 5.6 a), we compare the two events presented in fig. 5.9. Supposing that we iterate through a gaussian kernel along the inclined LOR, the same gaussian kernel along a horizontal LOR would have a contribution to the neighboring voxels. This is purely a geometrical effect. However, the overall contribution to the 9 presented voxels, which define a VOI, is identical.

In fig. 5.10 a), the backprojection of the detected true events after performing the attenuation correction is presented. The elongated spheres 1, 3, 4, and 6 become spherical. In fig. 5.10 b) and c), we present the reconstructed images corresponding to the iteration 1 and 10 of the MLEM algorithm, respectively. As expected, due to the effect presented in fig. 5.9, spheres 1, 3 , 4, and 6 have their closest region to the detector (highest solid angle) crossed by diagonal LORs while for spheres 2 and 5, the closest region to the detector is crossed by horizontal LORs. Therefore, the spheres gain this shape with a higher intensity concentration in inner voxels, which becomes more

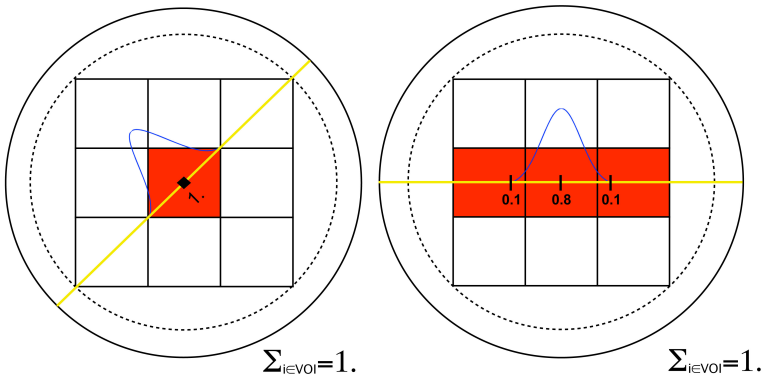


**Figure 5.9:** Scheme of the contribution of an inclined LOR (left) and an horizontal LOR (right) to the TOF kernel filling of the gaussian. Despite the dispersion of the sample filling in the right image to the neighboring voxels, the overall contribution to the 9 voxels is equal in both images.

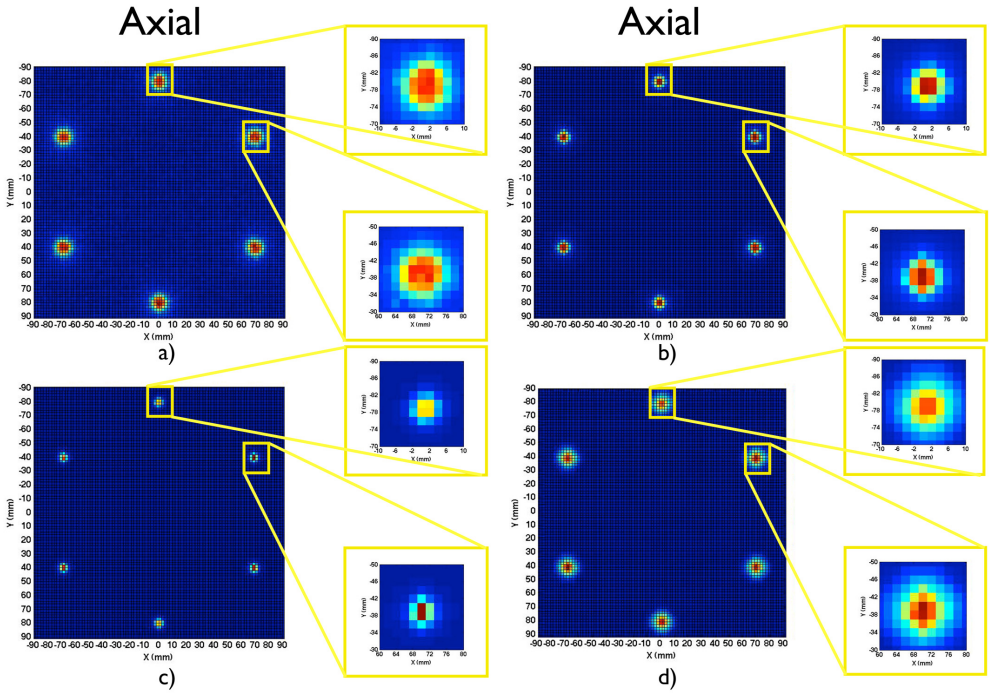


**Figure 5.10:** Reconstruction of six simulated spheres immersed in a homogeneous background (axial view): a) backprojection of the data; b) iteration 1; c) iteration 10; d) iteration 20 with gaussian blurring along the three coordinates in the detection position.

accentuated with increasing iterations. It is a purely geometrical effect that is solved with a gaussian blurring on the detection position, as can be seen in fig. 5.10 d). If the detector effects were included, this problem would vanish due to the large contribution of the scattered events on the detectors in comparison to these small variations. As we will see in next section, for anthropomorphic studies these issues do not arise, since the reconstruction is also dominated by other variables.

In fig. 5.11, the corresponding sagittal views of the preceding images are shown. Both the attenuation correction and the gaussian blurring generate a homogenous cylinder and the spheres maintain their original shape.

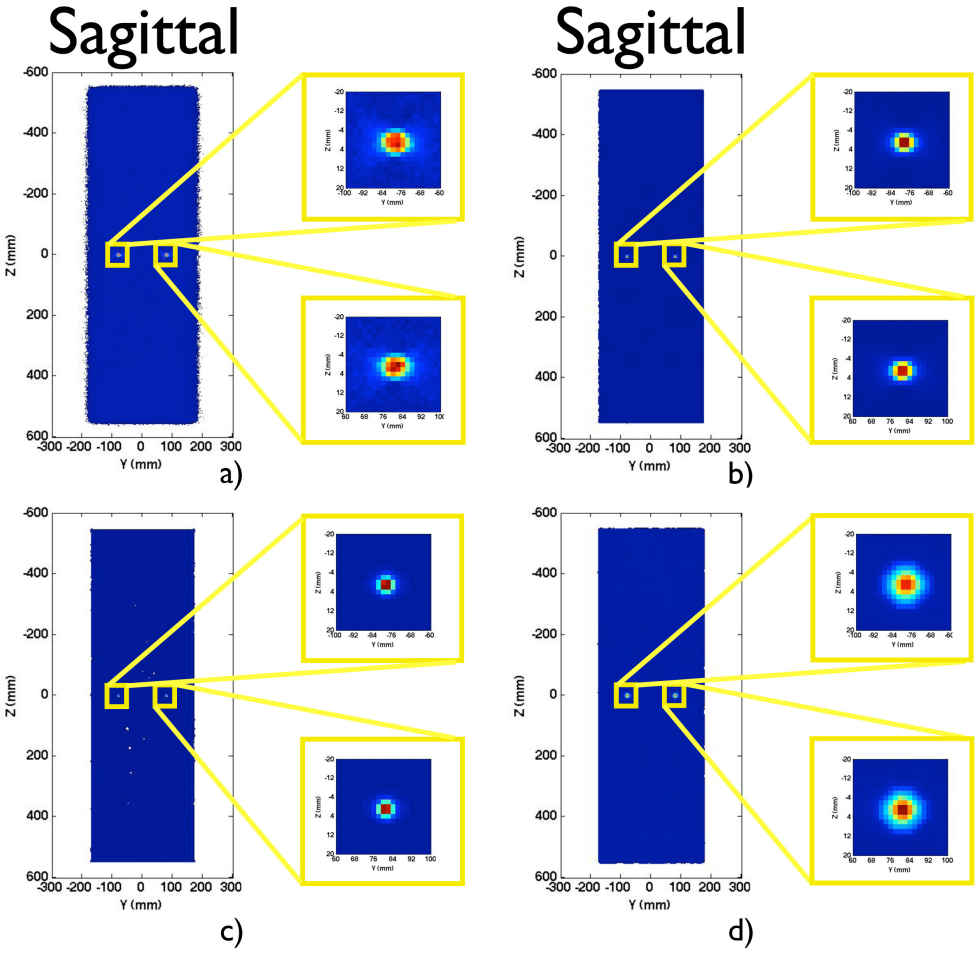


**Figure 5.11:** Reconstruction of six simulated spheres immersed in a homogeneous background (sagittal view): a) backprojection of the data; b) iteration 1; c) iteration 10; d) iteration 20 of MLEM algorithm with a gaussian blurring along the three coordinates in the detection position.

#### 5.2.1.2 Quantitative analysis

To reinforce the consistency of the reconstructed images shown above, we calculated the VOI in a similar region around the 6 spheres. We compared the images generated by the annihilations points and the ones resulting from the reconstruction of the detected events, with and without the inclusion of the attenuation correction and the gaussian blurring on the detected events position.

The total intensity in the VOI for the 6 spheres is presented in table 5.2. The variations between the 6 spheres after performing the attenuation correction and the

**Table 5.2:** Relative intensity in the volume of interest for 6 spheres immersed in a homogeneous background

| | **Without attenuation correction** | | | | | |
|---|---|---|---|---|---|---|
| Spheres | 1 | 2 | 3 | 4 | 5 | 6 |
| Backprojection | 98.2% | 97.7% | 98.9% | 98.9% | 97.3% | 100% |
| Iteration 1 | 96.9% | 97.9% | 98.8% | 100% | 96.9% | 98.7% |
| Iteration 3 | 95.7% | 97.5% | 100% | 99.0% | 96.7% | 99.3% |
| Iteration 10 | 91.4% | 98.8% | 99.1% | 100% | 97.4% | 97.3% |
| | **With attenuation correction** | | | | | |
| Spheres | 1 | 2 | 3 | 4 | 5 | 6 |
| Backprojection | 97.2% | 97.5% | 98.9% | 98.2% | 96.3% | 100% |
| Iteration 1 | 95.7% | 97.8% | 99.8% | 99.0% | 96.5% | 100% |
| Iteration 3 | 95.1% | 97.4% | 99.3% | 100% | 96.7% | 99.4% |
| Iteration 10 | 91.1% | 94.8% | 100% | 99.7% | 92.5% | 97.0% |

| | **With attenuation correction and gaussian blurring** | | | | | |
|---|---|---|---|---|---|---|
| Spheres | 1 | 2 | 3 | 4 | 5 | 6 |
| Iteration 1 | 98.3% | 97.0% | 98.6% | 98.9% | 97.2% | 100% |
| Iteration 3 | 96.3% | 95.7% | 98.5% | 97.9% | 97.3% | 100% |
| Iteration 10 | 95.7% | 96.9% | 100% | 99.0% | 98.1% | 99.5% |

| | **Annihilation points** | | | | | |
|---|---|---|---|---|---|---|
| Spheres | 1 | 2 | 3 | 4 | 5 | 6 |
| Trues + Scatters | 99.9% | 99.7% | 99.6% | 99.7% | 99.8 | 100% |
| Trues | 97.1% | 97.6% | 98.7% | 98.6% | 97.5% | 100% |

gaussian blurring remain below 5%, which confirms the predictions and motivates a detectability study.

Fig. 5.12 shows six simulated and reconstructed spherical sources immersed in a homogeneous background with a signal-to-background activity ratio of 6:1. The recon-

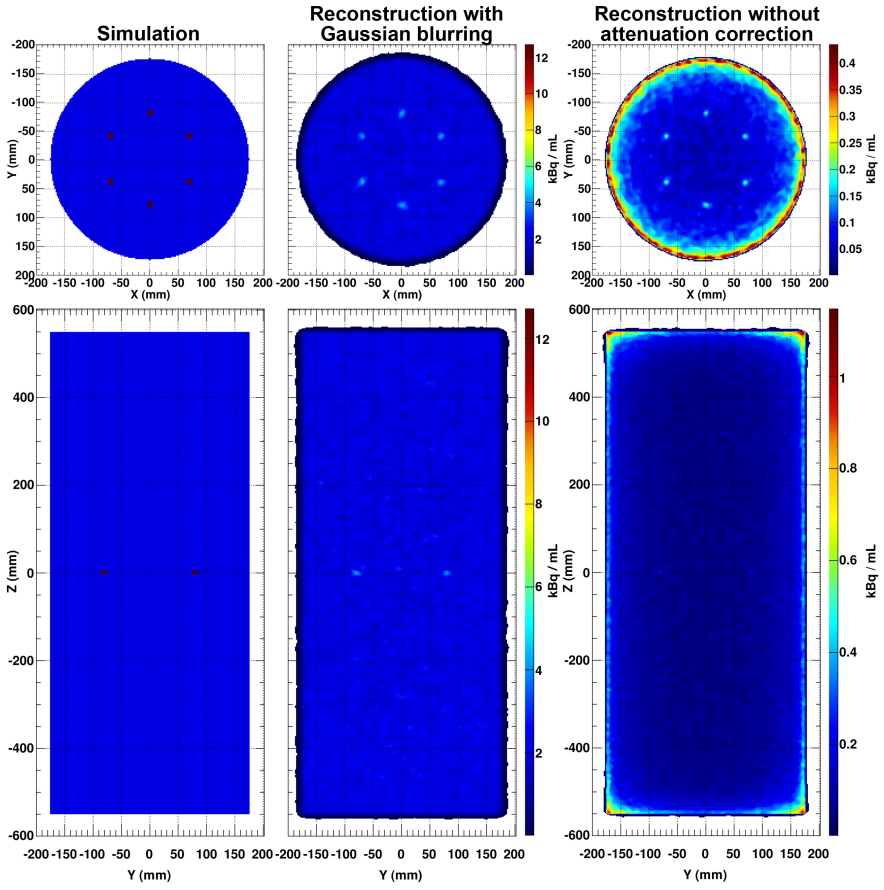


**Figure 5.12:** Six simulated and reconstructed spherical sources immersed in a homogeneous activity background. The top images represent the axial view of the cylinder with 35 cm diameter: simulated emission phantom (left), reconstruction image without attenuation correction (right), and corrected by attenuation on-the-fly on a LOR-to-LOR basis (middle). The bottom row presents the corresponding sagittal views. A cut on the intensity scale was performed on the reconstructed images. Reconstructed image reproduces well simulation phantom, despite the lower visual contrast of the spheres.

struction was blindly applied to 36 M lesions-plus-background detected true events and the result after 20 MLEM iterations is presented in fig. 5.12, middle and right columns. Fig. 5.12, left column, presents the simulated emission phantom, while the difference

between figs. 5.12 (middle) and (right) lies in the implementation of attenuation correction and a gaussian blurring on the detection position. Reconstruction and simulated phantom demonstrate a good agreement in quantitative values of the background despite the lower contrast of the spheres in the reconstructed images and the increased statistical noise and background variability caused by a low statistics dataset.

### 5.2.2 A whole-body single-bed TOF-based reconstruction for RPC-PET

#### 5.2.2.1 Attenuation correction

Fig. 5.13 illustrates the contribution of attenuation correction to the full-body reconstruction. The edges of the body, which are falsely increased in intensity on a non-attenuation-corrected image (right), become homogeneously represented, upon correction (middle). Regions of the body showing the presence of a lesion (fig. 5.13, middle) loose such information due to the absence of proper attenuation correction which would contribute to the decrease of specificity of the system. In addition, in fig. 5.13, left and

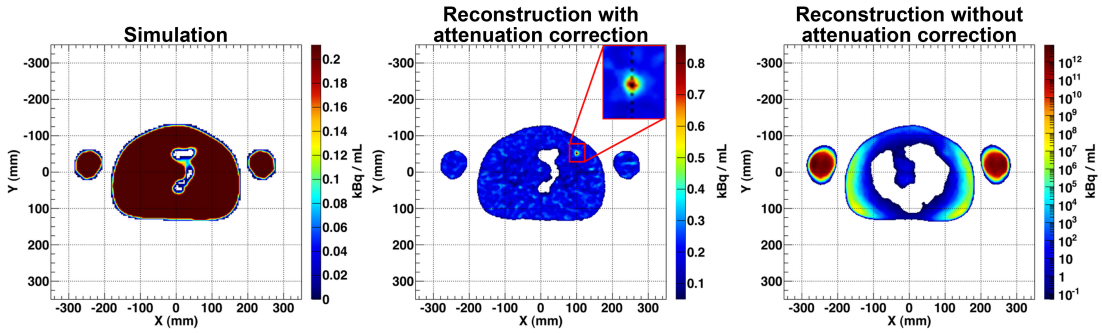


**Figure 5.13:** Comparison between 2 mm thick slices along the axial view of a a simulated image (left) and two reconstructed images with (middle) and without (right) attenuation correction. A lesion positioned in the inguinal region can only be seen in the left and middle image. The lack of attenuation correction makes this lesion invisible in the right image, therefore contributing to a decrease of system specificity. In addition, the middle column shows the empty space of the intestine, in agreement with the simulation (left), with this information being largely disturbed without attenuation correction (right).

middle, it is possible to visualize the empty space of the intestine in an axial view at bowel level, with this information being largely disturbed without attenuation correction.

#### 5.2.2.2 TOF kernel

A study of the contribution of the TOF kernel filling to the quality of the images is shown in fig. 5.14. By comparison of the evolution of the root mean squared error

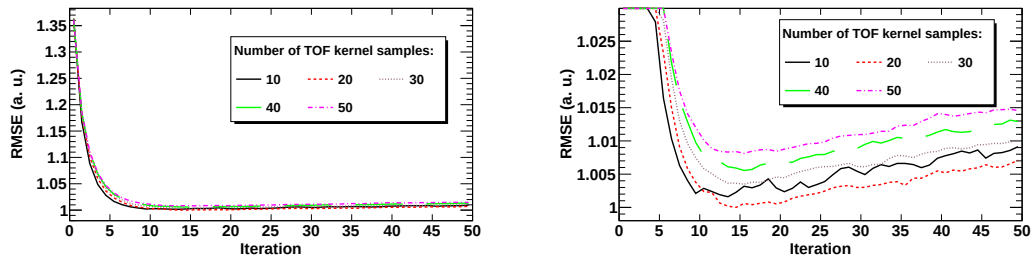


**Figure 5.14:** Comparison between different number of TOF kernel sample values, ranging from 10 to 50. For a TOF kernel filling inside the Gaussian above 20 samples there is no remarkable improvement in the error.

(RMSE) for different number of TOF kernel samplings, it can be seen that there is no significant improvement in the convergence of the algorithm for a number of kernel samples superior to 20. The images comparing a TOF kernel of 20 and 50 samples depicted in fig. 5.15 are almost indistinguishable and are in good agreement with the

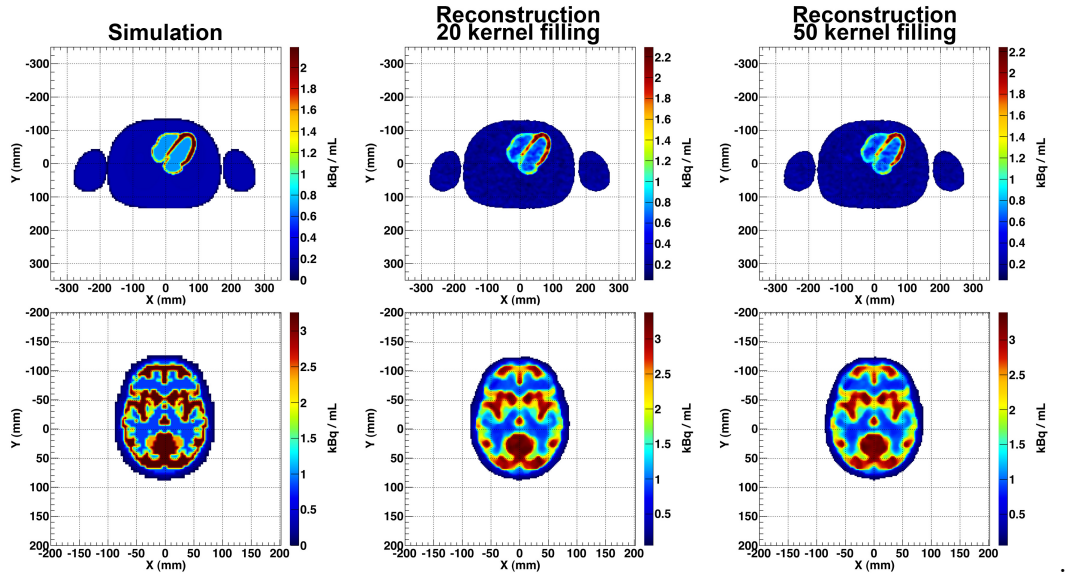


**Figure 5.15:** Two millimeter thick slices showing the contribution of the TOF kernel filling to the image structural information. Left: simulation. Middle and right: reconstruction obtained with a TOF kernel filling of 20 and 50 samples, respectively. It can be seen that the improvement in image quality with a TOF kernel sampling above 20 is marginal.

simulation image. For a TOF with a kernel sampling of 1 and 5 the algorithm did not converge due to lack of enough statistics, resulting from a under-sampled TOF kernel.

#### 5.2.2.3 Reconstructed images

Fig. 5.16 shows the results of the RPC-PET reconstruction applied to Geant4 simulated data based on the NCAT anthropomorphic phantom. The images on the left of fig. 5.16

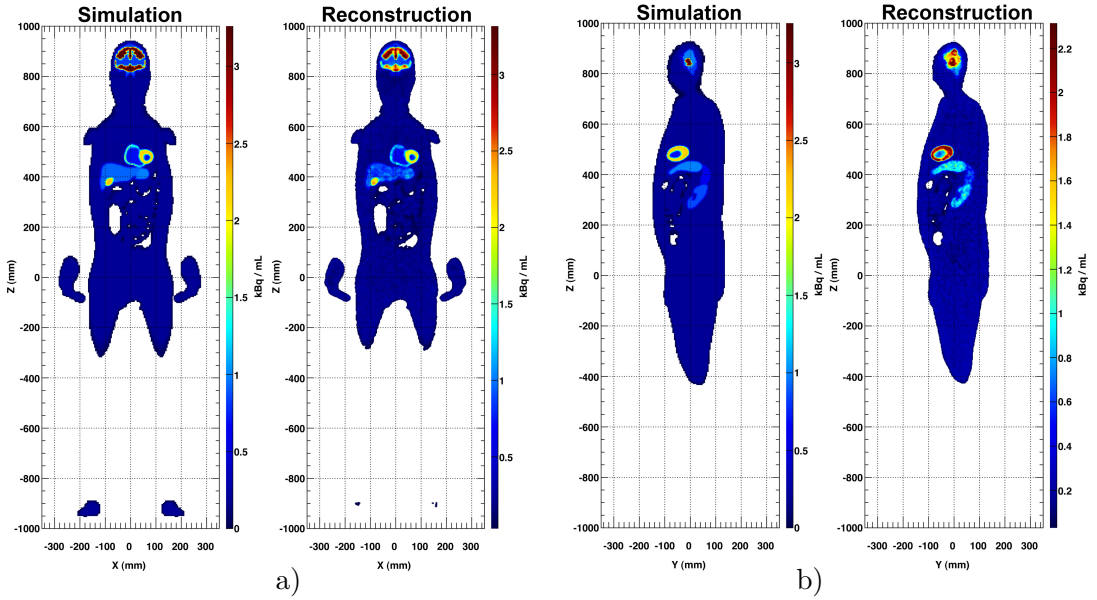


**Figure 5.16:** Results of the RPC-PET reconstruction applied to Geant4 simulated data based on the NCAT anthropomorphic phantom (left columns in a) and b)). The right column in a) and b) shows reconstructed results after 20 MLEM iterations. The two views represent 2 mm thick slices across the heart region. Sagittal view (b) shows left ventricle, stomach, spleen and kidney, while coronal view (a) shows both ventricles of the heart well separated from liver and stomach. Gallbladder and intensity depressions on the intestine region are also visible.

a) and b) represent the coronal and sagittal views of the NCAT simulation phantom, respectively. The images on the right of the same figure show the reconstruction images of 49 M true events after 20 MLEM iterations. A lower cut on the intensity scale was performed, as well as on the following reconstructed images, in order to remove the very-low intensity from voxels filled with the tails of the Gaussian TOF kernel. Coronal and sagittal views of the brain are also included in fig. 5.17 demonstrating the capabilities of RPC-PET to reveal the detailed structures of the brain.

Fig. 5.18 a) presents the coronal and sagittal views of the TOF-based backprojection

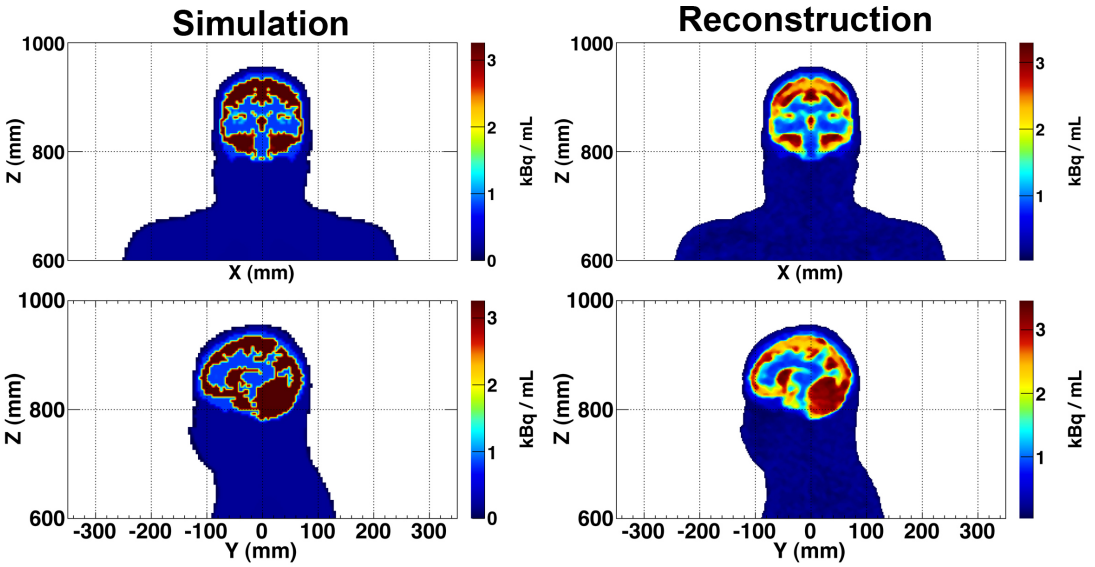


**Figure 5.17:** Comparison between NCAT anthropomorphic phantom brain simulated (left) and reconstructed (right) image. A very good agreement between cerebellum and other activated regions of the brain is observed, revealing detailed structural information of the brain.

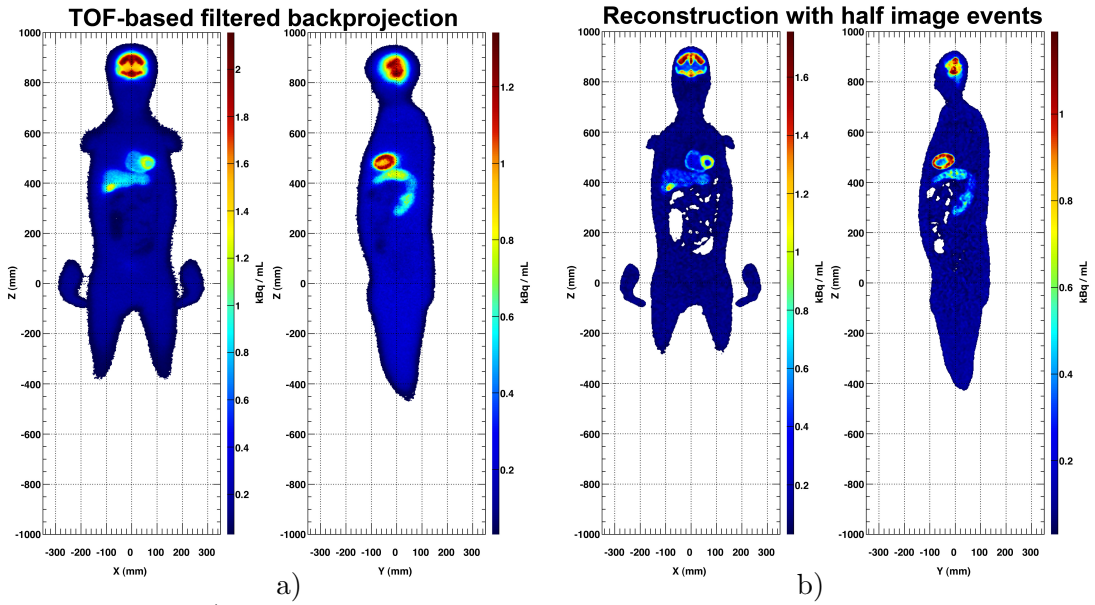


**Figure 5.18:** a) Coronal and sagittal view of a TOF-based backprojection of all detected data. A median filter was applied to denoise the image. All organs aforementioned are already visible. Potential real-time visualization feasibility. b) Reconstructed image of half of the events hitherto considered. A degradation on the homogeneity of the organs is notorious, inducing possible false lesions.

of 49 M true events, after applying a median filter. This image calls for the potential real-time visualization capability in RPC-PET scans, due to the TOF benefit.

A reconstruction of half of the events considered hitherto was performed to compare with the images of fig. 5.16. The same image slices are displayed in fig. 5.18 b). All organs, particularly the stomach and the kidney, become less homogeneous, noisier, hindering the possibility of detecting a lesion. This shows that a predominant variable for improving image quality is the number of events, which takes us to the conclusion that the increase of sensitivity is one of the main achievements of RPC-PET.

### 5.2.3 Scatter rejection fraction

As can be seen in fig. 5.19, with an increasing TOF resolution, the probability of the calculated annihilation scatter point being within the human body decreases exponentially, leading to an increase in the scatter rejection fraction (SRF). For 2.5 ns, which corresponds almost to the non-TOF case, there are still scattered LORs that do not cross the NCAT phantom and contribute to the SRF.

$$SRF = \frac{scattered\ events\ rejected\ with\ TOF}{total\ scattered\ events\ detected} \tag{5.7}$$

Since RPC-PET does not have energy resolution, although it has energy sensitivity [210], even for a poorer TOF resolution, there is still a high SRF.

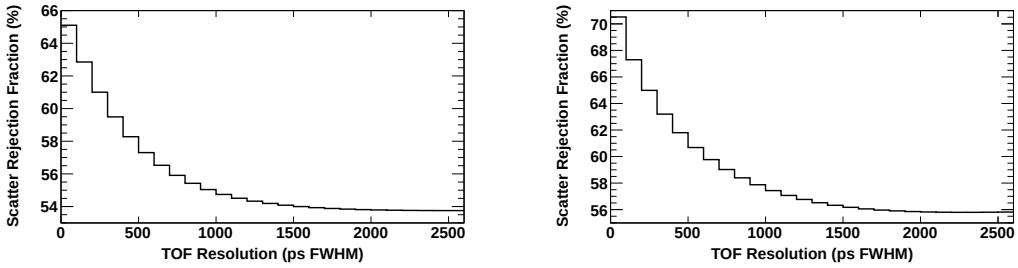


**Figure 5.19:** Curve of the scatter rejection fraction (SRF) for a decreasing TOF resolution, calculated for the homogeneous cylindrical phantom (left) and for the NCAT phantom (right). We observe that the SRF grows exponentially with an increasing TOF resolution. For a 300 ps FWHM TOF resolution, the SRF is 60% and 63% for the homogeneous cylindrical phantom and for the NCAT phantom, respectively. For a 600 ps FWHM TOF resolution, these values decrease to 57% and 60%, respectively.

### 5.2.4 Six lesions in anthropomorphic phantom: towards lesion detectability

Fig. 5.20 shows two sets of 2 mm thick slice images, each presenting five simulated lesions. We compare the images containing the original annihilation points with those reconstructed from true events with a 300 ps FWHM TOF kernel, after 20 MLEM iterations. All lesions are perfectly distinguishable. Figs. 5.20 and 5.21, as well as all figures hereinafter presented containing the three views of the five lesions, were normalized to 80% of the maximum intensity in the brain.

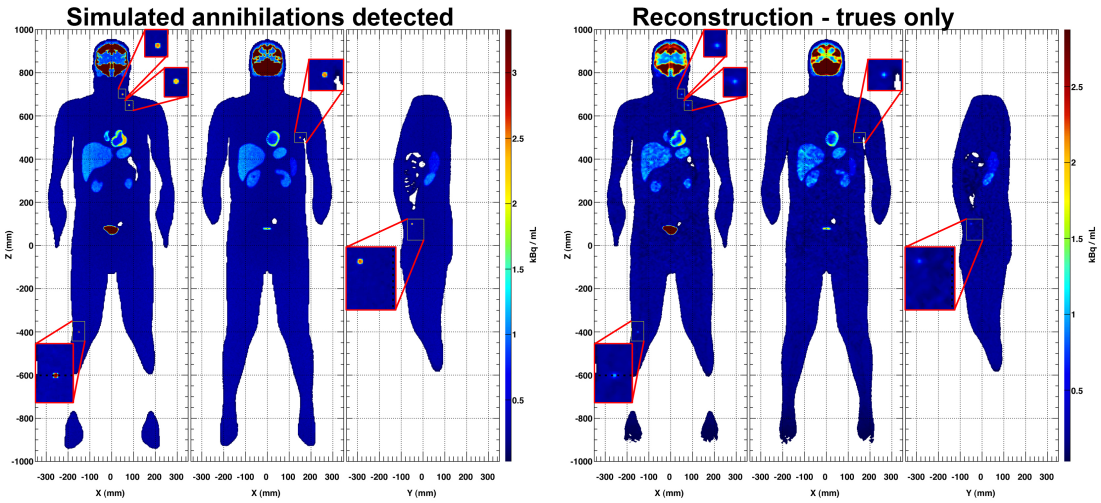


**Figure 5.20:** Whole-body 2 mm thick slice images showing five lesions: cervical, subclavicular, knee, axillary, and inguinal. The reconstructed results were obtained after 20 MLEM iterations. A windowing on the intensity scale was performed to distinguish the lesions. The left image shows the original annihilation points, while the right image presents the reconstructed images of the trues events with a 300 ps FWHM TOF kernel. In both, lesions are perfectly visible.

In fig. 5.21 we included the body-scattered events detected by an RPC-PET system with 120 gaps (fig. 2.36 (right)) and compared the 300 ps and 600 ps FWHM TOF kernels, after performing the TOF-based scatter rejection. The comparison with the 600 ps FWHM TOF case is in line with the state of the art commercial PET scanners and with the work developed by the instrumentation group that created the $LaBr_3$ PET scanner [323].

Comparing to the reconstructed images after performing the rejection cuts with a 600 ps FWHM TOF kernel (fig. 5.21, right), all lesions observed in the 300 ps FWHM

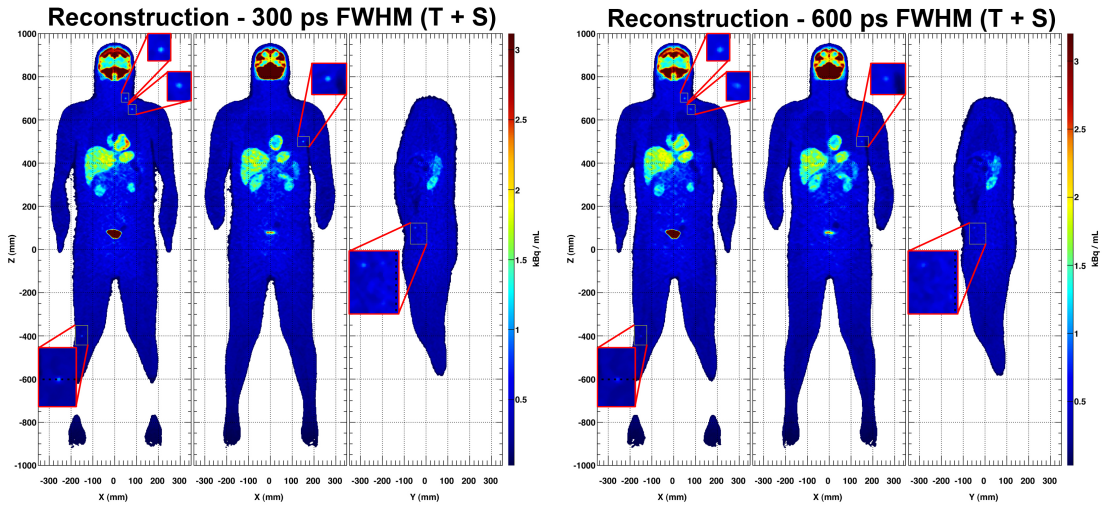


**Figure 5.21:** Reconstructed images of the data detected by an RPC-PET system after including the scattered events and performing the rejection cuts with a 300 ps (left) and a 600 ps (right) FWHM TOF kernel. The abdominal region is more contaminated by scatters, however this region becomes cleaner due to the scatter rejection properties of RPC-PET. The organs are still well separated: the heart from the stomach, and the right kidney from the liver. The spleen is still visible. The visual contrast improves in all lesions for a 300 ps FWHM TOF resolution (left), mainly the inguinal one, which is almost undistinguishable with a 600 ps FWHM TOF resolution (right).

images (fig. 5.21, left) improve visual contrast, mainly the inguinal one, which is almost undistinguishable in the 600 ps FWHM TOF kernel case. The contribution of the scatters in the abdomen region is highly suppressed and the organs appear well separated and partly visible. The spleen is also visible and visually separated from the left kidney. The stomach can be observed separated from the heart and the liver, and the right kidney is also detached from the liver. Therefore, the combination of an RPC-PET detector with a higher TOF resolution increases the detectability, mainly in regions more sensitive to the contribution of the scattered events, such as those closer to the abdomen.

To better distinguish each of the six lesions we display the corresponding axial slices crossing the maximum intensity voxel of each lesion in fig. 5.22. The line profiles shown in the images in the bottom of fig. 5.22 allow discriminating the presence of a lesion in all six cases, including the inguinal one, which was more difficult to detect in the coronal and sagittal views in fig. 5.21. This is due to its location in the outer region of the abdomen, where contaminating background is less prone than in the center. The

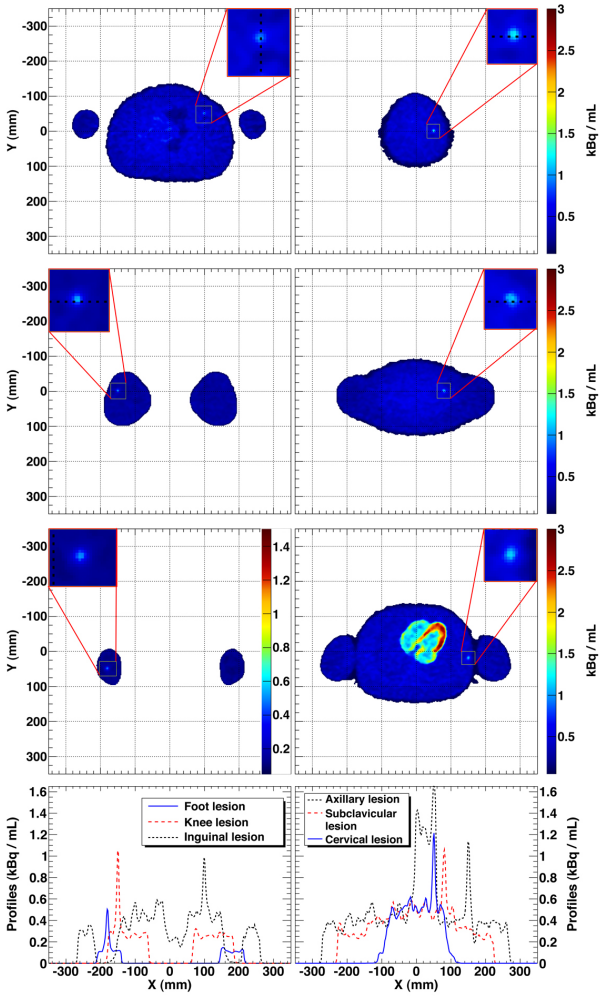


**Figure 5.22:** Axial views corresponding to 2 mm thick slices crossing the six lesions. On the left column, it is exhibited the: foot (bottom); knee (middle); inguinal (top) lesions. On the right column it is shown the: axillary (bottom); subclavicular (middle); cervical (top) lesions. All lesions are well distinguished from background and have the expected spherical shape with 10 mm diameter. The knee lesion has the highest contrast and the axillary lesion is easily detected despite the presence of the heart. The inguinal lesion can still be distinguishable, despite the contribution of the scattered events in the inner region of the abdomen. All lesions have a similar maximum intensity, except the foot lesion, which is not covered by the whole RPC-PET solid angle acceptance.

knee lesion has the best contrast, while the axillary lesion shows up with good contrast despite the presence of the heart in the image. All images, except the one containing the foot lesion, were normalized to the maximum activity in the heart walls. The foot lesion loses activity due to its presence in the extremity of the RPC detection system

and was then normalized to half of the maximum intensity in the heart walls.

In order to evaluate the influence of all aforementioned contributions to the reconstruction image in the case of an inguinal lesion, which is the most critical, we present a comparison concerning TOF resolution, scatter rejection by TOF, and image median filtering influence. In fig. 5.23 (left) a distribution of the annihilation points after (top) and before (middle) performing a median filter is shown. Median filter reduces the

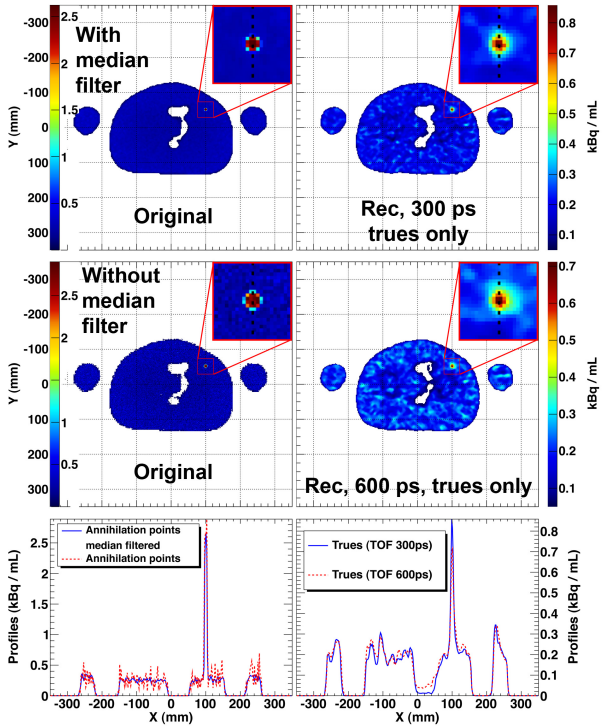


**Figure 5.23:** Axial views corresponding to 2 mm thick slices containing the inguinal lesion. On the left column, the original annihilation points after (top) and before (bottom) passing through a median filter are shown. The profiles show the "salt-and-pepper" noise arising from the lack of statistics, which are flattened with the median filter. On the right column, the reconstruction of the true events with a 300 ps FWHM TOF resolution (top) and a 600 ps FWHM TOF resolution (middle) is shown. A TOF resolution of 300 ps FWHM results in a more homogeneous image, gives more contrast to the lesion, and resolves the non-activity region of the intestine.

so-called "salt-and-pepper" noise due to the lack of statistics and distorts the lesion shape as a result of the non-uniform activity in the neighboring voxels of the lesion. This effect (left images) vanishes in the reconstruction (right images) due to the sample filling of the TOF kernel. Fig. 5.23 (right) presents the reconstruction of the true events

with a TOF resolution of 300 ps FWHM (top) and 600 ps FWHM (middle). The top image is more uniform, the lesion has a better visual contrast and the intestine region is well resolved.

Fig. 5.24 illustrates the effectiveness of an RPC-PET system with a 300 ps FWHM TOF resolution to remove the scatters and detect the inguinal and axillary lesions. For

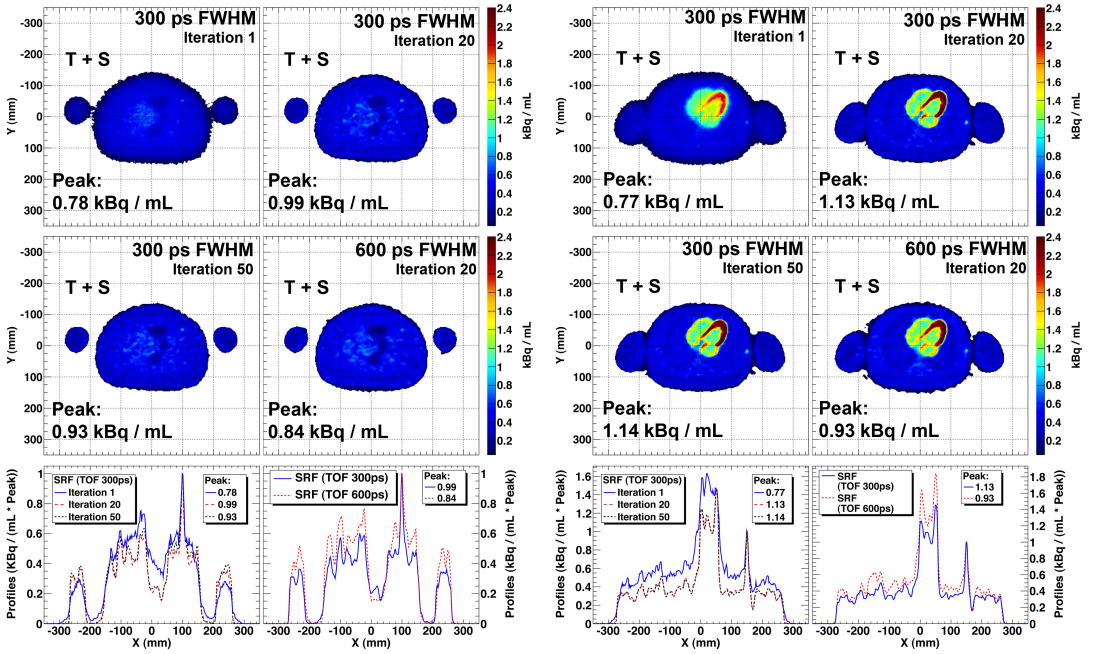


**Figure 5.24:** Axial views of 2 mm thick slices containing the inguinal (left) and the axillary (right) lesions. The profiles on the left column compare iteration 1, 20, and 50. The images corresponding to iteration 20 (top right) and 50 (middle left) are very similar, as well as their profiles (bottom left). The lesion is discernible from the neighbouring regions, due to the decreasing contribution of the scattered events. Top and middle images have their intensity normalized to 80% maximum in the heart. Profiles (bottom) were normalized to the maximum intensity in the lesion (peak).

both lesions, the top and middle axial views of the right column correspond to a TOF resolution of 300 ps FWHM and 600 ps FWHM, respectively (both at the $20^{th}$ iteration). As aforementioned, a 300 ps TOF resolution increases the lesion contrast. The number of iterations are also compared to verify their influence on lesion detectability. There is a convergence of the reconstructed image at iteration 20, with the heart becoming well delimited and all structural information, including the one influenced by the scattered events, stabilized. The lesion uptake value (peak) increases both with iterations and improved TOF resolutions. The inguinal lesion, due to its presence in the outer region

of the abdomen, is better distinguished from the scattered contaminated inner region in the 300 ps FWHM TOF resolution case. The uptake value of this lesion is, however, slightly reduced between iteration 20 and 50, while for the axillary lesion, it stabilizes around 1.14 kBq/mL.

### 5.2.5 Performance

#### 5.2.5.1 RMSE evolution

Fig. 5.25 presents the RMSE evolution for the MLEM reconstruction along 200 iterations for the NCAT (left), and along 80 iterations for the spheres in a homogenous background (right). The RMSE was calculated between the simulated or mathematical

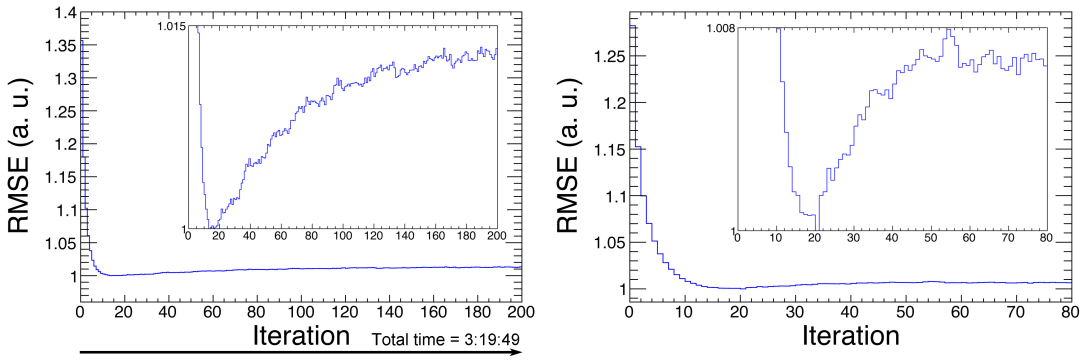


**Figure 5.25:** Graph of the evolution of the RMSE along 200 iteration calculated between NCAT simulated image and the reconstructed true events image (left), and along 80 iteration calculated between the mathematical image of the spheres in a homogeneous background and the reconstructed true events image (right). In both, the convergence is reached after 20 iterations.

image and the reconstructed true events image. The metrics could take into account the trues or the scattered events. Reconstruction with scattered events was not considered, due to a consequent bias, unless a scatter correction would be proper implemented. RMSE converges after 20 iterations, a fact that led us to the decision of stopping the reconstruction at iteration 20 (in this study).

#### 5.2.5.2 Image division

As an alternative approach to a whole-body reconstruction, we propose to divide the reconstructed image, based on the data arising from nine different regions of the body. Fig. 5.26 a) presents the results of the nine independent reconstructions after 20 MLEM iterations, whose resulting images are then summed and displayed as shown in

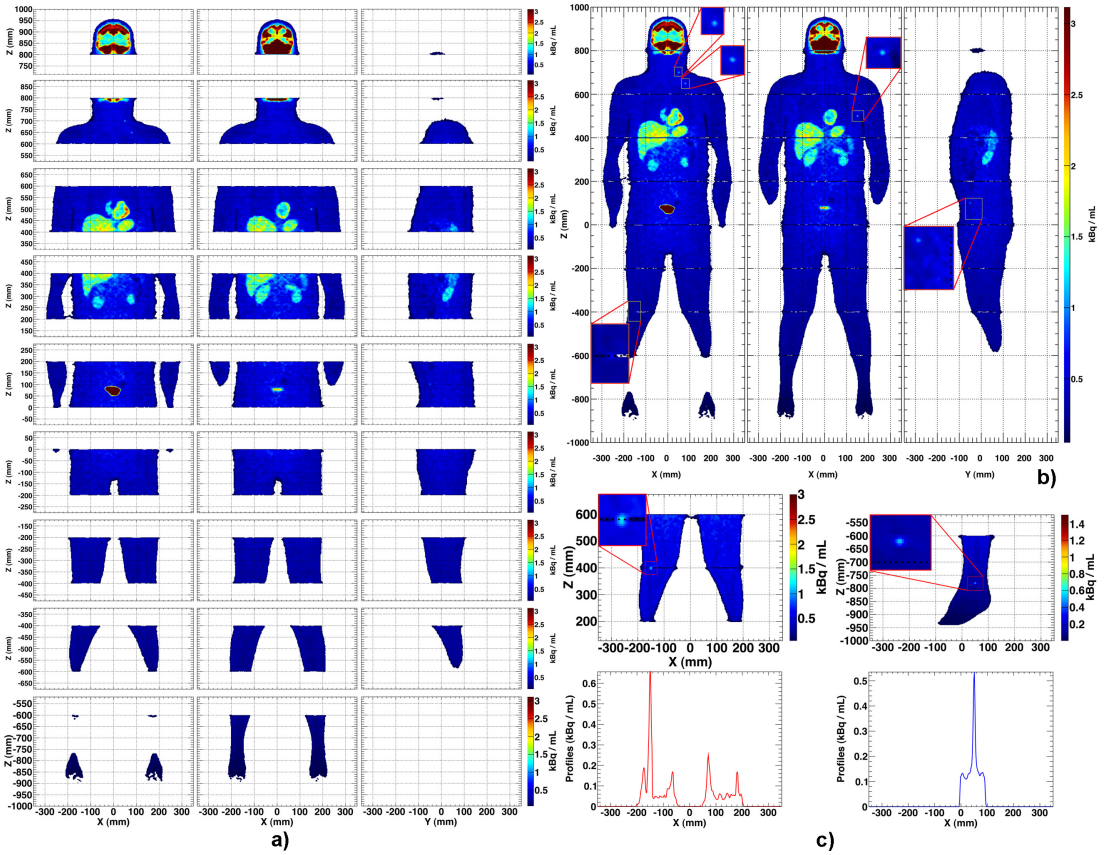


**Figure 5.26:** a) Reconstruction method based on the division of the data through nine different regions of the body. This image represents the nine independent reconstructions, obtained after 20 MLEM iterations. This strategy allows for the full whole-body reconstruction to be performed in 4 minutes only, which compares with 21 minutes if the whole-body is considered. b) Reconstructed image resulting from the sum of the nine independent reconstructions depicted in a). There is no substantial difference to the whole-body reconstruction shown in fig. 5.21 (left), except for the borders between each of the nine summed images. This is a consequence of the median filter used between iterations to stabilize the convergence of the algorithm. c) Reconstructed images of the legs (left) and the right foot (right). Although the lack of activity in the inner part of the leg where the two images sum, this does not affect greatly the lesion detectability. Doing an analysis of each of the nine independent reconstructions, it is possible to detect a lesion in the foot, which could go undetected in a whole-body reconstruction due to the lack of intensity in this region in respect to the rest of the body, the latter being fully covered by the solid angle of the RPC-PET system.

fig. 5.26 b). This method improves the reconstruction speed as presented in table 5.3. A margin of $3\sigma$ has to be given in order to consider the events laying outside the image

**Table 5.3:** Reconstruction time (minutes) for the presented images. Timing in bold indicates largest computing time.

| | | **SRF (300 ps FWHM) - Body divided into nine regions** | | | | | |
|---|---|---|---|---|---|---|---|
| | Body Region | Head Superior | Head Inferior | Torso Superior | Torso Inferior | Abdominal Superior | Abdominal Inferior |
| Pre-processing | Scatter Rejection | 0:06 | 0:02 | 0:05 | 0:04 | 0:03 | 0:03 |
| | Attenuation correction | 0:06 | 0:03 | 0:05 | 0:04 | 0:04 | 0:03 |
| | Total | 0:12 | 0:05 | 0:10 | 0:08 | 0:07 | 0:06 |
| | Backprojection | 0:14 | 0:11 | 0:13 | 0:13 | 0:13 | 0:11 |
| Reconstruction | 16 CPUs - 20 iterations | 7:16 | 4:52 | 6:55 | 6:16 | 5:51 | 5:16 |
| | 16 CPUs - LUT (300 ps) | 4:13 | 3:38 | 4:44 | 4:28 | 4:20 | 4:06 |
| | GPU - 20 iterations | **4:39** | 3:29 | 4:23 | 4:01 | 4:02 | 3:46 |
| | GPU - LUT (300 ps) | 3:30 | 2:48 | **3:33** | 3:14 | 3:04 | 2:51 |

| | | | | | **Whole Body** | | | |
|---|---|---|---|---|---|---|---|---|
| | | **SRF (300 ps FWHM)** | | | SRF | SRF | Trues | Trues |
| | | Legs Superior | Legs Inferior | Feet | 300 ps FWHM | 600ps FWHM | 300 ps FWHM | 600 ps FWHM |
| Pre-processing | Scatter Rejection | 0:03 | 0:02 | 0:02 | 0:27 | 0:44 | - | - |
| | Attenuation correction | 0:03 | 0:02 | 0:02 | 0:41 | 0:52 | 0:25 | 0:25 |
| | Total | 0:06 | 0:04 | 0:03 | 1:08 | 1:36 | 0:25 | 0:25 |
| | Backprojection | 0:10 | 0:10 | 0:12 | 1:40 | 2:16 | 1:20 | 1:53 |
| Reconstruction | 16 CPUs - 20 iterations | 4:37 | 4:05 | 4:14 | 41:33 | 1:05:10 | 34:07 | 50:57 |
| | 16 CPUs - LUT (300 ps) | 3:51 | 3:32 | 3:51 | 33:52 | - | 27:00 | - |
| | GPU - 20 iterations | 3:17 | 2:51 | 3:08 | **24:15** | 28:04 | 22:03 | 22:49 |
| | GPU - LUT (300 ps) | 2:36 | 2:22 | 2:40 | **21:11** | - | 17:03 | - |

while iterating on the TOF-kernel.

The images obtained from the image division approach, when summed, still lack of some intensity in the borders between those images. This effect becomes more visible the greater the number of iterations performed. It arises due to the median filter applied between iterations to stabilize the reconstruction, avoiding instability of the algorithm due to the so-called "salt-and-pepper" noise. This kind of filter tends to

reduce the intensity in a voxel if several surrounding voxels are null, which actually occurs in the borders of the divided images. Nevertheless, this lack of intensity in the borders between divided images affect just two slices of 2 mm each, and mainly the background. As depicted in fig 5.26 c) (left), the knee lesion positioned in the divided image borders, despite the contrast loss, still preserves its shape and remains visible. This image division method allows a quick detection of unexpected lesions, like the one in the foot presented in fig. 5.26 c) (right). Even for this region, where the RPC-PET detector is less sensitive, this lesion is well detected, mainly due to the absence of other organs.

#### 5.2.5.3 Constant Gaussian look-up-table

In order to improve even further the reconstruction speed, a different routine was implemented to reconstruct the RPC-PET data. As aforementioned, instead of generating random time uncertainty numbers, which is computationally time consuming, a LUT was generated with the 300 ps FWHM TOF uncertainties transformed in the corresponding space variables with their respective weights. As depicted in fig. 5.27 and comparing with fig. 5.26 b), the two approaches produce similar images.

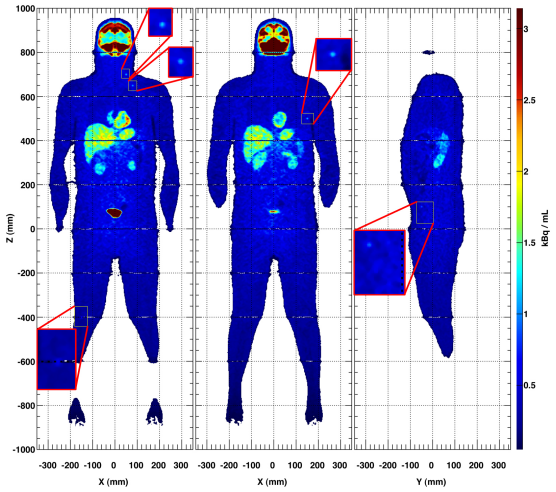


**Figure 5.27:** Reconstructed images resulting from a different reconstruction routine adapted to speedup the convergence of the algorithm. In this approach, a LUT with the space uncertainty associated to TOF and its corresponding weight is generated and stored in the constant memory of the GPU, increasing the compute-to-memory access ratio. The image is quite similar to the ones depicted in fig. 5.26 b) and fig. 5.21 (left) and results from the sum of the nine divided reconstructed images.

Fig. 5.28 compares the axial slices of the reconstructed images, containing the inguinal and axillary lesion, and obtained from the two proposed routines. On the left

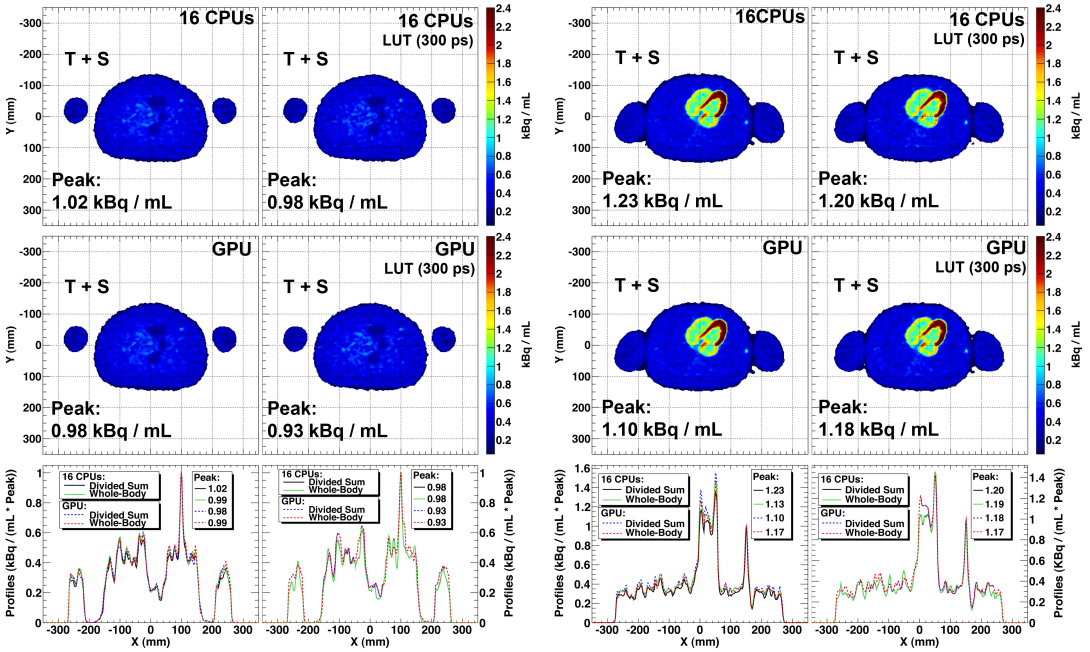


**Figure 5.28:** Comparison between the axial views containing the inguinal (left) and axillary (right) lesions for the two proposed routines, the one with a random filling of the TOF kernel giving an equal weight to all samples (left) and the routine that resorts to the previously defined LUT with the space uncertainties associated to TOF and their respective weight (right). They are quite similar and their profiles confirm it. The top images were reconstructed with 16-threads CPUs while the bottom images resorts to the GPU to increase the convergence speed. The four images resemble themselves and the difference between the profiles of the sum of the divided images and the whole-body reconstruction using the second routine is negligible. The same intensity normalization applied to the images of fig. 5.24 was used here.

column the images resulting from the random sampling of the TOF kernel are displayed. On the right column, we show the images corresponding to the application of the LUT containing the space uncertainty associated to TOF and its respective weight. The top images arise from the 16-threads CPUs implementation of both routines, while the bottom images result from the GPU assisted by 16-threads CPUs implementation of those same routines. Because the second routine reproduce always the same output image, the whole-body reconstruction and the sum of the divided images are virtually identical. This can be observed on the superposition of the profiles of the right column. This confirms the reliability of the reconstructed image division method. The

first routine also reproduces very similar images, regardless of the statistical variations associated to the random sampling of the TOF kernel.

#### 5.2.5.4 TOF-OSEM algorithm and independent reconstructions

Fig. 5.29 a) corresponds to the axial view containing the inguinal lesion. The difference

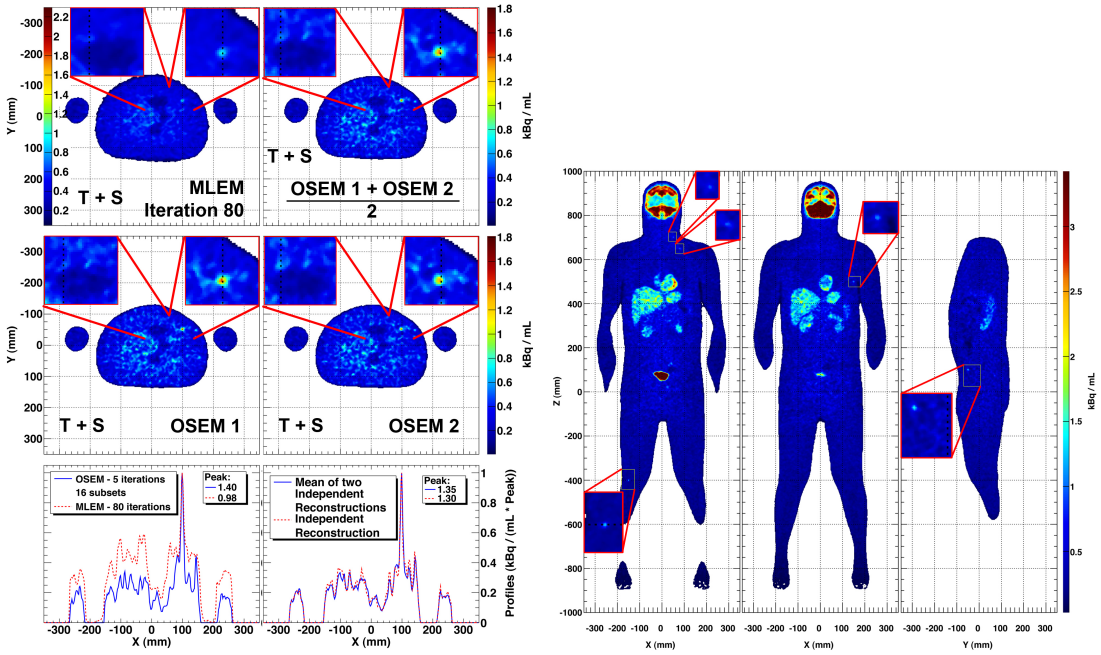


a) b)

**Figure 5.29:** a) Comparison between the MLEM and OSEM algorithms and evaluation of the usefulness of performing similar independent reconstructions to improve system specificity. The images in the middle row correspond to two similar independent OSEM reconstructions. Some false hot spots are present in different locations from image to image corresponding to statistical fluctuations that differ between the two images and that could lead to false lesion triggers (false positives). The top right image results from the mean of the middle images. It can be seen that the real lesion does not lose contrast, whereas the intensity of the peaks due to statistical fluctuations is decreased. The bottom line profiles corroborate this observation. b) Whole-body 2 mm thick slice images showing the five lesions obtained from the implementation of the OSEM algorithm. Comparing to fig. 5.21, the inguinal and knee lesion seem to improve contrast. However, by cause of lack of statistics, the organs show up less homogeneous and the cervical, subclavicular and axillary lesion appear to loose contrast.

between the images lies on the implementation of the MLEM (top left) and OSEM (top right and middle) algorithm. While applying the MLEM algorithm to independent reconstructions reproduces indistinguishable images, when adopting the OSEM

algorithm, statistical fluctuations emerge in different places in similar independent reconstructions (two middle images in fig. 5.29 a)). This effect arises from the random sampling of the TOF kernel, which culminates in different reconstructed images, as observed. The middle images exhibit two independent OSEM reconstructions. Some regions were zoomed to observe that, on the top left of each image, some fluctuations near the intestine do not appear in both independent reconstructions, while the structural information about the intestine remains. The same happens for the lesion. The top right image displays the mean of the two independent OSEM reconstructions. Without correlation analysis, these hot spots present in just one of the two images could trigger false positives, hence decreasing system specificity.

We observe, as well, that comparing to the MLEM algorithm, the OSEM algorithm reduces the noise in the inner regions of abdomen contaminated by scattered events, increasing lesion detectability. The contrast of this specific lesion is also improved and the space between the arms and the body is better resolved. However, this behavior is not regular for other lesions. Comparing fig. 5.29 b) with figs. 5.21 (left), 5.26 b), and 5.27, the cervical, subclavicular, and axillary lesions loose contrast and the organs become less homogeneous due to lack of statistics. Nevertheless, the inguinal lesion is undoubtedly better perceptible and the knee lesion increases its visual contrast.

In conclusion, MLEM vs. OSEM results suggest that both approaches yield clinically relevant information. Which algorithm performs better seems to be a matter of the body region being imaged.

#### 5.2.5.5 Contrast recovery coefficients

The CRC values for the six spheres in homogeneous phantom obtained from the reconstruction of the true events, with a TOF resolution of 300 ps FWHM, and at iteration 20 (MLEM) are presented in table 5.4.

Analyzing the results from the reconstruction of the NCAT data presented in table 5.5, we observe that there is a good agreement between the CRC values obtained

**Table 5.4:** CRC values for six spheres in homogeneous phantom (%)

| | **Trues (300 ps)** | | | | | |
|---|---|---|---|---|---|---|
| Lesions | 1 | 2 | 3 | 4 | 5 | 6 |
| Iteration 20 | 18.1 ± 2.0 | 19.4 ± 2.1 | 24.3 ± 3.6 | 17.7 ± 2.0 | 22.0 ± 2.4 | 16.0 ± 1.4 |

**Table 5.5:** CRC values for six lesions immersed in the NCAT phantom (%). Vertical time values are presented in FWHM.

| | | **16 CPUs** | | | | | |
|---|---|---|---|---|---|---|---|
| | Lesions | Foot | Knee | Inguinal | Axillary | Subclavicular | Cervical |
| Trues (300 ps) | Iteration 1 | 19.9 ± 3.3 | 18.5 ± 3.7 | 17.8 ± 3.4 | 18.5 ± 3.8 | 20.8 ± 4.6 | 18.9 ± 3.8 |
| | Iteration 20 | 32.5 ± 8.4 | 26.4 ± 7.2 | 23.5 ± 4.7 | 23.7 ± 6.9 | 30.3 ± 7.7 | 26.6 ± 7.5 |
| | LUT (Iter. 20) | 28.0 ± 6.6 | 28.9 ± 7.4 | 28.0 ± 6.1 | 23.8 ± 6.5 | 32.9 ± 9.1 | 32.4 ± 8.5 |
| | Iteration 50 | 31.8 ± 8.0 | 27.3 ± 7.6 | 25.3 ± 5.6 | 23.9 ± 7.3 | 27.9 ± 7.5 | 28.0 ± 7.5 |
| Trues (600 ps) | Iteration 1 | 15.9 ± 2.4 | 12.2 ± 2.0 | 10.7 ± 1.5 | 9.1 ± 1.4 | 10.5 ± 1.4 | 10.3 ± 1.5 |
| | Iteration 20 | 29.0 ± 6.7 | 23.6 ± 5.6 | 20.2 ± 3.6 | 18.8 ± 4.4 | 23.9 ± 5.4 | 21.6 ± 5.0 |
| | Iteration 50 | 27.9 ± 5.9 | 24.9 ± 5.4 | 19.2 ± 3.6 | 16.6 ± 4.2 | 23.4 ± 5.6 | 22.8 ± 5.2 |
| SRF (300 ps) | Iteration 1 | 16.7 ± 2.3 | 15.3 ± 2.6 | 6.4 ± 0.8 | 7.5 ± 0.7 | 7.1 ± 1.0 | 7.5 ± 0.8 |
| | Iteration 20 | | | | | | |
| | Division Sum | 27.1 ± 6.0 | 11.7 ± 1.8 | 11.6 ± 2.2 | 12.5 ± 1.9 | 10.5 ± 1.8 | 10.3 ± 1.5 |
| | Whole-Body | 26.6 ± 5.5 | 22.7 ± 4.7 | 11.2 ± 1.8 | 12.0 ± 1.8 | 10.5 ± 1.7 | 10.4 ± 1.6 |
| | LUT (Iter. 20) | | | | | | |
| | Division Sum | 27.8 ± 6.0 | 12.5 ± 1.9 | 12.5 ± 2.5 | 14.1 ± 2.4 | 10.0 ± 1.8 | 10.9 ± 2.0 |
| | Whole-Body | 27.8 ± 5.9 | 24.3 ± 4.7 | 12.5 ± 2.5 | 14.1 ± 2.4 | 10.0 ± 1.8 | 10.9 ± 2.0 |
| | Iteration 50 | 27.5 ± 6.3 | 23.2 ± 4.8 | 11.0 ± 1.6 | 12.4 ± 1.5 | 10.5 ± 1.8 | 11.1 ± 1.7 |
| SRF (600 ps) | Iteration 1 | 13.6 ± 1.7 | 9.6 ± 1.2 | 4.2 ± 0.3 | 4.2 ± 0.4 | 4.4 ± 0.3 | 4.1 ± 0.3 |
| | Iteration 20 | 23.1 ± 4.4 | 16.1 ± 2.9 | 10.2 ± 1.1 | 7.6 ± 1.0 | 8.4 ± 1.1 | 8.3 ± 0.9 |
| | Iteration 50 | 25.5 ± 5.0 | 17.3 ± 3.2 | 9.9 ± 1.1 | 7.7 ± 0.8 | 8.0 ± 1.1 | 8.6 ± 1.0 |

| | | **GPU** | | | | | |
|---|---|---|---|---|---|---|---|
| | Lesions | Foot | Knee | Inguinal | Axillary | Subclavicular | Cervical |
| Trues (300 ps) | Iteration 1 | 19.5 ± 3.2 | 18.9 ± 3.9 | 17.6 ± 3.2 | 18.7 ± 3.6 | 21.6 ± 4.6 | 19.0 ± 4.0 |
| | Iteration 20 | 32.4 ± 7.4 | 28.0 ± 7.7 | 24.5 ± 5.7 | 23.9 ± 6.9 | 30.7 ± 9.3 | 29.0 ± 7.8 |
| | LUT (Iter. 20) | 28.2 ± 6.9 | 28.1 ± 7.1 | 25.5 ± 5.7 | 19.9 ± 5.7 | 29.1 ± 7.8 | 28.8 ± 7.9 |
| | Iteration 50 | 29.7 ± 7.4 | 27.2 ± 6.8 | 24.9 ± 5.7 | 26.5 ± 7.8 | 31.7 ± 9.3 | 28.9 ± 7.4 |
| SRF (300 ps) | Iteration 1 | 16.6 ± 2.3 | 14.9 ± 2.3 | 6.9 ± 0.9 | 7.6 ± 0.8 | 7.5 ± 1.0 | 7.3 ± 0.8 |
| | Iteration 20 | | | | | | |
| | Division Sum | 26.6 ± 5.9 | 12.1 ± 1.8 | 11.4 ± 1.8 | 12.9 ± 1.7 | 10.2 ± 1.8 | 11.5 ± 1.6 |
| | Whole-Body | 26.3 ± 6.0 | 23.6 ± 5.3 | 11.9 ± 1.9 | 12.7 ± 1.9 | 9.9 ± 1.7 | 11.1 ± 1.8 |
| | LUT (Iter. 20) | | | | | | |
| | Division Sum | 27.6 ± 5.7 | 11.0 ± 1.5 | 9.6 ± 1.4 | 12.7 ± 2.0 | 9.6 ± 1.5 | 9.9 ± 1.5 |
| | Whole-Body | 27.8 ± 5.7 | 22.1 ± 4.4 | 9.6 ± 1.4 | 12.6 ± 2.0 | 9.6 ± 1.5 | 10.0 ± 1.5 |
| | Iteration 50 | 26.8 ± 5.5 | 22.1 ± 4.9 | 12.3 ± 1.8 | 12.2 ± 1.7 | 10.5 ± 1.8 | 10.0 ± 1.5 |
| | OSEM | | | | | | |
| | Reconst. 1 | 55.2 ± 15.9 | 25.1 ± 6.7 | 17.0 ± 4.1 | 12.4 ± 2.5 | 7.8 ± 1.9 | 10.2 ± 2.1 |
| | Reconst. 2 | 54.2 ± 18.4 | 25.2 ± 5.8 | 14.6 ± 3.8 | 10.6 ± 2.1 | 9.1 ± 2.2 | 10.4 ± 1.7 |
| | Mean | 54.7 ± 16.8 | 25.2 ± 6.1 | 15.8 ± 3.7 | 11.5 ± 2.2 | 8.4 ± 2.0 | 10.3 ± 1.8 |

with the GPU and the 16-threads CPUs implementations of the reconstruction routines. Both reconstruction routines presented return similar values, as well. Fig. 5.30 plots the profiles taken along the 6 lesions and corresponding background. They were obtained from the reconstruction of the simulated data with and without the inclusion of the datasets of lesions. For all lesions, there is a large contribution of the TOF resolu-

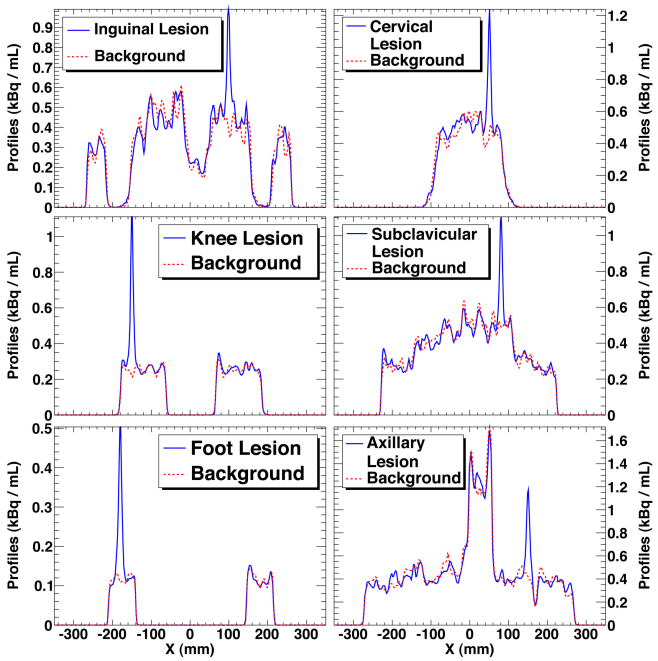


**Figure 5.30:** Profiles taken along the 6 lesions and corresponding background for the reconstructed images including trues and scatters and a TOF resolution of 300 ps FWHM. The background region overlap in both independent reconstructions, conferring reliability to the evaluation of the CRC values.

tion to the increase of CRC values, either considering only the true events (not shown) or including also the scatters after performing a scatter rejection by TOF (fig. 5.30). If taking into account only the trues, the foot and subclavicular lesions have the higher values followed by the knee and cervical lesions, and the inguinal and axillary lesions present the lower values. If we include the scattered events after the scatter rejection by TOF, only the foot and the knee lesions maintain higher values, while the other lesions suffer a major signal loss due to the contribution of the scattered events. The background in both reconstructions has a quantitatively conformity, conferring reliability to the evaluation of the CRC values. The observed contrast agrees with the calculated CRC values.

As can be seen in fig. 5.31, there is a large gain between iterations (its.) 1 and 20 and a stabilization for increasing iterations. We present the $CRC_{mean}$ (top, left) and

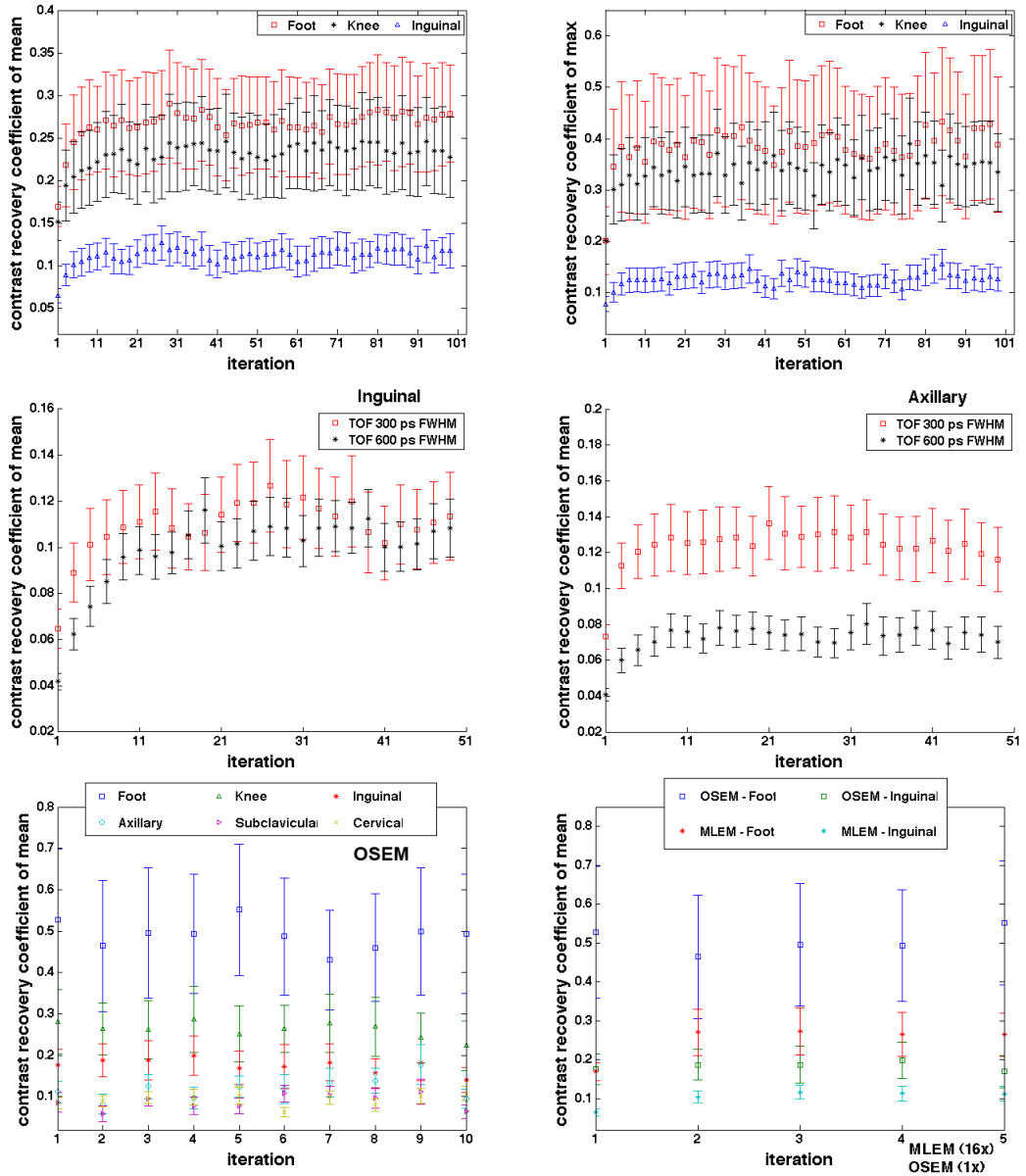


**Figure 5.31:** Contrast recovery coefficients evolution with iterations for the images reconstructed with true and scatter events. Top: $CRC_{mean}$ (left) and $CRC_{max}$ (right) in foot, knee and inguinal lesions (MLEM, SRF (300 ps FWHM)). Middle: comparison between a TOF resolution of 300 and 600 ps FWHM for the inguinal (left) and axillary (right) lesions (MLEM). Bottom: $CRC_{mean}$ in the six lesions with OSEM (left), and comparison between $CRC_{mean}$ in foot and inguinal using MLEM (80 it.) and OSEM (5 it., 16 subsets) (right).

$CRC_{max}$ (top, right) in the foot, knee and inguinal lesions. The $CRC_{max}$ considers the maximum voxel value in each lesion, while the $CRC_{mean}$ takes into account the region average for each lesion. The latter metric has a smoother performance, thus being chosen for table 5.5. The CRC values in other lesions evolve similarly, i.e., they stabilize after iteration 20.

The advantage of a TOF resolution of 300 ps FWHM is clear for the axillary lesion (middle, right), however, the $CRC_{mean}$ values for the inguinal lesion are not so distant for both resolutions, despite the almost constant higher values for a 300 ps FWHM TOF resolution. The OSEM reconstruction increases largely the $CRC_{mean}$ of the foot lesion (bottom, left) and provides a constant better value for the inguinal lesion in respect to the MLEM reconstruction (bottom, right), as already observed. The OSEM algorithm, despite the fact of increasing the image noise by reason of lack of statistics, has a considerable impact on the contrast of the inguinal lesion.

In table 5.5, we also observe that the proposed image division method kept the CRC values, when comparing to a whole-body reconstruction, except for the knee lesion, where a decreasing factor two is noticed, resulting from its location in the boarders of two independent images. This was expected and has already been perceived by image visualization.

#### 5.2.5.6 Speed

For the pre-processing and the starting backprojection which feeds the reconstruction routines, we opted for employing the 16-threads CPUs alone, since the time gain for the GPU implementation of those routines was not remarkable. The values for the reconstruction times presented in fig. 5.3 already include the contribution of the pre-processing and backprojection time. Both reconstruction routines run faster with the GPU plus 16-threads CPUs implementation than with the 16-threads CPUs alone. Table 5.3 also presents the reconstruction time for the presented images, considering the two different approaches: whole-body and division method. For the whole-body, GPU takes 24:15 to perform the reconstruction of the data for the SRF (300 ps FWHM) case. Considering the image division approach, a performance of 4:39 was achieved for the superior head region, where most of the events come from. The implementation of the second routine, which accesses to the LUT containing the space uncertainties associated to TOF and their respective weight, supports the access to constant memory

resources of the GPU, pushing even further the reconstruction speed. A performance time below 4 minutes (3:33, 20 iterations) for the superior torso region was reached, the worst case in terms of computation burden. This time includes the total image reconstruction process.

## 5.3 Discussion

The large AFOV and the 300 ps FWHM TOF resolution combine in RPC-PET to make this detector relevant for low injection doses and short scan periods. We expect to obtain the images presented in this chapter with a 7 minutes scan and an injected activity of 2 mCi, a value well below the activities currently administered to patients (10 to 20 mCi). A reconstruction routine capable of providing images for RPC-PET technology was materialized. A direct TOF implementation of the MLEM and OSEM algorithms allows for all events to be directly processed and inserted inside the object image by means of a TOF kernel, while handling list-mode data iteratively. A proper attenuation correction was successfully implemented and a study on the TOF kernel sampling was carried out, leading to a RMSE minimum for 20 samples inside the kernel. Nevertheless, by considering image improvement stabilization, a TOF kernel with 30 samples inside the Gaussian was taken into account to obtain the reconstructed images.

Concerning only the true events, the presented reconstructed images showed a considerable agreement (both qualitatively and quantitatively) with the simulation phantom, with almost all organs showing up with acceptable homogeneity and well separated from each other. The image statistics revealed to be a determinant variable for improving image quality, confirming that the increase of sensitivity is one of the main achievements of RPC-PET.

A method of rejection of the scattered events was presented, leading to a scatter rejection fraction of 63% for a 300 ps FWHM TOF resolution expected for a whole-body RPC-PET.

To study the potential of TOF resolution on lesion detectability, we evaluated its impact on the detection of six simulated lesions spread over the anthropomorphic phantom in critical regions. Lesions close to abdomen, such as the inguinal one, are harder to detect. In comparison to a 600 ps FWHM TOF detector (typical for present commercial crystal-based PET scanners), the 300 ps FWHM whole-body RPC-PET represents a

detector with increasing detectability potential. Furthermore, we confirmed that TOF resolution is the prevailing variable for lesion detectability.

As an alternative approach to whole-body reconstruction, a method based on the division of the data through nine different regions was proposed, resulting in an enhancement in the reconstruction performance. The proposed method provided a six times faster reconstruction. Making use of GPUs assisted by 16-threads CPUs, we expect to reach a reconstructed image from a 300 ps FWHM RPC-PET scanner in less than 4 minutes after the end of data acquisition. To achieve this reconstruction performance, an alternative routine was accomplished to handle the time uncertainty associated to TOF. By virtue of GPU constant memory, all uncertainty TOF variables were stored in a LUT, reducing the compute-to-memory access ratio, thus enhancing the computational performance. Comparing to our first attempt to reconstruct the whole-body data, which took approximately 90 hours, this represents a huge progress. We also concluded that images generated using CPU and GPU are essentially identical.

An analysis of the RMSE took us to stop the reconstruction at iteration 20 of MLEM algorithm, with image visualization corroborating this choice. Despite the fact that the reconstruction routine deals with a random filling of the TOF kernel, thus generating different images in similar but independent reconstructions, the MLEM based reconstruction routine concluded with nearly identical images. OSEM-based independent reconstructions generate images susceptible to statistical fluctuations which can be correlated with each other, thus eventually increasing system specificity.

A CRC analysis corroborates the conclusions we have drawn so far: the inner lesions in the body have a higher loss of contrast due to the contribution of the scattered events in those regions; the TOF resolution dictates the largest contribution to contrast gain; the CRC stabilizes at iteration 20; the OSEM reconstruction performs better than the MLEM reconstruction for the inguinal lesion; and there is no substantial difference between GPU and CPU reconstructions.

# 5. A DIRECT TIME-OF-FLIGHT RECONSTRUCTION FOR WHOLE-BODY SINGLE-BED RPC-PET

# 6

# Conclusion

## 6.1 Summary and conclusions

Two main objectives were pursued within the present work: the determination of the image spatial resolution of a small-animal RPC-PET prototype; and the development of a reconstruction routine capable of providing images from a whole-body single-bed RPC-PET scanner.

### 6.1.1 Small-animal RPC-PET

An experimental setup was assembled for testing the ability of two small-animal RPC-PET modules to image and distinguish two small sources closely located. The detector modules were constructed and placed at a distance of 4 cm from each other, and a custom-made needle-like source was positioned between them. A step-motor allowed moving the source in the vertical direction. The joint reconstruction of the data from both positions produced images where the two points are clearly distinguished. A fit by the sum of gaussian functions to the reconstructed activity profile along a line crossing the most active voxel in each source position yielded a spatial resolution close to 0.4 mm FWHM.

The **first goal** of this work was to produce 40 RPC detector modules, 10 for each of the heads of the scanner. This task lasted for several months, since each detector needs at least 3-4 hours to be assembled and around 12 hours to let the resin dry. As a matter of fact, we were able to assemble one detector per day. Additional time to glass cleaning, setup disassembly, painting and insulation was required. The learning

time to refine the technique has also to be taken into account, because the processes involved were very delicate and prone to glass break. So far, we assembled around 70 such detectors, 40 of which reached their final stage and have just been fitted into the scanner, and the remaining were kept as spare detectors.

The **second goal** of this research was to assemble an experimental setup with two modules parallel to each other, separated by 4 cm, and image a source placed between them. A base made of PVC ensured the alignement between the detector modules. The latter were mounted on a scanner head and carefully positioned each at 2 cm from the source. We tested the proper operation of the detector modules in what concerns counting rate capabilities and electric current consumed as a function of the voltage applied to the electrodes. We adopted the detectors painted with resistive ink instead of the ones epoxied with *SEMITRON*, because of their consumed current stability and the steady multiplicity in all detectors channels along the time. The aluminium box container, sealed against gas leakage, worked perfectly as a *Faraday cage* to avoid environment RF noise from reaching the charge amplifiers.

The **third goal** was to outline a processing chain capable of providing the charge and time signal information for coincidence events. Software to decode the raw data provided by the DAQ system was created, serving as an input for the digital pulse processing of the charge collected by each ADC channel. The decoder ran in the DAQ server, and the output was sent to the GRID to be processed. The processor was able to remove most of the random events from data and provide the coincidences between the detector pairs. A joint decoding and processing time below 30 s was reached for approximately 20k triggered events. From these, approximately 30% were accepted as valid coincidences. A maximum coincidence trigger rate of approximately 1 kHz was achieved. This value is within the present DAQ capabilities, considering the number of ADC samples defined (32).

The **fourth goal** was to develop an event analysis capable of identifying the gap where the avalanche developed and its fine positioning in the detector. The gap identification was achieved by means of multivariate (principal component analysis) and clustering ("$k$-means" algorithm) statistical techniques. The events were analysed based on classes defined by the strip with largest charge signal. For each strip, we identified the gap where each avalanche developed, thus providing a fine measurement of the depth of interaction. The data included LORs inclined up to 58°, demonstrating the

parallax-free property inherent to RPC-PET. To determine the photon hits position in the detector, we made use of the variable, $\alpha$, obtained from the principal component analysis, verifying that a relationship exists between $\alpha$ and the relative position of the avalanche to the center of the strip with largest charge signal [19]. To calculate the fine coordinate position of the avalanche in the detector, we took into consideration the calculated induction functions generated by the induced charge on the read-out-strips. In order to determine the most likely position of the photon hit in the detector, we followed a least-squares method partially similar to [20, 21]. We observed the presence of shadows (lines) in the hitmap corresponding to the 0.35 mm spacers used to define the gap width and some differential non-linearity (DNL) in the $X$ and $Y$ coordinates of both detectors.

The **fifth goal** was to develop a reconstruction routine tailored to the needs of the small-animal RPC-PET scanner and determine its image spatial resolution. A MLEM-based reconstruction was developed to provide PET images of the sources. The algorithm was validated with Monte Carlo simulated data, reproducing very well the original simulated phantoms. A performance test to the parallelized code yielded a reconstruction time of 16 minutes for 23 million events, after 20 MLEM iterations. Images were reconstructed from the collected LORs considering all LOR angles ("full 3D mode"), all gas gaps and the full pulse-height spectrum. The ultimate target of the experimental part of this work has been successfully achieved: we obtained images from two $^{22}$Na radioactive sources (planar and needle-like shaped); and we demonstrated sub-millimeter image spatial resolution. We can conclude that a MLEM-based image reconstruction of PET data obtained on a realistic prototype of an RPC-PET small-animal imager demonstrated world-class resolutions close to, respectively, 0.4 mm and 0.5 mm FWHM for needle-like and planar $^{22}$Na radioactive sources. It should be noted that, for the 0.4 mm FWHM value, no deconvolution of the source size was performed.

### 6.1.2 Human RPC-PET

The large AFOV and the 300 ps FWHM TOF resolution combine in RPC-PET to make this detector relevant for low injection doses and short scan periods. We expect to obtain the images presented in chapter 5 with a 7 minutes scan and an injected activity of 2 mCi, a value well below the activities currently administered to patients

(10 to 20 mCi). The **final goal** of this thesis has been largely fulfilled. A reconstruction routine capable of providing images for RPC-PET technology was materialized. A direct TOF implementation of the MLEM and OSEM algorithms allows for all events to be directly processed and inserted inside the object image by means of a TOF kernel, while handling list-mode data iteratively. A proper attenuation correction was successfully implemented and a study on the TOF kernel sampling was carried out, leading to a RMSE minimum for 20 samples inside the kernel. Nevertheless, by considering image improvement stabilization, a TOF kernel with 30 samples inside the Gaussian was taken into account to obtain the reconstructed images.

Concerning only the true events, the presented reconstructed images showed a considerable agreement (both qualitatively and quantitatively) with the simulation phantom, with almost all organs showing up with acceptable homogeneity and well separated from each other. The image statistics revealed to be a determinant variable for improving image quality, confirming that the increase of sensitivity is one of the main achievements of RPC-PET.

A method of rejection of the scattered events was presented, leading to a scatter rejection fraction of 63% for a 300 ps FWHM TOF resolution expected for a whole-body RPC-PET.

To study the potential of TOF resolution on lesion detectability, we evaluated its impact on the detection of six simulated lesions spread over the anthropomorphic phantom in critical regions. Lesions close to abdomen, such as the inguinal one, are harder to detect. In comparison to a 600 ps FWHM TOF detector (typical for present commercial crystal-based PET scanners), the 300 ps FWHM whole-body RPC-PET represents a detector with increasing detectability potential. Furthermore, we confirmed that TOF resolution is the prevailing variable for lesion detectability.

As an alternative approach to whole-body reconstruction, a method based on the division of the data through nine different regions was proposed, resulting in an enhancement in the reconstruction performance. The proposed method provided a six times faster reconstruction. Making use of GPUs assisted by 16-threads CPUs, we expect to reach a reconstructed image from a 300 ps FWHM RPC-PET scanner in less than 4 minutes after the end of data acquisition. To achieve this reconstruction performance, an alternative routine was accomplished to handle the time uncertainty associated to TOF. By virtue of GPU constant memory, all uncertainty TOF variables

were stored in a LUT, reducing the compute-to-memory access ratio, thus enhancing the computational performance. Comparing to our first attempt to reconstruct the whole-body data, which took approximately 90 hours, this represents a huge progress. We also concluded that images generated using CPU and GPU are essentially identical.

An analysis of the RMSE took us to stop the reconstruction at iteration 20 of MLEM algorithm, with image visualization corroborating this choice. Despite the fact that the reconstruction routine deals with a random filling of the TOF kernel, thus generating different images in similar but independent reconstructions, the MLEM based reconstruction routine concluded with nearly identical images. OSEM-based independent reconstructions generate images susceptible to statistical fluctuations which can be correlated with each other, thus eventually increasing system specificity.

A CRC analysis corroborates the conclusions we have drawn so far: the inner lesions in the body have a higher loss of contrast due to the contribution of the scattered events in those regions; the TOF resolution dictates the largest contribution to contrast gain; the CRC stabilizes at iteration 20; the OSEM reconstruction performs better than the MLEM reconstruction for the inguinal lesion; and there is no substantial difference between GPU and CPU reconstructions.

## 6.2 Future work

Since the full small-animal scanner is totally assembled, further work with the small-animal RPC-PET prototype will now focus on the imaging of mice with the full scanner totally assembled. Meanwhile, several imaging tests with the sources reported in this work will be accomplished. To deal with the expected trigger rate ($1.5 \times 10^4$ Hz) resulting from the imaging of a mouse injected with 100 $\mu Ci$, we have to improve the acquisition performance. Meanwhile, the trigger efficiency has been increased and the number of sums of samples per ADC channel reduced. The digital processing stage may be performed in the FPGA, saving time and storage needs. A local farm is being prepared to process the data and reconstruct the images in a short time. The reconstruction algorithm has to be improved with attenuation, scatter and positron modeling enabled. A possible implementation of the algorithm on the GPUs will be considered. A performance evaluation of the RPC-PET with the NEMA NU-4 protocol

will be accomplished in order to make a standard comparison with other commercial small-animal PET scanners.

Differential non-linearity patent in the position distribution maps of the triggered events seems to have a strong impact on the measured image spatial resolution. A possible way to solve this issue has been pointed out in section 4.8, nevertheless a deeper study is required. The contribution of the non-collinearity effect to the image spatial resolution has been investigated, but the results are not yet conclusive. An experiment with more detector modules and a larger distance separating the two heads will be carried out. The inclusion of detectors painted with resistive ink will make the results more comparable with those presented for the inner detectors.

Future work with the whole-body single-bed RPC-PET reconstruction will include an appropriate scatter correction. Improvements in the reconstruction speed are still possible with a broad range of optimization strategies to be implemented in the GPUs. Reconstruction with multi-GPUs are also an option. Contrast recovery will be addressed for smaller lesions and lower lesion to background activity concentration ratios. A more quantitative analysis will be performed, including other numerical observables to quantify lesion detectability. Background noise can be quantified by using several figures of merit (e.g., image roughness and background variability). Other metrics used to evaluate the quantitation performance (SNR for quantitation) and to measure the detection task performance (SNR non-prewhitening filter) are an option too. These metrics are meant to be computed for a single realization. Conversely, other metrics (e.g., ensemble noise and standard deviation image) are measured across independent realizations. Therefore, they may be appropriate for the evaluation of the background noise properties of the averaged images obtained from independent reconstructions.

We expect in the future to integrate the simulated detector contributions into the reconstruction and assess the figures of merit mentioned above. A complete reconstruction with all data corrections (random, normalization, dead time, scatter and attenuation) will provide an assessment of RPC-PET system performance.

# Appendices

# Appendix A

# Clinical applications of a true whole-body PET

The applications of PET/CT are fundamentally concentrated in the oncologic medical field. Despite the increasing contribution of this instrument for the study of neurological, psychiatric and cardiac diseases, the vast majority of the examinations are focused on finding lesions associated to several kinds of cancer. PET with $^{18}$F-FDG is used to diagnose and stage many cases of cancer. The accuracy ranges from 80% to 90% and is often better than of anatomic imaging [324]. This accuracy associated to the anatomic information provided by the CT has rendered PET/CT the most important cancer imaging modality in present time [325].

PET/CT has been advocated as a first-line imaging technique for whole-body tumor staging, restaging, and assessing response to therapy. It is also applied in recurrence suspicion, follow-up and radiotherapy (RT) planning. Numerous studies have shown that whole-body multimodality imaging is better than PET or CT alone for staging and restaging most cases of cancer [325].

The request of a PET/CT examination depends on the cancer type and corresponding clinical application. It may be classified as appropriate, potentially appropriate, possibly appropriate, or inappropriate. For instance, FDG-PET is appropriate for the diagnosis and staging of non-small-cell lung carcinoma (NSCLC), however it is inappropriate for the diagnosis and follow-up of lymphoma. Concerning the RT planning of head and neck cancer, it is potentially appropriate, since it may help in the modification of the dose and target volumes.

The term whole-body used in PET/CT is misleading because the most commonly used FOV (160 cm), for arms up PET/CT whole-body protocols, covers only the base of the skull to the upper tights, or the head to the pelvic floor, commonly referred to as eyes-to-thighs or lips-to-hips [226, 326]. Such FOV may underestimate the true extent of the malignancy, because it does not include the brain, skull, or significant portions of the upper and lower extremities. Therefore, it became necessary to include the term "true whole-body" for a scan range from the top of the head to bottom of feet (193cm) [227, 228]. Fig. A.1 shows the five FOV categories of anatomic scan lengths,

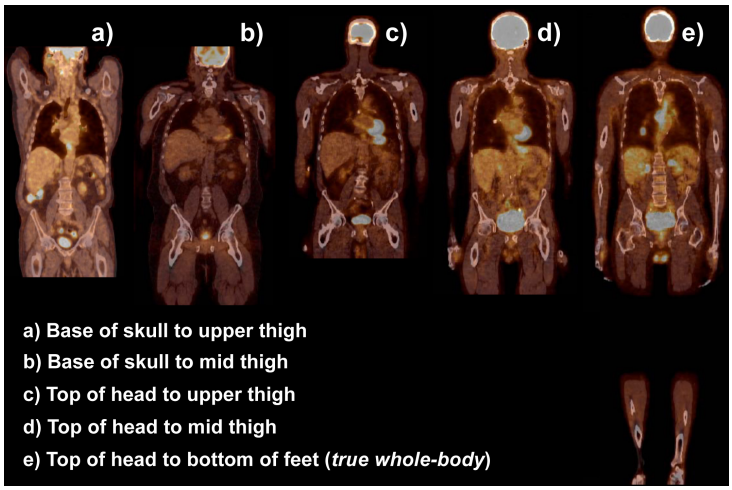


**Figure A.1:** FOV categories of five anatomical scan lengths. Adapted from [228].

and table A.1 presents the current procedural terminology codes of the centers for Medicaid and Medicare services of the USA.

The need of a true whole-body scan has been argued between several groups, on the basis of large population studies. In fig. A.2, we present three cases where the true whole-body PET/CT yielded benefits: a) a patient with inconclusive results of biopsy of a lung mass. PET/CT revealed an asymptomatic soft-tissue lesion in the distal right thigh. Biopsy of the lesion revealed metastatic carcinoma consistent with a lung primary, precluding repeated lung biopsy; inclusion of the lower extremities in the PET/CT FOV helped in location of a more accessible biopsy site, facilitated diagnosis, and improved staging accuracy for this patient; b) for a patient with a known history of melanoma, a true whole-body PET/CT helped identifying coexisting metastatic thyroid cancer, the biopsy specimen of which was performed on the right distal femur;

| Code | Description | Physician Fee | HOP |
|---|---|---|---|
| 78811 | Tumor-imaging PET; limited area (e.g., chest, head/neck) | $80.96 | $1,310.60 |
| 78812 | Tumor-imaging PET; skull base to mid thigh | $97.44 | $1,310.60 |
| 78813 | Tumor-imaging PET; whole body | $102.45 | $1,310.60 |
| 78814 | Tumor-imaging PET; with concurrently acquired CT for attenuation correction and anatomical localization; limited area (e.g., chest, head/neck) | $112.84 | $1,310.60 |
| 78815 | Tumor-imaging PET; with concurrently acquired CT for attenuation correction and anatomical localization; skull base to mid thigh | $124.31 | $1,310.60 |
| 78816 | Tumor-imaging PET; with concurrently acquired CT for attenuation correction and anatomical localization; whole body | $125.38 | $1,310.60 |

**Table A.1:** 2014 Current Procedural Terminology (CPT) coding, description and Medicare payment rates (hospital outpatient payment - HOP) for Oncology PET protocols in USA.

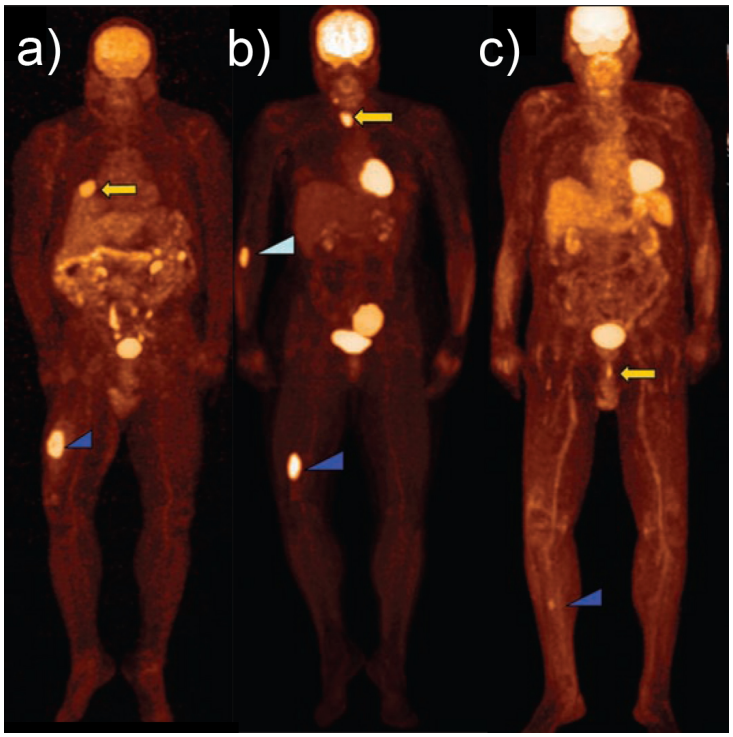


**Figure A.2:** Coronal true whole-body maximum-intensity projection PET images for patients with lesions outside of the typical FOV. Adapted from [228].

c) an unexpected skin cancer was diagnosed from a right lower leg biopsy of a patient with rectal cancer [227].

Compared to the limited FOV imaging, the true whole-body imaging may increase the staging accuracy, modify the treatment planning, and help on the selection of more accessible biopsy locations, thus avoiding the need of unnecessary surgical and imaging procedures. It may also provide an overview of the extension of the disease, once a considerable number of metastases occur outside the limited FOV [229].

A study with 1000 patients concluded that the true whole-body PET/CT may have a crucial role in lung cancer. The accuracy in the detection of bone metastases in patients with NSCLC was superior with PET/CT in comparison with scintigraphy [327]. Another study with 556 patients evaluated the number of examinations detecting a lesion outside the limited FOV, and from those, the ones that modify the treatment plan. It detected metastases outside the FOV in 8.6% of the cases and modified the staging in one patient and the treatment in six others [328].

The main shortcomings are the increased scanning time of 30-40% that may require an adjustment of the daily clinic schedule and creates discomfort to the patient. The additional radiation dose to the patient from the CT of supplementary portions of the body has also to be considered. Nevertheless, a chest, abdomen and pelvis CT which delivers a dose of 14.8-53 mSv may be exchanged by a low-dose whole body PET/CT which delivers a dose $< 20$ mSv. For instance, by including the brain in the PET/CT imaging of patients with lung cancer, the brain CT can be avoided.

There are studies that show that true whole-body PET imaging does not add considerable information to justify its choice. They conclude that for patients with melanoma with unknown or unsuspicious primary lesion/metastases in the brain or upper/lower limbs, a limited FOV examination should be more adequate [329, 330].

Brain imaging is not routinely performed and is reserved for patients with changes in mental statues, neurologic deficits, or both [227]. Nevertheless, it is accepted that MRI is more efficient in the detection of brain metastases than CT. The brain is often excluded from PET/CT imaging, by reason of the lower sensitivity to the detection of brain metastases. Nonetheless, two studies with 8431 and 2502 patients concluded that the inclusion of the head in the PET/CT imaging detected brain metastases in $\sim$1% of the patients with cancer [331, 332]. A study on 16,210 patients showed that approximately one half of the patients with metastases developed brain metastases (9.6% of total). They are more frequent in patients with lung (19.9%), kidney (6.5%), breast (5.1%) and gastrointestinal (1.8%) cancer, and melanoma (6.9%) [333].

A study on the sensitivity and specificity of the PET imaging for the detection of brain metastases showed that from 40 patients, MRI detected 16 patients with brain metastases and PET identified 12 true positives, 4 false positives, 20 true negatives and 4 false positives. Thus, the calculated sensitivity and specificity of the PET imaging was 75% and 83%, respectively. The main reason for the lower lesion detectability of the PET system was related with the size of the lesions [230]. The RPC-PET system may provide an increasing lesion detectability as we will show in chapter 5, thus increasing the RPC-PET sensitivity and specificity.

The acquisition and reconstruction times can also be dramatically reduced with an RPC-PET system covering an AFOV of 2.4 m. In old PET/CT scanners, emission data were acquired for 12-13 bed positions (coaxial scan range of 193 cm), at 3 minutes per bed position, resulting in a total scan time of 36-39 mins. Nowadays, for instance, at ICNAS, the acquisition takes 20 minutes and the reconstruction needs approximately 15 minutes do display the image. The time required for true whole-body acquisitions and processing will continue to decrease and the co-axial scan range will continue to expand. It is therefore expected that RPC-PET will contribute to push even further the acquisition and reconstruction times (see chapter 5).

In Coimbra, we have two PET scanners: a Philips Gemini GXL operating in ICNAS and a GE Discovery ST4 operating in CHUC. In ICNAS are executed approximately 6-8 PET examinations per day. The imaging FOV covers the top of the head to middle thighs (including the brain). A true whole body imaging is performed for tumors of unknown origin. Sometimes, it is necessary to carry out an imaging at later stages to solve any doubts arising from first examination. In a population of 1500 patients, $\sim$22% required an imaging at later stages, and $\sim$16% of the imaging scans were true whole-body covering the top of the head to bottom of feat. In CHUC, there are approximately 1800 examinations per year. The imaging FOV is also from the top of the head to middle thighs. Each examination takes $\sim$30 minutes (3 min/bed, 10-13 beds). Imaging scans at later stages are also performed in 33% of the cases, 40-60 mins after the first examination. The pathologic uptake has its maximum peak after 3 hours, but the physiologic uptake maximum peak appears much earlier. The true whole-body imaging represents 13% of the total PET examinations and is mainly advised for lung cancer and mandatory for melanoma. For patients taller than 1.60 m, the examination is interrupted and the bed position is inverted. PET imaging with NaF is also an option

for the substitution of bone scintigraphy. Approximately 3% of the PET examinations carried out in CHUC use $^{11}$C-Choline for prostate imaging. The uptake time peak occurs within 2-3 mins and the FOV is limited to 15 cm. A dynamic study usually takes 25 min. Then, the patient urine and the true whole-body is imaged.

To conclude, the true and limited whole-body imaging have equal technical fees with a negligible difference in professional fees [228]. The additional costs may be caused by the additional time required by a true whole-body examination, leading to a reduced number of examinations, thus constraining clinical schedule planning. The amount of data to process contributes to the total time as well. The discomfort for the patient is also increased and the extra dose of the CT constitutes an additional source of radiation. The trade-off between the time and the relevance of the extended FOV examination must be carefully evaluated by the clinicians. True whole-body examinations allows detecting lesion outside typical FOV. It is essential to detect the maximum number of lesions in order to provide the best patient staging and treatment. It has been shown that true whole-body imaging increase the accuracy of staging, change treatment of cancer patients, and help in the selection of more accessible locations for biopsy, avoiding unnecessary invasive surgical procedures and eliminates irrelevant imaging and its additional cost in time and money.

# Appendix B

# Applications in small-animal PET

The development of tumors in mice represents virtually all major human cancers, including those of the lung, gastrointestinal system, nervous system, breast, liver, prostate, pancreas, reproductive system, and metastases. Glucose metabolism monitored with the $^{18}$F-FDG is the most widely used technique. Many other targeted mechanisms are still object of study, such as tumor cell proliferation, gene expression, tumor angiogenesis, tumor hypoxia, and tumor apoptosis.

Cardiovascular research of animals permits studying the hormonal pathways involved in the regulation of hypertension and hypertension therapy, cardiac electrophysiology, mechanisms of apoptosis, effects of exercise, lipid metabolism and insulin sensitivity, atherosclerosis, and angiogenesis [261]. Electrocardiogram-gated data acquisitions can be used on rat or mouse imaging to minimize wall motion effects. It is possible to assess myocardial wall thickness and irrigation, distinguishing a normal heart from an infarcted one [260]. One may also distinguish the right ventricle, which statistically has much lower signal strength than the left ventricle. Quantitative gated SPECT (QGS) [334], a quantitative analysis package, is used to reorient the gated image sequences and obtain quantitative cardiac function parameters such as end-diastolic (ED) and end-systolic (ES) ventricular volumes, stroke volume, left ventricular ejection fraction (EF), polar maps of ED and ES tracer distribution, wall thickening, and wall motion (see fig. B.1).

Several PET radiotracers have been developed for brain imaging, such as $^{15}$O-$H_2O$ for measuring cerebral blood flow, $^{18}$F-FDG for measuring glucose metabolism, $^{11}$C-raclopride for quantifying the postsynaptic $D_2$ receptor level, $^{11}$C-Pittsburgh com-

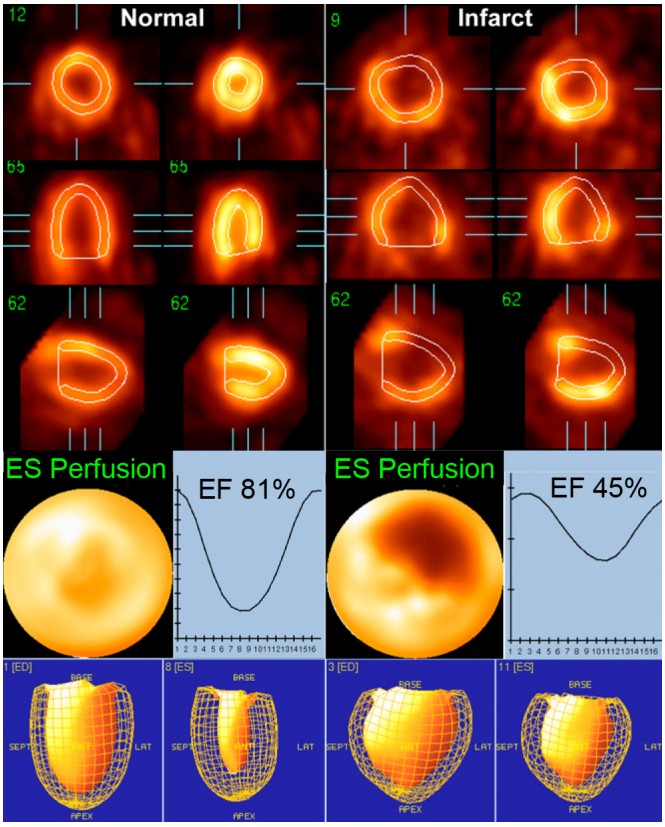


**Figure B.1:** Example of an electrocardigram-gated $^{18}$F-FDG study in normal and infarcted rats. Adapted from [260] after [335].

pound B for imaging $\beta$-amyloid deposition. Through these tracers, we may study the pathophisiology, pharmacology an drug mechanisms of the brain [336].

Transgenic and knock-out mice play a significant role in biomedical research. Transgenic animals (mice and rats) can be designed and created with unlimited possibilities for addressing questions concerning the genetic, molecular, and cellular basis of biology and disease. Biologists can now tailor animal models that accurately fit biologic and biochemical processes in the human through the manipulation of the genome in small-animals [261].

The greatest advantages of imaging techniques are the reduction of biological variability (each animal works as its own control), thus reducing substantially the number of animal required for a particular study [231]. Complex interactions between the physiological/biochemical processes that occur in biological systems is only possible

with intact animals in which variables related to immunological, nutritional, or hormonal aspects are present, as well as systemic responses [232]. Ex vivo systems, such as vitro autoradiography, despite its exquisite spatial resolution, are time consuming, labor intensive and invasive. Furthermore, small-animal PET techniques can be easily translated to humans.

# Appendix C

# Reconstruction algorithms

Fully 3D PET imaging differs from 2D in what concerns spatially-varying scanner response and data redundancy. The 3D counterpart of 2D imaging would be a spherical scanner surrounding the object, however most PET scanners are cylindrical and the projections are truncated in the axial direction, resulting in a spatially-variant scanner response. Fully 3D PET data contains detections from both transverse and oblique planes, resulting in data redundancy, which can be utilized to improve signal-to-noise performance [269].

Rebinning methods convert 3D data to decoupled sets of 2D data and apply 2D reconstruction algorithms. Among the rebinning methods, the most straightforward is single-slice rebinning (SSRB) [337]. It calculates the average axial position of a coincidence event, and places the event in the sinogram closest to that average position. A more accurate algorithm is the Fourier rebinning (FORE) [338]. It relates the Fourier transform of oblique sinograms to the Fourier transform of transverse sinograms. The reconstruction of rebinned 3D PET data may be accomplished either with analytic or iterative 2D reconstruction algorithms. The FBP algorithm can be extended to 3D reconstruction, but spatial variance of 3D PET data complicates the analytic reconstruction. The 3D reprojection algorithm [339] overcomes this issue, thus restoring the spatial invariance by taking advantage of data redundancy. Further details of implementation can be found in [340]. This algorithm can improve significantly the signal-to-noise performance in respect to the 3D FBP algorithm, allowing a higher spatial resolution.

Among iterative algorithms, the algebraic reconstruction techniques (ART) make use of constraints (e.g., non-negative pixels) as prior knowledge to the image reconstruction [341]. However, they are incompatible with statistical modeling of PET data, and become useless in the presence of statistical noise. Maximum *a posteriori* (MAP) reconstruction incorporates a statistical model both for data and image, thus looking for a maximization of the posterior probability density, instead of maximizing the likelihood function. An *a priori* model of the image distribution is required, usually a smoothness constraint [342], or even an anatomical information from other imaging modalities such as CT and MRI [343, 344]. The priors in MAP reconstruction can be considered as a penalty on solutions to carry out desirable properties. The penalized weighted least square algorithm [343] is the extension of penalization formulation to traditional least square methods.

Fessler has defined the desired properties of an iterative reconstruction algorithm: (i) stable and convergent ($x^n$ converges to $x^*$ if run indefinitely); (ii) converges quickly ($x^n$ gets "close" to $x^*$ in just a few iterations); (iii) globally convergent ($\lim_n x^n$ independent of starting image $x^0$); (iv) fast (requires minimal computation per iteration); (v) robust (insensitive to finite numerical precision); (vi) parallelizable (multi-core and GPU friendly); (vii) flexible (accommodates any type of system model); (viii) user friendly (nothing to adjust); (ix) easy to program and debug [288].

In what concerns TOF reconstruction, the combination of list-mode acquisition and iterative reconstruction of 3D data is today widely accepted, as list-mode acquisition preserves the intrinsic spatial and temporal information of the data. Additionally, the list-mode storage is more efficient than the binned format for 3D data due to the large number of possible LORs with respect to the number of detected events [101]. List-mode reconstruction methods have greatly developed [345, 346], as well as the inclusion of both TOF and other physical effects in the system model [116, 320, 347]. Despite the computational challenges introduced by list-mode reconstruction, its practical implementation is already well-established and becoming increasingly more attractive with the advent of fast computers and parallelization [348, 349, 350, 351].

One important component of the physics modeling in iterative image reconstruction is the detector PSF [269]. This can be achieved through analytical derivations [352], Monte Carlo simulations [353], experimental measurements [354, 355], or directly per-

formed in the reconstructed image space [356]. This usually leads to an improved spatial resolution [353, 354], contrast recovery [357] and lesion detectability [358].

An extensive research study about the compensation for non-rigid cardiac and respiratory motion within NCAT phantom has been developed by Segars [28]. Correction methods for patient motion (head, cardiac and respiratory) include: registering images obtained at different frames [359]; using forward-projected data for motion detection [360]; using deconvolution algorithms in postprocessing [361]; employing gating methods, with each gate representing a particular cardiac or respiratory cycle [362].

Dynamic PET imaging is currently used to image the activity distribution in a specific time frame, thus allowing for an estimation of the changing activity over time. This method has applications in the evaluation of metabolic rate and tissue perfusion for a selected region of the body, with the help of tracer kinetic models [363]. List-mode acquisitions are here very useful for the specification of time frames. There are alternatives to the frame-by-frame approach, by including temporal modeling in the 4D reconstruction.

Among the challenges of image reconstruction is its contribution for a better quantitative accuracy of PET. An accurate and precise estimation of tracer distribution, regardless of feature size, shape and location, accompanied with advances in instrumentation and data processing is driving the growth of PET/CT and PET/MRI imaging in the study of pathophysiology and therapeutics.

There is a fast expanding universe of methods for image reconstruction, e.g., semi-norm penalties (total variance, TV), pre-conditioning, coordinate descent, scaled gradient projection, augmented lagrangian, variable splitting and Bregmans's algorithm, Cambolle and Pock algorithm, iterative shrinkage/thresholding algorithm (ISTA) and fast ISTA (FISTA), and alternate direction of minimization method (ADMM). An in-depth analysis of these methods is though out of the scope of this work.

# Appendix D

# Principal component analysis

## D.1 Algebraic formulation

We will follow the definition and derivation of principal components given by [312]. Supposing that $\mathbf{x}$ is a vector of $p$ random variables and we want to know the variance (a measure of the dispersion of values around the mean) of the $p$ random variables and the structure of the covariances or correlation, we can derive a few variables that preserve most of the information given by these variances and correlations or covariances through PCA.

We search a linear function $\boldsymbol{\alpha_1'}\mathbf{x}$ of the elements of $\mathbf{x}$ having maximum variance, where $\boldsymbol{\alpha_1}$ is a vector of $p$ constants, so that $\boldsymbol{\alpha_1'}\mathbf{x} = \sum_{j=1}^{p} \alpha_{1j} x_j$. Next, we look for a linear function $\boldsymbol{\alpha_2'}\mathbf{x}$, uncorrelated with $\boldsymbol{\alpha_1'}\mathbf{x}$ having maximum variance, and so on. We find a linear $\boldsymbol{\alpha_k'}\mathbf{x}$ at $k$th stage that has maximum variance that must be uncorrelated with $\boldsymbol{\alpha_1'}\mathbf{x}$, $\boldsymbol{\alpha_2'}\mathbf{x}$, ..., $\boldsymbol{\alpha_{k-1}'}\mathbf{x}$. The $k$th derived variable, $\boldsymbol{\alpha_k'}\mathbf{x}$ is the $k$th PC. Although $p$ PCs can be found, usually, most of the variation in $\mathbf{x}$ is explained by few PCs. If a set of $p$ variables has substantial correlations among them, then the first few PCs will account for most of the variation in the original variables. Conversely, the last few PCs identify directions in which there is very little variation; that is, they identify near-constant linear relationships among the original variables.

If a vector of random variables $\mathbf{x}$ has a known covariance matrix $\boldsymbol{\Sigma}$, it turns out that for $k = 1, 2, ..., p$, the $k$th PC is given by $y_k = \boldsymbol{\alpha_k'}\mathbf{x}$ where $\boldsymbol{\alpha_k'}$ is an eigenvector of $\boldsymbol{\Sigma}$ corresponding to the $k$th largest eigenvalue $\lambda_k$. In addition, if $\boldsymbol{\alpha_k}$ is normalized, so it has unit length, i.e., $\boldsymbol{\alpha_k'}\boldsymbol{\alpha_k} = 1$, then $\text{var}(y_k) = \lambda_k$. The $k$th PC, $y_k$, represents

the PC with the $k$th largest variance. The PCs are defined by a orthonormal linear transformation of $\mathbf{x}$, $\boldsymbol{y} = \boldsymbol{A}'\boldsymbol{x}$, where $\mathbf{y}$ is the vector whose $k$th element is $y_k$, $\mathbf{A}$ is the orthogonal matrix whose $k$th column, $\boldsymbol{\alpha_k}$, is the $k$th eigenvector of the covariance matrix $\boldsymbol{\Sigma}$. PCA is based on the diagonalisation of $\boldsymbol{\Sigma}$,

$$\boldsymbol{\Sigma A} = \boldsymbol{A\Lambda}, \tag{D.1}$$

where $\boldsymbol{\Lambda}$ is a diagonal matrix $(r \times r)$ with the $r$ non-null eigenvalues of $\boldsymbol{\Sigma}$ ($\boldsymbol{\Lambda} = diag(\lambda_1, \lambda_2, ..., \lambda_r)$) sorted in decreasing order ($\lambda_1 > \lambda_2 > ... > \lambda_r > 0$) and $\boldsymbol{A}$ contains the $r$ associated orthonormal eigenvectors. Two alternative ways of expressing (D.1) are $\boldsymbol{A'\Sigma A = \Lambda}$ and $\boldsymbol{\Sigma = A\Lambda A'}$.

When dealing with the statistical properties of PCs from a sample covariance (or correlation) matrix, rather than from a population covariance (or correlation) matrix, a different notation is established. Let $\tilde{y}_{i1} = \boldsymbol{a_1'x_i}$, where $\mathbf{x}$ is is the $p-$element random vector and $\boldsymbol{x_1, x_2, ..., x_n}$ are independent n observations, we choose the vector of coefficients $\boldsymbol{a_1'}$ that maximizes the sample variance

$$\frac{1}{n-1}\sum_{i=1}^{n}(\tilde{y}_{i1} - \overline{y}_1)^2 \tag{D.2}$$

normalized to $\boldsymbol{a_1'a_1} = 1$. Then, we have $\tilde{y}_{i2} = \boldsymbol{a_2'x_i}$, where $\boldsymbol{a_2'}$ maximizes the sample variance of $\tilde{y}_{i2}$, $\boldsymbol{a_2'a_2 = 1}$, and $\tilde{y}_{i2}$ is uncorrelated with $\tilde{y}_{i1}$ in the sample. Thus $\boldsymbol{a_k'x}$ is defined as the $k$th sample PC and $\tilde{y}_{ik}$ is the *score* for the $i$th observation of the $k$th PC. The sample variance of the PC scores for the $k$th sample PC is $l_k$, the $k$th largest eigenvalue of the sample covariance matrix $\boldsymbol{S}$ for $\boldsymbol{x_1, x_2, ..., x_n}$, and $\boldsymbol{a_k}$ is the corresponding eigenvector. The matrix $\boldsymbol{S}$ can be written as $\boldsymbol{S} = \frac{1}{n-1}\boldsymbol{X}'\boldsymbol{X}$, where $\boldsymbol{X}$ is a $(n \times p)$ matrix with $(i,j)$th element $(\tilde{x}_{ij} - \overline{x}_j)$. The matrix of PC scores is given by $\boldsymbol{Y = XA}$, and will have zero means, rather than means $\overline{y}_k$.

## D.2 Geometrical interpretation

PCA is relevant if at least some of the variables in the data set are inter-correlated. If none of the $p$ variables is correlated with any other, there exists already a set of uncorrelated axes, and performing a PCA becomes meaningless. Correlation determines the association between two variables - the amount they covary. The Pearson's product moment correlation coefficient is given by

$$\rho = \frac{Cov(X_1, X_2)}{sd(X_1)sdX_2} = \frac{\sigma_{X_1X_2}}{\sigma_{X_1} \cdot \sigma_{X_2}} \quad (-1 \leq \rho_{X_1,X_2} \leq 1) \tag{D.3}$$

If there are two uncorrelated variables, with a bivariate normal distribution, then the equiprobability contours (concentric lines indicating equal probability of occurrence) are circular (see fig. D.1, left). If the two variables are correlated, the contours of equiprobability are elliptic, and the cosine of the acute angle of intersection is equal to the correlation coefficient, $\rho$, (fig. D.1, middle). If the correlation is perfect ($\rho = \pm 1$), the ellipse contracts to a straight line, where the members of the population are located, and consequently one variable is totally characterized by the other (fig. D.1, right).

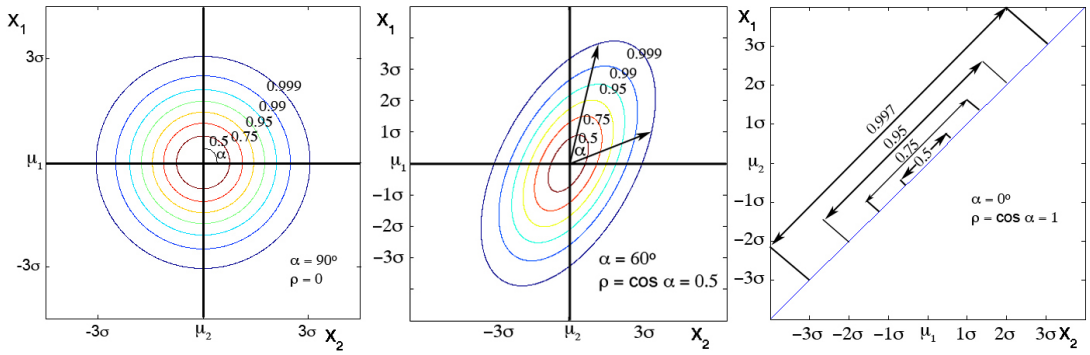


**Figure D.1:** Equiprobability contours for: two uncorrelated variables (left); two correlated variables (middle); two perfectly correlated variables (right).

Three correlated variables may be represented by ellipsoidal equiprobability surfaces. Considering the data plotted in fig D.2, left, there is an ellipsoidal equiprobability surface, defined by three vectors whose cosines of the angles of intersection relates to the correlation coefficients (fig. D.2, middle). Fig. D.2, right, shows the three principal components of the ellipsoid, where the first component corresponds to longest axis (the one that express the maximum possible proportion of the total variance). The second component refers to the second longest axis at right angles to the first axis (explaining the maximum proportion of the remaining variance), and the third component is the one at right angles to the other two (describing the remaining variance).

Fig D.3 illustrates the relationship between the variable axes and the principal components, in the case of two variables. The original coordinates of point D $(x_1, y_2)$ are transformed into coordinates of the two principal components $(y_1, y_2)$. The relation

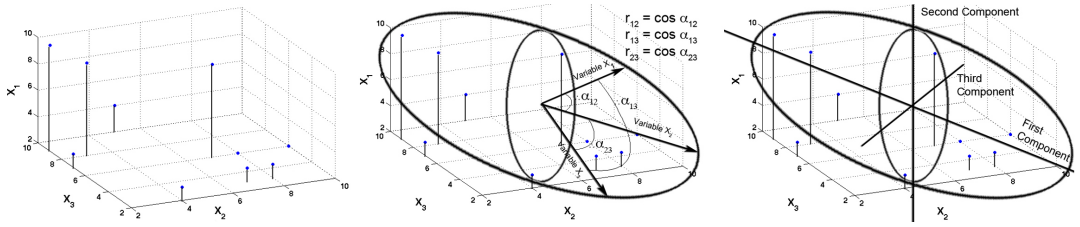


**Figure D.2:** Random data for three variables (left) and the corresponding equiprobability surface (middle). The three principal components (right) account for most of the variation in the original variables, while being at right angles to each other.

between the axes $X_1, X_2$ and $Y_1$,$Y_2$ is defined by the angle between them, $(\theta)$. Therefore, we have

$$\begin{bmatrix} y_1 \\ y_2 \end{bmatrix} = \begin{bmatrix} cos(\theta) & sin(\theta) \\ -sin(\theta) & cos(\theta) \end{bmatrix} \begin{bmatrix} x_1 \\ x_2 \end{bmatrix}$$

or

$$[y] = [A]\,[x]$$

Since matrix **A** is orthogonal it follows

$$A^{\mathrm{T}} = A^{-1} = \begin{bmatrix} cos(\theta) & -sin(\theta) \\ sin(\theta) & cos(\theta) \end{bmatrix}$$

When the variances of the individual variables are widely different some problems on the behavior of PCs for a covariance matrix may arise. It can happen that the PCs are

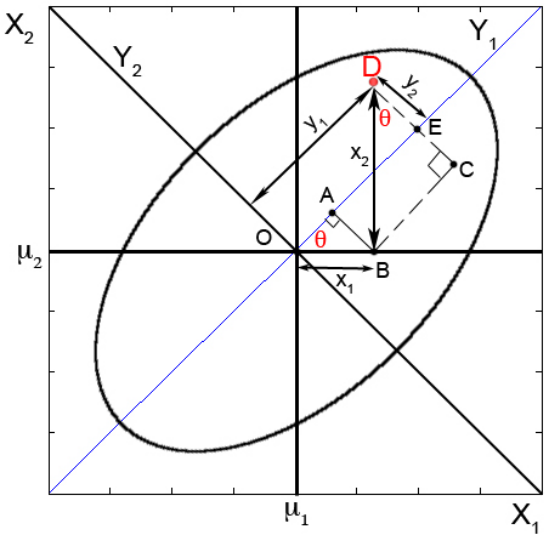


**Figure D.3:** Transformation of coordinate systems for two variables into the coordinates of the two principal components. Adapted from [364].

pretty similar to the original variables, just rearranged in decreasing order of the size of their variances. In such circumstances, transformations to PCs are useless. Usually, it is undesirable to use PCs on a covariance matrix when $\mathbf{x}$ consists of measurements of different types. The covariance matrix will not provide useful PCs if the variables have large contrasting variances. Conversely, for correlation matrices, the standardized variates are all dimensionless and can be combined to give PC scores [365]. Additionally, patterns of coefficients in PCs can be compared for different correlation matrices to check if both matrices give identical PCs, whereas comparisons for covariance matrices are more complex. Standardizing the variables is a way of removing the problem of scale dependence from PCA. Deriving the PCs from the correlation matrix hold other interesting properties: the PCs depend not on the absolute values of correlations, but only on their ratios [366]; and instead of the normalization $\boldsymbol{\alpha_k'}\boldsymbol{\alpha_k} = 1$, Hotelling suggests to use $\tilde{\boldsymbol{\alpha}}_{\boldsymbol{k}}'\tilde{\boldsymbol{\alpha}}_{\boldsymbol{k}} = \lambda_k$, so then, $\tilde{\alpha}_{kj}'$ is the correlation between the $j$th standardized variable $x_j^*$ and the $k$th PC [311].

Adapting equation D.1, the variance-covariance matrix of the principal components can also be written as

$$\boldsymbol{\Lambda} = \boldsymbol{A}'\boldsymbol{R}\boldsymbol{A}, \tag{D.4}$$

where $\boldsymbol{\Lambda}$ will have different $\lambda_i$ from the matrix in equation D.1, and $\mathrm{tr}(\boldsymbol{\Lambda}) = \mathrm{tr}(\boldsymbol{R}) = p$, the number of variables. $\boldsymbol{R}$ is the correlation matrix. Equation D.4 can also be written as

$$\boldsymbol{A}'\boldsymbol{R} = \boldsymbol{\Lambda}\boldsymbol{A}', \tag{D.5}$$

which for a non-zero solution for the $a_{ik}$ to exist must satisfy the condition for each of the $\lambda_k$ that

$$\left|\boldsymbol{R} - \lambda_k(\boldsymbol{I})\right| = 0 \tag{D.6}$$

The solution of the characteristic equation of the matrix $\boldsymbol{R}$ (eq. D.6) gives us the latent roots of $\boldsymbol{R}$, or its eingenvalues, $\lambda_k$. The eigenvectors associated with each eigenvalue are the columns of matrix $\boldsymbol{A}$. This matrix relates the principal components to the original variables. The components have variances described by $\boldsymbol{\Lambda}$, consequently, the product of the matrices $\boldsymbol{A}$ and $\boldsymbol{\Lambda}^{\frac{1}{2}}$, known as the matrix of component loadings, $\boldsymbol{L}$, represent the weighted contribution of the principal components to the original variables.

As Hotelling suggested, the elements of the matrix $\boldsymbol{L}$ are the correlation coefficients between the $i$th variable and the $k$th component. Therefore, they represent the cosines of the angles between the $i$th unit vector and the $k$th component, and can be visualized as the projections of the variables onto the principal components. The square of any $l_{ik}$ is the proportion of the variance of the $i$th variable explained by the $k$th component, thus $\sum_k l_{ik}^2 = 1$ and $\sum_i l_{ik}^2 = \lambda_k$.

The aforementioned definition $\boldsymbol{Y} = \boldsymbol{X}\boldsymbol{A}$ expresses that the coordinates of any point measured on the variable axes multiplied by the matrix of eigenvectors gives that point measured on the component axes. The so-called component scores, $y_{ik}$, will be uncorrelated with the scores on any other component.

# Appendix E

# The *k*-means clustering technique

An efficient and effective cluster tool should use as few clusters as possible, but at the same time being able of classifying all statistically relevant clusters. The term similarity in cluster analysis corresponds to the proximity of the points, how closer are them to each other in the input space. To calculate the distance between the points, one can use different metrics. We adopted the Minkowski distance, $L_1$ (also known as Manhattan or city block distance), which is given by

$$d_1(\mathbf{c}, \mathbf{x}) = \sum_{i=1}^{k} |c_i - x_i|, \tag{E.1}$$

where $c$ is the cluster center, $x$ is the case it is compared to, $i$ is the dimension of $x$ (or $c$) being compared and $k$ is total number of dimensions. The $k$-means technique partitions a set of $n$ data points $x_1$, ..., $x_n$ into a fixed known number of non-empty disjoint classes (clusters) $c_1$, ..., $c_k$, say, that are "homogeneous as possible" with respect to some given data [367]. This technique is considered a variance minimization technique, since it tries to minimize the sum of the variances within the clusters. Given $n$ data points $x_1$, ..., $x_n$ in $\mathbb{R}^p$ and a $k$-partition $\mathcal{C} = \{C_1, ..., C_k\}$ of the set $\mathcal{O} = \{1, ..., n\}$ of underlying "objects" with non-empty classes $C_i \subset \mathcal{O}$, the discrete variance criterion (also termed sum-of-squares (SSQ) criterion) is given by

$$g_n(\mathcal{C}) := \sum_{i=1}^{k} \sum_{l \in C_i} |x_l - \bar{x}_{C_i}| \rightarrow \min_{\mathcal{C}}, \tag{E.2}$$

where $\bar{x}_{C_i}$ denotes the centroid of the data points $x_l$ "belonging" to class $C_i$. We look for a $k$-partition of $\mathcal{O}$ with minimum criterion value $g_n(\mathcal{C})$ [367].

## E. THE *K*-MEANS CLUSTERING TECHNIQUE

In MATLAB, the *kmeans* function partitions data into $k$ mutually exclusive clusters. It implements the $k$-means clustering technique using a batch (also called offline) algorithm in a first phase, and an iterative algorithm in a second phase. Batch algorithms are algorithms where a transformative step is applied to all cases at once, being well suited to analyse large data sets [306]. In this way, the first phase of *kmeans* is closer to the Lloyd algorithm [368] and the second phase is nearer to the MacQueen algorithm [305]. The latter is an iterative (also called online) algorithm and differs from the Lloyd algorithm in the sense that the centroids are recalculated every time a case change cluster and also after each pass through all cases. Both algorithms have an initial similar procedure. The first step is to choose the $k$ initial centroids. In our work, we knew previously the number of expected clusters corresponding to each gap (which is 5), but sometimes, this information is not available and several attempts are needed to achieve the best result, which we will define later on. Once the initial centroids have been chosen, each case is assigned to each cluster based on its $L_1$ distance from the cluster centroids. Then, the value of the centroid is updated using the component-wise median of the points in each cluster. As a coordinate-wise order-statistic, the coordinate-wise median together with $L_1$ distance in the assignment step, is inherently more appropriate for discrete than continuous data [369]. In the MacQueen algorithm, for each case, if the centroid of the cluster it currently belongs to is the nearest, nothing is done. Otherwise, if a centroid of other cluster is closest, the case is reassigned to that centroid and the component-wise median of the points on both old and new cluster centroids are recalculated. This algorithm usually needs to perform one complete pass through the cases to converge on a solution and it is more efficient than Lloyd algorithm as it performs more centroid updates [306]. The online phase guarantees to find a local minimum, by moving points between cluster until the total sum of distances cannot be further reduced. Nevertheless, there may be other local minima with lower total sum of distances. The batch mode may provide points inside a cluster that moved to a different cluster, thus increasing the total sum of distances, this being more likely for small data sets. As said before, the batch mode is fast, but potentially approximates a solution as a starting point for the online phase. The *kmeans* function provided by MATLAB will always converge, but it is liable to find a local minimum instead of a global one, and as such may not find the optimal partition. It is common to consider heuristics based on local search, in which centers are swapped in and out of an existing solution. Therefore,

$k$-means algorithms are sensitive to the initial chosen centroids [369]. Exhaustive (or clever, or lucky) choice of starting points for multiple applications (replicates) typically results in a solution that is a global minimum, or at least a more stable solution.

The $k$-means algorithm has a bias to create clusters of equal size, thus working better for clusters that are globular in shape, have equivalent size and equivalent data densities [306, 369]. In our study, we deal with such conditions with the five clusters being similar in shape, size and density.

Finally, there are some indices capable of evaluating the quality of the achieved solution. The Dunn index [370] corresponds to the ratio of the inter-cluster similarity (distance between cluster centroids) over the intra-cluster similarity (inner cluster variation) and should be as high as possible for compact clusters. The Davies-Bouldin index [371] presenting lower values indicate the existence of compact clusters with their centers far away from each other. The C-index [372] compares the sum of smallest and largest distances over all pair of data points forming the same cluster and should be also minimized. The Jaccard index [373] compares the obtained solution with a previous reliable classification, by intersecting the cases present in the same clusters in both solutions and dividing by all the cases from both subsets. A silhouette plot [374] displays a measure of how close each point in one cluster is to points in the neighboring clusters. A good classification provides a silhouette plot with similar high silhouette values.

# References


[1] J. Bateman and J. Connolly. A hybrid MWPC gamma ray detecting system for applications in nuclear medicine. *Nucl. Instrum. Meth.*, 156(12):27 – 31, 1978. 1

[2] S. R. Cherry and M. Dahlbom. PET: Physics, Instrumentation, and Scanners. In M. Phelps, editor, *PET*, pages 1–117. Springer New York, 2006. 1, 20, 25, 29, 35, 37, 38, 89

[3] P. Fonte, A. Smirnitsky, and M. Williams. A new high-resolution TOF technology. *Nucl. Instrum. Meth. A*, 443(1):201–204, 2000. 1, 43, 44, 46, 47

[4] A. Blanco, V. Chepel, R. Ferreira Marques, et al. Perspectives for positron emission tomography with RPCs. *Nucl. Instrum. Meth. A*, 508:88–92, 2003. 1, 30, 34, 43, 63, 183

[5] A. Gouvêa. Medida da resolução temporal de um detector gasoso RPC destinado a TOF–PET, 2007. MSc. thesis. Universidade de Coimbra. (In Portuguese). 1, 34, 62, 107

[6] A. Blanco, N. Carolino, C. Correia, et al. RPC–PET: A new very high resolution PET technology. *IEEE Trans. Nucl. Sci.*, 53(5):2489–2494, 2006. 2, 29, 63

[7] M. Couceiro, A. Blanco, N. C. Ferreira, et al. RPC–PET: status and perspectives. *Nucl. Instrum. Meth. A*, 580:915–918, 2007. 2, 30, 54, 63

[8] M. Couceiro, N. C. Ferreira, and P. Fonte. Sensitivity assessment of wide Axial Field of View PET systems via monte carlo simulations of NEMA-like measurements. *Nucl. Instrum. Meth. A*, 580(1):485 – 488, 2007. Proceedings of the 10 th International Symposium on Radiation Physics – ISRP 10. 2, 31, 63

[9] P. Crespo, J. Reis, M. Couceiro, et al. Whole-body single-bed time-of-flight RPC–PET: simulation of axial and planar sensitivities with NEMA and anthropomorphic phantoms. *IEEE Trans. Nucl. Sci.*, 59(3):520–529, 2012. 2, 7, 35, 63, 64, 66, 67, 68, 69, 70, 180, 181

[10] M. Couceiro, P. Crespo, R. Ferreira Marques, and P. Fonte. Scatter fraction, count rates, and noise equivalent count rate of a single-bed position RPC TOF–PET system assessed by simulations following the NEMA NU2-2001 standards. *IEEE Trans Nucl. Sci.*, 61(3):1153–1163, June 2014. 2, 53, 70, 71, 72, 73

[11] P. Crespo, A. Blanco, M. Couceiro, et al. Resistive plate chambers in positron emission tomography. *The European Physical Journal Plus*, 128(7):1–35, 2013. 2, 6, 52

[12] A. Jeavons, R. Chandler, and C. Dettmar. A 3D HIDAC-PET camera with sub-millimetre resolution for imaging small animals. *IEEE Trans Nucl. Sci.*, 46(3):468–473, Jun 1999. 2

[13] D. Burdette, E. Chesi, N. Clinthorne, et al. First results from a test bench for very high resolution small animal PET using solid-state detectors. In *Conf. Record of the 2005 IEEE Nucl. Sci. Symp. & Med. Imag. Conf. (NSS/MIC)*, volume 4, pages 2376–2380, Oct 2005. 2

[14] K. Ishii, Y. Kikuchi, S. Matsuyama, et al. First achievement of less than 1 mm FWHM resolution in practical semiconductor animal PET scanner. *Nucl. Instrum. Meth. A*, 576(23):435 – 440, 2007. 2, 77

[15] P. Reynolds, F. Lau, A. Vandenbroucke, et al. Characterization of detector layers from a 1 $mm^3$ resolution clinical PET system. In *Conf. Record of the 2012 IEEE Nucl. Sci. Symp. & Med. Imag. Conf. (NSS/MIC)*, pages 3804–3807, Oct 2012. 2, 28, 77

[16] K. Nagy, M. Tóth, P. Major, et al. Performance evaluation of the small-animal nanoscan PET/MRI system. *J. Nucl. Med.*, 2013. 2, 29, 76, 78

[17] J. M. C. Pedroso de Lima. *Quantificação em Hepatologia Nuclear*. PhD thesis, Universidade de Coimbra, Portugal, 1997. 4

[18] J. Michel, M. Böhmerb, M. Kajetanowicz, et al. The upgraded HADES trigger and data acquisition system. *JINST*, 6, 2011. 4, 112, 113

[19] A. Blanco, P. Fonte, L. Lopes, et al. TOFtracker: gaseous detector with bidimensional tracking and time-of-flight capabilities. *JINST*, 7(11):P11012, 2012. 5, 46, 63, 107, 108, 123, 134, 138, 221

[20] A. Morozov, I. Defendi, R. Engels, et al. ANTS – a simulation package for secondary scintillation Anger-camera type detector in thermal neutron imaging. *JINST*, 7(08):P08010, 2012. 5, 143, 221

[21] V. Solovov, V. Belov, D. Akimov, et al. Position reconstruction in a dual phase xenon scintillation detector. *IEEE Trans Nucl. Sci.*, 59(6):3286–3293, Dec 2012. 5, 142, 143, 221

[22] P. Martins, A. Blanco, P. Crespo, et al. Towards very high resolution RPC–PET for small animals. Manuscript submitted for publication, 2014. 7

[23] P. Martins, P. Crespo, R. Ferreira Marques, et al. Experimental sub-millimeter resolution with a small-animal RPC–PET prototype. In *Conf. Record of the 2012 IEEE Nucl. Sci. Symp. & Med. Imag. Conf. (NSS/MIC)*, pages 3760–3764, Anaheim, CA, USA, Oct 2012. 7

[24] P. Martins, A. Blanco, P. Crespo, et al. Achieving 0.4-mm FWHM spatial resolution with an RPC-based small-animal PET prototype. In *Conf. Record of the 2013 IEEE Nucl. Sci. Symp. & Med. Imag. Conf. (NSS/MIC)*, pages 1–2, Seoul, Korea, Oct 2013. 7

[25] P. Martins, M. Couceiro, N. Ferreira, et al. A direct time-of-flight reconstruction for whole-body single-bed RPC–PET: Results from lesion and anthropomorphic simulated data. Manuscript submitted for publication, 2014. 8

[26] P. Martins, A. Blanco, F. Caramelo, et al. A direct time-of-flight reconstruction for whole-body single-bed RPC–PET: Results from lesion and anthropomorphic simulated data. In *Conf. Record of the 2011 IEEE Nucl. Sci. Symp. & Med. Imag. Conf. (NSS/MIC)*, pages 2610–2616, Valencia, Spain, Oct 2011. 8

[27] P. Martins, M. Couceiro, N. Ferreira, et al. On lesion detectability by means of 300 ps–FWHM TOF whole-body RPC–PET: An experiment-based simulation study. In *Conf. Record of the 2012 IEEE Nucl. Sci. Symp. & Med. Imag. Conf. (NSS/MIC)*, pages 2440–2444, Anaheim, CA, USA, Oct 2012. 8

[28] W. Segars. *Development of a new dynamic NURBS-based cardiac-torso (NCAT) phantom.* PhD thesis, The University of North Carolina, USA, May 2001. 10, 180, 183, 239

[29] J. Bushberg. *The Essential Physics of Medical Imaging.* Lippincott Williams & Wilkins, 2002. 10, 13, 15

[30] R. Evans. *The Atomic Nucleus.* McGraw-Hill, 1955. 11, 13, 17, 18

[31] C. Davisson and R. Evans. Gamma-ray absorption coefficients. *Rev. Mod. Phys.*, 24:79–107, Apr 1952. 11, 13

[32] F. Sauter. Über den atomaren Photoeffekt bei großer Härte der anregenden Strahlung. *Annalen der Physik*, 401(2):217–248, 1931. 11

[33] M. Stobbe. Zur Quantenmechanik photoelektrischer Prozesse. *Annalen der Physik*, 399(6):661–715, 1930. 11

[34] H. Hulme, J. McDougall, R. Buckingham, and R. Fowler. The photoelectric absorption of $\gamma$-rays in heavy elements. *Proceedings of the Royal Society of London. Series A - Mathematical and Physical Sciences*, 149(866):131–151, 1935. 11

[35] H. Hall. The photoelectric effect for high energy quanta. *Phys. Rev.*, 45:620–627, May 1934. 11

[36] H. Hall. The theory of photoelectric absorption for x-rays and $\gamma$-rays. *Rev. Mod. Phys.*, 8:358–397, Oct 1936. 11

[37] H. Hall. Note on the relativistic formula for photoelectric absorption. *Phys. Rev.*, 84:167–168, Oct 1951. 11

[38] O. Klein and Y. Nishina. Über die Streuung von Strahlung durch freie Elektronen nach der neuen relativistischen Quantendynamik von Dirac. *Zeitschrift für Physik*, 52(11-12):853–868, 1929. 12

[39] G. Knoll. *Radiation detection and measurement.* Wiley, 2000. 12, 144

[40] J. Thomson. *Conduction of electricity through gases.* Cambridge physical series. University press, Cambridge, England, 2 edition, 1906. 12

[41] D. L. Bailey, J. S. Karp, and S. Surti. Physics and Instrumentation in PET. In D. L. Bailey, D. W. Townsend, P. E. Valk, and M. N. Maisey, editors, *Positron Emission Tomography*, pages 13–39. Springer London, 2005. 12, 17, 19, 22, 28

[42] D. González-Días. *Research and Developments on Timing RPCs. Application to the ESTRELA Detector of the HADES Experiment at GSI.* PhD thesis, Universidad de Santiago de Compostela, Spain, 2006. 12, 50

[43] C. Grupen, A. Böhrer, and L. Smolík. *Particle Detectors.* Cambridge monographs on particle physics, nuclear physics, and cosmology. Cambridge University Press, 1996. 12

[44] C. Lippmann. *Detector Physics of Resistive Plate Chambers.* PhD thesis, Johann Wolfgang Goethe-Universitaet, Germany, 2003. 13, 49

[45] J. H. Hubbell. Review of photon interaction cross section data in the medical and biological context. *Phys. Med. Biol.*, 44(1):R1, 1999. 14, 15

[46] J. H. Hubbell, H. A. Gimm, and I. Øverbø. Pair, triplet, and total atomic cross sections (and mass attenuation coefficients) for 1 MeV–100 GeV photons in elements Z=1 to 100. *Journal of Physical and Chemical Reference Data*, 9(4):1023–1148, 1980. 14

[47] M. Phelps. *PET: Molecular Imaging and Its Biological Applications.* Springer, 2004. 16

[48] M. E. Phelps, E. J. Hoffman, N. A. Mullani, and M. M. Ter-Pogossian. Application of annihilation coincidence detection to transaxial reconstruction tomography. *J. Nucl. Med.*, 16(3):210–224, 1975. 16

[49] K. Krane. *Introductory Nuclear Physics.* John Wiley and Sons, 1988. 18

[50] A. Blanco. *A small animal PET prototype with submillimetre spatial resolution based on tRPCs.* PhD thesis, Universidad de Santiago de Compostela, Spain, Dec 2012. 19, 20, 21, 27, 43, 49, 51, 52, 76

[51] S. Derenzo. Precision measurement of annihilation point spread distributions for medically important positron emitters. In *Proceedings of the 5th International Conference on Positron Annihilation*, pages 819–823, Sendai, Japan, Eds. Hasiguti, R.R. and Fujiwara, K. The Japan Insitute of Metals, Apr 1979. 21, 102

[52] M. Palmer and G. L. Brownell. Annihilation density distribution calculations for medically important positron emitters. *IEEE Trans Med Imaging*, 11(3):373–378, Sep 1992. 21

[53] C. S. Levin and E. J. Hoffman. Calculation of positron range and its effect on the fundamental limit of positron emission tomography system spatial resolution. *Phys. Med. Biol.*, 44(3):781, 1999. 21

[54] H. Iida, I. Kanno, S. Miura, et al. A simulation study of a method to reduce positron annihilation spread distributions using a strong magnetic field in positron emission tomography. *IEEE Trans Nucl. Sci.*, 33(1):597–600, Feb 1986. 21

[55] B. E. Hammer, N. L. Christensen, and B. G. Heil. Use of a magnetic field to increase the spatial resolution of positron emission tomography. *Medical Physics*, 21(12):1917–1920, 1994. 21

[56] A. Wirrwar, H. Vosberg, H. Herzog, et al. 4.5 tesla magnetic field reduces range of high-energy positrons-potential implications for positron emission tomography. *IEEE Trans Nucl. Sci.*, 44(2):184–189, Apr 1997. 21

[57] H. Peng and C. S. Levin. Study of pet intrinsic spatial resolution and contrast recovery improvement for PET/MRI systems. *Phys. Med. Biol.*, 57(9):N101, 2012. 21

[58] S. Derenzo. Mathematical removal of positron range blurring in high resolution tomography. *IEEE Trans Nucl. Sci.*, 33(1):565–569, Feb 1986. 21, 166

[59] S. F. Haber, S. Derenzo, and D. Uber. Application of mathematical removal of positron range blurring in positron emission tomography. *IEEE Trans Nucl. Sci.*, 37(3):1293–1299, Jun 1990. 21

[60] S. DeBenedetti, C. E. Cowan, W. R. Konneker, and H. Primakoff. On the angular distribution of two-photon annihilation radiation. *Phys. Rev.*, 77:205–212, Jan 1950. 21, 165, 166

[61] W. W. Moses. Fundamental limits of spatial resolution in PET. *Nucl. Instrum. Meth. A*, 648, Supplement 1(0):S236 – S240, 2011. NIMA 4th International Conference on Imaging techniques in Subatomic Physics, Astrophysics, Medicine, Biology and Industry. 21, 26, 27

[62] P. Colombino, B. Fiscella, and L. Trossi. Study of positronium in water and ice from 22 to -144 °C by annihilation quanta measurements. *Nuovo Cimento Serie*, 38:707–723, July 1965. 22

[63] *Anatomical Terminology, accessed 20 March 2014.* Available at http://training.seer.cancer.gov/anatomy/body/terminology.html. 22

[64] D. L. Bailey. Data acquisition and performance characterization in PET. In D. L. Bailey, D. W. Townsend, P. E. Valk, and M. N. Maisey, editors, *Positron Emission Tomography*, pages 41–62. Springer London, 2005. 23, 24, 25

[65] National Electrical Manufacturers Association. NEMA Standards Publication NU 2–2001: Performance measurements of positron emission tomographs, 2001. 25, 29, 72, 73

[66] National Electrical Manufacturers Association. NEMA Standards Publication NU 2–1994: Performance measurements of positron emission tomographs, 1994. 25, 63

[67] J. S. Karp, M. E. Daube-Witherspoon, E. J. Hoffman, et al. Performance standards in positron emission tomography. *J. Nucl. Med.*, 32(12):2342–2350, December 1991. 25

[68] M. E. Daube-Witherspoon, J. S. Karp, M. E. Casey, et al. PET performance measurements using the NEMA NU 2-2001 standard. *J. Nucl. Med.*, 43(10):1398–1409, October 2002. 25

[69] P. Zanzonico. Positron emission tomography: a review of basic principles, scanner design and performance, and current systems. *Seminars in nuclear medicine*, 34(2):87–111, April 2004. 26

[70] S. Silva. *Small Animal PET Imaging Using GATE Monte Carlo Simulations: implementation of physiological and metabolic information.* PhD thesis, Universidade de Lisboa, Portugal, 2010. 26

[71] A. Sánchez-Crespo, P. Andreo, and S. A. Larsson. Positron flight in human tissues and its influence on PET image spatial resolution. *Eur. J. Nucl. Med. Mol. Imaging*, 31(1):44–51, 2004. 26

[72] S. Derenzo, T. Budinger, R. Huesman, J. L. Cahoon, and T. Vuletich. Imaging properties of a positron tomograph with 280 BGO crystals. *IEEE Trans Nucl. Sci.*, 28(1):81–89, Feb 1981. 26, 27

[73] M. Couceiro, P. Crespo, L. Mendes, et al. Spatial resolution of human RPC–PET system. *Nucl. Instrum. Meth. A*, 661, Supplement 1(0):S156 – S158, 2012. X. Workshop on Resistive Plate Chambers and Related Detectors (RPC 2010). 27, 64, 166

[74] L.-E. Adam, J. Zaers, H. Ostertag, et al. Performance evaluation of the whole-body PET scanner ECAT EXACT HR + following the IEC standard. *IEEE Trans Nucl. Sci.*, 44(3):1172–1179, Jun 1997. 27

[75] C. Carrier, C. Martel, D. Schmitt, and R. Lecomte. Design of a high resolution positron emission tomograph using solid state scintillation detectors. *IEEE Trans Nucl. Sci.*, 35(1):685–690, Feb 1988. 28

[76] M. V. Green, H. G. Ostrow, J. Seidel, and M. G. Pomper. Experimental evaluation of depth-of-interaction correction in a small-animal positron emission tomography scanner. *Molecular imaging*, 9(6):311–318, December 2010. 28

[77] J. Huber, W. Moses, S. Derenzo, et al. Characterization of a 64 channel PET detector using photodiodes for crystal identification. *IEEE Trans Nucl. Sci.*, 44(3):1197–1201, Jun 1997. 28

[78] P. D. Reynolds, P. D. Olcott, G. Pratx, F. W. Y. Lau, and C. S. Levin. Convex optimization of coincidence time resolution for a high-resolution PET system. *IEEE Trans Med Imaging*, 30(2):391 –400, 2011. 28

[79] R. Wiener, S. Surti, and J. Karp. DOI determination by rise time discrimination in single-ended readout for TOF PET imaging. *IEEE Trans Nucl. Sci.*, 60(3):1478–1486, June 2013. 28

[80] H. Thoen, V. Keereman, P. Mollet, R. Van Holen, and S. Vandenberghe. Influence of detector pixel size, TOF resolution and DOI on image quality in MR-compatible whole-body PET. *Phys. Med. Biol.*, 58:6459–6479, 2013. 28, 29, 158

[81] E. Hoffman and M. Phelps. Positron emission tomography: principles and quantitation. In M. Phelps, J. Mazziotta, and H. Schelbert, editors, *Positron emission tomography and autoradiography. Principles and applications for the brain and heart*, pages 237–86. New York: Raven Press, 1986. 29

[82] G. Muehllehner. Effect of resolution improvement on required count density in ECT imaging: a computer simulation. *Phys. Med. Biol.*, 30(2):163, 1985. 29

[83] S. Metzler, S. Matej, and J. Karp. Resolution enhancement in PET reconstruction using collimation. *IEEE Trans Nucl. Sci.*, 60(1):65–75, Feb 2013. 29

[84] D. L. Bailey, T. Jones, and T. J. Spinks. A method for measuring the absolute sensitivity of positron emission tomographic scanners. *Eur. J. Nucl. Med.*, 18(6):374–379, 1991. 29

[85] N. C. Ferreira. *Contribuição para a quantificação em Tomografia por Emissão de Positrões no modo 3D*. PhD thesis, Universidade de Coimbra, Portugal, 2001. 30, 36, 37, 38, 39

[86] C. Burnham and G. Brownell. A multi-crystal positron camera. *IEEE Trans Nucl. Sci.*, 19(3):201–205, June 1972. 31

[87] J. Neves. Desenvolvimento de um protótipo RPC–PET, 2008. MSc. thesis. Universidade de Coimbra. (In Portuguese). 31, 48, 50, 52, 53, 57, 58, 59

[88] S. Strother, M. Casey, and E. Hoffman. Measuring PET scanner sensitivity: relating countrates to image signal-to-noise ratios using noise equivalents counts. *IEEE Trans Nucl. Sci.*, 37(2):783–788, Apr 1990. 32

[89] L. R. MacDonald, R. L. Harrison, A. M. Alessio, et al. Effective count rates for PET scanners with reduced and extended axial field of view. *Phys. Med. Biol.*, 56(12):3629–3643, June 2011. 32

[90] C. Lartizien, C. Comtat, P. E. Kinahan, et al. Optimization of injected dose based on noise equivalent count rates for 2- and 3-dimensional whole-body PET. *J. Nucl. Med.*, 43(9):1268–1278, September 2002. 32

[91] H. Anger. Survey of radioisotope cameras. *ISA Trans.*, 5:311–334, 1966. 32

[92] G. Brownell, C. Burnham, S. Wilensky, et al. New developments in positron scintigraphy and the application of cyclotron produced positron emitters. *Medical Radioisotope Scintigraphy*, 1:163–176, Oct 1969. 32

[93] T. F. Budinger. Instrumentation trends in nuclear medicine. *Seminars in Nuclear Medicine*, 7(4):285 – 297, 1977. Advances in Imaging Instrumentation. 32

[94] M. M. Ter-Pogossian, D. C. Ficke, J. T. S. Hood, M. Yamamoto, and N. A. Mullani. PETT VI: a positron emission tomograph utilizing cesium fluoride scintillation detectors. *Journal of computer assisted tomography*, 6(1):125–133, February 1982. 32

[95] R. Allemand, C. Gresset, and J. Vacher. Potential advantages of a cesium fluoride scintillator for a time-of-flight positron camera. *J. Nucl. Med.*, 21(2):153–155, Feb 1980. 32

[96] W. Wong, N. Mullani, E. Philippe, et al. Performance characteristics of the University of Texas TOFPET-I PET camera. *J. Nucl. Med.*, 25:46–47, 1984. 32

[97] T. Lewellen, A. N. Bice, R. Harrison, M. Pencke, and J. Link. Performance measurements of the SP3000/UW time-of-flight positron emission tomograph. *IEEE Trans Nucl. Sci.*, 35(1):665–669, Feb 1988. 32

[98] B. Mazoyer, R. Trebossen, C. Schoukroun, et al. Physical characteristics of TTV03, a new high spatial resolution time-of-flight positron tomograph. *IEEE Trans Nucl. Sci.*, 37(2):778–782, Apr 1990. 32

[99] W. W. Moses. Current trends in scintillator detectors and materials. *Nucl. Instrum. Meth. A*, 487(12):123 – 128, 2002. 3rd International Workshop on Radiation Imaging Detectors. 32

[100] C. W. E. van Eijk. Inorganic scintillators in medical imaging. *Phys. Med. Biol.*, 47(8):R85, 2002. 32

[101] J. Karp, S. Surti, M. Daube-Witherspoon, and G. Muehllehner. Benefit of time-of-flight in PET: experimental and clinical results. *J. Nucl. Med.*, 49:462–470, 2008. 32, 34, 238

[102] P. Crespo. *Optimization of In-Beam Positron Emission Tomography for Monitoring Heavy Ion Tumor Therapy*. PhD thesis, TU Darmstadt, Germany, 2006. 33, 34, 83, 87

[103] D. L. Snyder, L. J. Thomas, and M. M. Ter-Pogossian. A mathematical model for positron-emission tomography systems having time-of-flight measurements. *IEEE Trans Nucl. Sci.*, 28(3):3575–3583, June 1981. 34

[104] T. F. Budinger. Time-of-flight positron emission tomography: status relative to conventional PET. *J. Nucl. Med.*, 24(1):73–78, January 1983. 34

[105] T. Tomitani. Image reconstruction and noise evaluation in photon time-of-flight assisted positron emission tomography. *IEEE Trans Nucl. Sci.*, 28(6):4581–4589, Dec 1981. 34

[106] W. W. Moses. Time of flight in PET revisited. *IEEE Trans Nucl. Sci.*, 50(5):1325–1330, Oct 2003. 34

[107] W. W. Moses and M. Ullisch. Factors influencing timing resolution in a commercial LSO PET camera. *IEEE Trans Nucl. Sci.*, 53(1):78–85, Feb 2006. 34

[108] S. Surti, A. Kuhn, M. E. Werner, et al. Performance of Philips Gemini TF PET/CT scanner with special consideration for its time-of-flight imaging capabilities. *J. Nucl. Med.*, 48:471–480, 2007. 34, 42, 72, 73

[109] B. W. Jakoby, Y. Bercier, M. Conti, et al. Physical and clinical performance of the mCT time-of-flight PET/CT scanner. *Phys. Med. Biol.*, 56(8):2375, 2011. 34, 42, 63

[110] V. Bettinardi, L. Presotto, E. Rapisarda, et al. Physical performance of the new hybrid PET/CT Discovery-690. *Medical physics*, 38(10):5394–5411, October 2011. 34, 42

[111] S. Surti, J. Karp, L. Popescu, M. Daube-Witherspoon, and M. Werner. Investigation of time-of-flight benefit for fully 3-D PET. *IEEE Trans Med Imaging*, 25(5):529–538, May 2006. 34

[112] S. Surti and J. S. Karp. Experimental evaluation of a simple lesion detection task with time-of-flight PET. *Phys. Med. Biol.*, 54(2):373, 2009. 34

[113] A. M. Morey and D. J. Kadrmas. Effect of varying number of OSEM subsets on PET lesion detectability. *Journal of nuclear medicine technology*, 41(4):268–273, December 2013. 34

[114] M. Conti, L. Eriksson, and V. Westerwoudt. Estimating image quality for future generations of TOF PET scanners. *IEEE Trans Nucl. Sci.*, 60(1):87–94, Feb 2013. 34

[115] V. Westerwoudt, M. Conti, and L. Eriksson. Advantages of improved time resolution for TOF PET at very low statistics. *IEEE Trans Nucl. Sci.*, 61(1):126–133, Feb 2014. 34

[116] M. Daube-Witherspoon, S. Matej, M. Werner, S. Surti, and J. Karp. Comparison of list-mode and DIRECT approaches for time-of-flight PET reconstruction. *IEEE Trans Med Imaging*, 31(7):1461–1471, July 2012. 34, 187, 238

[117] L. Eriksson, D. W. Townsend, M. Conti, et al. Potentials for large axial field of view positron camera systems. In *Conf. Records 2008 IEEE Nucl. Sci. Symp. & Med. Imag. Conf. (NSS/MIC)*, pages 1632–1636, Dresden, Germany, Oct. 19–25 2008. 35, 63, 64, 67, 68

[118] E. J. Hoffman, S. C. Huang, M. E. Phelps, and D. E. Kuhl. Quantitation in positron emission computed tomography: 4. Effect of accidental coincidences. *Journal of computer assisted tomography*, 5(3):391–400, June 1981. 35

[119] S. R. Meikle and R. D. Badawi. Quantitative techniques in PET. In D. L. Bailey, D. W. Townsend, P. E. Valk, and M. N. Maisey, editors, *Positron Emission Tomography*, pages 93–126. Springer London, 2005. 35, 37

[120] S. R. Cherry, J. A. Sorenson, and M. E. Phelps. Chapter 18 - positron emission tomography. In S. R. Cherry, J. A. Sorenson, and M. E. Phelps, editors, *Physics in Nuclear Medicine*, pages 307 – 343. W.B. Saunders, Philadelphia, fourth edition, 2012. 35, 36

[121] M. E. Casey, H. Gadagkar, and D. Newport. A component based method for normalization in volume PET. In *3rd International Meeting on Fully Three-Dimensional Image Reconstruction in Radiology and Nuclear Medicine*, Aix les Bains, France, 1995. 36, 37

[122] P. Zanzonico. Routine quality control of clinical nuclear medicine instrumentation: A brief review. *J. Nucl. Med.*, 49(7):1114–1131, 2008. 36, 37

[123] M. Defrise, D. W. Townsend, D. Bailey, A. M. C. Geissbuhler, and T. Jones. A normalization technique for 3D PET data. *Phys. Med. Biol.*, 36(7):939, 1991. 36

[124] E. Hoffman, T. Guerrero, G. Germano, W. Digby, and M. Dahlbom. PET system calibrations and corrections for quantitative and spatially accurate images. *IEEE Trans Nucl. Sci.*, 36(1):1108–1112, Feb 1989. 37

[125] R. D. Badawi and P. K. Marsden. Developments in component-based normalization for 3D PET. *Phys. Med. Biol.*, 44(2):571, 1999. 37

[126] J. Ollinger. Detector efficiency and compton scatter in fully 3D PET. *IEEE Trans Nucl. Sci.*, 42(4):1168–1173, Aug 1995. 37

[127] F. Hermansen, T. J. Spinks, P. G. Camici, and A. A. Lammertsma. Calculation of single detector efficiencies and extension of the normalization sinogram in PET. *Phys. Med. Biol.*, 42(6):1143, 1997. 37

[128] B. Bai, Q. Li, C. H. Holdsworth, et al. Model-based normalization for iterative 3D PET image reconstruction. *Phys. Med. Biol.*, 47(15):2773, 2002. 37

[129] T. Oakes, V. Sossi, and T. Ruth. Normalization in 3D PET: comparison of detector efficiencies obtained from uniform planar and cylindrical sources. In *Conf. Record of the 1997 IEEE Nucl. Sci. Symp. & Med. Imag. Conf. (NSS/MIC)*, volume 2, pages 1625–1629 vol.2, Nov 1997. 37

[130] E. Vicente, J. J. Vaquero, S. Espana, et al. Normalization in 3D PET: Dependence on the activity distribution of the source. In *Conf. Record of the 2006 IEEE Nucl. Sci. Symp. & Med. Imag. Conf. (NSS/MIC)*, volume 4, pages 2206–2209, Oct 2006. 37

[131] C. Watson, D. Newport, and M. Casey. A single scatter simulation technique for scatter correction in 3D PET. In P. Grangeat and J.-L. Amans, editors, *Three-Dimensional Image Reconstruction in Radiology and Nuclear Medicine*, volume 4 of *Computational Imaging and Vision*, pages 255–268. Springer Netherlands, 1996. 37

[132] C. Watson. New, faster, image-based scatter correction for 3D PET. *IEEE Trans Nucl. Sci.*, 47(4):1587–1594, Aug 2000. 37

[133] D. Bailey. Quantitative procedures in 3D PET. In B. Bendriem and D. W. Townsend, editors, *The Theory and Practice of 3D PET*, volume 32 of *Developments in Nuclear Medicine*, pages 55–109. Springer Netherlands, 1998. 38

[134] S. Grootoonk, T. Spinks, T. Jones, C. Michel, and A. Bol. Correction for scatter using a dual energy window technique with a tomograph operated without septa. In *Conf. Record of the 1991 IEEE Nucl. Sci. Symp. & Med. Imag. Conf. (NSS/MIC)*, pages 1569–1573 vol.3, Nov 1991. 38

[135] B. Bendriem, R. Trebossen, V. Frouin, and A. Syrota. A PET scatter correction using simultaneous acquisitions with low and high lower energy thresholds. In *Conf. Record of the 1993 IEEE Nucl. Sci. Symp. & Med. Imag. Conf. (NSS/MIC)*, pages 1779–1783 vol.3, Oct 1993. 38

[136] L. Shao, R. Freifelder, and J. Karp. Triple energy window scatter correction technique in PET. *IEEE Trans Med Imaging*, 13(4):641–648, Dec 1994. 38

[137] M. Bentourkia, P. Msaki, J. Cadorette, and R. Lecomte. Assessment of scatter components in multispectral PET imaging. In *Conf. Record of the 1993 IEEE Nucl. Sci. Symp. & Med. Imag. Conf. (NSS/MIC)*, pages 1505–1509 vol.3, Oct 1993. 38

[138] M. Bergstrom, L. Eriksson, C. Bohm, G. Blomqvist, and J. Litton. Correction for scattered radiation in a ring detector positron camera by integral transformation of the projections. *Journal of computer assisted tomography*, 7(1):42–50, February 1983. 38

[139] L. Shao and J. Karp. Cross-plane scattering correction-point source deconvolution in PET. *IEEE Trans Med Imaging*, 10(3):234–239, Sep 1991. 38

[140] P. Prat, P. Lanza, P. Corvisiero, R. Guzzardi, and O. Sorace. Verification of the integral transformation of the projections technique for scatter correction in positron tomographs. *Eur. J. Nucl. Med.*, 20(3):255–259, 1993. 38

[141] D. Townsend, A. Geissbuhler, M. Defrise, et al. Fully three-dimensional reconstruction for a PET camera with retractable septa. *IEEE Trans Med Imaging*, 10(4):505–512, Dec 1991. 38

[142] D. L. Bailey and S. R. Meikle. A convolution-subtraction scatter correction method for 3D PET. *Phys. Med. Biol.*, 39(3):411, 1994. 38

[143] J. Barney, R. Harrop, and C. Dykstra. Source distribution dependent scatter correction for PVI. *IEEE Trans Nucl. Sci.*, 40(4):1001–1007, Aug 1993. 38

[144] L. G. Hiltz and B. T. A. McKee. Scatter correction for three-dimensional PET based on an analytic model dependent on source and attenuating object. *Phys. Med. Biol.*, 39(11):2059, 1994. 38

[145] J. M. Ollinger. Model-based scatter correction for fully 3D PET. *Phys. Med. Biol.*, 41(1):153, 1996. 38

[146] J. S. Barney, J. Rogers, R. Harrop, and H. Hoverath. Object shape dependent scatter simulations for PET. *IEEE Trans Nucl. Sci.*, 38(2):719–725, Apr 1991. 38

[147] C. Thompson. The problem of scatter correction in positron volume imaging. *IEEE Trans Med Imaging*, 12(1):124–132, Mar 1993. 38

[148] A. Goggin and J. Ollinger. A model for multiple scatters in fully 3D PET. In *Conf. Record of the 1994 IEEE Nucl. Sci. Symp. & Med. Imag. Conf. (NSS/MIC)*, volume 4, pages 1609–1613 vol.4, Oct 1994. 38

[149] C. Levin, M. Dahlbom, and E. Hoffman. A Monte Carlo correction for the effect of Compton scattering in 3-D PET brain imaging. *IEEE Trans Nucl. Sci.*, 42(4):1181–1185, Aug 1995. 39

[150] C. Holdsworth, C. Levin, T. Farquhar, M. Dahlbom, and E. Hoffman. Investigation of accelerated Monte Carlo techniques for PET simulation and 3D PET scatter correction. *IEEE Trans Nucl. Sci.*, 48(1):74–81, Feb 2001. 39

[151] C. Holdsworth, C. Levin, M. Janecek, M. Dahlbom, and E. Hoffman. Performance analysis of an improved 3-D PET Monte Carlo simulation and scatter correction. *IEEE Trans Nucl. Sci.*, 49(1):83–89, Feb 2002. 39

[152] C. Watson. Extension of single scatter simulation to scatter correction of time-of-flight PET. *IEEE Trans Nucl. Sci.*, 54(5):1679–1686, Oct 2007. 39

[153] M. Werner, S. Surti, and J. Karp. Implementation and evaluation of a 3D PET single scatter simulation with TOF modeling. In *Conf. Record of the 2006 IEEE Nucl. Sci. Symp. & Med. Imag. Conf. (NSS/MIC)*, volume 3, pages 1768–1773, Oct 2006. 39

[154] J. Reis. Simulação da biodistribuição, aniquilação e escape de fotões PET no corpo humano, 2008. MSc. thesis. Universidade de Coimbra. (In Portuguese). 39, 180

[155] S. Carvalho. Contribuição para o estudo de viabilidade de um tomógrafo de longo campo de visão axial baseado em RPCs: correcção da radiação dispersa, 2008. MSc. thesis. Universidade de Coimbra. (In Portuguese). 39

[156] L. Martins. Correcção da dispersão de compton em PET utilizando informação da energia dos fotões, 2012. MSc. thesis. Universidade de Coimbra. (In Portuguese). 39

[157] T. Beyer. *Design, Construction and Validation of a Combined PET/CT Tomograph for Clinical Oncology.* PhD thesis, University of Surrey, Dec 1999. 41

[158] P. E. Kinahan, D. W. Townsend, T. Beyer, and D. Sashin. Attenuation correction for a combined 3D PET/CT scanner. *Medical physics*, 25(10):2046–2053, October 1998. 41

[159] B. Kemp, J. Williams, R. Ruter, V. Lowe, and B. Mullan. Performance measurements of a whole body PET/CT system with time-of-flight capability. *J. Nucl. Med.*, 50(2):1546, 2009. 42

[160] S. J. Townsend. *The Theory of Ionization of Gases by Collision.* London: Constable, 1910. 43

[161] O. C. Allkofer. *Spark Chambers.* Verlag Karl Thiemig, München, 1969. 44

[162] R. Santonico and R. Cardarelli. Development of resistive plate counters. *Nucl. Instrum. Meth.*, 187(2–3):377–380, 1981. 43, 44

[163] Y. N. Pestov. Timing below 100 ps with spark counters. In *36th International Winter Meeting on Nuclear Physics*, pages 604–621, Bormio, Italy, 1998. 43

[164] P. Fonte. Applications and new developments in resistive plate chambers. *IEEE Trans. Nucl. Sci.*, 49(3):881–887, 2002. 43, 44, 45, 46, 48, 49

[165] R. Cardarelli, R. Santonico, A. di Biagio, and A. Lucci. Progress in resistive plate counters. *Nucl. Instrum. Meth. A*, 263:20–25, 1988. 43

[166] R. Cardarelli, A. di Ciaccio, and R. Santonico. Performance of a resistive plate chamber operating with pure $CF_3Br$. *Nucl. Instrum. Meth. A*, 333(2–3):399–403, 1993. 44

[167] E. Cerron Zeballos, I. Crotty, D. Hatzifotiadou, et al. A new type of resistive plate chamber: the multigap RPC. *Nucl. Instrum. Meth. A*, 374:132–135, 1996. 44, 46

[168] P. Breuil, P. Fonte, E. Nappi, R. Oliveira, and V. Peskov. Advances in the development of micropattern gaseous detectors with resistive electrodes. *The European Physical Journal Plus*, 128(12):1–16, 2013. 44

[169] M. Alviggi, G. Carlino, F. Conventi, et al. Results on long-term performances and laboratory tests of the L3 RPC system at LEP. *Nucl. Instrum. Meth. A*, 515(12):328 – 334, 2003. Proceedings of the International Workshop on Aging Phenomena in Gaseous Detectors. 44

[170] A. Bertolin, R. Brugnera, A. Candela, et al. Long term performances of OPERA bakelite RPC system. *Nucl. Instrum. Meth. A*, 661, Supplement 1(0):S60 – S63, 2012. X. Workshop on Resistive Plate Chambers and Related Detectors (RPC 2010). 44

[171] F. Anulli, R. Baldini, A. Calcaterra, et al. Performance of second generation BABAR resistive plate chambers. *Nucl. Instrum. Meth. A*, 552(3):276 – 291, 2005. 44

[172] Y. Hoshi, N. Kikuchi, T. Nagamine, K. Neichi, and A. Yamaguchi. Performance of the endcap RPC in the Belle detector under high luminosity operation of the KEKB accelerator. *Nuclear Physics B - Proceedings Supplements*, 158(0):190 – 194, 2006. Proceedings of the 8th International Workshop on Resistive Plate Chambers and Related Detectors Proceedings of the 8th International Workshop on Resistive Plate Chambers and Related Detectors. 44

[173] P. Camarri. Operation and performance of RPCs in the ARGO-YBJ experiment. *Nucl. Instrum. Meth. A*, 602(3):668 – 673, 2009. Proceedings of the 9th International Workshop on Resistive Plate Chambers and Related Detectors {RPC08}. 44

[174] G. Barr, D. Dedovich, A. D. Min, et al. Performance of multigap RPC detectors in the HARP experiment. *Nucl. Instrum. Meth. A*, 533(12):214 – 220, 2004. Proceedings of the Seventh International Workshop on Resistive Plate Chambers and Related Detectors. 44

[175] W. J. Llope. Multigap RPCs in the STAR experiment at RHIC. *Nucl. Instrum. Meth. A*, 661, Supplement 1(0):S110 – S113, 2012. X. Workshop on Resistive Plate Chambers and Related Detectors (RPC 2010). 44

[176] A. Schüttauf, K. Hildenbrand, M. Ciobanu, et al. Performance of the Multistrip-MRPCs for FOPI. *Nuclear Physics B - Proceedings Supplements*, 158(0):52 – 55, 2006. Proceedings of the 8th International Workshop on Resistive Plate Chambers and Related Detectors Proceedings of the 8th International Workshop on Resistive Plate Chambers and Related Detectors. 44

[177] P. Paolucci, R. Hadjiiska, L. Litov, et al. CMS Resistive Plate Chamber overview, from the present system to the upgrade phase I. *JINST*, 8(04):P04005, 2013. 44

[178] G. Aielli, M. Bindi, and A. Polini. Performance, operation and detector studies with the ATLAS Resistive Plate Chambers. *JINST*, 8(02):P02020, 2013. 44

[179] A. Collaboration, F. Boss, M. Gagliardi, and M. Marchisone. Performance of the RPC-based ALICE muon trigger system at the LHC. *JINST*, 7(12):T12002, 2012. 44

[180] A. Alici. Status and performance of the ALICE MRPC-based Time-Of-Flight detector. *JINST*, 7(10):P10024, 2012. 44

[181] A. Blanco, P. Fonte, J. A. Garzon, et al. Performance of the HADES-TOF RPC wall in a Au + Au beam at 1.25 AGeV. *JINST*, 8(01):P01004, 2013. 46

[182] P. Fonte, R. Ferreira Marques, J. Pinhão, N. Carolino, and A. Policarpo. High-resolution RPC's for large TOF systems. *Nucl. Instrum. Meth. A*, 449:295–301, 2000. 46

[183] D. Belver, A. Blanco, P. Cabanelas, et al. The HADES RPC inner TOF wall. *Nucl. Instrum. Meth. A*, 602(3):687 – 690, 2009. Proceedings of the 9th International Workshop on Resistive Plate Chambers and Related Detectors RPC08. 46

[184] L. Lopes, R. Ferreira Marques, P. Fonte, et al. Development of high-rate timing RPCs. *Nucl. Instrum. Meth. A*, 533(12):69 – 73, 2004. Proceedings of the Seventh International Workshop on Resistive Plate Chambers and Related Detectors. 46

[185] L. Naumann, R. Kotte, D. Stach, and J. Wüstenfeld. High-rate timing RPC with ceramics electrodes. *Nucl. Instrum. Meth. A*, 635(1, Supplement):S113 – S116, 2011. PhotonDiag 2010. 46

[186] E. Ceron Zeballos, I. Crotty, D. Hatzifotiadou, et al. Resistive plate chambers with secondary electron emitters and microstrip readout. *Nucl. Instrum. Meth. A*, 392(13):150 – 154, 1997. Position-Sensitive Detectors Conference 1996. 46

[187] A. Blanco, R. Ferreira-Marques, C. Finck, et al. Single-gap timing RPCs with bidimensional position-sensitive readout for very accurate TOF systems. *Nucl. Instrum. Meth. A*, 508(12):70 – 74, 2003. Proceedings of the Sixth International Workshop on Resistive Plate Chambers and Related Detectors. 46

[188] V. Peskov. Challenges for RPCs and resistive micropattern detectors in the next few years. *PoS*, RPC2012:083, 2012. 46

[189] D. Gonzalez-Diaz and A. Sharma. Challenges for resistive gaseous detectors towards RPC2014. *JINST*, 8(02):T02001, 2013. 46

[190] J. Bateman, J. Connolly, R. Stephenson, G. Tappern, and A. Flesher. The Rutherford Appleton laboratory's mark I multiwire proportional counter positron camera. *Nucl. Instrum. Meth.*, 225(1):209 – 231, 1984. 47

[191] S. C. Haydon. *Electrical Breakdown of Gases*. MacMillan, London, 1973. 47

[192] I. Kitayama, H. Sakai, Y. Teramoto, et al. Optical observation of discharge in resistive plate chamber. *Nucl. Instrum. Meth. A*, 424:474–478, 1999. 47

[193] A. Semak, V. Ammosov, V. Gapienko, et al. Properties of discharge in the narrow gap glass RPC. *Nucl. Instrum. Meth. A*, 456:50–54, 2000. 47

[194] P. Fonte, N. Carolino, L. Costa, et al. A spark-protected high-rate detector. *Nucl. Instrum. Meth. A*, 433331(1–2):154–159, 1999. 47

[195] J. T. Bromley. Investigation of the operation of Resitive Plate Chambers, 1994. MSc. thesis. University of Manchester. 48, 49

[196] R. Arnaldi, A. Baldit, V. Barret, et al. Study of the resistive plate chambers for the ALICE Dimuon Arm. *Nucl. Instrum. Meth. A*, 456(12):73 – 76, 2000. Proceedings of the 5th Int. Workshop on Resistive Plate Chambers and Related Detectors. 48

[197] C. Bacci, K. Bao, F. Barone, et al. High altitude test of RPCs for the Argo YBJ experiment. *Nucl. Instrum. Meth. A*, 443(23):342 – 350, 2000. 48

# REFERENCES


[198] P. Camarri, R. Cardarelli, A. Di Ciaccio, and R. Santonico. Streamer suppression with $SF_6$ in RPCs operated in avalanche mode. *Nucl. Instrum. Meth. A*, 414(2):317–324, 1998. 48, 49

[199] V. Koreshev, V. Ammosov, A. Ivanilov, et al. Operation of narrow gap RPC with tetrafluoroethane based mixtures. *Nucl. Instrum. Meth. A*, 456(1–2):46–49, 2000. 48

[200] P. Fonte. A model of breakdown in parallel-plate detectors. *IEEE Trans. Nucl. Sci.*, 43(3):2135–2146, 1996. 49

[201] C. Lippmann and W. Riegler. Space charge effects in resistive plate chambers. *Nucl. Instrum. Meth. A*, 517(13):54 – 76, 2004. 49

[202] H. Raether. *Electron Avalanches and Breakdown in Gases*. Butterworths, London, 1984. 49, 51, 52

[203] M. Abbrescia, A. Colaleo, G. Iaselli, et al. Progresses in the simulation of resistive plate chambers in avalanche mode. *Nucl. Phys. B*, 78(1):459–465, 1999. 49

[204] P. Fonte and V. Peskov. High-resolution TOF with RPCs. *Nucl. Instrum. Meth. A*, 477:17–22, 2002. 49

[205] P. Fonte. High-resolution timing of MIPs with RPCs – a model. *Nucl. Instrum. Meth. A*, 456(1–2):6–11, 2000. 49

[206] P. Fonte. *Realimentação e Disrupção em Detectores Gasosos de Faces Paralelas*. PhD thesis, Universidade de Coimbra, Portugal, 1993. 50

[207] A. Davies and C. Evans. *The Theory of Ionization Growth in Gases Under Pulsed and Static Fields*. Number 10 in CERN (Series). CERN, 1973. 50

[208] P. Fonte. Survey of physical modelling in resistive plate chambers. *JINST*, 8(11):P11001, 2013. 52

[209] S. Ramo. Currents induced by electron motion. In *Proceedings of the IRE*, volume 27, pages 584–585, 1939. 53

[210] A. Blanco, M. Couceiro, P. Crespo, et al. Efficiency of RPC detectors for whole-body human TOF–PET. *Nucl. Instrum. Meth. A*, 602(3):780–783, 2009. 54, 55, 56, 58, 59, 60, 61, 199

[211] A. Pullia, W. Müller, C. Boiano, and R. Bassini. Resistive or capacitive charge-division readout for position-sensitive detectors. *IEEE Trans. Nucl. Sci.*, 49(6):3269–3277, 2002. 57

[212] P. D. Shreve. Whole-body PET imaging methods. In D. L. Bailey, D. W. Townsend, P. E. Valk, and M. N. Maisey, editors, *Positron Emission Tomography*, pages 267–280. Springer London, 2005. 63

[213] D. Crosetto. The 3D complete body screening (3D-CBS) features and implementation. In *Conf. Record of the 2003 IEEE Nucl. Sci. Symp. & Med. Imag. Conf. (NSS/MIC)*, volume 4, pages 2415–2419, Oct 2003. 63

[214] G. Borasi, F. Fioroni, A. Del Guerra, and G. Lucignani. PET systems: the value of added length. *Eur. J. Nucl. Med. Mol. Imaging*, 37(9):1629–1632, 2010. 63

[215] P. JK, D. ML, M. WW, et al. Optimal whole-body PET scanner configurations for different volumes of lso scintillator: a simulation study. *Phys. Med. Biol.*, 57(13):4077, 2012. 63

[216] L.-F. de Geus-Oei, E. P. Visser, P. F. Krabbe, et al. Comparison of image-derived and arterial input functions for estimating the rate of glucose metabolism in therapy-monitoring $^{18}$F-FDG PET studies. *J. Nucl. Med.*, 47(6):945–949, 2006. 63

[217] M. E. Daube-Witherspoon, J. S. Karp, M. E. Casey, et al. PET performance measurements using the NEMA NU 2-2001 standard. *J. Nucl. Med.*, 43:1398–1409, 2002. 64

[218] C.-M. Kao, Q. Xie, Y. Dong, L. Wan, and C.-T. Chen. A high-sensitivity small-animal PET scanner: development and initial performance measurements. *IEEE Trans. Nucl. Sci.*, 56(5):2678–2688, 2008. 65

[219] V. Kapoor, B. M. McCook, and F. S. Torok. An introduction to PET-CT imaging. *Radiog.*, 24:523–543, 2004. 66

[220] S. Robinson, P. J. Julyan, D. L. Hastings, and J. Zweit. Performance of a block detector PET scanner in imaging non-pure positron emitters-modelling and experimental validation with $^{124}$I. *Phys. Med. Biol.*, 49(24):5505–5528, 2004. 66

[221] O. Barret, T. A. Carpenter, J. C. Clark, R. E. Ansorge, and T. D. Fryer. Monte Carlo simulation and scatter correction of the GE Advance PET scanner with SimSET and Geant4. *Phys. Med. Biol.*, 50:4823–4840, 2005. 68

[222] S. G. Khohlmyer, C. W. Stearns, P. E. Kinahan, and T. K. Lewellen. NEMA NU2-2001 performance results for the GE Advance PET system. In *Conf. Records 2002 IEEE Nucl. Sci. Symp. & Med. Imag. Conf. (NSS/MIC)*, pages 890–894, Norfolk, VA, USA, Nov. 10–16 2002. 68

[223] R. Schmitz, R. Harrison, C. Stearns, T. Lewellen, and P. Kinahan. Optimization of noise equivalent count rate performance for a partially collimated PET scanner by varying the number of septa. *IEEE Trans Med Imaging*, 26(7):935–944, July 2007. 70

[224] S. Agostinelli, J. Allison, K. Amako, et al. Geant4: A simulation toolkit. *Nucl. Instrum. Meth. A*, 506(3):250–303, 2003. 71

[225] J. Allison, K. Amako, J. Apostolakis, et al. Geant4 developments and applications. *IEEE Trans. Nucl. Sci.*, 53(1):270–8, 2006. 71

[226] G. K. von Schulthess, H. C. Steinert, and T. F. Hany. Integrated PET/CT: Current applications and future directions. *Radiology*, 238(2):405–422, 2006. PMID: 16436809. 73, 228

[227] M. M. Osman, B. T. Chaar, R. Muzaffar, et al. 18F-FDG PET/CT of patients with cancer: Comparison of whole-body and limited whole-body technique. *American Journal of Roentgenology*, 195(6):1397–1403, December 2010. 73, 228, 229, 230

[228] S. F. Huston, A. G. Abdelmalik, N. C. Nguyen, H. R. Farghaly, and M. M. Osman. Whole-body 18F-FDG PET/CT: The need for a standardized field of view – a referring-physician aid. *Journal of Nuclear Medicine Technology*, 38(3):123–127, 2010. 73, 228, 229, 232

[229] N. Nguyen, B. Chaar, and M. Osman. Prevalence and patterns of soft tissue metastasis: detection with true whole-body F-18 FDG PET/CT. *BMC Medical Imaging*, 7(1):8, 2007. 73, 230

[230] E. M. Rohren, J. M. Provenzale, D. P. Barboriak, and R. E. Coleman. Screening for cerebral metastases with FDG PET in patients undergoing whole-body staging of noncentral nervous system malignancy. *Radiology*, 226(1):181–187, 2003. PMID: 12511688. 74, 231

[231] P. Zanzonico. Small animal imaging – basics and practical guide. In M. Wernick and J. Aarsvold, editors, *Small Animal Imaging*, chapter 1: Noninvasive Imaging for Supporting Basic Research. Springer, Heidelberg, 2011. 75, 234

[232] L. Cunha, I. Horvath, S. Ferreira, et al. Preclinical imaging: an essential ally in modern biosciences. *Molecular Diagnosis & Therapy*, 18(2):153–173, 2014. 75, 82, 235

[233] M. S. Judenhofer and S. R. Cherry. Applications for preclinical PET/MRI. *Seminars in Nuclear Medicine*, 43(1):19 – 29, 2013. PET/MRI. 75, 79, 81

[234] National Electrical Manufacturers Association. Nema Standards Publication NU 4–2008: Performance measurements of small animal positron emission tomographs, 2008. 75, 76

[235] Y. C. Tai, A. Chatziioannou, S. Siegel, et al. Performance evaluation of the microPET P4: a PET system dedicated to animal imaging. *Phys. Med. Biol.*, 46(7):1845, 2001. 76

[236] C. Knoess, S. Siegel, A. Smith, et al. Performance evaluation of the microPET R4 PET scanner for rodents. *Eur. J. Nucl. Med. Mol. Imaging*, 30(5):737–747, 2003. 76

[237] Y.-C. Tai, A. Ruangma, D. Rowland, et al. Performance evaluation of the microPET Focus: A third-generation microPET scanner dedicated to animal imaging. *J. Nucl. Med.*, 46(3):455–463, 2005. 76

[238] J. S. Kim, J. S. Lee, K. C. Im, et al. Performance measurement of the microPET Focus 120 scanner. *J. Nucl. Med.*, 48(9):1527–1535, 2007. 76

[239] Q. Bao, D. Newport, M. Chen, D. B. Stout, and A. F. Chatziioannou. Performance evaluation of the Inveon dedicated PET preclinical tomograph based on the NEMA NU-4 standards. *J. Nucl. Med.*, 50(3):401–408, 2009. 76

[240] S. Surti, J. Karp, A. Perkins, et al. Imaging performance of a-PET: a small animal PET camera. *IEEE Trans Med Imaging*, 24(7):844–852, July 2005. 76

[241] M. Cañadas, M. Embid, E. Lage, et al. NEMA NU 4-2008 performance measurements of two commercial small-animal PET scanners: ClearPET and rPET-1. *IEEE Trans Nucl. Sci.*, 58(1):58–65, Feb 2011. 76

[242] Y. Wang, J. Seidel, B. M. Tsui, J. J. Vaquero, and M. G. Pomper. Performance evaluation of the GE healthcare eXplore VISTA dual-ring small-animal PET scanner. *J. Nucl. Med.*, 47(11):1891–1900, 2006. 76

[243] E. Lage, J. J. Vaquero, A. Sisniega, et al. Design and performance evaluation of a coplanar multimodality scanner for rodent imaging. *Phys. Med. Biol.*, 54(18):5427, 2009. 76

[244] M. Bergeron, J. Cadorette, M.-A. Tétrault, et al. Imaging performance of LabPET APD-based digital PET scanners for pre-clinical research. *Phys. Med. Biol.*, 59(3):661, 2014. 76

[245] K. P. Schäfers, A. J. Reader, M. Kriens, et al. Performance Evaluation of the 32-Module quadHIDAC Small-Animal PET Scanner. *J. Nucl. Med.*, 46(6):996–1004, 2005. 76

[246] I. Szanda, J. Mackewn, G. Patay, et al. National Electrical Manufacturers Association NU-4 performance evaluation of the PET component of the nanoPET/CT preclinical PET/CT scanner. *J. Nucl. Med.*, 2011. 76, 77

[247] F. Sánchez, A. Orero, A. Soriano, et al. ALBIRA: A small animal PET/SPECT/CT imaging system. *Medical Physics*, 40(5):–, 2013. 76

[248] G. Cucciati, E. Auffray, R. Bugalho, et al. Development of ClearPEM-Sonic, a multimodal mammography system for PET and Ultrasound. *JINST*, 9(03):C03008, 2014. 76

[249] A. L. Goertzen, Q. Bao, M. Bergeron, et al. NEMA NU 4-2008 Comparison of Preclinical PET Imaging Systems. *Journal of Nuclear Medicine*, 2012. 75

[250] C. Woody, P. Vaska, D. Schlyer, et al. Initial studies using the RatCAP conscious animal PET tomograph. *Nucl. Instrum. Meth. A*, 571(12):14 – 17, 2007. Proceedings of the 1st International Conference on Molecular Imaging Technology EuroMedIm 2006. 77

[251] E. Tsyganov, J. Anderson, G. Arbique, et al. UTSW small animal positron emission imager. *IEEE Trans Nucl. Sci.*, 53(5):2591–2600, Oct 2006. 77

[252] N. Shehad, A. Athanasiades, C. Martin, L. Sun, and J. Lacy. Small animal PET camera design based on 2-mm straw detectors. In *Conf. Record of the 2006 IEEE Nucl. Sci. Symp. & Med. Imag. Conf. (NSS/MIC)*, volume 4, pages 2462–2468, Oct 2006. 77

[253] A. Athanasiades, L. Sun, C. Martin, et al. A new PET scanner for functional brain imaging based on 2-mm straw detectors. In *Conf. Record of the 2008 IEEE Nucl. Sci. Symp. & Med. Imag. Conf. (NSS/MIC)*, pages 5445–5451, Oct 2008. 77

[254] R. Miyaoka, X. Li, W. Hunter, et al. Resolution properties of a prototype continuous miniature crystal element (cMiCE) scanner. *IEEE Trans Nucl. Sci.*, 58(5):2244–2249, Oct 2011. 77

[255] X. Li, A. Alessio, T. Burnett, T. Lewellen, and R. Miyaoka. Performance evaluation of small animal PET scanners with different system designs. *IEEE Trans Nucl. Sci.*, 60(3):1495–1502, June 2013. 77

[256] Y. Gu, J. L. Matteson, R. T. Skelton, et al. Study of a high-resolution, 3D positioning cadmium zinc telluride detector for PET. *Phys. Med. Biol.*, 56(6):1563, 2011. 77

[257] C. S. Levin. Promising new photon detection concepts for high-resolution clinical and preclinical PET. *J. Nucl. Med.*, 53(2):167–170, 2012. 77

[258] S. Yamamoto, H. Watabe, Y. Kanai, et al. Development of an ultrahigh resolution Si-PM based PET system for small animals. *Phys. Med. Biol.*, 58(21):7875, 2013. 77

[259] G. Pratx and C. S. Levin. Bayesian reconstruction of photon interaction sequences for high-resolution PET detectors. *Phys. Med. Biol.*, 54(17):5073, 2009. 77

[260] R. Yao, R. Lecomte, and E. S. Crawford. Small-animal PET: What is it, and why do we need it? *Journal of Nuclear Medicine Technology*, 40(3):157–165, 2012. 77, 78, 82, 233, 234

[261] C. S. Levin and H. Zaidi. Current trends in pre-clinical positron emission tomography system design. *PET Clinics*, 2(2):125–160, 2007. 78, 79, 182, 233, 234

[262] F. Habte, A. M. K. Foudray, P. D. Olcott, and C. S. Levin. Effects of system geometry and other physical factors on photon sensitivity of high-resolution positron emission tomography. *Phys. Med. Biol.*, 52(13):3753, 2007. 78

[263] P. D. Acton, H. Zhuang, and A. Alavi. Quantification in PET. *Radiologic clinics of North America*, 42(6):1055–62– viii, November 2004. 79

[264] H.-M. Wu, G. Sui, C.-C. Lee, et al. In vivo quantitation of glucose metabolism in mice using small-animal PET and a microfluidic device. *J. Nucl. Med.*, 48(5):837–845, 2007. 79

[265] W. Koba, K. Kim, M. L. Lipton, et al. Imaging devices for use in small animals. *Seminars in nuclear medicine*, 41(3):151–165, May 2011. 80

[266] H. F. Wehrl, M. Hossain, K. Lankes, et al. Simultaneous PET-MRI reveals brain function in activated and resting state on metabolic, hemodynamic and multiple temporal scales. *Nature Medicine*, 19(9):1184–1189, 2013. 81, 82

[267] J. Comley. In vivo preclinical imaging: an essential tool in translational research. *Drug Discovery World*, pages 58 – 71, 2011. 81

[268] *Pre-clinical imaging (in vivo) market – by systems and reagents [micro-PET, optical imaging, micro-MRI, micro-SPECT, micro-Ultrasound, micro-CT & multimodality/hybrid imaging modalities] – competitive analysis & global forecasts to 2017, accessed 4 April 2014.* Available at http://www.marketsandmarkets.com/Market-Reports/pre-clinical-molecular-imaging-market-841.html. 82

[269] S. Tong, A. M. Alessio, and P. E. Kinahan. Image reconstruction for PET/CT scanners: past achievements and future challenges. *Imaging in medicine*, 2(5):529–545, October 2010. 83, 84, 85, 237, 238

[270] J. Hadamard. Sur les problèmes aux dérivés partielles et leur signification physique. *Princeton University Bulletin*, 13:49–52, 1902. 83

[271] M. Defrise, P. E. Kinahan, and C. J. Michel. Image reconstruction algorithms in PET. In D. L. Bailey, D. W. Townsend, P. E. Valk, and M. N. Maisey, editors, *Positron Emission Tomography*, pages 63–91. Springer London, 2005. 84, 86, 87, 89

[272] A. Kak and M. Slaney. *Principles of Computerized Tomographic Imaging*. IEEE Press, 1988. 84

[273] P. E. Kinahan, M. Defrise, and R. Clackdoyle. Chapter 20 - analytic image reconstruction methods. In M. N. Wernick and J. N. Aarsvold, editors, *Emission Tomography*, pages 421 – 442. Academic Press, San Diego, 2004. 85

[274] A. P. Dempster, N. M. Laird, and D. B. Rubin. Maximum likelihood from incomplete data via the EM algorithm. *Journal of the Royal Statistical Society: Series B*, 39(1):1–38, 1977. 86

[275] L. Shepp and Y. Vardi. Maximum likelihood reconstruction for emission tomography. *IEEE Trans Med Imaging*, 1(2):113–122, Oct 1982. 86

[276] K. Lange and R. Carson. EM reconstruction algorithms for emission and transmission tomography. *Journal of Computer Assisted Tomography*, 8(2):306–316, April 1984. 86

[277] E. Veklerov and J. Llacer. Stopping rule for the MLE algorithm based on statistical hypothesis testing. *IEEE Trans Med Imaging*, 6(4):313–319, Dec 1987. 87

[278] V. Johnson. A note on stopping rules in EM-ML reconstructions of ECT images. *IEEE Trans Med Imaging*, 13(3):569–571, Sep 1994. 87

[279] F. Hofheinz, J. Langner, B. Beuthien-Baumann, et al. Suitability of bilateral filtering for edge-preserving noise reduction in PET. *Eur. J. Nucl. Med. Mol. Imaging research*, 1(1):23, 2011. 87

[280] W. Luo, M. Harz, and C. Matthews. Improving lesion detectability of a PEM system with post-reconstruction filtering. In *Conf. Record of the 2009 IEEE Nucl. Sci. Symp. & Med. Imag. Conf. (NSS/MIC)*, pages 3218–3224, Oct 2009. 87

[281] W. Wong, A. Chung, and S. Yu. Trilateral filtering for biomedical images. In *Biomedical Imaging: Nano to Macro, 2004. IEEE International Symposium on*, pages 820–823 Vol. 1, April 2004. 87

[282] D. L. Snyder and M. Miller. The use of sieves to stabilize images produced with the EM algorithm for emission tomography. *IEEE Trans Nucl. Sci.*, 32(5):3864–3872, Oct 1985. 87

[283] H. Hudson and R. Larkin. Accelerated image reconstruction using ordered subsets of projection data. *IEEE Trans Med Imaging*, 13(4):601–609, Dec 1994. 87

[284] C. Byrne. Block-iterative methods for image reconstruction from projections. *Image Processing, IEEE Transactions on*, 5(5):792–794, May 1996. 88

[285] J. Browne and A. De Pierro. A row-action alternative to the EM algorithm for maximizing likelihood in emission tomography. *IEEE Trans Med Imaging*, 15(5):687–699, Oct 1996. 88

[286] T. Hebert and R. Leahy. Fast methods for including attenuation in the EM algorithm. *IEEE Trans Nucl. Sci.*, 37(2):754–758, Apr 1990. 88, 184

[287] C. Comtat, P. Kinahan, M. Defrise, C. Michel, and D. Townsend. Fast reconstruction of 3D PET data with accurate statistical modeling. *IEEE Trans Nucl. Sci.*, 45(3):1083–1089, Jun 1998. 88, 184

[288] J. Fessler. Statistical methods for image reconstruction. In *Conf. Record of the 2004 IEEE Nucl. Sci. Symp. & Med. Imag. Conf. (NSS/MIC)*. Presented at the IEEE NSS/MIC/SNPS and RTSD, Rome, Italy, 2004. 89, 238

[289] W. Brandt and R. Paulin. Positron implantation-profile effects in solids. *Phys. Rev. B*, 15:2511–2518, Mar 1977. 102

[290] A. P. de Lima and P. M. Gordo. Chapter 3 – Positron Physics. In J. J. P. de Lima, editor, *Nuclear Medicine Physics*, pages 76 – 77. Taylor & Francis, Boca Raton, 2011. 103

[291] D. Belver, J. Garzn, A. Gil, et al. The front-end electronics for the HADES RPC wall (ESTRELA-FEE). *Nuclear Physics B - Proceedings Supplements*, 158(0):47 – 51, 2006. Proceedings of the 8th International Workshop on Resistive Plate Chambers and Related Detectors. 107

[292] W. R. Leo. *Techniques for Nuclear and Particle Physics Experiments: A How-to Approach*. Springer Berlin Heidelberg, 1994. 109

[293] A. Tarantola. A new electronic readout for the multiwire drift chambers in the HADES experiment at GSI. In *International Winter Meeting on Nuclear Physics*. Presented at XLVI International Winter Meeting on Nuclear Physics, Bormio, Italy, 2008. 112

[294] A. Neiser, J. Adamczewski-Musch, M. Hoek, et al. TRB3: a 264 channel high precision TDC platform and its applications. *JINST*, 8(12):C12043, 2013. 112

[295] M. Capeans, R. Guida, F. Hahn, S. Haider, and B. Mandelli. RPC performances and gas quality in a closed loop gas system for the new purifiers configuration at LHC experiments. *JINST*, 8(08):T08003, 2013. 119

[296] *HPTDC – High Performance Time to Digital Converter, accessed 21 June 2014*. Available at http://tdc.web.cern.ch/TDC/hptdc/docs/hptdc_manual_ver2.2.pdf. 125

[297] *Big file transfer in Linux, accessed 13 June 2014*. Available at http://www.pixelstech.net/article/index.php?id=1357818928. 126

[298] *Summary of the multiple file compression benchmark tests, accessed 13 June 2014*. Available at http://www.maximumcompression.com/data/summary_mf3.php. 126

[299] E. Gatti and P. Manfredi. Processing the signals from solid-state detectors in elementary-particle physics. *La Rivista del Nuovo Cimento*, 9(1):1–146, 1986. 127

[300] E. Baldinger and W. Franzen. Amplitude and time measurement in nuclear physics. In L. Marton, editor, *Advances in Electronics and Electron Physics*, volume 8, pages 255 – 315. Academic Press, 1956. 127

[301] V. Radeka and N. Karlovac. Least-square-error amplitude measurement of pulse signals in presence of noise. *Nucl. Instrum. Meth.*, 52(1):86 – 92, 1967. 127

[302] V. Radeka. Trapezoidal filtering of signals from large germanium detectors at high rates. *Nuclear Instruments and Methods*, 99(3):525 – 539, 1972. 127

[303] IAEA – International Atomic Energy Agency. Signal processing and electronics for nuclear spectrometry. In *Proceedings of a technical meeting*, Vienna, Austria, 2009. 127

[304] E. Gatti, A. Geraci, S. Riboldi, and G. Ripamonti. Digital penalized LMS method for filter synthesis with arbitrary constraints and noise. *Nucl. Instrum. Meth. A*, 523(12):167 – 185, 2004. 127, 128

[305] J. B. Macqueen. Some methods of classification and analysis of multivariate observations. In *Proceedings of the Fifth Berkeley Symposium on Mathematical Statistics and Probability*, pages 281–297, 1967. 133, 248

[306] L. Morisette and S. Chartier. The k-means clustering technique: General considerations and implementation in Mathematica. *Tutorials in Quantitative Methods for Psychology*, 9(1):15 – 24, 2013. 133, 248, 249

[307] T. Hastie, R. Tibshirani, and J. Friedman. *The Elements of Statistical Learning: Data Mining, Inference, and Prediction, Second Edition*. Springer Series in Statistics. Springer, 2009. 133

[308] H. Abdi and L. J. Williams. Principal component analysis. *Wiley Interdisciplinary Reviews: Computational Statistics*, 2(4):433–459, 2010. 133

[309] F. Galton. *Natural Inheritance*. MacMillan, 1889. 133

[310] K. Pearson. On lines and planes of closest fit to systems of points in space. *Philosophical Magazine Series 6*, 2(11):559–572, 1901. 133

[311] H. Hotelling. Analysis of a complex of statistical variables into principal components. *Journal of Educational Psychology*, 24(6):417–441, 1933. 133, 245

[312] I. T. Jolliffe. *Principal Component Analysis*. Springer Series in Statistics. Springer, 2002. 133, 241

[313] V. Radeka. Low-noise techniques in detectors. *Annual Review of Nuclear and Particle Science*, 38(1):217–277, 1988. 134

[314] G. Bencze, A. Chikanian, M. D. Negra, et al. Position and timing resolution of interpolating cathode strip chambers in a test beam. *Nucl. Instrum. Meth. A*, 357(1):40 – 54, 1995. 138

[315] S. Jan, G. Santin, D. Strul, et al. Gate: a simulation toolkit for pet and spect. *Physics in Medicine and Biology*, 49(19):4543, 2004. 166

# REFERENCES


[316] P. Rodrigues, A. Trindade, and J. Varela. Clear PEM system couting rates: a Monte Carlo study. *JINST*, 2:P01004, 2007. 180

[317] A. Trindade, P. Almeida, F. Balau, et al. Clear-PEM: Monte Carlo performance and image reconstruction studies. In *Conf. Record of the 2003 IEEE Nucl. Sci. Symp. & Med. Imag. Conf. (NSS/MIC)*, pages M3–118, Portland, OR, USA, 2003. 180

[318] J. Mourik, F. van Velden, M. Lubberink, et al. Image derived input functions for dynamic high resolution research tomograph PET brain studies. *NeuroImage*, 43(4):676–686, 2008. 180

[319] M. Phelps and J. Mazziotta. Positron emission tomography: human brain function and biochemistry. *Science*, 228(4701):799, 1985. 182

[320] P. Crespo, G. Shakirin, F. Fiedler, W. Enghardt, and A. Wagner. Direct time-of-flight for quantitative, real-time in-beam PET: a concept and feasibility study. *Phys. Med. Biol.*, 52:6795–6811, 2007. 183, 238

[321] D. B. Kirk and W. W. Hwu. *Programming Massively Parallel Processors*. Morgan Kaufmann, Massachussets, 2010. 186

[322] J. Sanders and E. Kandrot. *CUDA by Example*. Addison Wesley, Massachussets, 2011. 186

[323] M. E. Daube-Witherspoon, S. Surti, A. Perkins, M. W. C.C.M. Kyba, R. Wiener, et al. The imaging performance of a $LaBr_3$-based PET scanner. *Phys. Med. Biol.*, 55:45–64, 2010. 200

[324] J. Czernin and M. E. Phelps. Positron emission tomography scanning: Current and future applications. *Annual Review of Medicine*, 53(1):89–112, 2002. PMID: 11818465. 227

[325] J. Czernin, M. Allen-Auerbach, and H. R. Schelbert. Improvements in cancer staging with PET/CT: Literature-based evidence as of september 2006. *J. Nucl. Med.*, 48(1 suppl):78S–88S, 2007. 227

[326] R. E. Coleman, D. Delbeke, M. J. Guiberteau, et al. Concurrent PET/CT with an integrated imaging system: Intersociety dialogue from the joint working group of the american college of radiology, the society of nuclear medicine, and the society of computed body tomography and magnetic resonance. *J. Nucl. Med.*, 46(7):1225–1239, 2005. 228

[327] J. W. Song, Y.-M. Oh, T.-S. Shim, et al. Efficacy comparison between 18F-FDG PET/CT and bone scintigraphy in detecting bony metastases of non-small-cell lung cancer. In *Lung cancer (Amsterdam, Netherlands)*, pages 333–338. Elsevier Scientific Publishers, September 2009. 230

[328] R. Sebro, C. Mari-Aparici, and M. Hernandez-Pampaloni. Value of true whole-body FDG-PET/CT scanning protocol in oncology: optimization of its use based on primary diagnosis. *Acta Radiologica*, 54(5):534–539, 2013. 230

[329] R. D. Niederkohr, J. Rosenberg, G. Shabo, and A. Quon. Clinical value of including the head and lower extremities in 18F-FDG PET/CT imaging for patients with malignant melanoma. *Nuclear medicine communications*, 28(9):688–695, September 2007. 230

[330] J. Kovacs. Added clinical value of "TRUE" whole-body 18F-FDG PET/CT imaging in patients with malignant melanoma. In *Annual Scientific Meeting of the Australian and New Zealand Society of Nuclear Medicine*. Presented at the 39th Annual Scientific Meeting of the Australian and New Zealand Society of Nuclear Medicine, Sydney, Australia, 2009. 230

[331] L. Sarajlic, C. Botkin, W. Hubble, A. Abdelmalik, and M. Osman. The incremental added value of including the head in the imaged field of view: A retrospective evaluation of 8431 18F-FDG PET/CT studies. *J. Nucl. Med. meeting abstracts*, 53(1):2719, 2012. 230

[332] P. Bochev, A. Klisarova, A. Kaprelyan, B. Chaushev, and Z. Dancheva. Brain metastases detectability of routine whole body (18)F-FDG PET and low dose CT scanning in 2502 asymptomatic patients with solid extracranial tumors. *Hellenic Journal of Nuclear Medicine*, 15(2):125–129, May 2012. 230

[333] J. S. Barnholtz-Sloan, A. E. Sloan, F. G. Davis, et al. Incidence proportions of brain metastases in patients diagnosed (1973 to 2001) in the Metropolitan Detroit Cancer Surveillance System. *Journal of clinical oncology: official journal of the American Society of Clinical Oncology*, 22(14):2865–2872, July 2004. 230

[334] E. Croteau, F. Bénard, J. Cadorette, et al. Quantitative gated PET for the assessment of left ventricular function in small animals. *J. Nucl. Med.*, 44(10):1655–1661, 2003. 233

[335] R. Lecomte, T. Croteau, M.-E. Gauthier, et al. Cardiac PET imaging of blood flow, metabolism, and function in normal and infarcted rats. *IEEE Trans Nucl. Sci.*, 51(3):696–704, June 2004. 234

[336] S. Lancelot and L. Zimmer. Small-animal positron emission tomography as a tool for neuropharmacology. *Trends in Pharmacological Sciences*, 31(9):411–417, September 2010. 234

[337] M. E. Daube-Witherspoon and G. Muehllehner. Treatment of axial data in three-dimensional PET. *J. Nucl. Med.*, 28(11):1717–1724, 1987. 237

[338] M. Defrise, P. Kinahan, D. Townsend, et al. Exact and approximate rebinning algorithms for 3-D PET data. *IEEE Trans Med Imaging*, 16(2):145–158, April 1997. 237

[339] P. Kinahan and J. Rogers. Analytic 3D image reconstruction using all detected events. *IEEE Trans Nucl. Sci.*, 36(1):964–968, Feb 1989. 237

[340] B. Bendriem and D. Townsend. *The Theory and Practice of 3D PET*. Developments in Nuclear Medicine. Springer, 1998. 237

[341] G. Herman and L. Meyer. Algebraic reconstruction techniques can be made computationally efficient [positron emission tomography application]. *IEEE Trans Med Imaging*, 12(3):600–609, Sep 1993. 238

[342] T. Hebert and R. Leahy. A generalized EM algorithm for 3-D Bayesian reconstruction from Poisson data using Gibbs priors. *IEEE Trans Med Imaging*, 8(2):194–202, Jun 1989. 238

[343] G. Gindi, M. Lee, A. Rangarajan, and I. Zubal. Bayesian reconstruction of functional images using anatomical information as priors. *IEEE Trans Med Imaging*, 12(4):670–680, Dec 1993. 238

[344] J. Bowsher, V. Johnson, T. Turkington, et al. Bayesian reconstruction and use of anatomical a priori information for emission tomography. *IEEE Trans Med Imaging*, 15(5):673–686, Oct 1996. 238

[345] L. Parra and H. Barrett. List-mode likelihood: EM algorithm and image quality estimation demonstrated on 2-D PET. *IEEE Trans Med Imaging*, 17(2):228–235, April 1998. 238

[346] R. Huesman, G. Klein, W. W. Moses, et al. List-mode maximum-likelihood reconstruction applied to positron emission mammography (PEM) with irregular sampling. *IEEE Trans Med Imaging*, 19(5):532–537, May 2000. 238

[347] V. Westerwoudt, M. Conti, and L. Eriksson. Comparison of TOF and non-TOF iterative reconstruction at low statistics. In *Conf. Record of the 2012 IEEE Nucl. Sci. Symp. & Med. Imag. Conf. (NSS/MIC)*, pages 2261–2269, Oct 2012. 238

[348] W. Wang, Z. Hu, E. E. Gualtieri, et al. Systematic and distributed time-of-flight list mode PET reconstruction. In *Conf. Record of the 2006 IEEE Nucl. Sci. Symp. & Med. Imag. Conf. (NSS/MIC)*, volume 3, pages 1715–1722, Oct 2006. 238

[349] G. Pratx, G. Chinn, P. Olcott, and C. Levin. Fast, accurate and shift-varying line projections for iterative reconstruction using the GPU. *IEEE Trans Med Imaging*, 28(3):435–445, March 2009. 238

[350] G. Pratx, S. Surti, and C. Levin. Fast list-mode reconstruction for time-of-flight PET using graphics hardware. *IEEE Trans Nucl. Sci.*, 58(1):105–109, Feb 2011. 238

[351] J. Cui, G. Pratx, S. Prevrhal, and C. S. Levin. Fully 3D list-mode time-of-flight PET image reconstruction on GPUs using CUDA. *Medical Physics*, 38(12):6775–6786, 2011. 238

[352] D. Strul, R. B. Slates, M. Dahlbom, S. R. Cherry, and P. K. Marsden. An improved analytical detector response function model for multilayer small-diameter PET scanners. *Phys. Med. Biol.*, 48(8):979, 2003. 238

[353] A. Alessio, P. Kinahan, and T. Lewellen. Modeling and incorporation of system response functions in 3-D whole body PET. *IEEE Trans Med Imaging*, 25(7):828–837, July 2006. 238, 239

[354] V. Panin, F. Kehren, C. Michel, and M. Casey. Fully 3-D PET reconstruction with system matrix derived from point source measurements. *IEEE Trans Med Imaging*, 25(7):907–921, July 2006. 238, 239

[355] A. Alessio, C. Stearns, S. Tong, et al. Application and evaluation of a measured spatially variant system model for PET image reconstruction. *IEEE Trans Med Imaging*, 29(3):938–949, March 2010. 238

[356] A. Reader, P. Julyan, H. Williams, D. Hastings, and J. Zweit. EM algorithm system modeling by image-space techniques for PET reconstruction. *IEEE Trans Nucl. Sci.*, 50(5):1392–1397, Oct 2003. 239

[357] S. Tong, A. M. Alessio, and P. E. Kinahan. Noise and signal properties in PSF-based fully 3D PET image reconstruction: an experimental evaluation. *Phys. Med. Biol.*, 55(5):1453, 2010. 239

[358] D. Kadrmas, M. Casey, N. Black, et al. Experimental comparison of lesion detectability for four fully-3D PET reconstruction schemes. *IEEE Trans Med Imaging*, 28(4):523–534, April 2009. 239

[359] L. Tellmann, R. Fulton, U. Pietrzyk, et al. Concepts of registration and correction of head motion in positron emission tomography. *Zeitschrift für medizinische Physik*, 16(1):67–74, 2006. 239

[360] B. F. Hutton, A. Z. Kyme, Y. H. Lau, D. W. Skerrett, and R. R. Fulton. A hybrid 3-D reconstruction/registration algorithm for correction of head motion in emission tomography. *IEEE Trans Nucl. Sci.*, 49(1):188–194, Feb 2002. 239

[361] M. Menke, M. Atkins, and K. Buckley. Compensation methods for head motion detected during PET imaging. *IEEE Trans Nucl. Sci.*, 43(1):310–317, Feb 1996. 239

[362] D. Visvikis, F. Lamare, P. Bruyant, N. Boussion, and C. C. L. Rest. Respiratory motion in positron emission tomography for oncology applications: Problems and solutions. *Nucl. Instrum. Meth. A*, 569(2):453 – 457, 2006. Proceedings of the 3rd International Conference on Imaging Technologies in Biomedical Sciences Innovation in Nuclear and Radiological Imaging: from Basic Research to Clinical Application. 239

[363] E. D. Morris, C. J. Endres, K. C. Schmidt, et al. Chapter 23 – Kinetic modeling in positron emission tomography. In M. N. Wernick and J. N. Aarsvold, editors, *Emission Tomography*, pages 499 – 540. Academic Press, San Diego, 2004. 239

[364] S. Daultrey. *Principal Components Analysis*. Concepts and techniques in modern geography. Geo Abstracts Limited, 1976. 244

[365] P. Legendre and L. F. J. Legendre. *Numerical Ecology*. Developments in Environmental Modelling. Elsevier Science, 1998. 245

[366] C. Chatfield and A. J. Collins. *Introduction to multivariate analysis*. Science paperbacks. Chapman and Hall, 1980. 245

[367] H.-H. Bock. Origins and extensions of the k-means algorithm in cluster analysis. *Journal Électronique d'Histoire des Probabilités et de la Statistique [electronic only]*, 4(2), 2008. 247

[368] S. Lloyd. Least squares quantization in PCM. *Information Theory, IEEE Transactions on*, 28(2):129–137, Mar 1982. 248

[369] S. Ayramo and T. Karkkainen. Introduction to partitioning-based cluster analysis methods with a robust example. *Reports of the Department of Mathematical Information Technology; Series C: Software and Computational Engineering*, C1:1–36, 2006. 248, 249

[370] J. C. Dunn. Well-separated clusters and optimal fuzzy partitions. *Journal of Cybernetics*, 4(1):95–104, 1974. 249

[371] D. L. Davies and D. W. Bouldin. A cluster separation measure. *Pattern Analysis and Machine Intelligence, IEEE Transactions on*, PAMI-1(2):224–227, April 1979. 249

[372] L. Hubert and J. Schultz. Quadratic assignment as a general data analysis strategy. *British Journal of Mathematical and Statistical Psychology*, 29(2):190–241, 1976. 249

[373] P. Jaccard. Étude comparative de la distribution florale dans une portion des Alpes et des Jura. *Bulletin del la Société Vaudoise des Sciences Naturelles*, 37:547–579, 1901. 249

[374] P. J. Rousseeuw. Silhouettes: A graphical aid to the interpretation and validation of cluster analysis. *Journal of Computational and Applied Mathematics*, 20(0):53 – 65, 1987. 249